

学位論文

Development of Neutron-Tagging Techniques and
Application to Atmospheric Neutrino Oscillation
Analysis in Super-Kamiokande

(スーパーカミオカンデにおける中性子検出手法の開
発と大気ニュートリノ振動解析への適用)

平成26年7月博士(物理学)申請

東京大学大学院理学系研究科

物理学専攻

アーヴィン トリスタン ジェームズ

by Tristan James Irvine

2014

Abstract

Neutrino oscillation theory is now well established. The neutrino mixing angles and mass-squared splittings have been precisely measured, by a variety of experiments. However our understanding of this field is still not complete - the neutrino mass hierarchy and CP violating phase continue to elude us.

Sensitivity to neutrino mass hierarchy in the water Cherenkov detector Super-Kamiokande is dependent on its ability to distinguish anti-neutrino and neutrino interactions. This is inherently a difficult task in water Cherenkov detectors, but one possible method is through the detection of neutrons. In a typical charged-current anti-neutrino interaction, $\bar{\nu}_e + p \rightarrow n + e^+$, a neutron is ejected, however this is not true of the corresponding neutrino interaction. In water, these neutrons then thermalize and are captured by hydrogen. A 2.2 MeV γ -ray is emitted, which can be used to tag the neutrons, and thus infer that the preceding interaction was that of an anti-neutrino.

This thesis describes the development of neutron tagging methods and application to the Super-Kamiokande atmospheric neutrino sample. This information is then used to help distinguish between neutrino and anti-neutrino interactions, thus increasing our sensitivity to the neutrino mass hierarchy. A neutron-tagging efficiency of 20.5% is achieved, with a background of 1.8% per atmospheric neutrino event. Enriched neutrino and anti-neutrino samples are constructed, improving the sensitivity of the detector to neutrino mass hierarchy by $\Delta\chi^2 = 0.06$. Three-flavour neutrino oscillation analysis is performed using all data from SK-I to IV (4581.5 days). The normal hierarchy is favoured, with a significance of $\Delta\chi^2(\text{NH-IH}) = -0.9$.

Acknowledgements

Writing this thesis would not have been possible without the support of many wonderful people.

Firstly I'd like to thank my family. There is no way I can list here everything you have done for me. Most of all, thank you for supporting me in all the crazy things I decide to do. I am sure I would not manage so well with a son like this!

Thank you to everyone who persevered in educating me up until this point. My first teacher, Pauline Wilson, for accepting me as a student under such absurd circumstances. My university tutors, Prof. Weidberg, Laura, Georg, and many others, for pushing me to the level I needed to succeed. Special thanks to my classmates and friends, Dan and Nick, without whom I am sure I would not have maintained my sanity until graduation.

I want to thank all my friends in RCCN. Thomas, Andrew, Maggie, Honda-san, Nishimura-san, Euan and Akutsu-kun, thank you for making my life so enjoyable while I have been here. Also Okumura-san, who in addition to being a good friend, has given me so much support and guidance in my time here, both in physics and life. Thank you also to all of my friends in Kashiwa campus, Yoshida-san, and all of my Japanese teachers, who helped me to remember that life is not just about physics!

I must also thank all the members of the SK collaboration, specifically the ATMPD group, for both your advice, and of course your unrelenting work to keep this experiment operational. Thank you to Shiozawa-san, Ed, Mark, Hayato-san and many more, for your critiques and advice that eventually managed to mould me into some sort of a scientist (I hope)! Thank you especially to Roger, for your tireless efforts in dealing with my constant barrage of problems, both in physics, and in real life. Without you I would never have been able to graduate on time.

I want to thank everyone especially for putting up with my health issues over the last few years. Especially to my doctors, Takagi-sensei and Dr. Wheldon, who were able to set me on the path to treating an illness which I thought I would be stuck with for life. I am happy to say today my health is almost totally recovered, a position I would never have thought possible 2 years ago.

My final thanks, must of course go to my advisor, Kajita-sensei, who gave me the opportunity to come here and study this amazing experiment. Thank you for giving me such an interesting and impactful analysis to work on, for letting me have the freedom to explore it, and helping me whenever I got lost. I could not have hoped for such a knowledgeable and kind person to advise me.

Contents

Abstract	i
Acknowledgements	ii
Contents	iii
List of Figures	viii
List of Tables	xx
1 Introduction	1
1.1 Thesis Overview	1
1.2 Author Contributions	2
2 Neutrinos	3
2.1 A History of Neutrinos	3
2.1.1 Neutrino Flavours	3
2.1.2 The Solar Neutrino Problem	5
2.1.3 The Atmospheric Neutrino Anomaly	7
2.1.4 The Solution	8
2.2 Neutrino Oscillation Theory	10
2.2.1 Oscillations in a Vacuum	10
2.2.2 Oscillations in Matter	13
2.2.3 CP Violation	15
2.3 State of the Art	16
2.3.1 Solar Parameters θ_{12} , Δm_{12}^2	17
2.3.2 Atmospheric Parameters θ_{23} , Δm_{23}^2	18
2.3.3 Reactor Experiments, θ_{13}	20
2.4 Summary, Remaining Issues	22
3 Super-Kamiokande	23
3.1 Overview	23
3.1.1 SK Periods	24
3.2 Detector Design	25
3.3 Cherenkov Radiation	26

3.4	Photo-multiplier tubes	27
3.5	The Water System	28
3.6	Air Purification	29
3.7	Front-end Electronics and Data Acquisition	30
3.7.1	Data Acquisition System for SK-I to SK-III	30
3.7.2	Data Acquisition System for SK-IV	33
4	Detector Calibration	35
4.1	PMT Calibration	35
4.1.1	Determining High Voltage for each PMT	36
4.1.2	Relative Gain	37
4.1.3	Absolute gain	37
4.1.4	Quantum Efficiency	39
4.1.5	Timing Calibration	40
4.2	Water Calibration	42
4.2.1	Passage of Photons through Water	42
4.2.2	PMT Surface Reflections, Black Sheet	45
4.3	Energy Scale Calibration	46
4.3.1	High Energy Cosmic-Rays	47
4.3.2	Low Energy Cosmic-Rays	47
4.3.3	π^0 Invariant Mass	49
4.3.4	Decay Electrons	50
4.3.5	Energy Scale Summary	50
5	Monte Carlo Simulation of Atmospheric Neutrinos	52
5.1	Atmospheric Neutrino Flux	52
5.2	Neutrino Interaction Generator	55
5.2.1	Elastic Scattering	56
5.2.2	Single Meson Production	57
5.2.3	Deep Inelastic Scattering	58
5.2.4	Nuclear Effects	59
5.3	Detector Simulation	61
6	Event Reconstruction	64
6.1	Vertex Fitting	64
6.1.1	Ring Counting	66
6.1.2	Precise Single Ring Fitting	67
6.2	Particle Identification	68
6.2.1	Electron-like and Muon-like rings	70
6.3	Momentum Reconstruction	73
6.4	Reconstruction of Single Ring π^0 events	74
6.5	Neutron Reconstructions	75
6.5.1	Bonsai Fit	75
6.5.1.1	Bonsai Vertex Reconstruction	76
6.5.1.2	Bonsai Energy Reconstruction	76
6.5.2	Neut-Fit	78
6.6	Upward-going Muon Reconstruction	79

7	Data Reduction	81
7.1	Fully Contained Reduction	83
7.1.1	1st Reduction (FC1)	83
7.1.2	2nd Reduction (FC2)	83
7.1.3	3rd Reduction (FC3)	84
7.1.3.1	Through-going muon cut	84
7.1.3.2	Stopping-muon cut	86
7.1.3.3	Cable Hole Muons	86
7.1.3.4	Flashers	87
7.1.3.5	Coincidence Muon	87
7.1.3.6	Low Energy Events	88
7.1.4	4th Reduction (FC4)	89
7.1.5	5th Reduction (FC5)	89
7.1.5.1	Invisible Muons	89
7.1.5.2	Coincidence Muons	90
7.1.5.3	Long Tail Flashers	90
7.1.6	Fiducial Volume Selection	90
7.1.7	FC Reduction Summary	92
7.2	Partially Contained Reduction	92
7.2.1	1st Reduction (PC1)	93
7.2.2	2nd Reduction (PC2)	94
7.2.2.1	PC2: SK-I	95
7.2.2.2	PC2: SK-II	95
7.2.2.3	PC2: SK-III and SK-IV	96
7.2.3	3rd Reduction (PC3)	97
7.2.4	4th Reduction (PC4)	97
7.2.4.1	PC4: SK-I and II	97
7.2.4.2	PC4: SK-III and IV	98
7.2.5	5th Reduction (PC5)	99
7.2.5.1	PC5: SK-I and SK-II	100
7.2.5.2	PC5: SK-III and SK-IV	102
7.2.6	Fiducial Volume Selection	105
7.2.7	PC Reduction Summary	106
7.3	Upward-going Muon Reduction	106
7.3.1	1st Reduction (UPMU1)	107
7.3.2	2nd Reduction (UPMU2)	107
7.3.3	Interlude	108
7.3.3.1	Showering Algorithm	109
7.3.4	3rd Reduction (UPMU3)	110
7.3.5	4th Reduction (UPMU4)	112
7.3.6	Background Subtraction	112
7.3.7	UPMU Reduction Summary	114
8	Neutron Tagging	116
8.1	Neutron Simulation	117
8.2	Neutron Tagging Algorithm	119
8.2.1	Initial Candidate Selection	120

8.2.2	Final Candidate Selection	121
8.2.2.1	Number of Hits in 10 ns: N_{10}	122
8.2.2.2	Number of Clustered Hits: N_c	123
8.2.2.3	Number of Hits on Low Probability PMTs: N_{low}	124
8.2.2.4	Number of Hits in 300 ns: N_{300}	125
8.2.2.5	Hit Vector RMS: ϕ_{rms}	126
8.2.2.6	Mean Opening angle: θ_{mean}	126
8.2.2.7	Root-mean-square of hit timing: t_{rms}	126
8.2.2.8	Minimum Root-mean-square of hit timing: $min - t_{rms}$	128
8.2.2.9	Bonsai Fit Variables: BS_{energy} and BS_{wall}	128
8.2.2.10	Neut-Fit Variables: NF_{wall} , ΔN_{10} , Δt_{rms}	130
8.2.2.11	Fit Agreement variables: $(NF - BS)_{dis}$, $(NF - AP)_{dis}$	131
8.2.3	Neural Network	131
8.2.4	Results	134
8.3	Atmospheric Neutrinos	134
8.4	Americium-Beryllium Systematic Error Study	136
8.4.1	Experimental Setup	138
8.4.2	Data Selection	138
8.4.3	Data Analysis	139
9	Oscillation Analysis	142
9.1	Calculation of χ^2	143
9.2	Analysis Binning	144
9.2.1	Neutrino and Anti-neutrino separation	146
9.2.2	Multi-Variate Analysis	151
9.2.2.1	Multi-GeV, Single-Ring, e-like sample	152
9.2.2.2	Multi-GeV, Multi-Ring, e-like samples	153
9.2.2.3	Multi-GeV, Single-Ring, μ -like samples	154
9.2.2.4	Multi-GeV, Multi-Ring, μ -like samples	155
9.3	Systematic Errors	156
9.3.1	Systematic Errors related to Neutrino Flux	158
9.3.1.1	Flux Ratios	158
9.3.1.2	K/ π ratio	159
9.3.1.3	Solar Activity	159
9.3.1.4	Neutrino Production Height	159
9.3.1.5	Matter Effect	160
9.3.1.6	Absolute normalization	160
9.3.2	Systematic Errors related to Neutrino Interactions	161
9.3.2.1	CCQE Cross Section	161
9.3.2.2	Axial Mass	161
9.3.2.3	Single Meson Production	161
9.3.2.4	Coherent Pion Production	163
9.3.2.5	Deep Inelastic Scattering	163
9.3.2.6	Other Cross Section Uncertainties	163
9.3.3	Systematic Errors related to Reduction and Reconstruction Processes	164
9.3.3.1	FC Reduction	164

9.3.3.2	PC Reduction	164
9.3.3.3	UPMU Reduction	165
9.3.3.4	Reconstruction errors	165
9.3.4	Event Selection errors	165
9.3.4.1	Multi-GeV Neutrino and Anti-Neutrino sample errors . .	165
9.4	Mass Hierarchy Sensitivity	166
9.5	Data Fit Results	168
9.6	Discussion and Comparison to other Experiments	174
9.7	The Future	176
10	Conclusion	180
A	Appendix: Systematic Error Tables	182
	Bibliography	185

List of Figures

2.1	Energy spectrum for neutrinos produced in the pp chain, predicted by Bachall’s Standard Solar Model	6
2.2	Hadronic shower and atmospheric neutrinos produced by cosmic rays. Figure from Los Alamos Science	7
2.3	Ratio of the data to the MC events as a function of L/E, from Super-Kamiokande. The solid black histogram represents the best fit for oscillation, whilst the disfavoured blue dashed, and dotted red lines are the best fit expectations for neutrino decay, and neutrino decoherence respectively.	9
2.4	This figure shows the oscillation probability of $\nu_e \rightarrow \nu_e$, for a 3MeV neutrino. It may be thought of as the probability that an initial electron neutrino will be observed as an electron neutrino after travelling distance L . For this plot, $\Delta m_{23}^2 = 2.4 \times 10^{-3} eV^2$, and $\Delta m_{12}^2 = 7.6 \times 10^{-5} eV^2$. The high frequency oscillations are due to Δm_{23}^2 , and if a detector is placed at 1km then you may approximate the mixing matrix to its 2-dimensional form considering only this mixing. Likewise, for the low frequency oscillations, the driving factor is Δm_{12}^2 , so to optimally measure this, a detector may be placed at 50km, and again the mixing matrix may be reduced to an oscillation between these two states.	12
2.5	This figure represents the difference between probability of oscillation $\nu_e \leftrightarrow \nu_\mu$, between normal and inverted mass hierarchies, for neutrinos incident on Super Kamiokande. The y-axis is zenith angle, such that the upper half of the plot represents downward going neutrinos, and the bottom half upward going neutrinos. The dominant area of resonant enhancement can be seen around $2 - 10 GeV$. If we instead look at anti-neutrino oscillation, the signs in this plot are switched, so the enhancement occurs in inverted, rather than normal hierarchy.	15
2.6	The two possibilities for neutrino mass states, known as the normal and inverted hierarchies. The green forward-slash fill represents ν_e , red back-slash is ν_μ , and vertical blue lines is ν_τ . The difference between the mass states Δm^2 is well known, thanks to neutrino oscillation experiments, but at the time of writing, which mass state is the heaviest is still unknown. This plot is not to scale.	16
2.7	This figure shows the combined result of 8B solar neutrino flux measurements, from the salt phase of SNO [1], and ES result from SK in 2002 [2]. The dotted line represents the standard solar model prediction, and the contours represent a joint fit between the two experiments. Figure source [1]	18

2.8	On the top is the energy spectrum for events reconstructed as CC, at the MINOS far detector. The bottom figure shows the ratio of data to a null oscillation prediction, with the disfavoured decay and decoherence models also shown. [3]	19
2.9	This plot shows 90% confidence level contours for T2K, MINOS, and SK superimposed. Taken from [4]	20
2.10	This plot shows the result from Daya-Bay in 2012. The observed energy spectrum, and ratio with the null-oscillation hypothesis are displayed on top and bottom figures respectively. Taken from [5]	21
3.1	A schematic of the layout of Super-Kamiokande	24
3.2	The frame structure of the PMT support system in the SK tank	26
3.3	The structure of an ID PMT in SK.	27
3.4	The wavelength dependent quantum efficiency of the bialkali photo-cathode.	28
3.5	A schematic of the water purification system used in SK.	29
3.6	The varying water temperature across the SK tank. Water input is at the bottom of the tank (negative z).	30
3.7	A schematic showing the layout of the DAQ used in SK-I to SK-III	31
3.8	Overview of the trigger system in SK-I to III	32
3.9	Block diagram for the new DAQ in SK-IV. Taken from [6]	33
4.1	Xe light emitting from a scintillator ball to calibrate the PMT high voltage in the tank. The red dots illustrate positions of the pre-calibrated reference PMTs.	36
4.2	The relative gain difference of each PMT from calibration using a nitrogen-laser-driven dye laser.	38
4.3	The charge distribution from Ni-Cf single p-e calibration source, after relative gain corrections had been applied.	39
4.4	This plot shows the relative PMT hit probability dependent on z (cm) position in the tank. The red points are from Ni-Cf source, and the blue points are the MC, before QE correction.	40
4.5	The setup of the dye laser used to calibrate the timing and relative gain of the ID PMTs.	41
4.6	Charge vs Time plot for readout channel 00010. The black line is a fitted polynomial used for calibration, referred to as the "TQ map".	42
4.7	The laser system used to calibrate light scattering and absorption through water. B1-5 represent different regions of the tank in which analysis was performed.	43
4.8	The results of the fit calibration for water scattering parameters, for April 2009. The dots represent values measured in data, and the lines are the corresponded fitted functions.	44
4.9	The split up of data taken from the laser beam (405 nm) used for water and PMT reflection calibration. Shown is the timing (ns) of each PMT hit, after ToF correction, for 6 different regions of the tank (the top plot is of the tank top wall, and the remaining 5 are barrel regions shown in figure 4.7). The hits between the two left-most blue lines, are used for water transparency calibration, and those between the two right-most lines are used for reflection calibration.	45
4.10	The experimental set-up used to tune the black sheet reflectivity.	46

4.11	High energy cosmic ray stopping muon sample, ratio between momentum P_{pe} , calculated from the total number of photo-electrons collected by each PMT, and the range of the particle in cm. The discrepancy between data and MC is used as energy calibration in this momentum range. Data shown is from the SK-II period.	48
4.12	Low energy cosmic ray muon sample, ratio between momentum P_{pe} , calculated from the total number of photo-electrons collected by each PMT, to P_θ , calculated from the Cherenkov opening angle. The discrepancy between data and MC is used as energy calibration in this momentum range. Data shown is from the SK-I period.	48
4.13	Reconstructed π^0 invariant mass, for data and MC in black and red respectively.	49
4.14	The summary of all absolute energy scale data-MC discrepancies, for SK-I to IV.	51
5.1	East-west asymmetry in neutrino flux at SK, due to deflection of primary cosmic rays by the Earth's geomagnetic field. Plots taken from [7].	53
5.2	Zenith angle distribution for neutrino flux incident on SK. You may note the peak at the horizon (around $\cos \theta = 0$), and the slight asymmetry between upward and downward going fluxes. These effects are more prominent in low energy particles, which are more sensitive to magnetic field deflection effects.	54
5.3	Additional cosmic ray vectors now contribute to the horizon neutrino flux in the 3-d calculation of Honda flux, compared to the previous 1-d version.	54
5.4	Flux comparison with cosmic ray muon data. From left to right, Tsukuba (ground), Norikura (mountain) and Ft. Summer (balloon)	55
5.5	Atmospheric neutrino flux incident on SK, taken from the Honda 2011 paper. Differences to other models are shown, and taken as a systematic error in analysis.	55
5.6	The breakdown of expected neutron multiplicity for each neutrino interaction mode. The plot shows SK-IV atmospheric neutrino MC Multi-GeV 1-ring electron like sample, normalized to the livetime of the equivalent data-set (shown in black dots). This is the most relevant sample for the neutrino mass hierarchy. In this sample the dominant production modes are CCQE and single-pion production.	57
5.7	The agreement of NEUT predictions (black line) of free nucleon charged current quasi-elastic scattering cross section, with experimental data. The experiments considered in figure (a) are ANL (triangle) [8], GGM (square) [9] and Serpukov (circle) [10]. In figure (b), these are GGM (square) [11] and Serpukov (circle) [10]. Figures taken from [12].	58
5.8	The agreement of NEUT predictions (black line) of single pion production cross section, with experimental data. The experimental data considered is from ANL (triangle) [13], and GGM (circle) [14]. The figures are taken from [12].	58

5.9	The agreement of the total neutrino and anti-neutrino charged current cross sections, between the NEUT model and experimental data. In figure (a), the data used is from experiments GGM73 [15], GGM79 [16], GGM81 [17], SKAT79 [18], BEBC79 [19], IHEP79 [20], ANL79 [21], BNL80 [22], BNL81 [23] and IHEP96 [24]. For the anti-neutrino figure (b), the experiments used are GGM79 [25], GGM81 [17], IHEP79 [20] and IHEP96 [24]. The figures are taken from [12].	59
5.10	Comparison between NEUT simulation, and experimental data. Cross section contributions from charged current elastic scattering, single pion production, and deep inelastic scattering are shown. Experimental data is overlaid from [26].	60
5.11	Tuning of nuclear effect cross sections to $\pi - {}^{12}\text{C}$ scattering data. The dots are taken from experimental data in [27]. The dashed and solid lines represent before and after tuning.	60
5.12	Absolute neutron yields after impact of 256 MeV protons on a sphere of ${}^{238}\text{U}$. Lines are simulated by CALOR, and experimental data is from [28]. This plot is taken from [29].	62
5.13	Neutron multiplicity simulated by HETC (open dots), compared to experimental data (solid triangles) for a 2 GeV proton interacting in Au. The solid dots are before detector efficiency is taken into account. This study and plot are from [30].	62
6.1	A depiction of the co-ordinate system used in SK. θ (zenith angle) is measured downwards from positive z	65
6.2	On the left, is a 2-d depiction of ring candidate searching. Each PMT has a charge-weighted cone drawn out from it at 42° , and the points with maximal charge are taken as ring candidates. The plot on the right is an example of the result of this, in a spherical co-ordinate system centred on the TDC-fit vertex. The angles with peaks of charge represent most probable rings.	66
6.3	Output of $L(2 \text{ rings}) - L(1 \text{ ring})$ for SK-IV, < 1330 MeV neutrino events. The fraction of different event modes in each sample is shown by the coloured lines.	67
6.4	Vertex resolution for SK-IV sub-GeV single-ring events, separated into μ -like and e-like.	68
6.5	Angular resolution for SK-IV fully contained sub-GeV single-ring events, separated into μ -like and e-like.	69
6.6	Example Cherenkov ring patterns for an electron (left), and a muon (right). The top and bottom circles represent the top and bottom of the SK tank, and the long rectangle represents the barrel. Auxiliary event information is provided around the edges (but it is not important to understand).	69
6.7	A depiction of how the muon track length is treated when calculating the expected charge. When a muon travels distance dx , Cherenkov photons are emitted to an area of $2\pi r \sin \theta(dx \sin \theta + rd\theta)$	72
6.8	Output particle identification likelihoods (definition here 6.12) for SK-IV, sub-GeV fully contained single-ring events. The left and right plots show true CC-quasi elastic electron and muon events respectively.	73

6.9	The timing residual probability density function measured by LINAC calibration data.	77
6.10	The energy distributions of upward-going muon showering, non-showering, and stopping events.	79
6.11	The vertex resolution of upward-going muon fitter precise-fit, based off a 40 year MC study.	80
6.12	The calculation of the end-point of a stopping muon track. The dotted line shows the 40% of the average value in the first 1.5 m of the track.	80
7.1	The different reduction types for selecting atmospheric neutrino events	82
7.2	The energy spectrum for each sample of events, after reduction.	82
7.3	FC2 distributions of NHITA ₈₀₀ , for data, MC, and then the final selection with data and MC superimposed. The MC is a pure atmospheric neutrino sample, so the second plot shows the efficiency of this cut. In the final sample the events which remain in the cut region have either $PE_{total} > 100,000$, or the OD trigger did not fire.	84
7.4	FC2 distributions of PE_{max}/PE_{300} . Plots of data, MC and then the final selection with data and MC superimposed are shown. The MC consists of pure atmospheric neutrino events.	85
7.5	A schematic of the cable hole veto counters in SK.	87
7.6	ID timing distributions of a typical flasher (i), and a typical neutrino (ii) event. The two lines indicate the timing region scanned in calculating $NMIN_{100}$	88
7.7	FC5 Coincidence muon cut variable PE_{late} . From top to bottom, the plots show the data, atmospheric neutrino MC, and then the final selection of events with data and MC superimposed. It is also required that $PE_{500} < 300$ p-e, so there are a few events remaining in the final sample that have $PE_{late} > 20$	91
7.8	The event rate for each of FC1-5, and FCFV reductions, for all of SK-IV. The increasing event rate is due to the PMT degradation causing gain increase of 2% per year, and is accounted for in analysis. The event rate spike around March 2009 is due to faults in the HV system.	92
7.9	Explanation of OD clustering algorithm. The charge in each patch is proportional to the size of the circle. The charge is added to a cluster in the direction of the largest charge gradient.	95
7.10	The number of hits in the 2nd largest OD charge cluster. If there are two large clusters, they likely represent entrance and exit points in an event. As PC events must originate in the ID, these events may be cut. The MC shows a simulated pure atmospheric neutrino sample, and the final sample is the agreement between data and MC for this variable after the final PC selection.	96
7.11	These are the selection criteria in PC4 for SK-III and IV, used to reject muon events that originated outside the inner detector. The dotted line shows the data, after the output of PC3. The solid line shows MC, which may be thought of as the expectation for a pure PC neutrino sample.	98
7.12	These plots show the distance from the reconstructed muon vertex to the nearest corner of the tank. MC is a sample of pure atmospheric neutrino. This cut is used to remove corner-clipping muons. The bottom plot shows data-MC agreement after the final selection of PC events.	104

7.13	NCLSTA5(x) gives the number of OD PMTs inside the x-th highest charge cluster. Large values for two clusters suggests a through-going muon event, which is then cut.	104
7.14	Total ID p-e as a function of track length. Data taken with down-going cosmic ray muon calibration sample.	108
7.15	Primary methods of muon energy loss, when travelling through water. The line (a) shows energy loss via ionization, (b) shows energy loss via Bremsstrahlung, and (c) is the total.	109
7.16	The thru-mu showering vs non-showering selection criteria, shown here with SK-IV dataset. Events above the red line are classified as showering, and below are classified as non-showering.	111
7.17	The zenith and azimuthal dependence of Stopping and through-going muons for SK-III. Some above horizon events have been included for demonstration of this effect.	113
7.18	The 1-dimensional projection of the azimuthal dependence of UPMU background. Events coming from above the horizon are shown with no fill, and upward-going muons are shown with hashed fill.	113
7.19	Extra background contamination in stop-mu and thru-mu samples, fitted to a constant + exponential function of zenith angle. The triangles represent the approximately constant background in azimuthal region 1, and the circles are the exponentially increasing background in region 2.	114
8.1	Construction of neutron MC. After $18\mu\text{s}$ dummy trigger data is convoluted with simulated neutrons produced by an atmospheric neutrino interaction.	117
8.2	Number of 2.2 MeV γ candidates (before neural network selection) per day, as a function of run number in SK-IV. The dummy trigger data taking period is shaded in red. The average candidates per event for the dummy trigger period is 5.34/event, and the average for all of SK-IV is 5.54/event. The gradient is consistent with a 2% increase in PMT gain per year.	118
8.3	Neutron travel distance from the initial neutrino interaction vertex, according to the atmospheric neutrino MC simulation.	118
8.4	Showing the time resolution of final selection of neutrons in 500 years of MC. The blue line shows the cut for calculating efficiency and background of the neutron tagging algorithm.	119
8.5	The increase in number of γ candidates due to the PMT after-pulse. Scanning is preformed after $18\mu\text{s}$	121
8.6	Values of N_{10} used to select initial 2.2 MeV candidates. Background increases exponentially as the required N_{10} is reduced.	121
8.7	N_{10} variable as a neural network input. The plot shows a comparison of neutron capture signal (green), background (blue), data (black dots) and MC total (red line). The normalization is explained in section 8.2.2	122
8.8	Clusters of hits variable, $N_{10} - N_c$. The plot shows a comparison of neutron capture signal (green), background (blue), data (black dots) and MC total (red line). The normalization is explained in section 8.2.2	123
8.9	The varying acceptance requirements for the N_{low} cut, shown as a function of tank coordinates.	124

8.10	Hits on low probability PMTs, $N_{10} - N_{low}$. The plot shows a comparison of neutron capture signal (green), background (blue), data (black dots) and MC total (red line). The normalization is explained in section 8.2.2	125
8.11	The utility of the N_{300} cut. Figure (a) shows a typical neutron capture event, and figure (b) shows a hypothetical background signal to be rejected. The blue lines correspond to PMT dark noise, and the red is some signal.	125
8.12	Number of hits in 300 ns, $N_{300} - N_{10}$. The plot shows a comparison of neutron capture signal (green), background (blue), data (black dots) and MC total (red line). The normalization is explained in section 8.2.2	126
8.13	Root-mean-square of the azimuthal angle of 2.2 MeV candidate hit vectors ϕ_{rms} . The plot shows a comparison of neutron capture signal (green), background (blue), data (black dots) and MC total (red line). The normalization is explained in section 8.2.2	127
8.14	Mean value of hit opening angles, θ_{mean} . The plot shows a comparison of neutron capture signal (green), background (blue), data (black dots) and MC total (red line). The normalization is explained in section 8.2.2	127
8.15	The root-mean-square of the timing of candidate hits, t_{rms} . The plot shows a comparison of neutron capture signal (green), background (blue), data (black dots) and MC total (red line). The normalization is explained 8.2.2	128
8.16	The selection of $min - t_{rms}$ hit clusters. Optimal selections for clusters of 3-6 hits are shown, for an example candidate where $N_{10} = 9$. Possible background hits on the fringes of the candidate time are ignored.	128
8.17	$min - t_{rms}$ of clusters of 6 hits (left) and 3 hits (right). The plot shows a comparison of neutron capture signal (green), background (blue), data (black dots) and MC total (red line) comparison. The normalization is explained 8.2.2	129
8.18	Distributions of BS_{wall} and BS_{energy} for 2.2 MeV γ candidate events. The normalization of BS_{energy} is different for signal and background, as many background events fail to reconstruct at this stage. The plots show a comparison of neutron capture signal (green), background (blue), data (black dots) and MC total (red line). The normalization is explained in section 8.2.2	129
8.19	The distance to the wall from Neut-Fit vertex, NF_{wall} . The plot shows a comparison of neutron capture signal (green), background (blue), data (black dots) and MC total (red line). The normalization is explained in section 8.2.2	130
8.20	The variables Δt_{rms} and ΔN_{10} are shown in the left and right figures, respectively. The plots show a comparison of neutron capture signal (green), background (blue), data (black dots) and MC total (red line). The normalization is explained in section 8.2.2	131
8.21	The variables $(NF - BS)_{dis}$ (distance between Bonsai reconstructed candidate vertex, and Neut-Fit reconstructed candidate vertex) and $(NF - AP)_{dis}$ (distance between Neut-Fit reconstructed candidate vertex, and APFit vertex), are shown in the left and right figures, respectively. The plots show a comparison of neutron capture signal (green), background (blue), data (black dots) and MC total (red line). The normalization is explained in section 8.2.2	132

- 8.22 The neural network output for selecting final neutron candidates. Everything to the right of the dotted cut line is selected as a neutron capture event. The small peak in the background histogram at NN output ~ 1 is due to events where the secondary particle bank is overfilled. For these events some true neutron capture information is not stored, and some candidates are mis-classified as background. The data-MC discrepancy in the far left bin looks drastic on a log-scale plot, but this represents $< 0.1\%$ of total background events. The plot shows a comparison of neutron capture signal (green), background (blue), data (black dots) and MC total (red line). The normalization is explained in section 8.2.2 133
- 8.23 The dependence of 2.2 MeV detection efficiency on the distance travelled by the neutron (left), and the visible energy from the neutrino interaction (right). Efficiency is defined as the number of selected candidates corresponding to true neutrons, per number of true neutron capture events in each bin. 135
- 8.24 The efficiency of detecting neutrons as a function of neutrino (APFit) vertex position throughout the ID. Only neutrino events passing the fiducial volume cut ($dWall > 200$ cm) are considered. 135
- 8.25 Final selected 2.2 MeV gamma candidates timing distribution. The primary trigger is at $t = 0$. Blue curve is a best exponential fit using chi-squared method. The neutron capture lifetime is calculated to be $205.2 \pm 3.7 \mu\text{s}$. The background rate is set to 0.0184 / neutrino event. Data is taken from all of SK-IV (1775.6 days) 136
- 8.26 These plots show data-MC comparisons for neutrons tagged in the SK-IV 1775.6 days dataset. The top left plot shows the average multiplicity of neutrons, the top right plot shows the number of neutrino events with ≥ 1 neutrons, the bottom left plot shows the neutron multiplicity in Sub-GeV events ($E_{vis} < 1330$ MeV), and the bottom right plot shows neutron multiplicity in Multi-GeV events ($E_{vis} \geq 1330$ MeV). The multiplicity plots are normalized to the number of neutrino events. The number of events plot (top right) is normalized to data livetime and oscillated under a 2 flavour approximation: $\Delta m^2 = 2.5 \times 10^{-3}$ and $\sin^2 2\theta = 1.0$ 137
- 8.27 Am-Be crystal embedded in a 5 cm cube of BGO scintillator. This is held in an acrylic case. 138
- 8.28 The total p-e from 4.4 MeV γ scintillation events, with the Am-Be source positioned at the centre of the tank. Events with $750 < \text{p-e} < 1050$ are selected. 139
- 8.29 The timing distribution of tagged 2.2 MeV γ candidates, after triggering on a prompt 4.4 MeV γ ray from the Am-Be neutron source. The dots are data-points, and the blue line is a best fit to a constant background + exponential decay, where τ is the neutron capture lifetime in μs , and signal fraction is the fraction of all tagged events expected to be neutrons. 141

9.1	The multiplicity of neutrons following neutrino interactions in the Multi-GeV 1-ring electron-like sample (left) and MultiGeV Multi-ring electron-like sample (right). The multi-ring sample consists of more deep inelastic scattering events, so neutrons are significantly less useful in this sample. However the excess in anti-neutrino 1-neutron events from CCQE interactions is still apparent. Only CC events corresponding to sample type are shown (i.e. for e-like samples, only CC ν_e and CC $\bar{\nu}_e$), and all histograms are normalized to 1. For use in analysis, any events producing >5 neutrons are added into the 5 neutron bin.	148
9.2	The number of decay electrons, following neutrino interactions in the MultiGeV 1-ring electron-like sample (left) and MultiGeV 1-ring muon-like sample (right). In the muon sample, many more decay-electrons are produced in general, however the excess in the neutrino sample is still apparent. Only CC events corresponding to sample type are shown (i.e. for e-like samples, only CC ν_e and CC $\bar{\nu}_e$), and all histograms are normalized to 1.	149
9.3	The number of Cherenkov rings, following neutrino interactions in the MultiGeV Multi-ring electron-like sample. There is some excess in the true CC ν sample, due to the additional charged hadrons produced in this interaction. Only CC events corresponding to sample type are shown (i.e. for e-like samples, only CC ν_e and CC $\bar{\nu}_e$), and all histograms are normalized to 1.	149
9.4	This plot shows the farthest decay-electron travel distance $ \text{neutrino vertex} - \text{decay electron vertex} $, in the Multi-GeV 1-ring μ -like sample. Only CC events corresponding to sample type are shown (i.e. for e-like samples, only CC ν_e and CC $\bar{\nu}_e$). All histograms are normalized to 1.	150
9.5	This plot depicts the fraction of reconstructed energy in the first ring divided by the total energy in the event for the MultiGeV Multi-Ring e-like sample. Only CC events corresponding to sample type are shown (i.e. for e-like samples, only CC ν_e and CC $\bar{\nu}_e$) and all histograms are normalized to 1.	150
9.6	The particle identification likelihood output, for the Multi-GeV 1-ring e-like sample. $\text{PID} < 0$ is required to classify the ring as e-like. Only CC events corresponding to sample type are shown (i.e. for e-like samples, only CC ν_e and CC $\bar{\nu}_e$), and all histograms are normalized to 1.	151
9.7	The decay time of the decay-electron reconstructed farthest from the neutrino interaction, for the MultiGeV Multi-Ring μ -like sample. Only CC events corresponding to sample type are shown (i.e. for e-like samples, only CC ν_e and CC $\bar{\nu}_e$), and all histograms are normalized to 1.	151
9.8	These plots show the data-MC agreement in SK-IV for the number of neutrons and number of decay-electrons in the MultiGeV 1 ring e-like sample. The colours represent the different event types each sample consists of: green and green-hashed are ν_e and $\bar{\nu}_e$ respectively. Purple is true ν_μ events, and yellow is neutral current events. The MC events are normalized to the livetime of the dataset, and oscillated in a 2 flavour framework with $\sin^2 2\theta = 1.0$, and $\Delta m^2 = 2.5 \times 10^{-3} eV^2$. Systematic errors are not included here.	153

- 9.9 These plots show the data-MC agreement, and the ν_e - $\bar{\nu}_e$ separation in the multi-variate analysis output. The event sample is the MultiGeV Multi-ring e-like sample for SK-IV. The cut position is shown here as a dotted blue line at 0.72, chosen automatically (see 9.2.2). Events >0.72 are classified as ν_e -like, and <0.72 are $\bar{\nu}_e$ -like. For the right-hand plot, both histograms are normalized to 1. In the left-hand plot, the MC events are normalized to the livetime of the dataset, and oscillated in a 2 flavour framework with $\sin^2 2\theta = 1.0$, and $\Delta m^2 = 2.5 \times 10^{-3} eV^2$. Systematic errors are not included here. 155
- 9.10 These plots show the data-MC agreement, and the ν_μ - $\bar{\nu}_\mu$ separation in the multi-variate analysis output. The event sample is Multi-GeV single-ring μ -like, for SK-III. The cut value is chosen automatically (described at 9.2.2), shown here as a dotted blue line at 0.62. Events >0.62 are classified as ν_μ -like, and <0.62 are $\bar{\nu}_\mu$ -like. For the right-hand plot, both histograms are normalized to 1. In the left-hand plot, the MC events are normalized to the livetime of the dataset, and oscillated in a 2 flavour framework with $\sin^2 2\theta = 1.0$, and $\Delta m^2 = 2.5 \times 10^{-3} eV^2$. Systematic errors are not included here. 156
- 9.11 These plots show the data-MC agreement, and the ν_μ - $\bar{\nu}_\mu$ separation in the multi-variate analysis output. The event sample is Multi-GeV multi-ring μ -like, for SK-II. The cut value is chosen automatically (described at 9.2.2), shown here as a dotted blue line at 0.75. Events >0.75 are classified as ν_μ -like, and <0.75 are $\bar{\nu}_\mu$ -like. For the right-hand plot, both histograms are normalized to 1. In the left-hand plot the MC events are normalized to the livetime of the dataset, and oscillated in a 2 flavour framework with $\sin^2 2\theta = 1.0$, and $\Delta m^2 = 2.5 \times 10^{-3} eV^2$. Systematic errors are not included here. 157
- 9.12 The flavour ratio between the Honda flux and competing flux models used for systematic error calculation. The solid black line shows the ratio FLUKA/Honda flux, and the dashed red line depicts the Bartol/Honda flux. The spike around 8 GeV in the FLUKA flux is due to a flux calculation technicality, and has been corrected for in the error evaluation. . . 158
- 9.13 The anti-neutrino / neutrino double ratio between the Honda flux and competing flux models used for systematic error calculation. The solid black line shows the ratio FLUKA/Honda flux, and the dashed red line depicts the Bartol/Honda flux. The left plot shows the double ratio of $\bar{\nu}_e/\nu_e$ and the right plot shows $\bar{\nu}_\mu/\nu_\mu$ 159
- 9.14 The neutrino path length, as a function of zenith angle. The solid line represents the path lengths provided in the default Honda flux model, and the dotted line shows the path-lengths after a 10% change in the atmospheric density. 160
- 9.15 The top plot shows the relative uncertainty in each aspect of the flux model, where δ_π , δ_K , δ_σ , and δ_{air} are the uncertainties on pion production, kaon production, hadronic interaction cross sections and atmospheric density profile respectively. The bottom plot is the calculated uncertainty on the absolute normalization of the neutrino flux. 162

- 9.16 These plots show the ratio of the CCQE cross section calculated by the Nieves model to that calculated by the fermi gas model used in SK. The top left plot displays $\nu_e + \bar{\nu}_e$ and $\nu_\mu + \bar{\nu}_\mu$ in the solid and dashed lines respectively. The top right plot shows the ratio $(\nu_\mu + \bar{\nu}_\mu)/(\nu_e + \bar{\nu}_e)$, and the bottom plot is $\bar{\nu}/\nu$ 163
- 9.17 Projected χ^2 plots for the mass hierarchy sensitivity. The true hierarchy is taken to be normal, and the black and green lines represent fits assuming the normal and inverted hierarchy respectively. The minimum $\Delta\chi^2$ value of the inverted hierarchy at $\Delta\chi^2 = 1.87$ represents our sensitivity to the mass hierarchy in this case. 168
- 9.18 Assuming the normal hierarchy, these plots show fitted χ^2 values for points across the oscillation parameter space. The minimum value of χ^2 is subtracted from every point. From top right going clockwise the plots show: $\sin^2 \theta_{23} - \Delta m_{23}^2$ contour plot, minimum Δm_{23}^2 , minimum δCP , and minimum $\sin^2 \theta_{23}$. The coloured lines on the plots represent the confidence level contours, 99% (orange), 90% (blue) and 68% (red). In the 1d plots, these correspond to $\Delta\chi^2 = 6.6, 2.7$ and 1.0 respectively. In the 2d case, these contours correspond to $\Delta\chi^2 = 9.2, 4.6$ and 2.3 . The black line in the 1d plots represents the projected minimum χ^2 values. The dataset is all of SK-I to IV. 170
- 9.19 Assuming the inverted hierarchy, these plots show fitted χ^2 values for points across the oscillation parameter space. The minimum value of χ^2 is subtracted from every point. From top right going clockwise, the plots show: $\sin^2 \theta_{23} - \Delta m_{23}^2$ contour plot, minimum Δm_{23}^2 , minimum δCP , and minimum $\sin^2 \theta_{23}$. The coloured lines on the plots represent the confidence level contours, 99% (orange), 90% (blue) and 68% (red). The black line in the 1d plots represents the projected minimum χ^2 values. The data-set is all of SK-I to IV. 171
- 9.20 The data-MC agreement for each sub-sample, after fitting, with combined data from SK-I to IV. The oscillation parameters used can be seen in table 9.9. Multi-GeV refers to the Multi-GeV 1-ring sample, and Multi-Ring refers to the Multi-GeV Multi-Ring sample. The inverted hierarchy best fit is in red, and normal hierarchy in green (these are mostly overlaid and cannot be distinguished). The 4 samples on the left are not divided into zenith bins during analysis, so they are shown in momentum bins. The remaining 4 columns of samples, are divided into momentum and zenith bins in analysis, but here only the projection onto zenith bins is shown. 172
- 9.21 Data vs MC for the new ν -like, $\bar{\nu}$ -like, and Multi-Ring Other samples. The dataset shown includes all of SK-I to IV. The MC is oscillated using the best fit parameters shown in table 9.9. Multi-GeV refers to the Multi-GeV 1-ring samples, and Multi-Ring to the Multi-GeV Multi-Ring samples. The x-axis shows the zenith angle $\cos \theta$, where $\cos \theta = -1$ represents upward-going events. The blue line represents the normal hierarchy expectation, and the red line the inverted hierarchy. The momentum shown at the top of each plot is the lower end of the momentum bin. 173
- 9.22 Comparison of the 90% confidence level contour between the current SK official analysis (green) and analysis with the updated samples presented in this thesis (blue). 174

9.23	The contribution to $\Delta\chi^2(\text{NH-IH})$ for each sample in the analysis. The samples favouring normal hierarchy are primarily the Multi-GeV 1-ring e-like samples, and the Multi-GeV Multi-Ring Other sample.	175
9.24	Comparison of the 90% confidence level contours between the analysis presented in this thesis (blue) and published results from the MINOS (green) [31] and T2K (red) [32] experiments.	175
9.25	Expected future significance of neutrino mass hierarchy in Super-Kamiokande. The green and red dotted lines indicate 1σ and 2σ significance respectively. The oscillation parameters are as described at 9.7.	176
9.26	Expected significance of neutrino mass hierarchy in the $\text{NO}\nu\text{A}$ experiment, after 3 years each of ν_μ and $\bar{\nu}_\mu$ beam. The blue (dashed red) curves show the significance assuming the normal (inverted) hierarchies. Plot taken from [33].	177
9.27	Expected sensitivity to the neutrino mass hierarchy of the proposed INO experiment. The blue shaded region represents different values for true $\sin^2\theta_{13}$. Plot taken from [34].	178
9.28	Expected sensitivity to the neutrino mass hierarchy of the Hyper-Kamiokande experiment. The different colours and shaded regions represent the expected hierarchy sensitivity given different true values of other neutrino oscillation parameters. Plot taken from [35].	179
9.29	Expected mass hierarchy sensitivity of various future experiments. The widths represent uncertainty due to oscillation parameters. Plot taken from [36].	179

List of Tables

3.1	A summary of the differences between each of the SK periods	25
3.2	Trigger thresholds for each trigger type in SK-I to III	32
3.3	Trigger information for SK-IV	34
4.1	Absolute gain conversion factors between single photo-electron events, and output PMT charge.	38
6.1	Vertex and angular resolutions for MS-Fit reconstruction of fully con- tained neutrino events.	68
7.1	Summary of the efficiencies, remaining background, and number of events remaining after the FC reduction process.	93
7.2	PC Summary Table	106
7.3	Approximate events remaining after each UPMU reduction step.	114
7.4	Summary of the remaining events, and background subtraction for the data sample remaining after UPMU reduction	115
8.1	The differences in neutron tagging efficiency, and training time, for each neural network layout that was tested. The efficiencies shown are relative to the result given by the 16:14:7:1 architecture.	133
8.2	Final efficiency and background rate of the neutron tag algorithm, after each stage of selection	134
8.3	A comparison of the expected and measured neutron capture events in the atmospheric neutrino SK-IV data-set (1775.6 days). Most of the data-MC discrepancy is from very high energy (>30 GeV events). The MC is nor- malized by data livetime, and oscillated under a 2 flavour approximation: $\Delta m^2 = 2.5 \times 10^{-3}$ and $\sin^2 2\theta = 1.0$	136
8.4	Estimated efficiency of neutron tagging, using Am-Be data, compared to the expectation from a 2.2 MeV γ -ray MC. The efficiencies here are higher than those quoted previously, as the neutron capture vertex is now known to < 20 cm.	140
9.1	Summary for selection of Fully Contained Sub-GeV event samples	145
9.2	Summary for selection of Fully Contained Multi-GeV event samples	146
9.3	Multi-GeV 1-ring e-like sample, split into ν_e -like and $\bar{\nu}_e$ -like. The top half of the table shows the estimated event breakdown of each sample, constructed with MC information. The bottom half shows a total data- MC comparison. The data used is all of SK-I to IV.	153

9.4	Multi-GeV Multi-ring e-like sample, split into ν_e -like and $\bar{\nu}_e$ -like. The top half of the table shows the estimated event breakdown of each sample, constructed with MC information. The bottom half shows a total data-MC comparison. The data used is all of SK-I to IV.	154
9.5	Multi-GeV 1-ring μ -like sample, split into ν_μ -like and $\bar{\nu}_\mu$ -like. The top half of the table shows the estimated event breakdown of each sample, constructed with MC information. The bottom half shows a total data-MC comparison. The data used is all of SK-I to IV.	155
9.6	Multi-GeV Multi-ring μ -like sample, split into ν_μ -like and $\bar{\nu}_\mu$ -like. The top half of the table shows the estimated event breakdown of each sample, constructed with MC information. The bottom half shows a total data-MC comparison. The data used is all of SK-I to IV.	157
9.7	Chosen “true” oscillation parameters for the mass hierarchy sensitivity study.	167
9.8	Improvement in sensitivity to neutrino mass hierarchy due to the new ν - $\bar{\nu}$ samples.	167
9.9	Oscillation analysis best fit point for normal and inverted hierarchy assumptions.	169
9.10	Oscillation analysis 90% confidence levels for normal and inverted hierarchy assumptions.	169

To my brother

Chapter 1

Introduction

Of the particles predicted by the Standard Model, the neutrino is undoubtedly among the most elusive. As leptons with no charge or mass, interacting with their surroundings only via the weak force, it is a considerable challenge to observe these particles at all. After neutrino mixing was observed for the first time in the 1990s, this experimental challenge was extended to a theoretical one - the otherwise well validated Standard Model could not justify neutrino mixing, unless the neutrinos had non-zero mass. Even today, while many important neutrino mixing parameters have now been precisely observed, still mysteries remain - what is the absolute mass and mass hierarchy of neutrinos? Can we see evidence of CP violation in the lepton sector, and possibly account for the matter-antimatter asymmetry of our universe? It is an exciting time to be a part of the neutrino physics community.

1.1 Thesis Overview

In chapter 2, basic neutrino physics will be explained, including a brief history of neutrino experiments, the current state of the art, and neutrino oscillation theory. The main content of this work relates to atmospheric neutrinos, which are explained here, as well as some overview of other prominent neutrino sources. The reader may thus gain the background necessary to understand the topics presented in later analysis.

Chapter 3 describes Super-Kamiokande, the light water Cherenkov detector used to collect data for this analysis, and chapter 4 goes into the work done to calibrate this detector. The various systems that come together to make the detector functional are explained - basic Cherenkov detector theory, photo-multiplier tubes, the water system, detector electronics, and others.

Chapter 5 covers neutrino event simulation, including the initial atmospheric neutrino flux prediction, neutrino interaction generation, and the simulation of the detector.

In chapter 6 are the reconstruction procedures, the methods by which the timing and charge information recorded by the photo-multiplier tubes are reconstructed into energy, direction, neutrino flavour.

The processes used to reduce the large amount of data observed, into a more manageable sample of pure neutrino events, is detailed in chapter 7.

In chapter 8, one of the focuses of this thesis is introduced - neutron tagging. Application and development of this technique to be applied to atmospheric neutrinos is discussed.

Finally, chapter 9 contains descriptions of the new anti-neutrino data samples which can be constructed by use of neutron information. Systematic errors and analysis methods are described, and then full neutrino oscillation analysis and sensitivity study are performed. The best fit neutrino mixing parameters are calculated here. The thesis is then concluded in chapter 10.

1.2 Author Contributions

Super-Kamiokande is a well established experiment, having been in operation for almost 20 years now. Thus, many of the analysis techniques are already mature, and it is important to identify my (the author's) personal contribution to the experiment. I have been responsible for updating the Fully-Contained neutrino dataset and reduction process, performing maintenance and updates that were required during my time here. I also worked to upgrade the atmospheric neutrino flux calculation.

The bulk of my contribution to the experiment, is in developing the neutron tagging software that may effectively identify neutrons, as well as Monte-Carlo modifications to correctly simulate and accurately predict neutron capture events. The basis for this study was pioneered by Haibing Zhang for study of relic supernova neutrinos, however this is the first time to apply and develop this technique for >100 MeV analyses. My software is currently being used by other members of Super-Kamiokande, for proton decay studies, and other high energy analysis, as well as preliminary work for usage in T2K.

For neutrino oscillation analysis, my contribution mainly consists of improvements to the Multi-GeV $\nu - \bar{\nu}$ separation, by use of neutron information and other techniques. Improved separation of ν and $\bar{\nu}$ events increases the detector's sensitivity to neutrino mass hierarchy, a prevalent topic in neutrino physics at this time.

Chapter 2

Neutrinos

2.1 A History of Neutrinos

2.1.1 Neutrino Flavours

The first prediction that a neutrino may exist, was made by Wolfgang Pauli, in December 1930. The problem which prompted this prediction, was observation of β -decay interactions, whereby a neutron decays to a proton inside a nucleus, emitting an electron, for example:



Of course, the electron produced was expected to be mono-energetic, similar to gamma or alpha-producing decays, however a continuous energy spectrum was observed [37]. This led Pauli to postulate that an additional, charge-less particle was being produced in this decay, sharing some of the energy of the electron, without being observed. This particle was initially named "neutron", however after what we now know as a neutron was observed by Chadwick in 1932 [38], Enrico Fermi distinguished this mysterious particle by renaming it a neutrino [39], the appellation which has stuck to this day.

The first direct observation of neutrinos however, did not come until 1956, when Fred Reines and Clyde Cowan measured electron anti-neutrinos via the inverse β -decay interaction

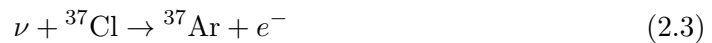


in a water tank. The e^{+} annihilated, producing two γ -rays in the water, which were amplified by surrounding organic scintillator, and could be observed. In addition, cadmium

was added to the water, increasing the efficiency of neutron capture events. These neutron capture events would produce a further, delayed γ -ray, and requiring observation of this in addition to the primary signal allowed background to be greatly reduced.

At this point there were only two known charged leptons, the electron and the muon, along with their corresponding anti-particles. However, it was still unknown whether both these leptons could produce different neutrinos, or if the anti-neutrino was distinct from the neutrino.

To solve the latter of these problems, a similar inverse beta decay experiment was conducted by Ray Davis [40], attempting to observe the interaction



from neutrinos produced by a nuclear reactor. This interaction is perfectly acceptable from a charge-conservation perspective, however in hindsight we now know that reactors produce $\bar{\nu}_e$, when ν_e is required to conserve lepton number in this interaction. So unfortunately, Davis was unable to observe the desired interaction. However, due to this work and subsequent experiments by Davis, we are able to establish that neutrino and anti-neutrino are separate entities, and that lepton number must be conserved in weak interactions.

The remaining uncertainty then, is whether the neutrino associated with an electron, is the same as the neutrino associated with a muon. This was studied using a π -decay based accelerator experiment, in Brookhaven, 1962, led by Lederman, Schwartz and Steinberger [41]. Charged pions dominantly decay via the mode:



Decay to electron is possible, but heavily suppressed due to helicity. Therefore using 15GeV protons fired at a Beryllium target, charged pions were produced, which decayed into ν_μ , creating a beam of these neutrinos. From previous reactor experiments, we already know that a neutrino can cause an inverse β -decay reaction, and produce an electron. Therefore if $\nu_\mu = \nu_e$, we expect electrons to be observed when this ν_μ beam interacts in a detector.

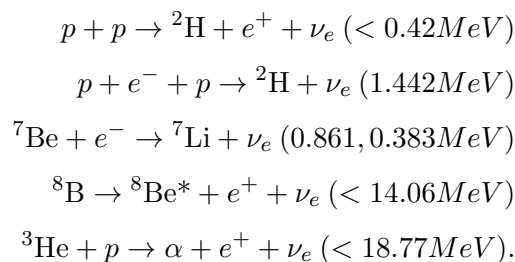
However, as we now know, this was not the case, and the experiment detected muons being produced as a result of the beam interaction, thus we may conclude that ν_μ , and ν_e are two distinct particles, and that lepton family number must be conserved in their interactions.

The last piece of the puzzle, ν_τ , was not discovered until much later. The τ lepton itself was revealed by Martin Perl et al., using an $e^+ - e^-$ collider at SLAC in 1974-1977 [42]. ν_τ was finally detected in 2000, by the DONUT collaboration, from study of the Tevatron (Fermilab) fixed target proton beam experiment [43].

So, up until now, it appears that we have a consistent model of neutrino physics, and the nature of these chargeless, massless, lepton number conserving particles is well understood. However, this is not all there is to this story.

2.1.2 The Solar Neutrino Problem

The Standard Solar Model [44] (SSM), as calculated by John Bahcall, posits that the Sun generates its energy through processes of nuclear fusion, primarily the fusion of hydrogen atoms, to create helium. This fusion interaction can occur in two ways, the carbon-nitrogen-oxygen (*CNO*) cycle, or the far more dominant proton-proton (*pp*) chain (accounting for $\sim 98.4\%$ of the Sun's total luminosity). In the *pp*-chain, five distinct reactions produce neutrinos of various energies:



Neutrinos are also produced in the *CNO* cycle, however the resultant flux is insignificant compared to the *pp*-chain. The SSM is constrained by the luminosity and radius of the Sun, as well as the observed ratio of heavy elements on the Sun's surface [45], and it is generally well accepted.

The Homestake experiment [46] was conducted in the 1960s, led by Ray Davis, to measure this flux of ν_e coming from Sun, and validate Bahcall's SSM. The experiment was conducted similarly to his previous reactor neutrino experiment, again utilising the reaction:



This time, it was a success, as the Sun does produce neutrinos, rather than anti-neutrinos. The experiment consisted of 615 tons of C_2Cl_4 , in a tank located in the

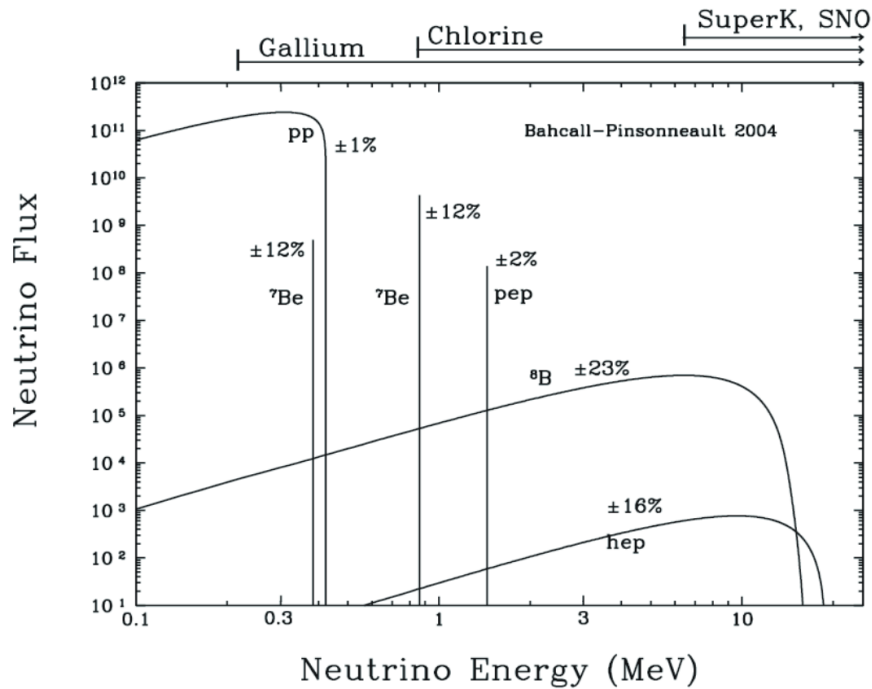


FIGURE 2.1: Energy spectrum for neutrinos produced in the pp chain, predicted by Bahcall's Standard Solar Model

Homestake mine, South Dakota. The ^{37}Ar produced is radioactive, with a half-life of 35 days, and could be siphoned out of the tank in bubbles of Helium gas. The quantity could then be ascertained by counting radioactive decays of the extracted argon, thus inferring the number of initial electron neutrino interactions.

However a problem arose. The number of ν_e detected by the Homestake experiment, was only around one third of the number predicted by the SSM [47]. Extensive investigation was performed, questioning both the efficiency of the detector, and the validity of the SSM, however nothing was found that could explain this discrepancy. Homestake continued running until 1994, consistently measuring the same deficit of neutrinos compared to prediction. A similar deficit was later observed by Kamiokande in 1989, by the GALLEX collaboration in 1992 [48], and at the SAGE experiment in 1994 [49].

Therefore we are led to the conclusion, that something must be wrong with the underlying particle physics model. The neutrinos are undergoing some unknown process which reduces the number of ν_e . Perhaps, as suggested by Pontecorvo in 1969, the neutrinos are oscillating between states [50]. While we now think this to be true, other explanations to the solar neutrino problem are possible, such as neutrinos decaying mid-flight [51]. More information is needed to confirm the cause of this anomaly.

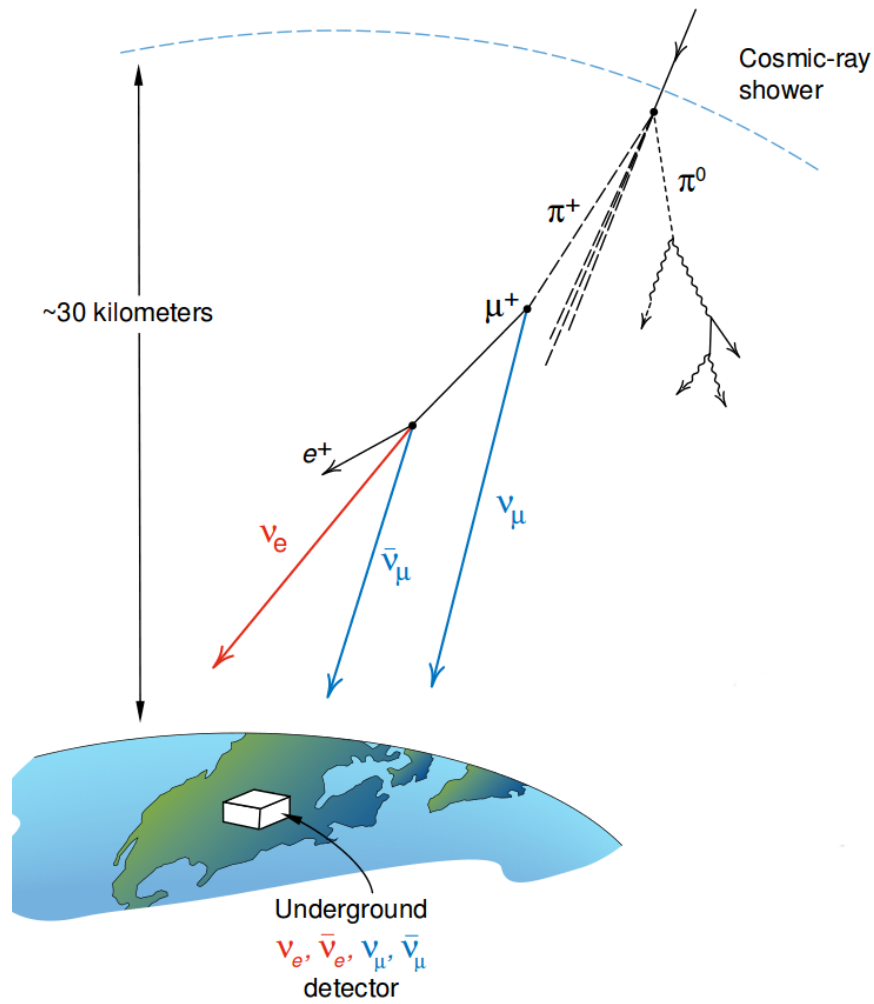


FIGURE 2.2: Hadronic shower and atmospheric neutrinos produced by cosmic rays.
Figure from Los Alamos Science

2.1.3 The Atmospheric Neutrino Anomaly

The solar neutrino problem was later compounded by confusing measurements from another dataset - atmospheric neutrinos. So called as they are neutrinos produced by cosmic rays interacting in the atmosphere. A cosmic ray (typically a proton) enters our atmosphere, interacting with nuclei and creating a hadronic shower. Amongst this hadronic shower are many charged pions, which decay to muons, and then to electrons, producing multiple neutrinos in the process:

$$\pi^+ \rightarrow \mu^+ + \nu_\mu \quad (2.6)$$

$$\mu^+ \rightarrow e^+ + \nu_e + \bar{\nu}_\mu \quad (2.7)$$

along with the corresponding interactions for π^- . Therefore our prediction for the ratio $R = (\bar{\nu}_\mu + \nu_\mu)/(\bar{\nu}_e + \nu_e)$ is ~ 2 for neutrinos $< 1\text{GeV}$. For high energy cosmic rays, some of the muons may reach the surface of the earth before decaying, so this ratio will be increasing with energy.

The Kamiokande experiment, a 3000 ton underground water Cherenkov detector, was originally designed to search for proton decays - a similarly rare (still unobserved) phenomenon. This required a large volume of matter, and very low background, to have a chance at observation. Coincidentally, these are also the qualities required for an effective neutrino detector, therefore Kamiokande was propelled into the limelight in 1987 for detecting neutrinos from the 1987a Large Magellanic Cloud supernova [52].

Kamiokande was also able to detect atmospheric neutrinos, reporting the above ratio $R = (\bar{\nu}_\mu + \nu_\mu)/(\bar{\nu}_e + \nu_e)$, in the form $R_{data}/R_{MC} = 0.60_{-0.06}^{+0.07}(stat) \pm 0.05(syst)$ [53]. Interestingly, this deficit of muon neutrinos had a strong energy and zenith angle dependence [54], suggestive of some travel distance dependent oscillation or decay effect. A similar discrepancy was detected by IMB (another proton-decay water-Cherenkov detector) [55], and Soudan-2 (an iron tracking-calorimeter experiment), leading this to be accepted as the "atmospheric neutrino anomaly".

2.1.4 The Solution

The cause of these neutrino anomalies could not be identified, until the successor to the Kamiokande experiment, "Super-Kamiokande" (SK), was constructed in 1996. As the topic of this thesis, this experiment will be described in detail in the following chapters, but for now it suffices to say that it is a large water Cherenkov detector, allowing much greater sensitivity to physics parameters than its predecessor.

Using a distribution of the ratio of reconstructed path length (L) to reconstructed energy (E), using only events where this reconstruction is possible at high resolution ($> 70\%$), SK was able to observe a dip corresponding to the first maximum of neutrino oscillation probability [56]. This was the first direct evidence for atmospheric neutrino oscillation (in this case $\nu_\mu \leftrightarrow \nu_\tau$) as the favoured explanation for the atmospheric neutrino anomaly.

Concurrently, the Sudbury Neutrino Observatory (SNO), announced direct observation of solar neutrino mixing [57][58] (SK measurements were also included to obtain this conclusion). SNO is a heavy water (D_2O) Cherenkov detector, designed to solve the solar neutrino problem by measurements of ν_e flux independently from the total neutrino flux.

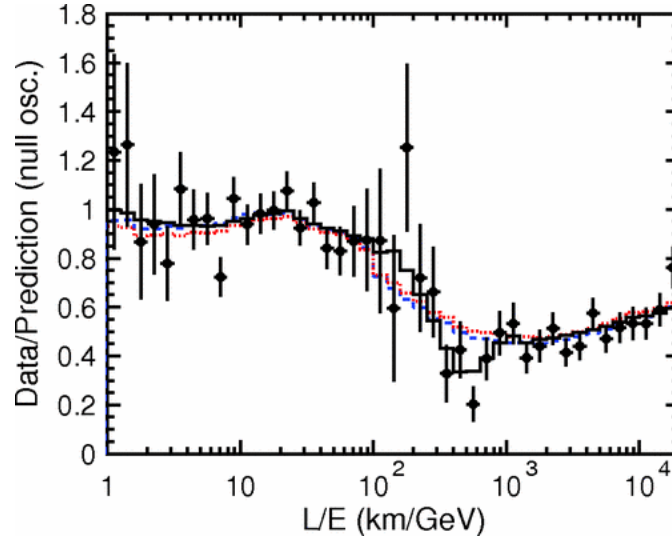


FIGURE 2.3: Ratio of the data to the MC events as a function of L/E , from Super-Kamiokande. The solid black histogram represents the best fit for oscillation, whilst the disfavoured blue dashed, and dotted red lines are the best fit expectations for neutrino decay, and neutrino decoherence respectively.

This is accomplished due to the differing nature of charged current (CC), and neutral current (NC) interactions in heavy water. In this context a CC interaction (which exchanges a charged W boson)

$$\nu_e + d \rightarrow p + p + e^- \quad (2.8)$$

only occurs for electron neutrinos, as solar neutrinos ($\sim 10\text{MeV}$), regardless of flavour, are too low energy to produce a muon ($\sim 106\text{MeV}/c$). The electron from CC interactions then produces Cherenkov light, and can be observed by the PMTs surrounding the detector.

By contrast a NC interaction (exchanging a neutral Z boson), can occur for any neutrino flavour:

$$\nu_x + d \rightarrow p + n + \nu_x. \quad (2.9)$$

Following this the produced neutron will be captured and emit a gamma ray, providing a distinct signature compared to the CC interaction. Thus the total number of neutrinos can be measured independently from the number of electron-neutrinos. You may have guessed by now, the results of SNO were consistent with $\nu_e \leftrightarrow \nu_\mu/\nu_\tau$ oscillation, and the solar neutrino problem could also be solved, using a single consistent theory.

2.2 Neutrino Oscillation Theory

2.2.1 Oscillations in a Vacuum

Neutrino oscillations are based on the idea that the neutrino mass eigenstates do not exactly match the weak interaction (flavour) states, but instead each flavour state is constructed by a combination of different mass eigenstates. That is to say, flavour states $|\nu_\alpha\rangle$ ($\alpha = e, \mu, \tau$), may be expressed as a superposition of three mass eigenstates $|\nu_i\rangle$, with mass m_i ($i = 1, 2, 3$) [59].

$$|\nu_\alpha\rangle = \sum_{i=1}^3 U_{\alpha i}^* |\nu_i\rangle, \quad (2.10)$$

where U represents the rotation matrix between these states. If U is not diagonal, then each flavour state will be a mixture of multiple mass states. This rotation matrix is known as the Pontecorvo-Maki-Nakagawa-Sakata (MNS) mixing matrix [60]. The total number of neutrino flavours is strongly limited to 3, by measurements of the Z boson total width [61]. Thus the matrix U may be characterized by only 4 independent parameters:

$$U = \begin{pmatrix} 1 & 0 & 0 \\ 0 & C_{23} & S_{23} \\ 0 & -S_{23} & C_{23} \end{pmatrix} \begin{pmatrix} C_{13} & 0 & S_{13}e^{-i\delta_{cp}} \\ 0 & 1 & 0 \\ -S_{13}e^{i\delta_{cp}} & 0 & C_{13} \end{pmatrix} \begin{pmatrix} C_{12} & S_{12} & 0 \\ -S_{12} & C_{12} & 0 \\ 0 & 0 & 1 \end{pmatrix}, \quad (2.11)$$

where $C_{ij} = \cos \theta_{ij}$ and $S_{ij} = \sin \theta_{ij}$ represent the mixing between states i and j , and δ_{cp} is the charge-parity (CP) symmetry violating phase ($\delta_{cp} \neq 0$ implies that CP violation is present).

You may consider a neutrino produced by a lepton capture interaction:

$$\alpha^- + p \rightarrow n + \nu_\alpha. \quad (2.12)$$

As the neutrino was produced in a weak interaction, its state at the instant of creation is known to be one of the three flavour eigenstates, ν_α .

The time propagation of a particle is governed by the Schrödinger equation, and if we assume propagation through a vacuum, may be simply solved as:

$$|\nu_i(t)\rangle = e^{-iE_i t} |\nu_i(0)\rangle. \quad (2.13)$$

However recall that $E_i = \sqrt{p^2 + m_i^2}$, so if a neutrino is made up of a superposition of mass states, they will each have an independent time evolution. Therefore to understand the state of our neutrino after some time t , we must first re-write it in its mass states:

$$|\nu_\alpha(t)\rangle = \sum_{i=1}^3 U_{\alpha i}^* e^{-i\sqrt{p^2 + m_i^2}t} |\nu_i\rangle. \quad (2.14)$$

This gives us the time evolution of the neutrino. However, as a neutrino must interact via the weak force, we must recast this equation in the flavour basis to understand our observations. The amplitude of finding the neutrino ν_α in flavour state ν_β after time t is then

$$\begin{aligned} A_{\nu_\alpha \rightarrow \nu_\beta}(t) &= \langle \nu_\beta | \nu_\alpha(t) \rangle = \sum_{i=1}^3 U_{\alpha i}^* e^{-iE_i t} \langle \nu_\beta | \nu_i \rangle \\ &= \sum_{i=1}^3 \sum_{j=1}^3 U_{\alpha i}^* U_{\beta j} e^{-iE_i t} \langle \nu_j | \nu_i \rangle \\ &= \sum_{i=1}^3 U_{\alpha i}^* U_{\beta i} e^{-iE_i t}. \end{aligned}$$

The transition probability can be expressed as

$$P_{\nu_\alpha \rightarrow \nu_\beta}(t) = |A_{\nu_\alpha \rightarrow \nu_\beta}(t)|^2 = \sum_{i=1}^3 \sum_{j=1}^3 U_{\alpha i}^* U_{\beta i} U_{\alpha j} U_{\beta j}^* e^{-i(E_i - E_j)t}. \quad (2.15)$$

So you can see, if the energy of any two neutrino mass states is different we will be able to see oscillatory effects in the transition probability. However it is still quite difficult to understand in this form. If we assume that the neutrinos are relativistic, we may make the approximation $E_i = \sqrt{p^2 + m_i^2} \simeq p + m_i^2/2p \simeq p + m_i^2/2E$.

$$P_{\nu_\alpha \rightarrow \nu_\beta}(t) = \sum_{i=1}^3 \sum_{j=1}^3 U_{\alpha i}^* U_{\beta i} U_{\alpha j} U_{\beta j}^* e^{-i\frac{\Delta m_{ij}^2}{2E}t} \quad (2.16)$$

where $\Delta m_{ij}^2 = m_i^2 - m_j^2$. Typically it is more useful to express this in terms of the distance travelled L by the neutrinos, rather than time t

$$P_{\nu_\alpha \rightarrow \nu_\beta}(L) = \sum_{i=1}^3 \sum_{j=1}^3 U_{\alpha i}^* U_{\beta i} U_{\alpha j} U_{\beta j}^* \exp\left(-i\frac{\Delta m_{ij}^2 L}{2E}\right). \quad (2.17)$$

So, just from this equation, you may form an understanding of the physics underlying neutrino oscillation. For oscillation to exist, it is necessary for flavour states to be comprised of a superposition of different mass states, where $\Delta m_{ij}^2 \neq 0$. Also, you may note that the oscillation probability depends on $\frac{L}{E}$, which may be helpful to explain some issues from the previous chapter -the atmospheric neutrino deficit that only appears in upwards travelling neutrinos, which have a larger L than their downward travelling counterparts, thus some oscillation effects have been revealed.

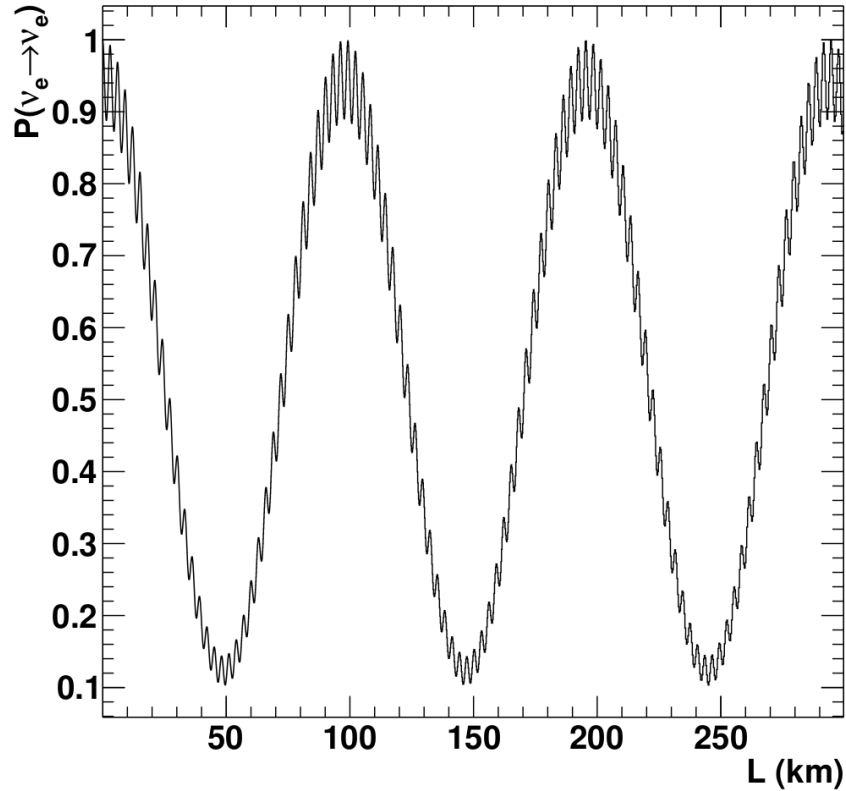


FIGURE 2.4: This figure shows the oscillation probability of $\nu_e \rightarrow \nu_e$, for a 3MeV neutrino. It may be thought of as the probability that an initial electron neutrino will be observed as an electron neutrino after travelling distance L . For this plot, $\Delta m_{23}^2 = 2.4 \times 10^{-3} eV^2$, and $\Delta m_{12}^2 = 7.6 \times 10^{-5} eV^2$. The high frequency oscillations are due to Δm_{23}^2 , and if a detector is placed at 1km then you may approximate the mixing matrix to its 2-dimensional form considering only this mixing. Likewise, for the low frequency oscillations, the driving factor is Δm_{12}^2 , so to optimally measure this, a detector may be placed at 50km, and again the mixing matrix may be reduced to an oscillation between these two states.

In some cases, it is possible to simplify mixing matrix U into an oscillation between just two mass states. This is possible as the frequency of the oscillations is essentially determined by Δm_{ij}^2 , so for example, if Δm_{23}^2 is significantly larger than Δm_{12}^2 , the oscillations caused by Δm_{12}^2 will require a larger L/E to be observed. It so happens, that Δm_{12}^2 is of an appropriate magnitude that large values of L/E , corresponding to solar neutrinos, are optimal for viewing the oscillation effect. Similarly, Δm_{23}^2 is

the dominant factor in oscillations for L/E values similar to that which we find in atmospheric neutrinos. Hence it is often suitable in these cases to simplify the problem to that of two flavour oscillation.

$$U = \begin{pmatrix} \cos \theta & \sin \theta \\ -\sin \theta & \cos \theta \end{pmatrix} \quad (2.18)$$

Here U becomes the familiar 2d rotation matrix, and in a similar manner to above, it may be shown that the transition probability becomes

$$P(\nu_\alpha \rightarrow \nu_\beta) = \sin^2 2\theta \sin \frac{\Delta m^2 L}{4E}. \quad (2.19)$$

This simple case demonstrates that both the Δm^2 term and mixing angle θ must be non-zero for oscillations to occur. To avoid confusion, it is worth remembering that θ is a constant, and $\sin \theta$ is not the term causing the oscillation effect. The goal of neutrino oscillation experiments then, is to measure the different parameters which control this effect: Δm^2 , θ , and Δ_{cp} .

2.2.2 Oscillations in Matter

Until now, we have been operating under the assumption that neutrinos move only through vacuum. However, as our detectors are generally built very close to a large amount of matter, we cannot always rely on this assumption. Neutrino transport through matter was first explored by Wolfenstein in 1978[62], and elaborated on by Smirnov and Mikheyev [63].

Neutrino scattering in matter can occur via a neutral current Z boson, in which case all neutrino flavours interact in the same way, so this just results in an additional common phase factor in the propagation Hamiltonian. Interactions may also take place via charged current bosons (W^\pm), but due to the high density of electrons in matter, a flavour asymmetry is introduced, enhancing electron neutrino scattering in a forward direction. The effective potentials of the different neutrino flavours are

$$V_e = V_{CC} + V_{NC} \quad (2.20)$$

$$V_{\mu,\tau} = V_{NC}, \quad (2.21)$$

where the charged and neutral current potentials are

$$V_{CC} = \pm \sqrt{2} G_F n_e \quad (2.22)$$

$$V_{NC} = \mp \frac{\sqrt{2}}{2} G_F n_n. \quad (2.23)$$

G_F is the weak coupling constant, and $n_{e,n}$ are the number densities of electrons and neutrons in the surrounding material. The sign flips for anti-neutrinos.

If we take a simple 2-flavour mixing case, recall that the time evolution of the mass states is given by the Schrödinger equation

$$i \frac{d}{dt} \begin{pmatrix} \nu_1 \\ \nu_2 \end{pmatrix} = \begin{pmatrix} E_1 & 0 \\ 0 & E_2 \end{pmatrix} \begin{pmatrix} \nu_1 \\ \nu_2 \end{pmatrix}. \quad (2.24)$$

Converting this into the flavour basis

$$i \frac{d}{dt} \begin{pmatrix} \nu_e \\ \nu_\mu \end{pmatrix} = U \begin{pmatrix} E_1 & 0 \\ 0 & E_2 \end{pmatrix} U^\dagger \begin{pmatrix} \nu_e \\ \nu_\mu \end{pmatrix} = \begin{pmatrix} -\frac{\Delta m^2}{4E} \cos 2\theta & \frac{\Delta m^2}{4E} \sin 2\theta \\ \frac{\Delta m^2}{4E} \sin 2\theta & \frac{\Delta m^2}{4E} \cos 2\theta \end{pmatrix} \begin{pmatrix} \nu_e \\ \nu_\mu \end{pmatrix}, \quad (2.25)$$

where Δm^2 , E , and θ are as defined in the previous section. The common phase is not included here, as it has no effect on neutrino oscillations. To add the effect of neutrino oscillations in matter, we must include the potentials defined above. V_{NC} is a common term applied to the diagonal components for both ν_e and ν_μ , thus may be taken as a phase shift, and safely ignored. The extra V_{CC} term must be added for $\nu_e \rightarrow \nu_e$ scattering.

$$i \frac{d}{dt} \begin{pmatrix} \nu_e \\ \nu_\mu \end{pmatrix} = \begin{pmatrix} -\frac{\Delta m^2}{4E} \cos 2\theta \pm \sqrt{2} G_F n_e & \frac{\Delta m^2}{4E} \sin 2\theta \\ \frac{\Delta m^2}{4E} \sin 2\theta & \frac{\Delta m^2}{4E} \cos 2\theta \end{pmatrix} \begin{pmatrix} \nu_e \\ \nu_\mu \end{pmatrix} \quad (2.26)$$

We may convert this back to the standard mixing matrix form of (2.25) by making the substitutions

$$\Delta m_M^2 = \Delta m^2 \sqrt{\sin^2 2\theta + (\cos 2\theta - A_{CC}/\Delta m^2)^2} \quad (2.27)$$

and

$$\sin^2 2\theta_M = \frac{\sin^2 2\theta}{\sin^2 2\theta + (\cos 2\theta - A_{CC}/\Delta m^2)^2}, \quad (2.28)$$

where

$$A_{CC} = \pm 2\sqrt{2} G_F n_e E. \quad (2.29)$$

You may note that as $n_e \rightarrow 0$, these formulae return to that of the vacuum. A resonance occurs when

$$\frac{A_{CC}}{\Delta m^2} = \cos 2\theta \quad (2.30)$$

is satisfied, representing the maximal mixing for neutrinos in matter. This is known as the Mikheyev-Smirnov-Wolfenstein (MSW) condition (the effect of matter on neutrino oscillation is also known as the MSW effect, after the same three scientists). The matter effect also allows us sensitivity to the sign of Δm^2 . However, as the sign of A_{CC} changes dependent on whether the neutrino is an antiparticle, this resonant enhancement will occur in either anti-neutrino or neutrino, depending on the mass hierarchy. A full three-flavour matter effect has been calculated [64], however the math is considerably more involved.

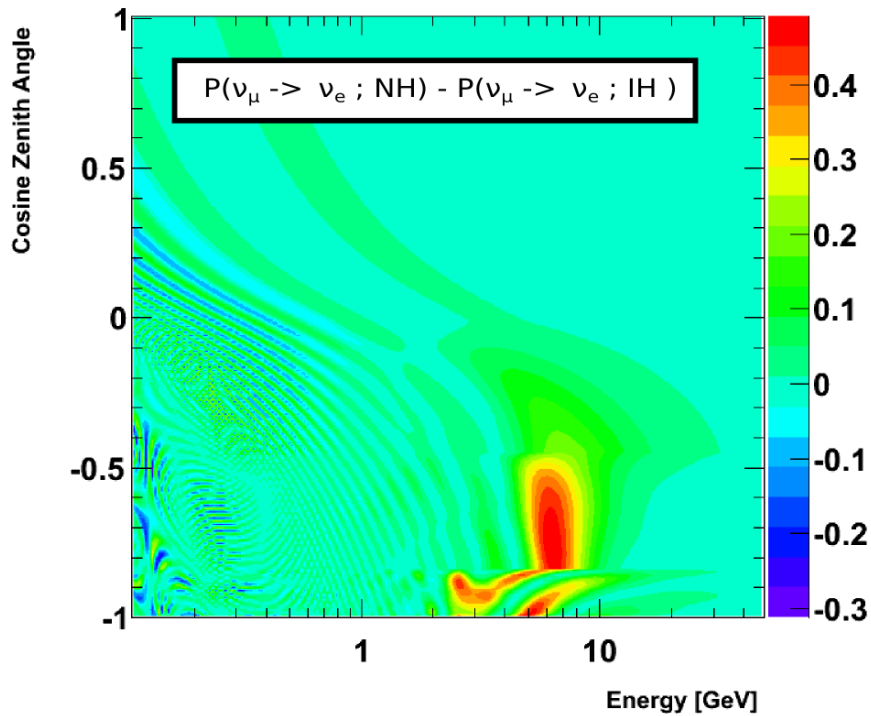


FIGURE 2.5: This figure represents the difference between probability of oscillation $\nu_e \leftrightarrow \nu_\mu$, between normal and inverted mass hierarchies, for neutrinos incident on Super Kamiokande. The y-axis is zenith angle, such that the upper half of the plot represents downward going neutrinos, and the bottom half upward going neutrinos. The dominant area of resonant enhancement can be seen around 2 – 10 GeV. If we instead look at anti-neutrino oscillation, the signs in this plot are switched, so the enhancement occurs in inverted, rather than normal hierarchy.

2.2.3 CP Violation

C and P refer to the transformations of charge conjugation (particle \leftrightarrow anti-particle), and parity (inversion of particle position). Symmetry of C and P may be either conserved or violated, dependent on whether these quantities are conserved in particle interactions.

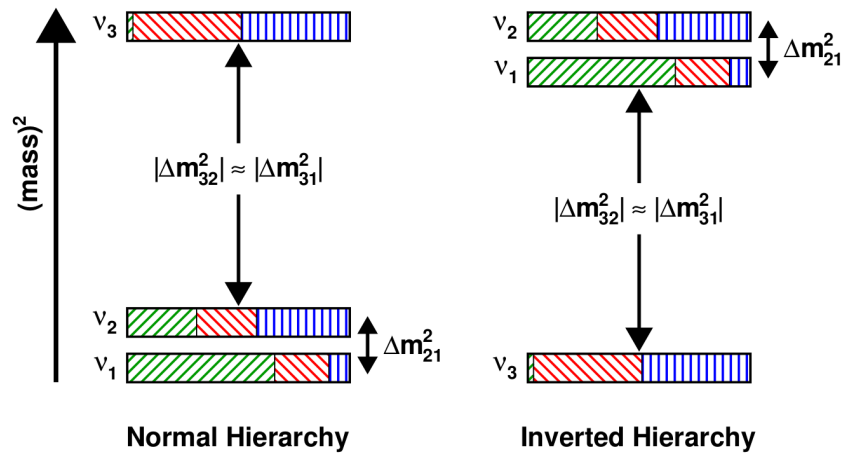


FIGURE 2.6: The two possibilities for neutrino mass states, known as the normal and inverted hierarchies. The green forward-slash fill represents ν_e , red back-slash is ν_μ , and vertical blue lines is ν_τ . The difference between the mass states Δm^2 is well known, thanks to neutrino oscillation experiments, but at the time of writing, which mass state is the heaviest is still unknown. This plot is not to scale.

CP violation therefore, refers to the symmetry-breaking of the quantity $C \times P$. This quantity is particularly interesting to measure, as it may provide an explanation to the outstanding problem of matter-antimatter asymmetry in our universe.

In terms of measurable quantities, CP invariance will be observed, only if the neutrino mixing matrix U is real, that is, $U^* = U$ [65]. To rephrase this, an off-diagonal non-zero imaginary phase δ would cause CP to be violated. The magnitude of the CP violation in neutrino mixing may be expressed as

$$J_{CP} = \text{Im}(U_{\mu 3} U_{e 3}^* U_{e 2} U_{\mu 2}^*) = \frac{1}{8} \cos \theta_{13} \sin 2\theta_{12} \sin 2\theta_{23} \sin 2\theta_{13} \sin \delta_{CP}. \quad (2.31)$$

CP violation in the quark sector is well established, having been measured in neutral kaon decay from 1964 [66], and later B (bottom quark) decay [67]. This stems from the imaginary phase in the analogous CKM (Cabibbo-Kobayashi-Maskawa) quark mixing matrix [68]. Recent discovery of non-zero θ_{13} allows for potential CP violation measurement in the neutrino sector, however at present no experimental information is available.

2.3 State of the Art

Assuming the above oscillation model is correct, the next task is to measure all the parameters of neutrino mixing, as accurately as possible. This includes all θ_{ij} mixing angles, Δm_{ij}^2 mass splitting, and δ_{CP} CP violation phase. As stated previously, most,

but not all measurable predictions made by the oscillation model are insensitive to the sign of Δm^2 , therefore it is potentially possible to measure the mass hierarchy of neutrinos. Here the best measurements of these quantities to date will be discussed.

2.3.1 Solar Parameters θ_{12} , Δm_{12}^2

These are the parameters that primarily control the oscillation of long baseline, low energy neutrinos, which were originally observed in solar neutrino data.

Solar neutrino flux has now been measured in many experiments - radiochemical detectors, such as Homestake, SAGE and GALLEX, the water Cherenkov detectors Kamiokande and Super-Kamiokande, and heavy water detector SNO. The liquid scintillator Borexino experiment has recently pioneered measurements of low energy solar neutrinos, sensitive down to 250keV, allowing observation of the 0.862 MeV ${}^7\text{Be}$ neutrinos $\phi = 3.10 \pm 0.15 \times 10^9 \text{cm}^{-2}\text{s}^{-1}$ [69].

For the ${}^8\text{B}$ neutrino flux, the SNO experiment, through CC, NC and ES observations, provides results for both the ν_e flux $\phi_{\nu_e} = 2.35 \pm 0.22 \pm 0.15(10^6 \text{cm}^{-2}\text{s}^{-1})$ [1], and the total solar neutrino flux $\phi_{\text{all } \nu} = 5.25 \pm 0.16_{-0.13}^{+0.11}(10^6 \text{cm}^{-2}\text{s}^{-1})$ [70]. Super Kamiokande is able to observe ES interactions, measuring direction sensitive electron neutrino flux $2.32 \pm 0.04 \pm 0.05(10^6 \text{cm}^{-2}\text{s}^{-1})$ [71]. Borexino also provides a ν_e ${}^8\text{B}$ measurement of $\phi = 2.4 \pm 0.4 \pm 0.1(10^6 \text{cm}^{-2}\text{s}^{-1})$.

The KamLAND experiment also provides important data when considering these mixing parameters. KamLAND is a 1-kTon liquid scintillator detector, located at the same site as Super-Kamiokande in Japan. The observation target here is not solar neutrinos, but the $\bar{\nu}_e$ produced by nuclear reactors. Reactor neutrinos have an energy spectrum $< 8\text{MeV}$, and are detected via the interaction $\bar{\nu}_e + p \rightarrow e^+ + n$. The neutron is then captured on a proton, emitting a characteristic 2.2MeV γ -ray. This delayed coincidence allows us to distinguish from the solar ν_e , which have a similar energy spectrum. KamLAND reported a deficit of $\bar{\nu}_e$ [72] events compared to no-oscillation expectation of

$$\frac{N_{\text{obs}} - N_{BG}}{N_{\text{NoOscillation}}} = 0.611 \pm 0.085 \pm 0.041 \quad (2.32)$$

which confirmed the neutrino oscillation hypothesis. KamLAND collaboration produced a combined fit for oscillation mixing parameters, including solar neutrino information, along with up to date θ_{13} results from short-baseline reactor experiments [73]. The results give $\tan^2 \theta_{12} = 0.436_{-0.025}^{+0.029}$, $|\Delta m_{21}^2| = (7.53 \pm 0.18) \times 10^{-5} \text{eV}^2$.

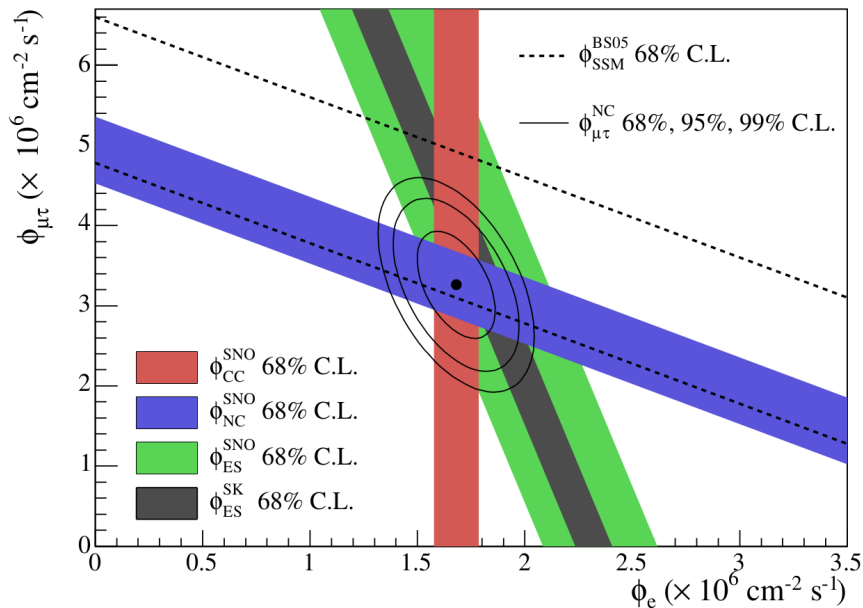


FIGURE 2.7: This figure shows the combined result of ^8B solar neutrino flux measurements, from the salt phase of SNO [1], and ES result from SK in 2002 [2]. The dotted line represents the standard solar model prediction, and the contours represent a joint fit between the two experiments. Figure source [1]

2.3.2 Atmospheric Parameters θ_{23} , Δm_{23}^2

High energy, long baseline neutrinos are sensitive to these parameters, which includes atmospheric neutrinos and accelerator experiments.

As the topic of this thesis, Super Kamiokande and atmospheric neutrinos will be discussed in detail later. SK provides strong evidence for zenith angle dependent atmospheric ν_μ disappearance [74], and using an L/E binning scheme, favours the oscillation model over decay and decoherence hypotheses. Recently, ν_τ appearance has been demonstrated at a 3.8σ level, using neural network analysis [75].

Accelerator neutrinos are also valuable to probe these mixing parameters. Utilizing a well known neutrino spectrum, and high statistics, accelerators can potentially provide tight constraints. The first accelerator-based experiment was K2K (KEK to Kamioka), constructed in Japan in 1999, running for a period of 5 years. K2K collided a 12GeV proton beam with a target, producing pions, which would then decay to muons and ν_μ , with an energy $E_\nu \sim 1.3\text{GeV}$. These then travelled over a distance of 250km, to reach the Super-Kamiokande detector. To better understand the neutrino energy spectrum, a near detector was used 300m from the beam target. K2K measured a deficit of ν_μ , detecting 112 events, compared to the expectation of $158.1_{-8.6}^{+9.2}$ with no oscillation - disfavouring statistical fluctuation by 4.3σ [76].

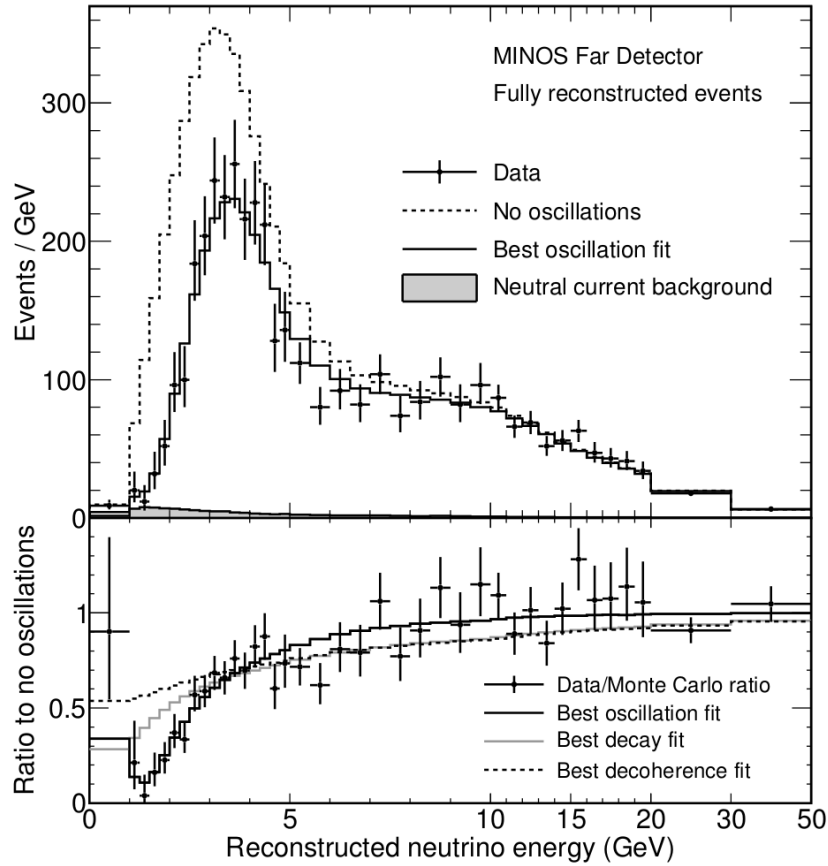


FIGURE 2.8: On the top is the energy spectrum for events reconstructed as CC, at the MINOS far detector. The bottom figure shows the ratio of data to a null oscillation prediction, with the disfavoured decay and decoherence models also shown. [3]

Following this in 2005, MINOS began data taking. Using neutrinos produced by a 120GeV proton beam at Fermilab, MINOS aimed to measure ν_μ disappearance in a 5.4kTon iron-scintillator in the Soudan mine, 735km away. Neutrino energy may be tuned by varying horn current and target position of the beam, but most data was taken with $E_\nu \sim 1 - 5\text{GeV}$. MINOS results disfavour the decoherence and decay models of ν_μ disappearance, by 7σ and 9σ respectively [3]. MINOS was also the first experiment to observe $\bar{\nu}_\mu$ disappearance [77]. By tuning the magnetic field of the beam line after the target, it is possible to focus either positive or negative mesons (and thus ν_μ or $\bar{\nu}_\mu$) towards the far detector. Using all of this data, MINOS reported $|\Delta m_{23}^2| = (2.41_{-0.10}^{+0.09}) \times 10^{-3}\text{eV}^2$, and $\sin^2 2\theta_{23} = 0.950_{-0.036}^{+0.035}$. MINOS is also able to oscillate ν_μ and $\bar{\nu}_\mu$ events independently, resulting in a best fit of $|\Delta m_{23}^2| - |\Delta \bar{m}_{23}^2| = (0.12_{-0.26}^{+0.24}) \times 10^{-3}\text{eV}^2$ [78].

K2K's successor, the T2K (Tokai to Kamioka) experiment, started data taking in 2010. Utilizing an off-axis narrow-band 0.6GeV ν_μ beam, it is tuned to the first oscillation maximum at SK, 295km away. Coherent with a ν_μ disappearance signal, 58 ν_μ -like events were observed at SK, compared to the expectation of 205 ± 17 for the no oscillation case

[79]. Assuming θ_{13} and solar mixing parameters from other experiments, T2K best-fit values give $\sin^2 \theta_{23} = 0.514 \pm 0.082$, and $\Delta m_{23}^2 = (2.44^{+0.17}_{-0.15}) \times 10^{-3} \text{eV}^2$.

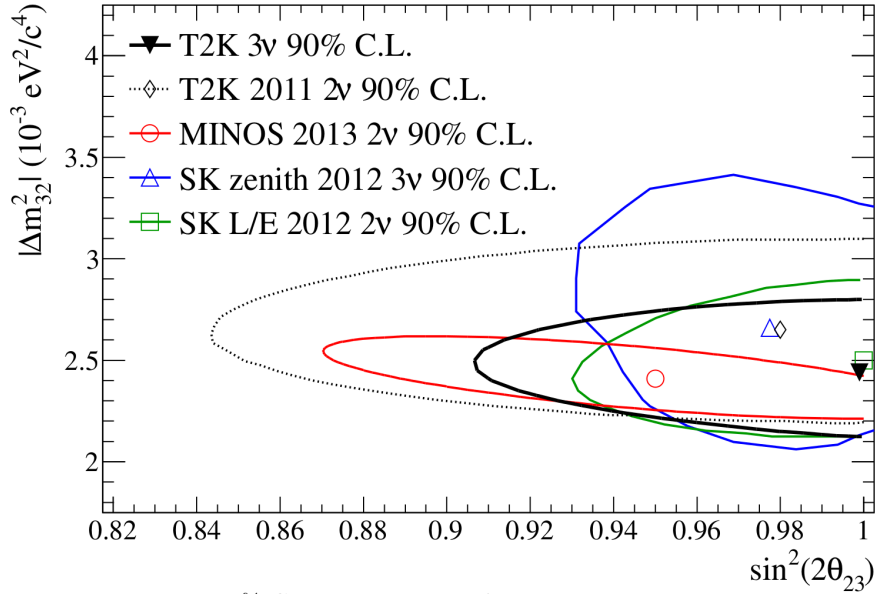


FIGURE 2.9: This plot shows 90% confidence level contours for T2K, MINOS, and SK superimposed. Taken from [4]

A further experiment that should be noted in this category is OPERA. OPERA is the first accelerator experiment designed to measure ν_τ appearance, and runs from a muon neutrino beam at CERN, over 730km to a detector at Gran Sasso. A high energy beam ($E_\nu \sim 17\text{GeV}$) is required for the ν_τ to produce τ particles upon interaction. Upon production, τ leptons quickly decay to μ or hadrons, giving a distinctive kink in the track after a few millimetres. OPERA has thus far observed 3 ν_τ candidates, giving a 3.2σ significance over null observation [80].

2.3.3 Reactor Experiments, θ_{13}

The primary method of measurement for θ_{13} mixing parameters is by use of short baseline ($\sim 1\text{km}$), low energy ($\sim 3\text{MeV}$) reactor neutrino experiments. Nuclear reactors typically produce many $\bar{\nu}_e$, from β -decay of heavy particles in the fission decay chain. Over the past two years, three similar reactor neutrino experiments reported observation of $\bar{\nu}_e$ disappearance, consistent with a non-zero θ_{13} . $|\Delta m_{13}^2|$ is generally not reported, as of course there are only two independent mass splittings between three different masses. As $|\Delta m_{12}^2| \ll |\Delta m_{23}^2|$, we may infer that $|\Delta m_{13}^2| \simeq |\Delta m_{23}^2|$.

The Daya-Bay experiment in China, measured $\bar{\nu}_e$ from six nuclear reactors, with six identical Gd-doped liquid scintillator detectors arranged in 0-2km from the reactors. The

Gadolinium maximizes neutron capture efficiency, which is useful to reduce background rates. These are surrounded by an outer (non-Gd loaded) scintillator detector. The fiducial volume is thus precisely defined by requiring that events are followed by a corresponding neutron capture γ -ray signal. Multiple detectors are used to reduce the errors due to nuclear reactor flux predictions. Daya-Bay reported a deficit in observed $\bar{\nu}_e$ in the far detector, compared to the null oscillation prediction, of $R = 0.944 \pm 0.007 \pm 0.003$. This fits to a mixing angle $\sin^2 2\theta_{13} = 0.089 \pm 0.010 \pm 0.005$, excluding null-oscillations by 7.7σ [81].

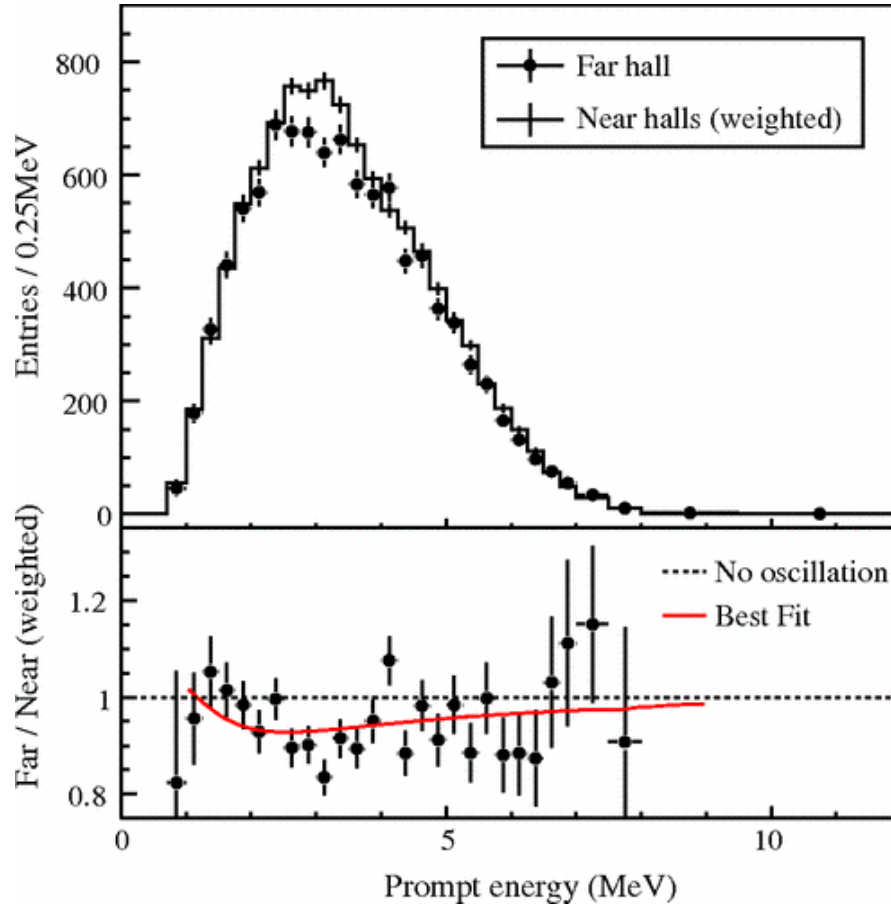


FIGURE 2.10: This plot shows the result from Daya-Bay in 2012. The observed energy spectrum, and ratio with the null-oscillation hypothesis are displayed on top and bottom figures respectively. Taken from [5]

The RENO experiment, in Yonggwang Korea, is a similar setup, again with 6 nuclear reactors producing neutrinos, which can be then measured by a near and far liquid scintillator detector. In this case, the reactors are arranged symmetrically in a line, thus a sufficiently small systematic error is obtainable with just two detectors, contrasting Daya Bay's six. In 2013, RENO reported fitted values of $\sin^2 2\theta_{13} = 0.100 \pm 0.010 \pm 0.015$ [82].

A similar experiment named Double Chooz is active in France, detecting $\bar{\nu}_e$ from two nuclear reactors. The construction of a near detector will be completed in 2014, but the results from just a single far detector at 1050m give $\sin^2 2\theta_{13} = 0.109 \pm 0.030 \pm 0.025$ after 227.9 days livetime [83].

While our most precise values for θ_{13} come from reactor experiments, the accelerators mentioned previously can also search for this value, using the ν_e appearance channel. However, as this appearance channel is also influenced by the yet unknown δ_{CP} , the uncertainty is higher on these measurements.

First came T2K, who presented initial results of $\nu_\mu \rightarrow \nu_e$ analysis in 2011, reporting six ν_e candidate events, above an expectation of 1.5 ± 0.3 for $\theta_{13} = 0$. The most recent result includes the observation of 28 ν_e appearance candidates, over a background of 4.64, excluding $\theta_{13} = 0$ at 7.5σ [84]. MINOS also observed a ν_e appearance signal, detecting 62 candidate events, over a $\theta_{13} = 0$ expectation of $49.6 \pm 7.0 \pm 2.7$. This may be interpreted as a restriction on $\sin^2 2\theta_{13} < 0.12$ at the 90% CL [85].

Solar and atmospheric neutrino experiments also have some sensitivity to θ_{13} , and SNO [86], SK [71], and KamLAND [73] have all published fit results consistent with the reactor and accelerator experiments.

2.4 Summary, Remaining Issues

Various global analyses have been performed, attempting to combine all of these results in a set of best fit parameters. Here the results are presented from a 2012 analysis by Fogli et. al. [87].

Parameter	Best-fit
$\Delta m_{21}^2 (10^{-5} \text{eV}^2)$	$7.54^{+0.26}_{-0.22}$
$ \Delta m_{32}^2 (10^{-3} \text{eV}^2)$	$2.43^{+0.06}_{-0.10}$
$\sin^2 \theta_{12}$	$0.307^{+0.018}_{-0.016}$
$\sin^2 \theta_{23}$	$0.386^{+0.024}_{-0.021}$
$\sin^2 \theta_{13}$	0.0241 ± 0.0025

Much is as of yet undetermined in the neutrino sector. The nature of neutrinos as either Majorana or Dirac particles (respectively whether the neutrino is its own antiparticle, or not), is unknown. The absolute scale of neutrino mass is not well constrained. Of particular interest to this thesis, are the CP violating phase δ_{CP} , and the sign of the large mass splitting parameter, Δm_{32} . After the recent high precision measurements of a relatively large θ_{13} , the possibility opens up for accelerator and atmospheric neutrino experiments, such as SK, T2K and NO ν A to measure these parameters. Measuring these, is the objective of this thesis.

Chapter 3

Super-Kamiokande

3.1 Overview

Super-Kamiokande (SK) is a 50kTon water Cherenkov detector, located in Kamioka mine beneath Mt. Ikenoyama, in Gifu Prefecture, Japan [88]. It is the successor of the Kamiokande experiment, which was originally named after its location and purpose: "Kamioka Nucleon Decay Experiment". After the experiment became famous for neutrino observation from supernova SN1987, the detector was often referenced colloquially as "Kamioka Neutrino Detection Experiment", conveniently having the same acronym. As the mine is horizontal, the detector is in fact 370m above sea level, however it is still shielded by 1000m of rock in the mountain above. This causes a reduction of cosmic ray muon background by ~ 5 orders of magnitude, down to 2.2Hz. The detector is comprised of a large cylindrical tank of light water (H_2O), split into an inner and outer detector (ID and OD) for additional reduction of extraneous background. Neutrinos interact in the water, producing charge particles, which in turn produce Cherenkov light that can be detected by the surrounding photomultiplier tubes (PMTs).

Water Cherenkov detectors benefit from a low energy threshold, allowing a large variety of different analyses to be performed at SK. Atmospheric neutrinos, solar neutrinos, supernova neutrinos, and artificial neutrinos from accelerators and nuclear reactors may all potentially be detected. On top of this, the detector is very competitive as a probe for various dark matter candidates, and search for different modes of proton decay.

Super Kamiokande and Kamioka Observatory are owned and operated by the University of Tokyo's Institute for Cosmic Ray Research (ICRR), receiving the bulk of its funding from Japan's Ministry of Education, Culture, Sports, Science and Technology (MEXT), the U.S. Department of Energy and National Science Foundation. There are over 100

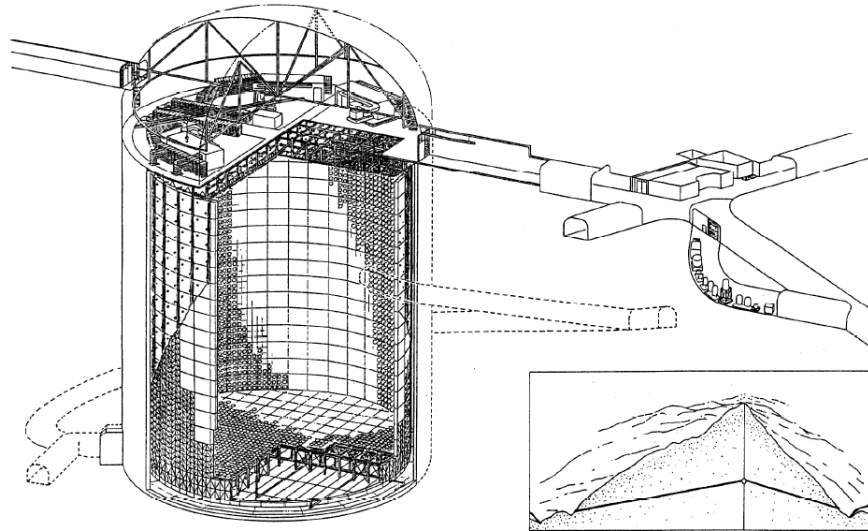


FIGURE 3.1: A schematic of the layout of Super-Kamiokande

collaborators to SK throughout the world, including scientists from Japan, Korea, USA, Canada, the UK, China and Spain.

3.1.1 SK Periods

The operation of SK is typically split into four different periods, referred to as SK-I to SK-IV. The first period of data-taking, SK-I, began in April 1996. The initial build consisted of 11,146 PMTs, and 1,885 PMTs in the ID and OD respectively. SK-I ran stably for 5 years, until April 2001, when the detector was stopped to replace faulty PMTs and other maintenance. Regrettably, while re-filling the tank with water one of the ID PMTs shattered, resulting in a shockwave that destroyed more than half of the PMTs. To avoid a repeat of this incident, a fibre reinforced plastic and acrylic case was used to protect the surviving PMTs. New PMTs were installed in the OD, and the remaining ID PMTs were redistributed to allow even coverage of the tank, before the detector was restarted in October 2002, as SK-II. During the SK-II running period, replacement PMTs were manufactured, and in October 2005 the detector was stopped, to mount these in the tank. The installation process carried on until July 2006, when data taking resumed, beginning SK-III. The final stop of the detector in August 2008 was to upgrade the data acquisition system (DAQ) and electronics. The SK-IV data taking period began on September 2008, and continues to run to this day.

SK Period	SK-I	SK-II	SK-III	SK-IV
Begin	Apr. 1996	Oct. 2002	Jul. 2005	Sep. 2008
End	Apr. 2001	Oct. 2005	Aug. 2008	Ongoing
Livetime (days)	1489.2	798.6	518.1	1775.6
No. ID PMTs	11,146	5,182	11,129	11,129
No. OD PMTs	1,885	1,885	1,885	1,885
Photo Coverage	40%	19%	40%	40%
Front-end Electronics	ATM	ATM	ATM	QBEE
Trigger	Hardware	Hardware	Hardware	Software

TABLE 3.1: A summary of the differences between each of the SK periods

3.2 Detector Design

The Super-Kamiokande detector is primarily made up of a cylindrical tank, 41.4m tall with a diameter of 39.3m. This tank is filled with 50kTon of ultra-pure water, and split into an outer, and inner detector (OD and ID), which are concentric cylinders. The OD extends ~ 2 m out from the ID, and acts as a veto for incoming cosmic ray muons. The walls of the cavity are covered in 40-50cm of reinforced concrete, to reduce radioactive backgrounds from the surrounding rock. A large dome above the tank is used to store DAQ electronics, calibration equipment and other related items. The surrounding area is covered in “Mineguard”, a polyurethane material used to reduce radon gas emanation from the rock wall.

The ID consists of 32kTon of water, surrounded by 11,146 inwardly facing 20 inch PMTs. The PMTs are evenly distributed 70cm from each other, allowing for $\sim 40\%$ photo-coverage. A supporting frame separates the ID and OD, housing all the PMTs and their cabling. This is covered with a black polyethylene terephthalate sheet, which prevents light leaks between the two detector regions. The OD side is covered in 1,885 outward facing 8 inch PMTs. As these are just used for vetoing, a lower photo-coverage is acceptable.

Before the start of SK-III, the OD was optically segmented from the ID, by covering the OD walls (barrel, top and bottom of tank) with reflective Tyvek sheeting (reflectivity $\sim 90\%$ at 400nm). This improved the collection efficiency of the OD PMTs, and allowed some previously difficult backgrounds such as corner-clipping muons to be removed more easily.

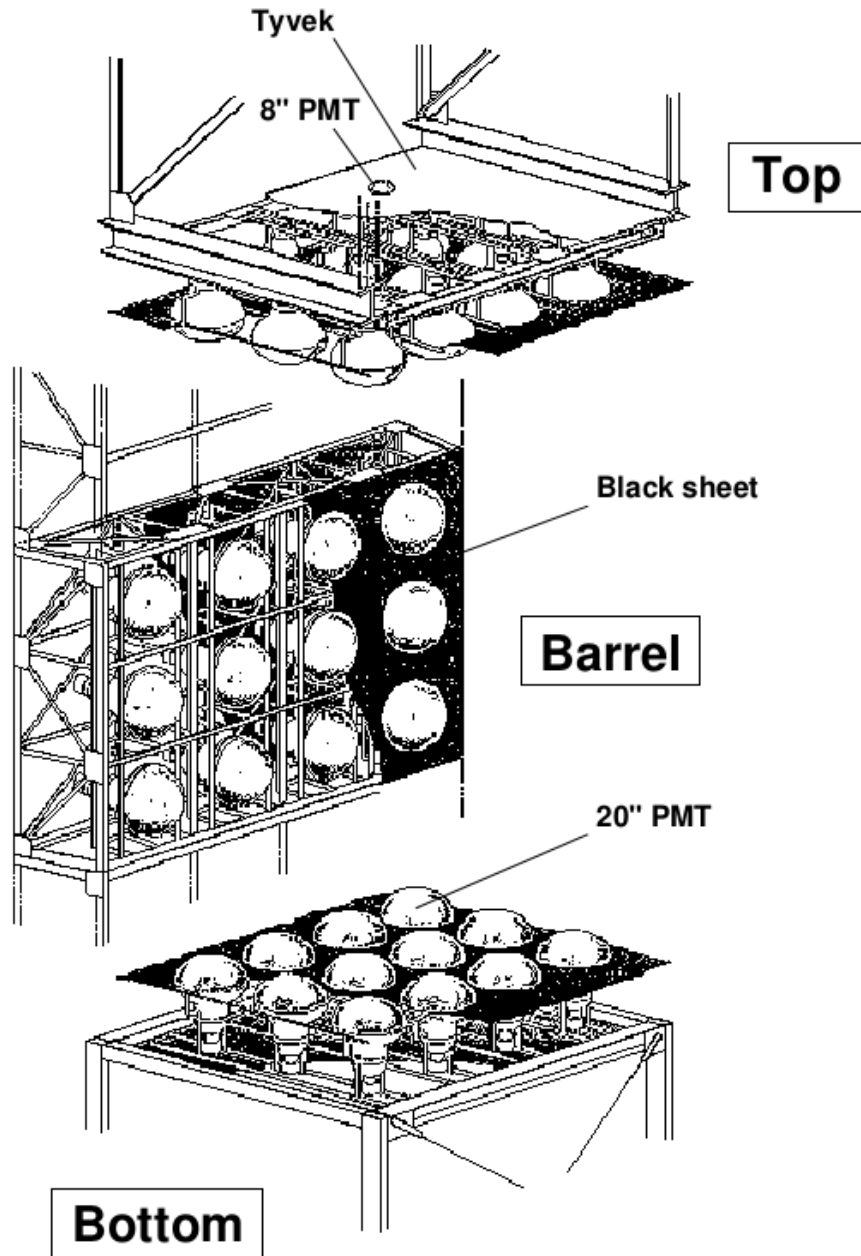


FIGURE 3.2: The frame structure of the PMT support system in the SK tank

3.3 Cherenkov Radiation

Upon interacting in the water tank, energy from the neutrino will be imparted into leptons, and any hadrons which are ejected from the interaction nucleus. These will then produce photons, through a process known as Cherenkov radiation, which can then be detected by the surrounding PMTs. Cherenkov radiation is generated when a charged particle passes through a material at a speed faster than that of light in that material, that is, $v > c/n$, where n is the refractive index of the medium. The Cherenkov light is emitted in a cone pattern, in the direction of travel of the particle, where the

critical cone half angle is given by

$$\cos \theta_C = \frac{1}{\beta n}, \quad (3.1)$$

where $\beta = v/c$. Assuming passage through water, $n \sim 1.33$ at 589nm, leading to a critical angle of $\sim 42^\circ$, and a threshold energy of 0.76MeV, and 158.7MeV for electrons and muons respectively.

The number of Cherenkov photons produced per unit wavelength $d\lambda$ per unit distance dx is given by

$$\frac{d^2 N}{dx d\lambda} = \frac{2\pi\alpha}{\lambda^2} \left(1 - \frac{1}{(n(\lambda)\beta)^2} \right) = \frac{2\pi\alpha}{\lambda^2} \sin^2 \theta_C, \quad (3.2)$$

where α is the fine structure constant. This relation allows us to reconstruct initial particle energy, by counting the number of detected Cherenkov photons.

3.4 Photo-multiplier tubes

The 11,146 inward facing ID PMTs (model R3600 developed by Hamamatsu Photonics [89]), each have a 20-inch diameter, resulting in total photo-coverage of $\sim 40\%$ (excluding SK-II). These PMTs are sensitive to wavelengths in a range 300-600nm, with a quantum efficiency peaking around 400nm of $\sim 21\%$.

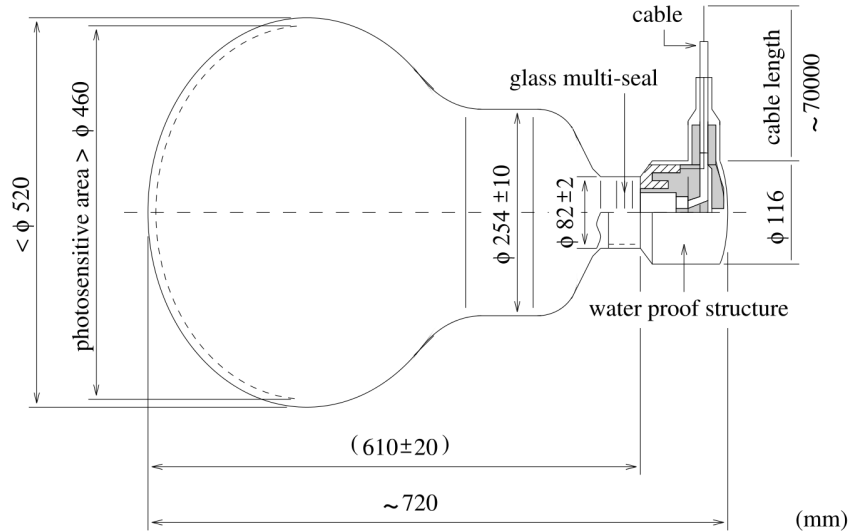


FIGURE 3.3: The structure of an ID PMT in SK.

Photons are collected by the bialkali photo-cathode, which then emits single or multiple photo-electrons. This photo-electron signal is then amplified by a venetian-blind multiplier, comprising of an 11-stage chain of dynodes, with a resultant gain of $\sim 10^7$. A large external magnetic field is liable to divert electrons out of the dynode chain,

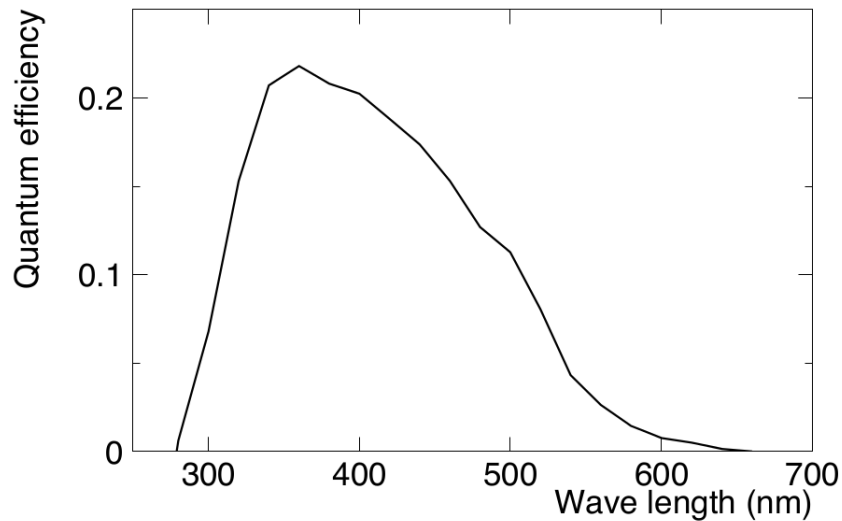


FIGURE 3.4: The wavelength dependent quantum efficiency of the bialkali photocathode.

lowering collection efficiency. To prevent the PMTs from being affected by the Earth's geomagnetic field, 26 Helmholtz coils are set up around the walls of the tank. These reduce the magnetic field effect from 450mG to 50mG.

In the OD, 1,885 8-inch Hamamatsu R1408 PMTs are used. These are covered by a wavelength shifting acrylic plate, which increases the wavelength of the incoming photons to better match the peak quantum efficiency of the PMT, increasing overall collection efficiency by 50%. Time resolution becomes worse, but since the OD is only used as a veto counter, this is of no serious consequence.

3.5 The Water System

It is very important to maintain the SK tank water at a constant and high level of purity. Firstly, a pure water supply for the tank ensures that the water has the highest possible transparency, and Cherenkov photons are less likely to be absorbed or scattered before they are detected at the PMTs. If the water transparency cannot be maintained at an approximately constant level, calibrating the energy reconstruction of particles would be difficult. In addition to this, it is important to remove any radioactive contaminants such as radon, which can constitute a significant source of background, especially for low energy neutrinos.

The water in SK is continuously circulated through a purification system, with a flow of ~ 60 tons/hour. Water entrance and removal points have been chosen to reduce

convection as much as possible, which can allow radioactive contaminants to seep into the surrounding tank structure. To further reduce convection, heat exchangers (HE) are used throughout the water purification system to maintain the supply at a very constant temperature ($\sim 13^\circ\text{C}$, with a variation of 0.01°C). This temperature is low, to suppress bacterial growth, and in addition a UV sterilizer is used to kill any present bacteria.

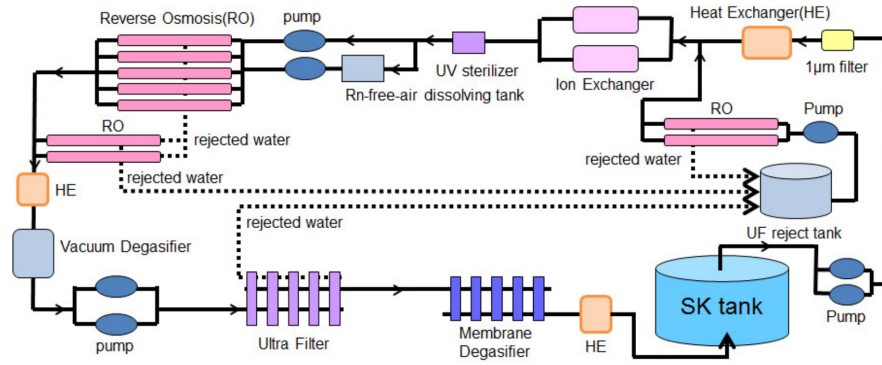


FIGURE 3.5: A schematic of the water purification system used in SK.

Various filters and systems are in operation for the removal of impurities. An Ion exchanger is used to remove Na^+ , Cl^- and others. Radon gas is removed from the water by a vacuum degasifier and membrane degasifier, reducing the water Rn concentration to $< 0.4 \pm 0.2 \text{mBq/m}^3$. Size specific filters are used for further removal of various particles - the ultra filter (UF) removes very small particles down to 10nm , the $1\mu\text{m}$ filters are suitable for removing dust, and the reverse osmosis (RO) filter is used to remove heavy particles, of over 1000 molecular weight.

3.6 Air Purification

The natural mine air is heavily contaminated with radon gas, which is continuously produced in the surrounding rocks from natural uranium decay. This represents both a potential background for low energy neutrino analyses, and a health risk for mine workers. The air flow patterns through the mine change with season, blowing air out of the mine during summer, and into the mine during winter. This results in a large seasonal variation in the radon contamination, with $\sim 30 \text{Bq/m}^3$ in winter, which rises to $\sim 1500 \text{Bq/m}^3$ in summer [90].

To reduce this peak summer level, an air purification system was constructed. Air is collected from outside the mine, passed through a system of filters, and then pumped into the mine, at a rate of up to $50 \text{m}^3/\text{minute}$ [91], maintaining radon levels in the experimental areas at $< 40 \text{Bq/m}^3$, all year round.

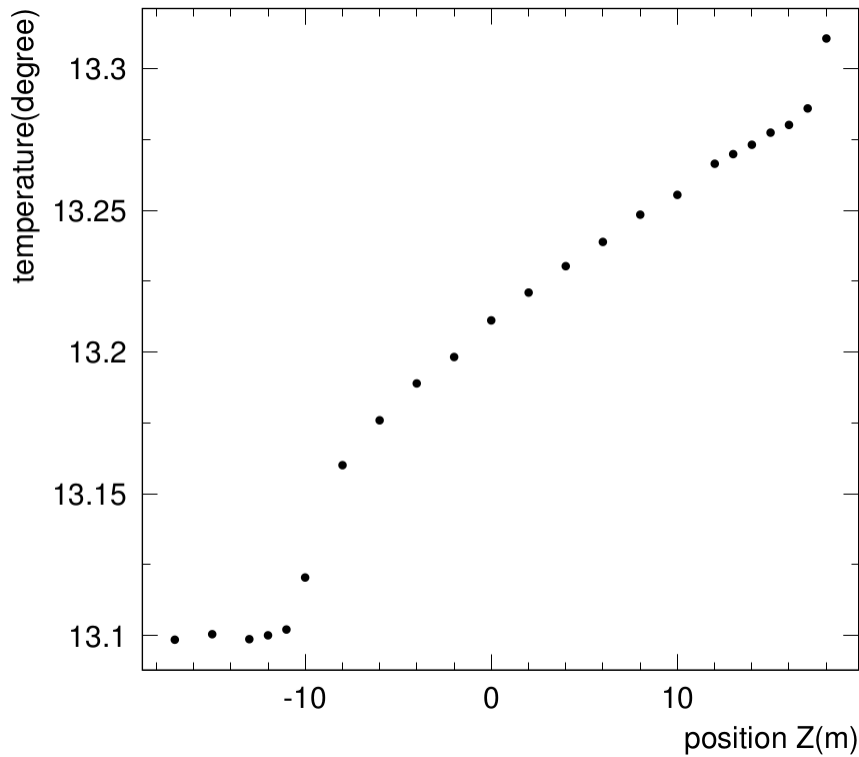


FIGURE 3.6: The varying water temperature across the SK tank. Water input is at the bottom of the tank (negative z).

3.7 Front-end Electronics and Data Acquisition

The data acquisition system (DAQ) used from SK-I to SK-III was upgraded in September 2008 for SK-IV, so these two systems will be described separately.

3.7.1 Data Acquisition System for SK-I to SK-III

An outline of the DAQ system used in SK-I to III can be seen here [3.7](#). Signal from the PMTs was first processed by front-end electronics "Analog-Timing-Modules" (ATMs), based on the TRISTAN KEV Online (TKO) standard [92]. Each ATM took inputs from up to 12 PMTs, requiring a total of ~ 1000 ATMs for the whole detector. The signal input from each PMT is initially amplified 100x, and then split into 4 separate signals.

The first of these was sent to a discriminator, checking the pulse height recorded from the PMT. If it exceeded a threshold of 0.23 photo-electrons, a trigger was sent allowing the other three signals to proceed.

In the second signal, a 15mV 200ns square wave is generated for each PMT, and then summed for every PMT connected to the ATM. This signal is known as HITSUM. The HITSUM result from each ATM module are then sent to a global trigger module, and

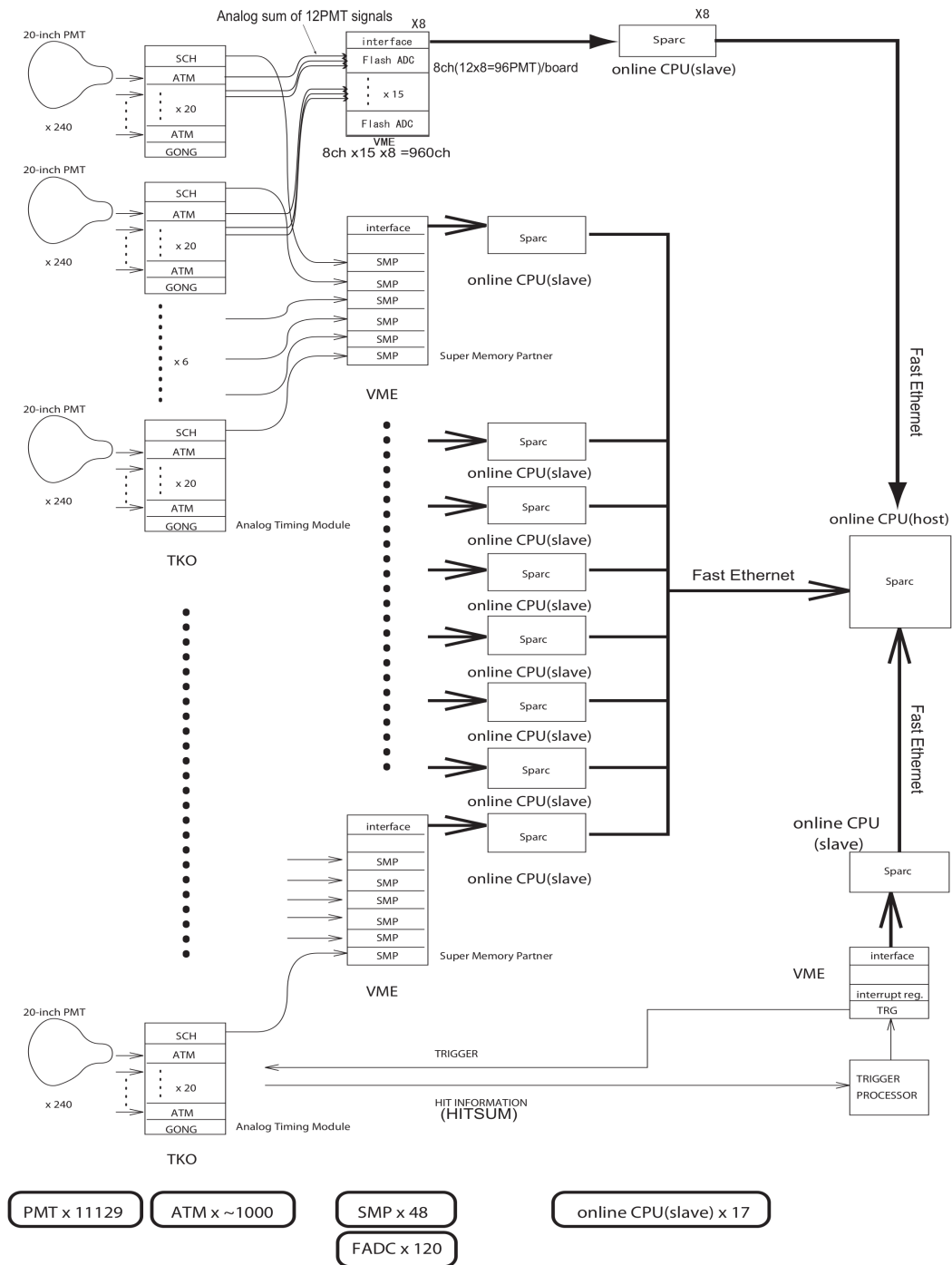


FIGURE 3.7: A schematic showing the layout of the DAQ used in SK-I to SK-III

added up, effectively counting up the number of PMT hits within this period. If found to exceed specific thresholds, a global trigger was executed. This signal was chosen to be 200ns wide, as this corresponds to the maximum time it would take light to travel across the tank.

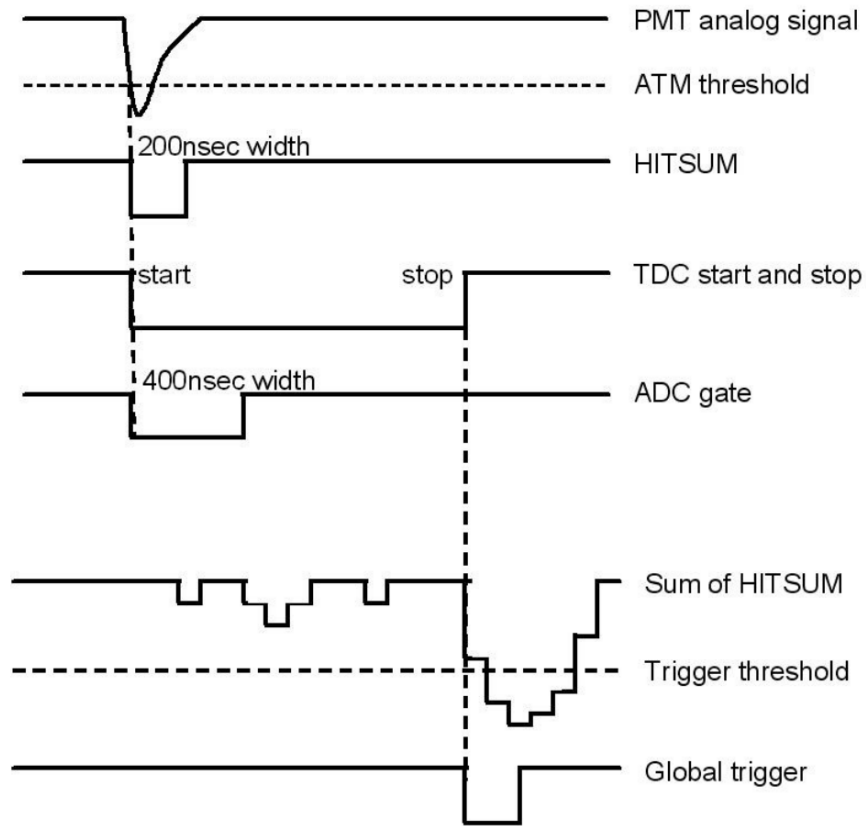


FIGURE 3.8: Overview of the trigger system in SK-I to III

The final two signals are sent to the charge-to-analog converter (QAC), and time-to-analog converter (TAC) to register the integrated charge over 400 ns for each PMT, and the PMT hit timing respectively.

There were three separate types of trigger derived from the HITSUM signal - Super Low Energy (SLE), Low Energy (LE) and High Energy (HE) triggers. The threshold for these varies dependent on SK period according to the varying amount of PMTs, as shown in table 3.2. An outer detector (OD) trigger also exists, for triggering on heavy activity in the OD.

SK Period	SK-I	SK-II	SK-III
SLE	186 mV	110 mV	186 mV
LE	320 mV	152 mV	302 mV
HE	340 mV	180 mV	320 mV

TABLE 3.2: Trigger thresholds for each trigger type in SK-I to III

The minimum threshold 186mV, approximately corresponds to a 4.6MeV electron.

3.7.2 Data Acquisition System for SK-IV

This electronics system was upgraded for SK-IV in 2008 [6]. This upgrade granted many improvements - every hit from PMTs is now quickly digitized, allowing a software-based trigger system to replace the hardware trigger of SK-I to III, and essentially remove electronics down time. Another aim of the upgrade was to allow different event widths to be stored for different trigger types. This is useful, because disk space is prohibitive in storing SLE trigger data, which occurs at a rate of $\sim 3\text{kHz}$, however for the higher energy triggers, we want to store a large amount of data, capturing any possible pre-activity, and allowing a more comprehensive view of decay electrons and neutron capture gammas following the initial interaction.

With this in mind, the ATM system was replaced by a new QBEE system (QTC-Based Electronics with Ethernet). QTC refers to an ASIC developed as a high-speed charge (Q)-Time converter. One QBEE module may take input from 24 PMTs, quickly digitalizing the PMT signal using QTC and multi-hit time-to-digital converters (TDC).

Similarly to the previous system, PMT charge is integrated over a 400ns gate, however here to expand the potential range of measurable charge, three different input channels are used, each with different gain. These channels have gains of 1, 1/7, and 1/49, allowing a range of charge from 0.2 to 2500pC to be observed.

The output from the QTC modules is then sent to the TDCs, which measure the width of the QTC output pulse. This data is then input to an FPGA, which digitalizes the charge and timing information, before sending it to the front end PCs (this is the ethernet part of QBEE). The front end PCs pass the hit information onto the merging PCs, which apply the trigger thresholds, before storing any selected events onto the disk for further reduction.

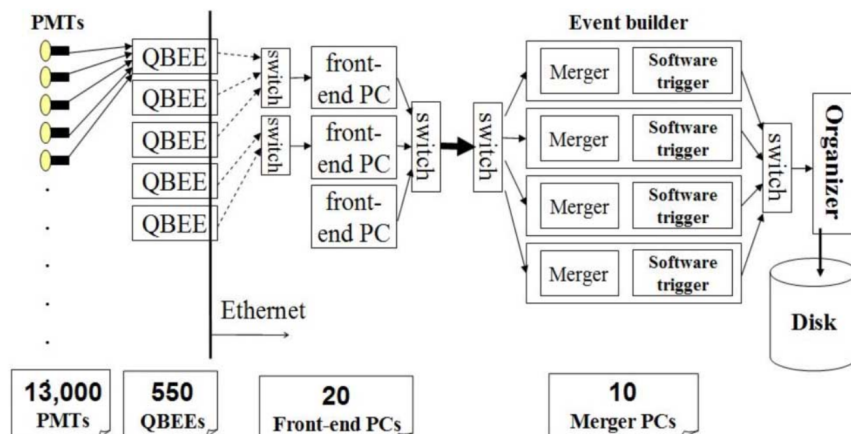


FIGURE 3.9: Block diagram for the new DAQ in SK-IV. Taken from [6]

In SK-IV, the trigger is applied emulating the HITSUM signal of SK-I to III, by calculating the number of PMT hits in a 200ns sliding window. If this value exceeds a trigger threshold, the event will be recorded. Under the ATM system, all triggers recorded for a period of $1.3\mu s$ surrounding the event. However using the QBEEs, the SLE trigger can be set to save only $1.5\mu s$ of data, while the much less frequently triggering LE and HE triggers can save data from $-5 \rightarrow +35\mu s$ surrounding the trigger time.

A special high energy (SHE) trigger was also introduced in SK-IV. This has a similar hit threshold as the existing HE trigger, but if a SHE triggered event is not accompanied by an OD trigger, an additional "After Trigger" (AFT) is issued, saving an additional $500\mu s$ of data, which can be used for analysing neutron captures. SHE was initially introduced with a threshold of 70 hits, but this was lowered to 58 hits in September 2011.

SK-IV Triggers	Hits/200ns Threshold	Event Width (μs)
OD	22	
SLE	34	$-0.5 \rightarrow 1.0$
LE	47	$-5 \rightarrow 35$
HE	50	$-5 \rightarrow 35$
SHE	70 - 58	$-5 \rightarrow 35$
AFT	SHE, no OD	$35 \rightarrow 535$

TABLE 3.3: Trigger information for SK-IV

Chapter 4

Detector Calibration

It is important to properly calibrate our detector, so that we may be confident in our knowledge of its performance, and thus apply smaller systematic errors during the reconstruction and analysis of data. The types of calibration performed may be split into three general areas: PMT calibration, water transparency calibration, and energy scale calibration. For further details, please see [93].

4.1 PMT Calibration

Calibrating PMTs is necessary to understand the charge and timing output of each PMT, and how it relates to the energy and timing of photons that were collected on the surface of the photo-cathode. PMT charge calibration consists largely of two factors: the PMT QE (quantum efficiency), and its gain.

Quantum efficiency (QE) refers to the efficiency with which photons are collected, and generate photo-electrons. For purposes of the calibration, this may be combined with the collection efficiency, which gives the efficiency for photo-electrons that have been released from the photo-cathode, to arrive at the first dynode. The product of the two, will be referred to as quantum efficiency. The second factor - gain - will be defined as the conversion factor between initial photo-electrons, to the charge output from the PMT in pC.

For Low-energy events, most PMT hits consist of a single photo-electron, so the charge output from each PMT is largely uniform, and the most important calibration is the QE. For higher energy events, where PMTs are likely to release more than a single photo-electron per hit, gain calibration is also necessary. Both of these must be known individually for each PMT. The calibration of PMT gain may be thought of as split into

an “absolute gain”, the average amplification factor applied to all PMTs, and a “relative gain”, which details the fluctuations on a PMT-by-PMT basis.

4.1.1 Determining High Voltage for each PMT

Before any calibration of output can be done, we must determine an appropriate voltage to apply to each PMT. To decide this, it was required that each PMT must produce the same output charge, for the same incident light intensity. As SK is not spherically symmetric, using the same light source we would expect to get different charges dependent on the PMT distance from the light source. So to compensate for this, 420 reference PMTs were individually calibrated before installation, so they could be mounted in the tank and serve as references for the un-calibrated PMTs.

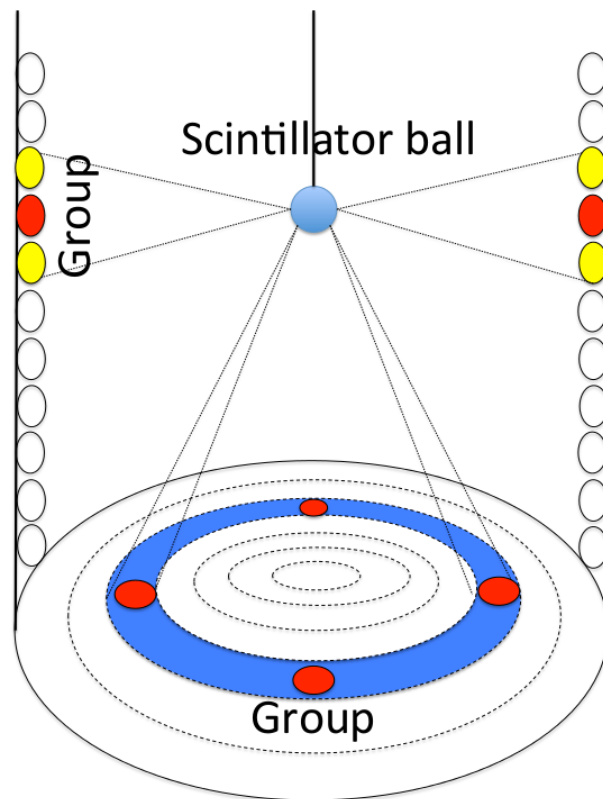


FIGURE 4.1: Xe light emitting from a scintillator ball to calibrate the PMT high voltage in the tank. The red dots illustrate positions of the pre-calibrated reference PMTs.

The light source used is a Xe lamp, the output from which is then passed through an optical fibre, and into a scintillator ball placed at the centre of the tank. This scintillator ball the scatters the light isotropically throughout the tank. The HV input of each PMT was then adjusted such that the output charge would match the pre-calibrated reference PMTs in similar geometrical locations. The Xe lamp and scintillator ball are a permanent fixture in the middle of the tank, for continuous monitoring of PMT gain.

4.1.2 Relative Gain

The relative gain calibration is performed to compensate for any differences in response between PMTs, and apply adjustments to each so the result will look uniform. To perform this calibration, a light source (nitrogen-laser-driven dye laser \rightarrow optical fibre \rightarrow diffuser ball in tank) is placed in the tank, and two measurements are performed. Firstly, using high-intensity flashes (I_s), to record the average charge observed $Q_{obs}(i)$ for each PMT i , and secondly, low intensity flashes (I_w) which are designed to produce single photo-electron ejection on every PMT. These single p-e events are counted, to give $N_{obs}(i)$ for each PMT. To change the intensity of the light source, a filter wheel with neutral density filters was set up between the output of the laser and the optical fibre. A diagram of this may be seen at [4.5](#).

$$Q_{obs}(i) \propto I_s \times a(i) \times \epsilon_{qe}(i) \times G(i) \quad (4.1)$$

$$N_{obs}(i) \propto I_w \times a(i) \times \epsilon_{qe}(i), \quad (4.2)$$

where $\epsilon_{qe}(i)$ is the QE, $a(i)$ is the acceptance and $G(i)$ is the gain of each PMT. As the light source is in the same position for both of these tests, the acceptance is the same in both equations, and we may cancel out the unknown QE factor, to find the gain of each PMT

$$G(i) \propto \frac{Q_{obs}(i)}{N_{obs}(i)}. \quad (4.3)$$

This is then normalized to the average gain, to find the relative gain difference for each PMT. The RMS was found to be 5.9%, and is used as a PMT-by-PMT correction factor on the conversion between observed charge and photo-electrons. As the HV system has already been calibrated to create uniform output intensity Q_{obs} on every PMT, we can conclude that these relative gain fluctuations are due to differences in QE between PMTs.

4.1.3 Absolute gain

Now that the relative gain corrections for each PMT are known, we can apply these corrections to align the single p-e distributions of all PMTs. Adding these distributions together for each PMT results in the average single p-e response of the detector. From this we can determine the absolute gain of all PMTs.

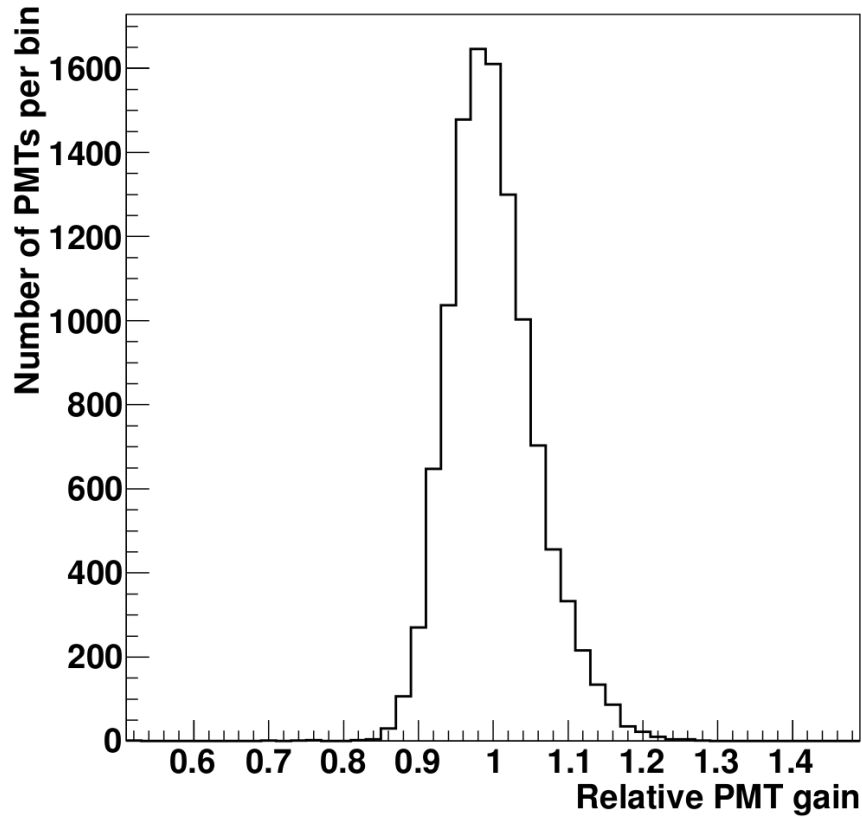


FIGURE 4.2: The relative gain difference of each PMT from calibration using a nitrogen-laser-driven dye laser.

A stable source of single p-e producing light is required for this calibration, for which nickel-californium (Ni-Cf) was chosen. The Cf decays via spontaneous fission, 3.8% of the time producing an average multiplicity of 3.8 neutrons (lifetime 2.65 years). These neutrons are then captured by the surrounding Nickel, and 6.1-9.0 MeV gamma rays are released isotropically. This was positioned at the centre of the tank, and the resultant PMT signals were 99% single p-e hits. To compensate for dark hits, the same distribution was taken without the Ni-Cf source, and then subtracted from the on-timing data. The relative gain corrections were applied, resulting in the plot 4.3.

The average value from plot 4.3 was taken to be the conversion factor between pC and single p-e signals.

	Absolute Gain (pC/1p-e)
SK-I	2.055
SK-II	2.297
SK-III	2.243
SK-IV	2.645

TABLE 4.1: Absolute gain conversion factors between single photo-electron events, and output PMT charge.

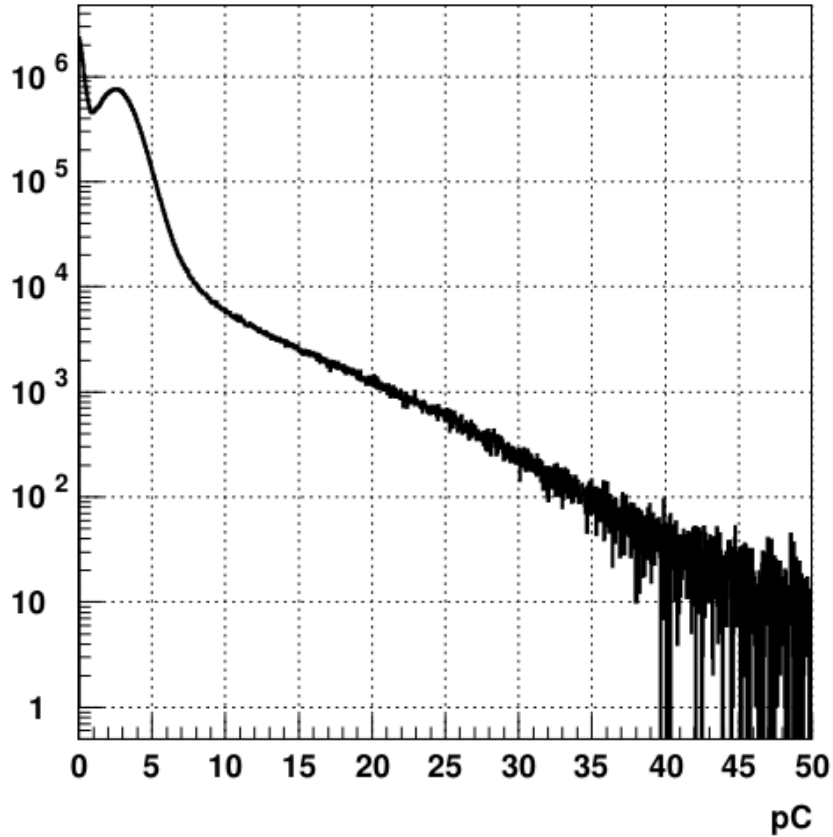


FIGURE 4.3: The charge distribution from Ni-Cf single p-e calibration source, after relative gain corrections had been applied.

This calculation was performed again before the start each SK period, and values found are recorded in table 4.1. The PMT gain is found to increase by 2-3% per year. The break in this pattern between SK-II and III is due to the installation of new PMTs in this interval. Although the reason for this increasing gain is currently unknown, it is taken account of in physics analyses.

4.1.4 Quantum Efficiency

To properly simulate PMT action in our MC simulation, it is required to know the QE of each PMT. To do this, the same Ni-Cf source was used to provide a sample of single p-e signals. We can then calculate the difference in MC predicted number of hits, to the observed number in data, and adjust the simulated QE to account for any discrepancy.

The geometry of the tank is adjusted by applying the following correction to the MC

$$N_{obs}(i) \times R(i)^2/a(\theta(i)), \quad (4.4)$$

where $R(i)$ is the distance from the source to PMT, and $a(\theta(i))$ is the acceptance of the PMT for a given incident angle θ . Further corrections for light propagation were applied, including modelling of the black sheet, reflections from PMT surface, and scattering or absorption in water. The remaining MC-data differences are attributed to varying QE between PMTs.

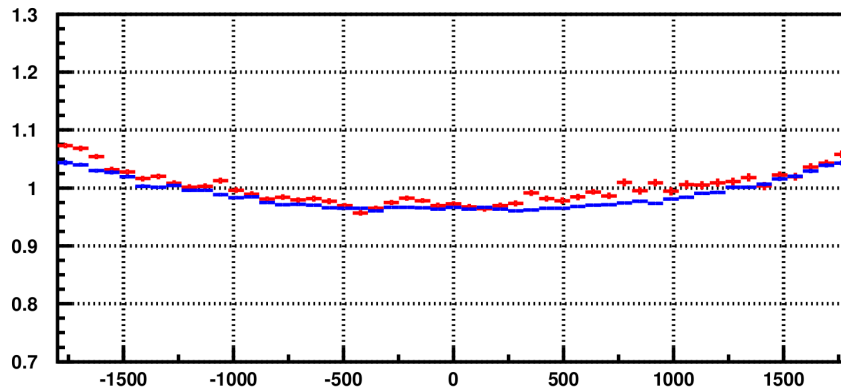


FIGURE 4.4: This plot shows the relative PMT hit probability dependent on z (cm) position in the tank. The red points are from Ni-Cf source, and the blue points are the MC, before QE correction.

It is of interest to note, that PMTs added between SK-II and SK-III (replacing those lost in the accident), were found to have a higher QE than the remaining original PMTs. Similarly, even out of the originally used PMTs, one batch produced between 1992 and 1995 were found to have 4.5% lower QE than the second batch, made in 1996-7. These improvements were attributed to improvements made by Hamamatsu in the PMT glass transparency.

4.1.5 Timing Calibration

To ensure accurate reconstruction of event vertices and track directions, it is important to understand the response time of each PMT and electronics channel. There are a number of effects which must be considered - length of PMT cabling, electronics processing time, PMT time-walk. The latter refers to an effect in which the response time of a PMT is reduced for large pulses, as the pulse rise time (and thus time to exceed trigger threshold) is faster.

To perform timing calculation, the dye laser is used again, the setup of which you may see in figure 4.5. The input nitrogen laser produces pulses 0.4ns wide at 337 nm, which are then used as input for the dye laser. This light is also observed by a monitoring PMT, to define the time of laser injection. The dye laser further shortens the pulse to 0.2 ns, and outputs a wavelength of 398 nm, better matching the optimal QE of

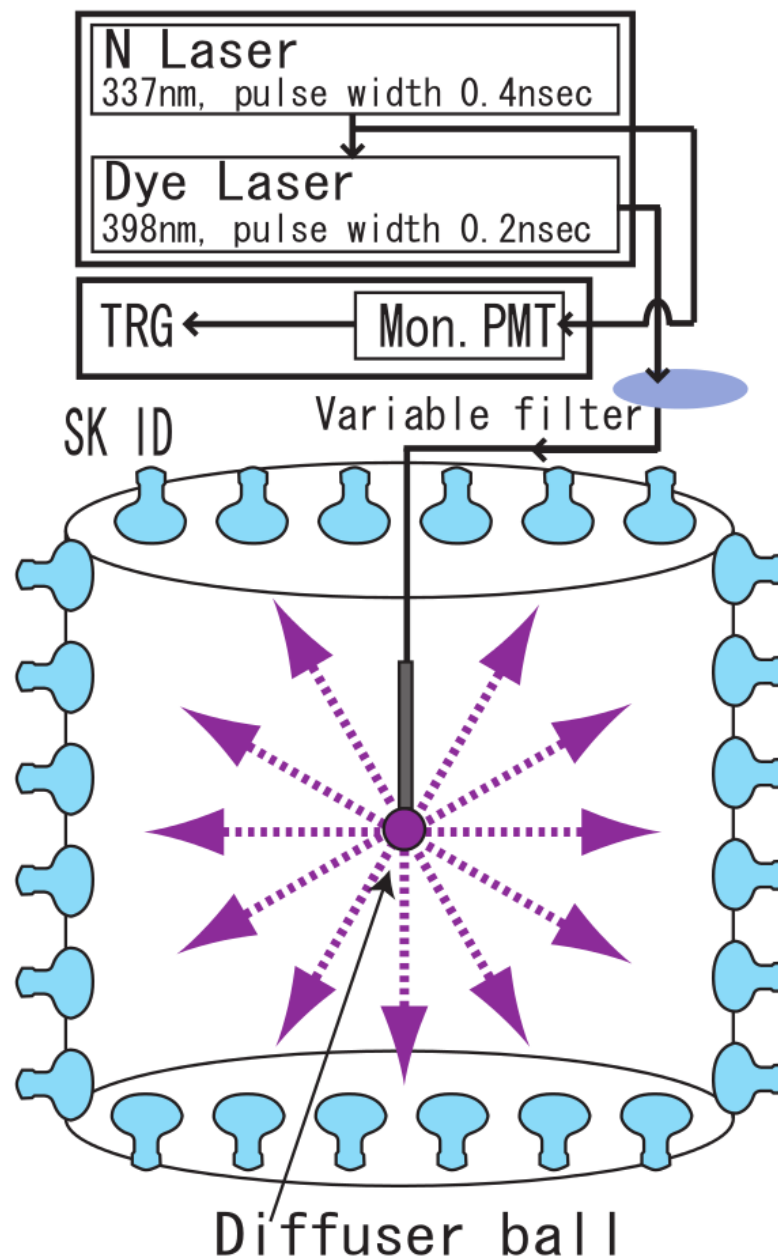


FIGURE 4.5: The setup of the dye laser used to calibrate the timing and relative gain of the ID PMTs.

our PMTs. This pulse is transmitted to the tank via a 400 nm optical fibre, where an isotropic distribution is produced using a diffuser ball.

Time-Charge (TQ) plots are then constructed for each readout channel, showing the response time of each channel as a function of its charge. The charge dependence is due to the aforementioned time-walk effect. To use this information in calibration, a "TQ-map" is constructed for each channel, by fitting a polynomial to each TQ plot.

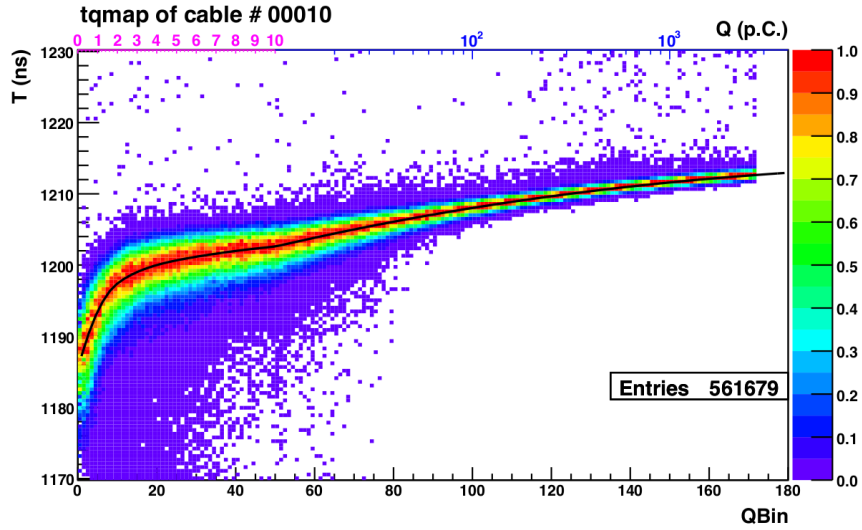


FIGURE 4.6: Charge vs Time plot for readout channel 00010. The black line is a fitted polynomial used for calibration, referred to as the "TQ map".

The selection for events used in this plot, is performed by subtracting time-of-flight (ToF) from the diffuser ball for each PMT in the tank, and then selecting all hits within ± 50 ns of the monitor PMT hit timing.

4.2 Water Calibration

To best model the passage of photons through water in our MC, we must calibrate to the properties of the SK tank water. Firstly, work on measuring the absorption and scattering of light is presented, followed by measurements of light reflection at the PMT surface, and properties of the black sheet.

4.2.1 Passage of Photons through Water

To calibrate the absorption and scattering of light in water, we fire a laser through an optical fibre and into the tank, at various different wavelengths. The output is recorded, and compared with MC estimates to fit the parameters for absorption and scattering. A depiction of the experimental setup may be seen in figure 4.7, and for a more detailed description, you may see [94].

The intensity of light of wavelength λ as it passes through a medium may be given by

$$I(\lambda) = I_0(\lambda)e^{-\frac{x}{L(\lambda)}}, \quad (4.5)$$

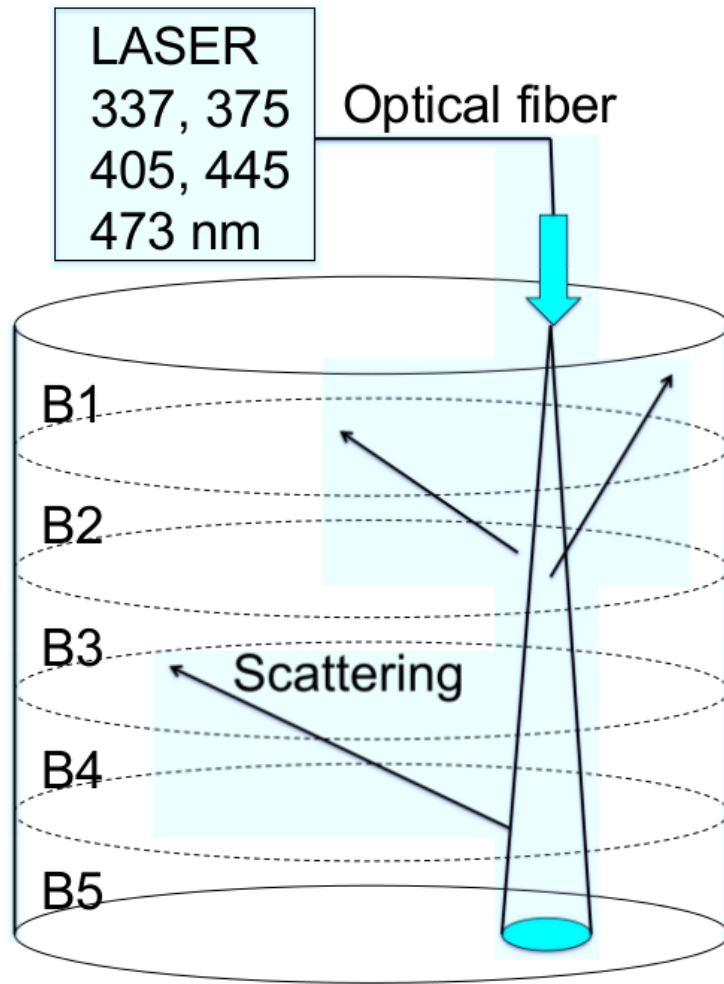


FIGURE 4.7: The laser system used to calibrate light scattering and absorption through water. B1-5 represent different regions of the tank in which analysis was performed.

where $L(\lambda)$ is the attenuation length (commonly referred to as water transparency within SK), and x is the distance travelled. Typically the attenuation length is described in terms of absorption and scattering, however in SK it is defined as

$$L(\lambda) = \frac{1}{\alpha_{abs}(\lambda) + \alpha_{sym}(\lambda) + \alpha_{asy}(\lambda)}, \quad (4.6)$$

where $\alpha_{abs}(\lambda)$, $\alpha_{sym}(\lambda)$ and $\alpha_{asy}(\lambda)$ are empirically fitted parameters, corresponding to absorption, symmetric and asymmetric scattering.

Symmetric scattering includes Rayleigh scattering, and the symmetric component of Mie scattering, described by $1 + \cos^2 \theta$. The asymmetric scattering term is used for the asymmetric component of Mie scattering, where scattering probability increases linearly for forward scattering angles. These terms are each represented by different functions,

for a total of 8 different fitting parameters, which are adjusted to minimize the χ^2 between the laser data, and MC fit:

$$\alpha_{abs}(\lambda) = P_0 \times \frac{P_1}{\lambda^4} + C(\lambda) \quad (4.7)$$

$$\alpha_{sym}(\lambda) = \frac{P_4}{\lambda^4} \times \left(1.0 + \frac{P_5}{\lambda^2}\right) \quad (4.8)$$

$$\alpha_{asy}(\lambda) = P_6 \times \left(1.0 + \frac{P_7}{\lambda^4} \times (\lambda - P_8)^2\right). \quad (4.9)$$

The term C is altered depending on wavelength: for $\lambda \geq 464$ nm, the function is based off an experimental measurement by Pope and Fry [95], and for $\lambda < 464$ nm, it is given by

$$C(\lambda) = P_0 \times P_2 \times \left(\frac{\lambda}{500}\right)^{P_3}. \quad (4.10)$$

An example of the results of this fit from April 2009 data can be seen in figure 4.8.

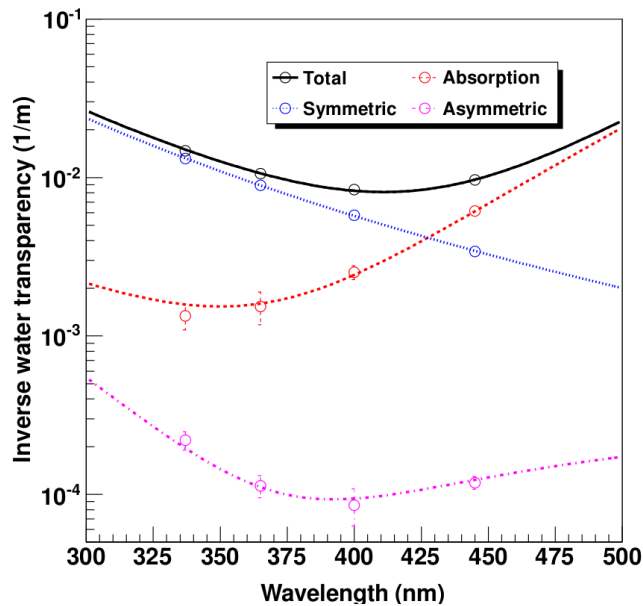


FIGURE 4.8: The results of the fit calibration for water scattering parameters, for April 2009. The dots represent values measured in data, and the lines are the corresponded fitted functions.

These fits are updated in real time, so we may constantly measure the water quality. Symmetric scattering is mostly stable in time, however asymmetric scattering and absorption have a time dependence of $\sim 20 - 40\%$ and $\sim 20 - 60\%$ respectively.

4.2.2 PMT Surface Reflections, Black Sheet

Light reflection at the surface of the PMT is tuned, by varying the refractive index of the bi-alkali photo-cathode until best fit is achieved. The same laser setup as in the water transparency calibration is used here (figure 4.7). However the samples used for determining reflections or scattering varies between the studies. All of the hits are ToF-corrected to the vertex of laser beam emission. After this, PMT hits that occur relatively early, are taken to be direct laser hits, and used in light transparency calibration. PMT hits coming later, are assumed to be due to reflections, and are used in this study. The exact timing criteria for this split is different depending on tank region, as depicted in figure 4.9.

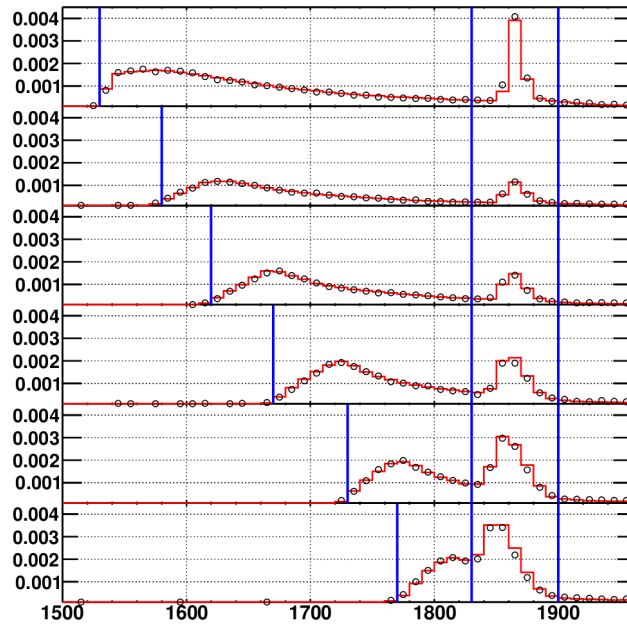


FIGURE 4.9: The split up of data taken from the laser beam (405 nm) used for water and PMT reflection calibration. Shown is the timing (ns) of each PMT hit, after ToF correction, for 6 different regions of the tank (the top plot is of the tank top wall, and the remaining 5 are barrel regions shown in figure 4.7). The hits between the two left-most blue lines, are used for water transparency calibration, and those between the two right-most lines are used for reflection calibration.

The bi-alkali refractive index was taken to be $n_{img} + n_{real}$, and fitted to the laser data as $n_{img} = 1.667$, and $n_{real} = 2.31, 2.69, 3.06$ and 3.24 for laser wavelengths $\lambda = 337, 365, 400,$ and 420 nm respectively.

The black sheet used to stop light leaks between the ID and OD must also have its reflectivity and absorptivity calibrated. For this purpose a sample of black sheet was placed inside the SK tank, and a laser was directed at it, reflecting into the tank. A diagram of this set-up can be seen in figure 4.10. The reflected charge ($Q_{scattered}$) was

then measured by the PMTs. As a comparison, the charge was also measured with no black sheet present (Q_{direct}). The ratio of these numbers, $R = Q_{scattered}/Q_{direct}$ was used to calibrate the black sheet reflectivity. This experiment was repeated for three different incident angles (30° , 45° and 60°), and three different laser wavelengths (337 nm, 400 nm and 420 nm).

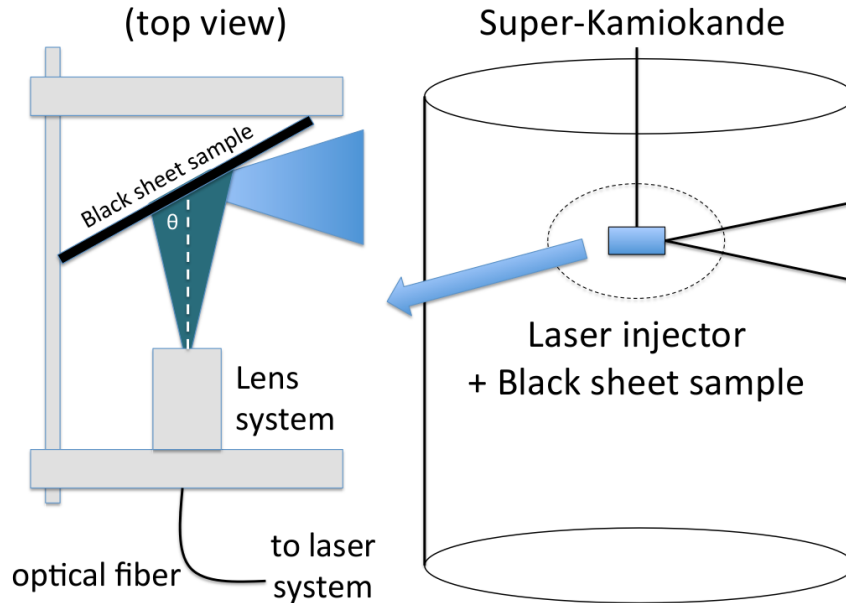


FIGURE 4.10: The experimental set-up used to tune the black sheet reflectivity.

4.3 Energy Scale Calibration

The conversion from observed photo-electrons to the output charge is now well calibrated, but for a reliable reconstruction we must also calibrate how many photo-electrons are produced by particles for a given energy. Knowing particle energy precisely is very important for any neutrino oscillation analysis, as we know the probability of flavour change is dependent on the neutrino energy (see chapter 2).

For energy scale calibration in high energy analyses, four separate calibration sources are considered, across a wide energy range.

- Track range of high energy cosmic rays (1~10 GeV)
- Cherenkov angle of low energy cosmic rays (200~500 MeV)
- Invariant mass of π^0 produced in neutrino interactions (~ 130 MeV)
- Decay electron momentum (~ 50 MeV)

A data vs MC comparison is performed for each of these event samples, and the simulation is calibrated to attain uniformity.

4.3.1 High Energy Cosmic-Rays

In this context, “cosmic-rays” refer to muons produced in the atmosphere by π -decay, which have successfully passed through the rock above SK and come to a stop within the detector. Electrons are generally thermalized in the atmosphere or rock, so there is no equivalent electron sample. Several selections must be passed for an event to be identified as a cosmic ray muon for this calibration:

- Enters through the top wall of the detector.
- Reconstructed direction must be downward ($\cos \theta > 0.94$, where θ is the zenith angle).
- A single decay electron is detected.
- The track length of the muon must be ($7 < L < 30$)m.

Energy calibration may be done using the range of the muons. The track length of the muon is approximately proportional to its initial momentum, thus the track length selection listed above may be thought of as a high energy selection, with the added criteria that the muon must stop inside the detector. The muon track length is calculated by taking the distance between the reconstructed entry point, and the reconstructed decay electron vertex.

The data-MC discrepancies before calibration are 0.7%, 1.1%, 2.0% and 2.2% for SK-I to IV respectively. The factor used for calibration is dependent on the track length of the particle, as shown in figure 4.11.

4.3.2 Low Energy Cosmic-Rays

This sample is similar to the previous, selecting down going cosmic muon events. However in the low energy case, energy reconstruction is performed based on the opening Cherenkov angle. Recall

$$\cos \theta_C = \frac{1}{n\beta} = \frac{1}{n} \sqrt{1 + \frac{m^2}{p^2}}, \quad (4.11)$$

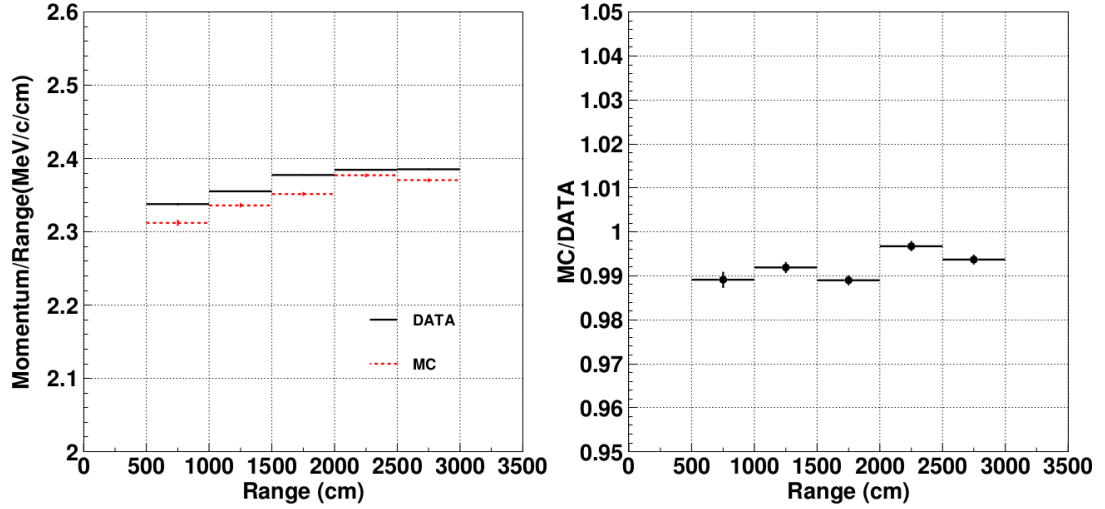


FIGURE 4.11: High energy cosmic ray stopping muon sample, ratio between momentum P_{pe} , calculated from the total number of photo-electrons collected by each PMT, and the range of the particle in cm. The discrepancy between data and MC is used as energy calibration in this momentum range. Data shown is from the SK-II period.

where θ_C is the critical Cherenkov opening angle, and n is refractive index. This sample of cosmic rays is selected the same as previously, except the track length requirement is now replaced by:

- Total ID photoelectrons < 1500 (750 for SK-II).

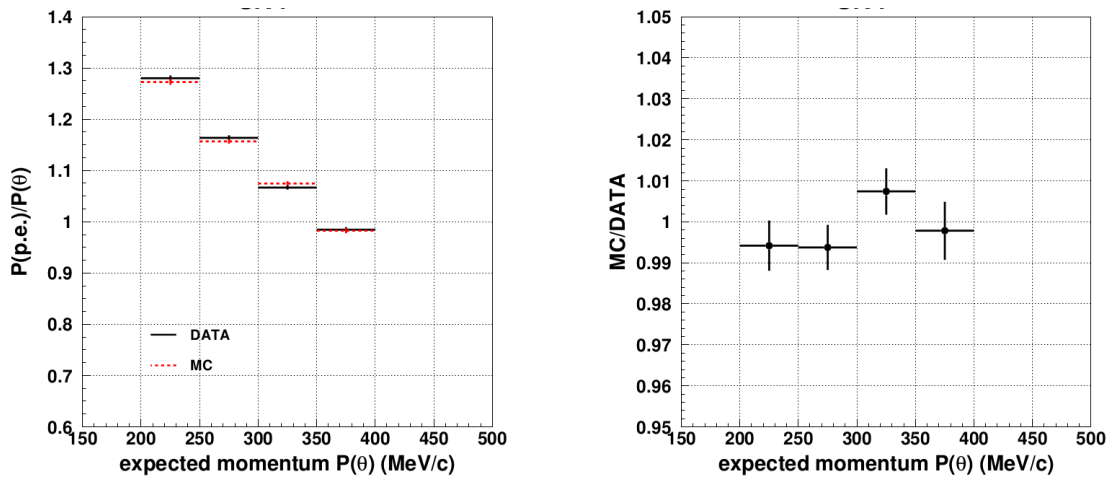


FIGURE 4.12: Low energy cosmic ray muon sample, ratio between momentum P_{pe} , calculated from the total number of photo-electrons collected by each PMT, to P_θ , calculated from the Cherenkov opening angle. The discrepancy between data and MC is used as energy calibration in this momentum range. Data shown is from the SK-I period.

The expected momentum for each event is then compared, as calculated from PMT photo-electrons, to the momentum calculated from Cherenkov opening angle. The ratio of these momenta P_{pe}/P_θ is compared for data and MC, and the discrepancy between

the two is used to calibrate the energy scale. You may see this in figure 4.12. The disagreement between data and MC pre-calibration is 0.7%, 1.3%, 2.1% and 2.1% for SK-I to IV respectively.

4.3.3 π^0 Invariant Mass

In some neutrino interactions, single π^0 are produced. These interactions are not used for oscillation analysis, so they may be used as a calibration source. Around 99% of π^0 decay to $\gamma\gamma$, and this signal may be identified by selecting events with:

- Event vertex reconstructed within tank fiducial volume (> 2 m from ID wall, no large clusters of hits in OD). This is a standard criteria for selecting any fully-contained neutrino events.
- Two electron-like Cherenkov Rings. All reconstructed Cherenkov rings in SK are classified as electron-like or muon-like. This will be discussed in greater detail in chapter 6, but it suffices to say that γ -rays produce Cherenkov rings very similar to those produced by electrons, so this criteria is just a search for the expected $\gamma\gamma$ signature from π^0 decay.
- No decay electron (as this would imply a muon was present in the interaction).

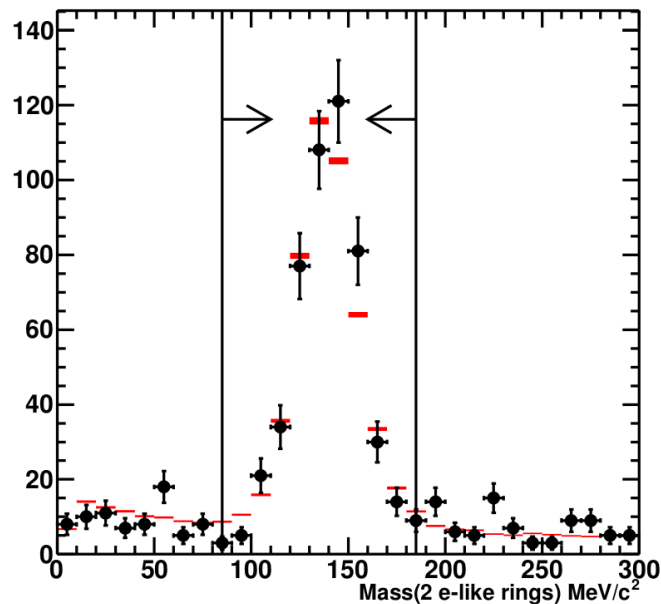


FIGURE 4.13: Reconstructed π^0 invariant mass, for data and MC in black and red respectively.

The π_0 invariant mass is calculated by

$$M_{\pi^0} = \sqrt{2P_{\gamma 1}P_{\gamma 2}(1 - \cos \theta)} \quad (4.12)$$

and fitted with a gaussian function. The difference between the fitted peak positions of the invariant mass for data and MC is used as an energy calibration. Before calibration, the discrepancies between data and MC are 0.7%, 1.3%, 0.3% and 1.7% for SK-I to IV.

4.3.4 Decay Electrons

As a low energy calibration, the reconstruction of decay electron energy is used. Only decay electrons produced by cosmic muon events are considered, to avoid interference with any neutrino analysis. The selection criteria for these is as follows:

- Must occur between 2 μ s and 8 μ s following a stopping cosmic ray event.
- More than 60 (30 for SK-II) PMT hits in a 50 ns window. This is required to reject signal from μ^- capture on oxygen.
- Vertex fit goodness > 0.5
- Vertex reconstructed inside the fiducial volume.

Similarly, the reconstructed decay electron momentum spectra are compared between data and MC, and the energy scale is calibrated by the difference. Pre-calibration discrepancy for SK-I to IV is 0.6%, 1.6%, 0.8% and 1.6% respectively.

4.3.5 Energy Scale Summary

These various calibrations are all effective for different momentum ranges, and may be combined to find an overall uncertainty of the absolute energy scale. This is estimated to be 0.88%, 0.55%, 1.79% and 2.19% for SK-I to IV respectively. A summary of the absolute energy scale calibrations can be found in figure [4.14](#).

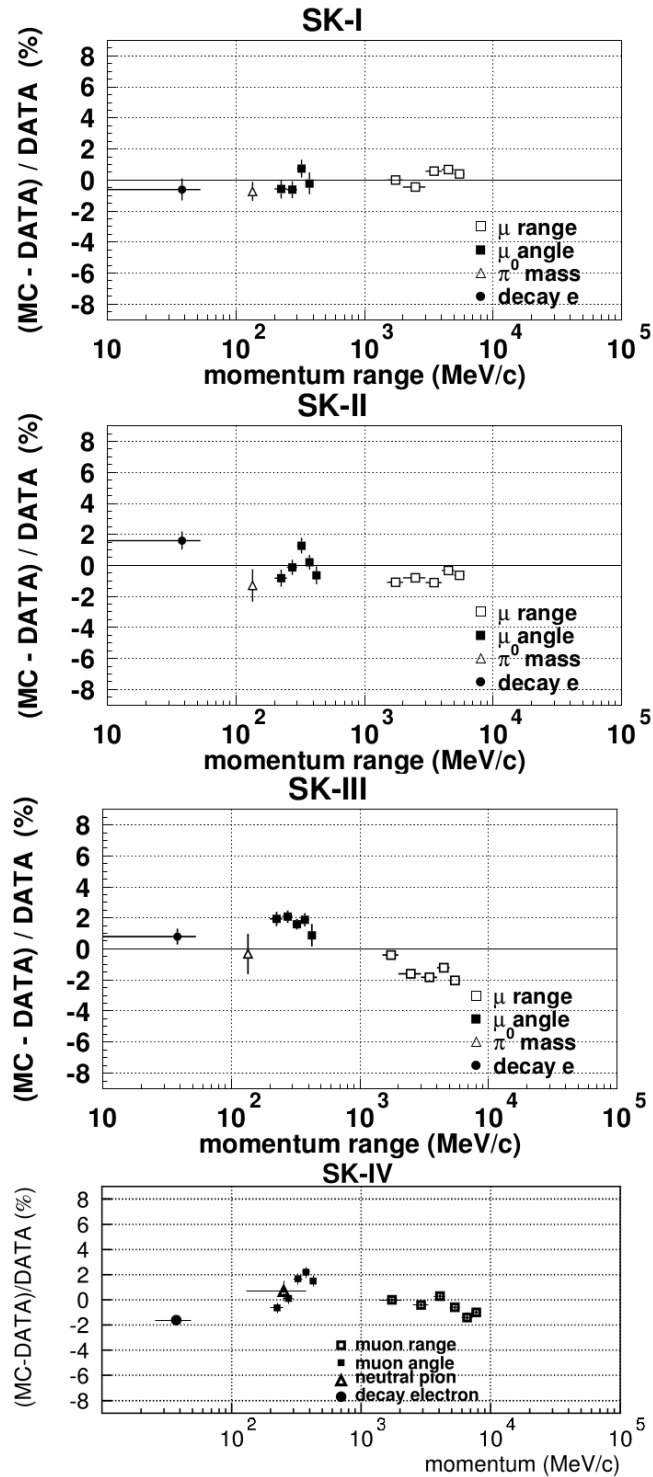


FIGURE 4.14: The summary of all absolute energy scale data-MC discrepancies, for SK-I to IV.

Chapter 5

Monte Carlo Simulation of Atmospheric Neutrinos

Generating a prediction for the number of atmospheric neutrino interactions observed in Super Kamiokande is no simple task. Results depend heavily on detector tuning, flux predictions, particle reconstruction and so forth. To create a reliable expectation on a bin-by-bin basis, it is necessary to simulate the entire process. Using a Monte Carlo (MC) method, inputs are taken from random sampling of atmospheric neutrino flux predictions, processed through the simulation, and finally expected output event rate distributions for each sample are generated. As the simulation is improved, we can be more confident (our degree of “confidence” is represented by the systematic error applied in the analysis) that differences between data and MC are due to real physics effects.

Our MC simulation is constructed in two stages - firstly the initial neutrino interaction in water is modelled, and then the particles output from this are input to a detector simulation, where we model their kinematics across the detector, and the expected number of hits in each PMT. However before any of this is possible, we must first discuss the atmospheric neutrino flux model, which is used as an input to the simulation.

5.1 Atmospheric Neutrino Flux

The flux model used to generate atmospheric neutrino events in our simulation is based on M. Honda’s 2011 model [7]. The Honda flux does not support neutrino energies above 10 TeV, so it is replaced by the Volkova flux in this region. Two additional flux

models, those by G. Battistoni (Fluka flux) [96] and G. Barr (Bartol flux) [97] are used to evaluate the systematic uncertainties on the Honda flux.

The flux model calculates the expected energy spectrum of incident neutrinos on SK. To reach this stage, broadly two processes must be understood - the primary flux of cosmic rays, and then simulation of the hadronic showers they cause, to allow estimation of resultant neutrino multiplicity. The primary flux of cosmic rays is directly measured by high altitude experiments, such as AMS (Alpha Magnetic Spectrometer, in the International Space Station) [98], and balloon-borne experiment BESS [99].

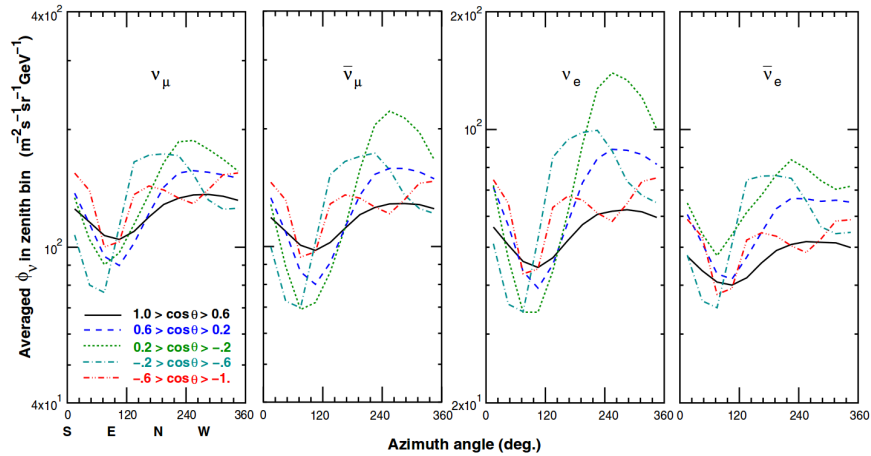


FIGURE 5.1: East-west asymmetry in neutrino flux at SK, due to deflection of primary cosmic rays by the Earth's geomagnetic field. Plots taken from [7].

Almost all incoming cosmic rays are protons, and as the Earth's magnetic field points to the south, these cosmic rays will be deflected in an eastward direction. This creates an east-west asymmetry in the cosmic ray flux (see fig. 5.1), and a rigidity cut off for low energy cosmic rays, below which they are simply deflected back into space. Similarly, around Kamioka the Earth's magnetic field is slightly stronger than average, so we observe a slight asymmetry in upward and downward going neutrino flux. The neutrino flux is peaked near the horizon (fig. 5.2), as muons approaching from this direction have more time to decay into neutrinos. The flux is also significantly affected by solar activity. At solar maximum the strong magnetic field due to solar winds reduces the flux of low energy cosmic rays to \sim half of its value at solar minimum. For higher energy cosmic rays, > 10 GeV, these deflection effects become negligible.

In 2004 Honda updated his flux model to include 3-dimensional interaction modelling, in which the outgoing particles may be deflected at a different angle than the incident cosmic ray [100]. This led to a larger enhancement of flux at the horizon compared to the 1-d flux, due to the larger effective area of cosmic rays which could contribute to these events (depiction in figure 5.3). In the Honda 2011 version, the 3-d scheme is

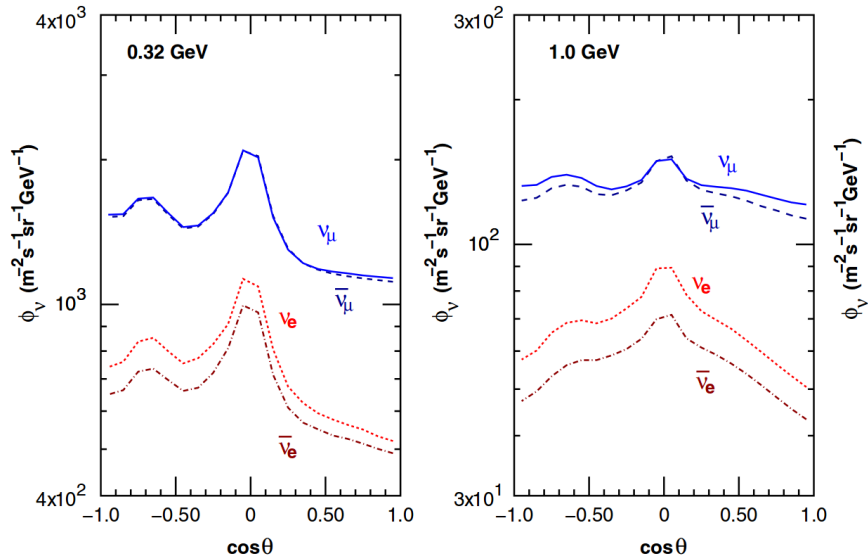


FIGURE 5.2: Zenith angle distribution for neutrino flux incident on SK. You may note the peak at the horizon (around $\cos\theta = 0$), and the slight asymmetry between upward and downward going fluxes. These effects are more prominent in low energy particles, which are more sensitive to magnetic field deflection effects.

used to calculate flux up to 32 GeV (after which required computational power becomes prohibitive).

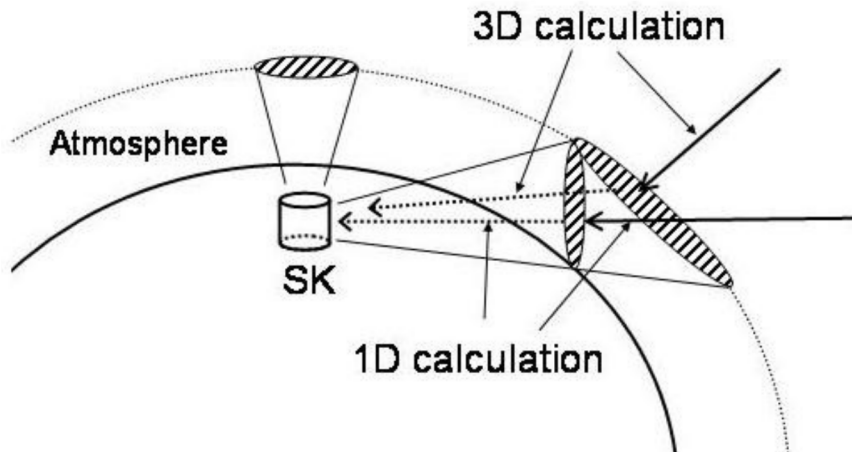


FIGURE 5.3: Additional cosmic ray vectors now contribute to the horizon neutrino flux in the 3-d calculation of Honda flux, compared to the previous 1-d version.

The second stage of modelling neutrino flux, is the simulation of hadronic showers produced when a cosmic ray interacts in the atmosphere. In the Honda flux 2011, two models are used: DPMJET-III [101] for hadronic interactions above 32 GeV, and JAM [102] for interactions between 0.2 and 32 GeV. The JAM model is an addition in the 2011 update, as it was found to agree more favourably with low energy cosmic ray muon data taken by the HARP experiment in 2008 [103]. For further tuning, the model was

compared to cosmic ray muon data was taken at three altitudes by the BESS group: Tsukuba (30 m) [104], Mt. Norikura (2770 m) [105] and Fort Summer (balloon) [106], as shown in figure 5.4. Modifications were made to the JAM model to optimize agreement with data at balloon altitudes, as this is thought to be where most neutrinos are produced.

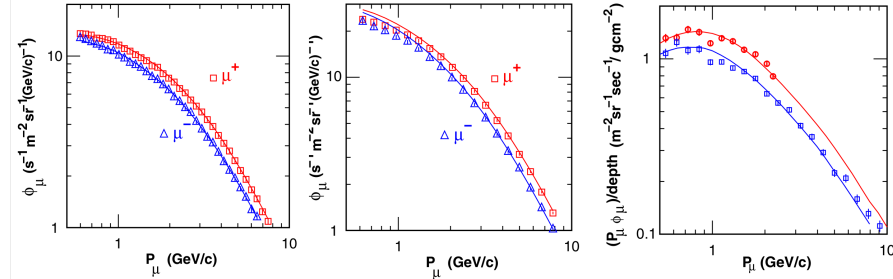


FIGURE 5.4: Flux comparison with cosmic ray muon data. From left to right, Tsukuba (ground), Norikura (mountain) and Ft. Summer (balloon)

The total atmospheric neutrino flux incident on SK can be seen in figure 5.5.

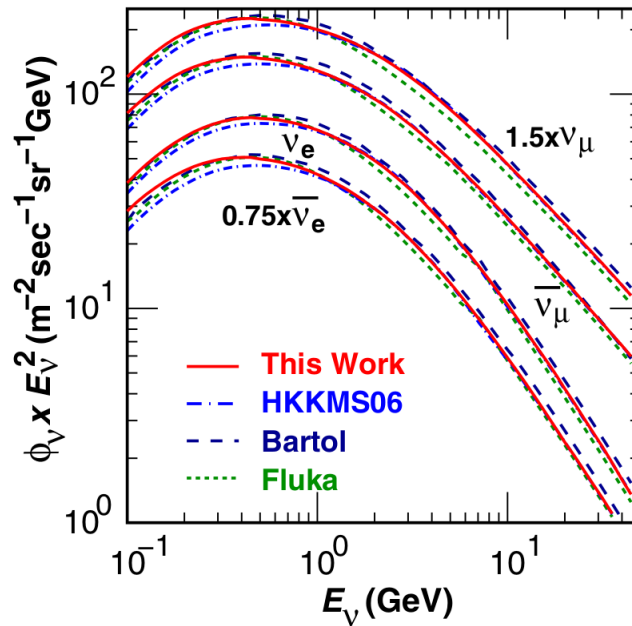


FIGURE 5.5: Atmospheric neutrino flux incident on SK, taken from the Honda 2011 paper. Differences to other models are shown, and taken as a systematic error in analysis.

5.2 Neutrino Interaction Generator

Using the previously described flux model as input, a neutrino interaction generator is used to calculate how often, and in what way these neutrinos will interact in our detector and the surrounding rock. For this purpose, we are using a software library called NEUT

(for details see [12]). NEUT was originally developed for the Kamiokande experiment, just for modelling atmospheric neutrino interactions in water, and has continuously expanded its functionality since then. Only neutrino-nucleon interactions are considered, as the cross-section for neutrino-electron interactions is a factor 10^3 smaller, so may be safely neglected.

The function of NEUT is divided into two distinct steps. Firstly, the initial interaction between incoming neutrino and target nucleon is simulated. Following this, for composite nuclei such as ^{16}O , output hadrons' passage through the nucleus is simulated, as there is a high chance for additional interactions before it escapes.

There are four basic types of interaction modes simulated inside NEUT:

$$\begin{aligned} \text{CC/NC elastic scattering: } & \nu_l + N \rightarrow l + N' \\ \text{CC/NC single meson production: } & \nu_l + N \rightarrow l + N' + \text{meson} \\ \text{CC/NC deep inelastic scattering (DIS): } & \nu_l + N \rightarrow l + N' + \text{hadrons} \\ \text{CC/NC coherent pion production: } & \nu_l + {}^{16}\text{O} \rightarrow l + {}^{16}\text{O} + \pi \end{aligned}$$

where l is a lepton, and N, N' are nucleons.

As the main topic of this thesis relates to using information about the number of neutrons in each event, it is important that this is simulated in each mode as best as possible. Figure 5.6 shows the expected breakdown of neutrons produced by different interaction modes in the sample selection most sensitive to the neutrino mass hierarchy. The total number of neutrons comes from a combination of those produced at the initial interaction (simulated by NEUT, described in this section), and those produced in secondary hadronic interactions in the tank (simulated by SKDetsim and GEANT, as described in the following section).

For each interaction mode, the models used are described, and where available comparisons with experimental data are shown.

5.2.1 Elastic Scattering

Elastic scattering in NEUT is modelled separately for free, and bound nucleons. For free nucleons, the calculation used is described by Llewellyn-Smith [107]. For bound nucleons, (neutrino interactions in ^{16}O), we must consider the whole nucleus in the calculation,

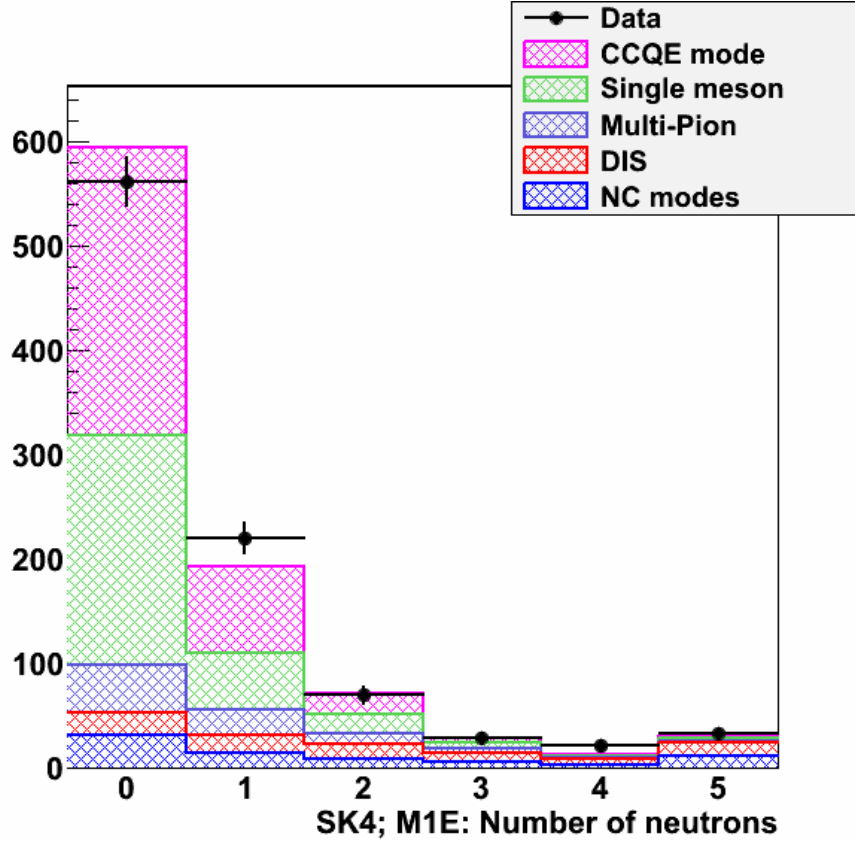


FIGURE 5.6: The breakdown of expected neutron multiplicity for each neutrino interaction mode. The plot shows SK-IV atmospheric neutrino MC Multi-GeV 1-ring electron like sample, normalized to the livetime of the equivalent data-set (shown in black dots). This is the most relevant sample for the neutrino mass hierarchy. In this sample the dominant production modes are CCQE and single-pion production.

which is done using the model of Smith and Moniz [108]. This model approximates the surrounding nucleons as a relativistic Fermi gas, taking the momentum distribution of the nucleons to be flat, up to a Fermi momentum $p_f = 225 \text{ MeV}/c$. To incorporate the Pauli-blocking effect, it is required that the momentum of the recoiling nucleus should be greater than p_f . NC interaction cross sections are calculated using the more well known charged current cross section [109][110]. The axial vector mass M_A is set based on experimental results from K2K and MiniBooNE [111][112].

The agreement between the modelled result and experimental data for neutrino and anti-neutrino interactions can be seen in figure 5.7.

5.2.2 Single Meson Production

The Rein and Sehgal model [113][114] is used to simulate single meson production of π , K and η . An intermediate baryon resonance with mass $< 2 \text{ GeV}/c^2$, is assumed, which then decays to a meson and nucleon. Most of the mesons produced are pions,

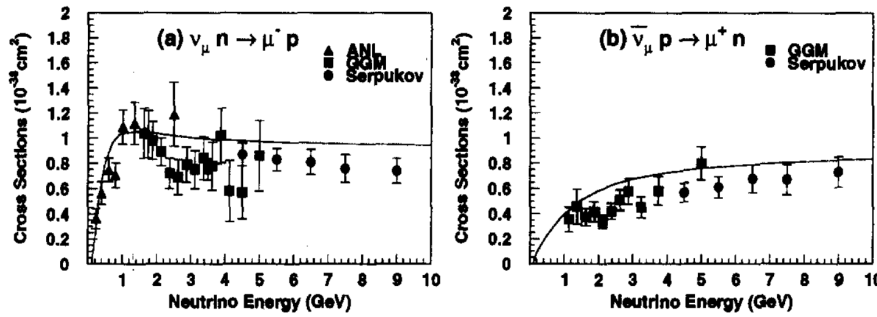


FIGURE 5.7: The agreement of NEUT predictions (black line) of free nucleon charged current quasi-elastic scattering cross section, with experimental data. The experiments considered in figure (a) are ANL (triangle) [8], GGM (square) [9] and Serpukov (circle) [10]. In figure (b), these are GGM (square) [11] and Serpukov (circle) [10]. Figures taken from [12].

but a small amount of K and η mesons represent a significant source of proton decay background. Most baryon resonances produce pions isotropically, with the exception of $\Delta(1232)$.

Another possibility is that the neutrino may react with the entire ^{16}O nucleus, rather than an individual nucleon. This is known as coherent pion production. As in this case the target is much heavier, the resulting decay products have a larger fraction of the neutrino momentum, and thus tend to be scattered in the forward direction. This interaction is described by Rein and Sehgal in [115].

Good agreement is seen between the single meson production cross sections and experimental data, as demonstrated in figure 5.8.

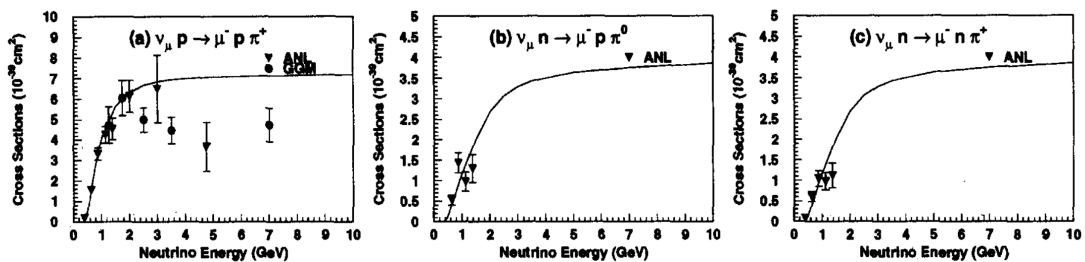


FIGURE 5.8: The agreement of NEUT predictions (black line) of single pion production cross section, with experimental data. The experimental data considered is from ANL (triangle) [13], and GGM (circle) [14]. The figures are taken from [12].

5.2.3 Deep Inelastic Scattering

Deep inelastic scattering refers to the interaction when a neutrino (or other particle) interacts with a constituent quark inside a nucleon, causing the nucleon itself to break up, and potentially generate multiple output hadrons. This process is considered for invariant mass $W > 1.3$ GeV, and becomes the dominant mode in multi-GeV interactions.

The parton distribution function (PDF) for this mode is taken from GRV98 [116], and then a correction by Bodek and Yang is applied to use the PDF at low Q^2 [117].

For invariant mass $1.3 < W < 2.0 \text{ GeV}/c^2$, single pion production interactions are generated as per the previous section, so $n_\pi > 1$ is required for DIS. In this energy range, the only outgoing mesons considered are pions, and their multiplicity is tuned using the results of a Fermilab hydrogen bubble chamber experiment [118]

$$\langle n_\pi \rangle = 0.09 + 1.83 \ln W^2 \quad (5.1)$$

For energies $W > 2.0 \text{ GeV}/c^2$, the hadronic final states are computed by PYTHIA - JETSET [119].

No experimental comparison of neutron production following deep inelastic scattering events was made, however the agreement of the total charged current cross section (which includes quasi-elastic scattering, single meson production and deep inelastic scattering) can be seen in figure 5.9. Another comparison of total cross section on a higher energy scale is in figure 5.10, showing good agreement in the DIS-dominated high energy interactions.

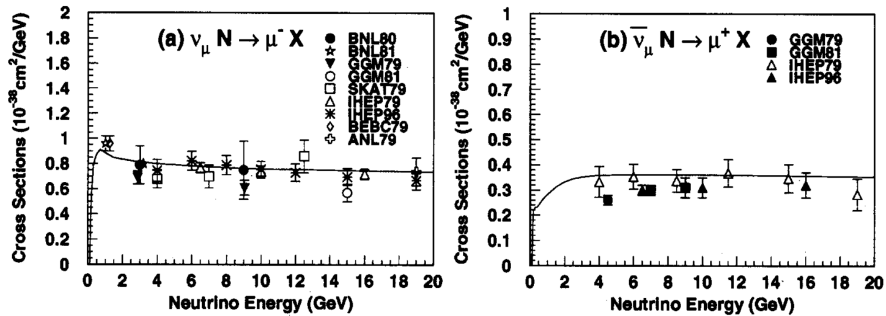


FIGURE 5.9: The agreement of the total neutrino and anti-neutrino charged current cross sections, between the NEUT model and experimental data. In figure (a), the data used is from experiments GGM73 [15], GGM79 [16], GGM81 [17], SKAT79 [18], BEBC79 [19], IHEP79 [20], ANL79 [21], BNL80 [22], BNL81 [23] and IHEP96 [24]. For the anti-neutrino figure (b), the experiments used are GGM79 [25], GGM81 [17], IHEP79 [20] and IHEP96 [24]. The figures are taken from [12].

5.2.4 Nuclear Effects

For interactions taking place in ^{16}O , hadrons that are produced may undergo secondary interactions before leaving the nucleus. To simulate these interactions in NEUT, particles are tracked as they propagate through the nucleus until exiting or absorption, and any secondary interactions which take place are calculated at each tracking step.

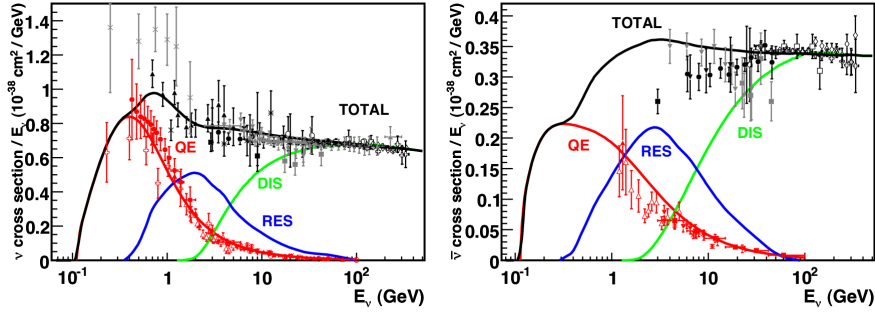


FIGURE 5.10: Comparison between NEUT simulation, and experimental data. Cross section contributions from charged current elastic scattering, single pion production, and deep inelastic scattering are shown. Experimental data is overlaid from [26].

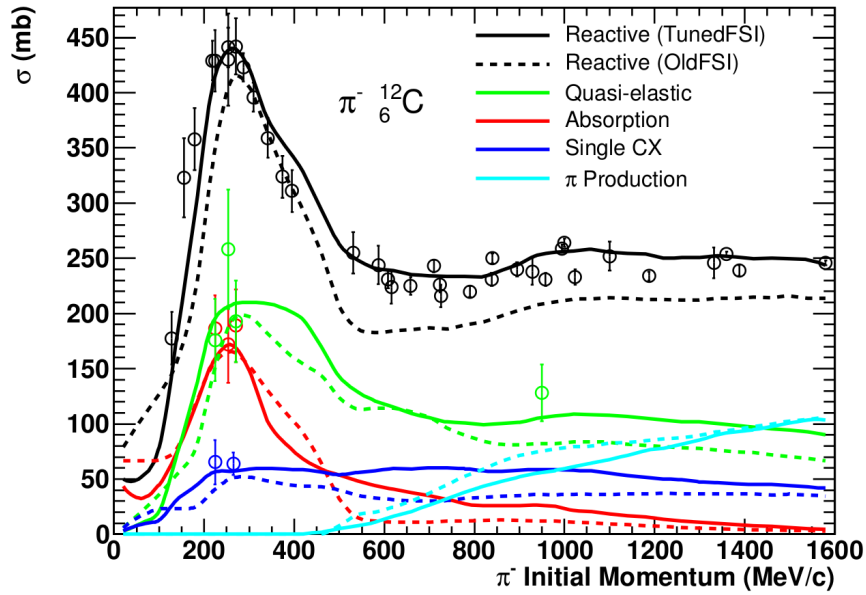


FIGURE 5.11: Tuning of nuclear effect cross sections to $\pi - {}^{12}\text{C}$ scattering data. The dots are taken from experimental data in [27]. The dashed and solid lines represent before and after tuning.

For interaction probabilities of low momentum pions $p_\pi \leq 500$ MeV/c, a model by Salcedo is used [120], which was tuned using experimental data from $\pi^+ - {}^{12}\text{C}$ [121]. Later this was further corrected to a larger value of charge exchange cross-section measured by Ashery [122]. For momentums $p_\pi > 500$ MeV/c, nucleons may be treated as free particles, so π -free proton scattering data is used, and again tuned by $\pi^+ - {}^{12}\text{C}$ results.

For K interactions, the cross sections are tuned to $K^\pm - N$ scattering experiments [123][124] and [125]. For η mesons, experimental data from the interaction ($\eta N \rightarrow N^* \rightarrow \pi N$) is used [126].

5.3 Detector Simulation

After the neutrino interaction has been simulated, the next step is to propagate the outgoing particles throughout a simulation of the SK tank. This involves tracking any further interactions and secondary particles that are produced, simulating Cherenkov photon production and propagation, light collection by PMTs, and the resulting response of the detector electronics. The simulation is carefully tuned using calibration data discussed in the previous chapter.

The detector simulation is constructed around a software package called SKDetsim. SKDetsim interfaces with CERN's GEANT package (v3.21)[127]. GEANT controls the production and propagation of Cherenkov light, as well as processing any particle decays that are required. As Cherenkov photons propagate through the tank, the primary scattering effects are through Rayleigh and Mie elastic scattering, which are tuned using the calibration data previously discussed. Photo-electric absorption is also recently added to our simulation.

For the simulation of hadronic interaction processes, an interface to package CALOR [128] is used. This is a hybrid package, containing various different interaction models, each of which is applicable to different particle types and energies. The models chosen for our simulation are as follows:

Criteria	Hadronic Interaction Model
Hadrons > 10 GeV	FLUKA [129]
Hadrons < 10 GeV	HETC [130]
Neutrons < 20 MeV	MICAP [131]
Pions < 500 MeV	Custom routine based off the NEUT cascade model

For nucleon interactions < 3.5 GeV, and charged pion interactions < 2.5 GeV, the HETC (High Energy Transport Code) uses the Nucleon-Meson-Transport-Code (NMTC), which is based off the Bertini intra-nuclear hadronic cascade model [132]. For energies above this, the particle energies and multiplicities are scaled to the centre of mass energy of the interaction.

For low energy neutron propagation the MICAP (Monte Carlo Ionization Chamber Analysis Package) code is employed. This uses all neutron scattering cross section data from the Evaluated Nuclear Data File (ENDF/B). For very low neutron energies, thermal scattering is calculated based on a free gas model, and the final neutron energy is determined by sampling from an isotropic (in neutron centre-of-mass frame) Maxwellian energy distribution. Neutrons are allowed to track until the lowest allowable energy (10^{-5} eV) to ensure that neutron capture interactions are simulated correctly.

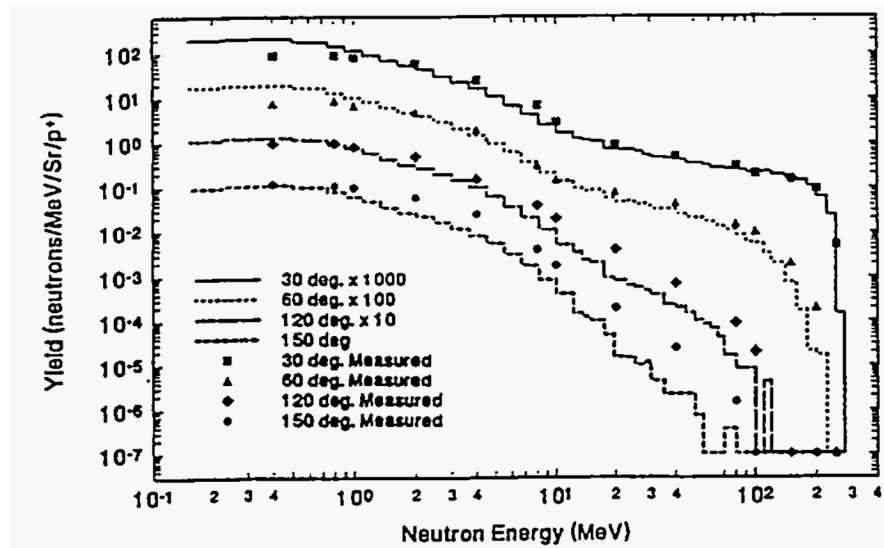


FIGURE 5.12: Absolute neutron yields after impact of 256 MeV protons on a sphere of ^{238}U . Lines are simulated by CALOR, and experimental data is from [28]. This plot is taken from [29].

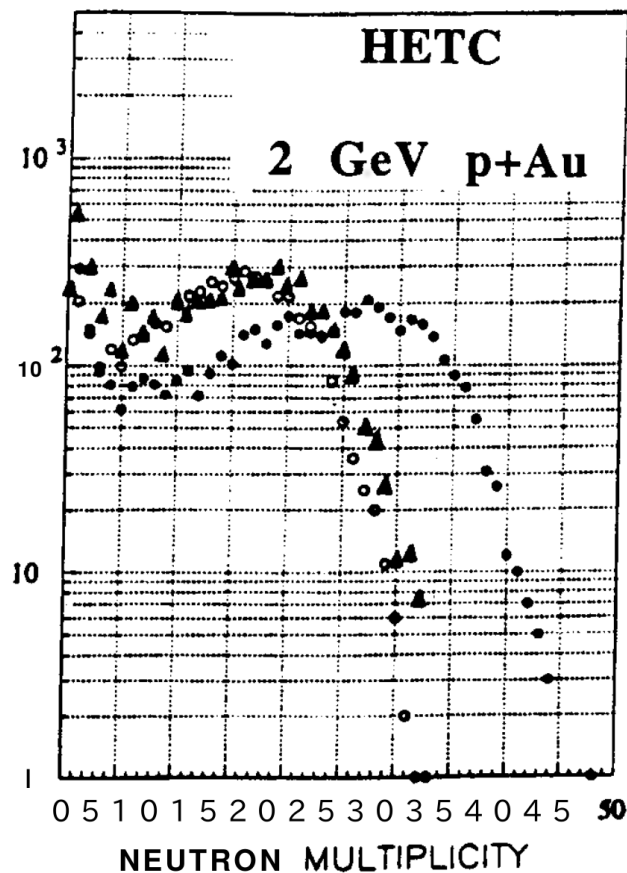


FIGURE 5.13: Neutron multiplicity simulated by HETC (open dots), compared to experimental data (solid triangles) for a 2 GeV proton interacting in Au. The solid dots are before detector efficiency is taken into account. This study and plot are from [30].

In the context of this thesis, a large amount of the neutrons produced following neutrino interactions are as a result of secondary hadronic interactions with the water nuclei. It is difficult to study each of these interactions individually, so the best course of action is to compare final neutron multiplicity, after passing through a body of matter. Studies of the agreement between simulated and measured neutron multiplicities can be seen in figures 5.12 and 5.13.

The electronic response of the detector is simulated down to the signal coming out of the PMTs. The quantum efficiency, gain and single-photon distributions of the PMTs are input from calibration data (described in chapter 4). The HITSUM signal is calculated, and then the same software trigger is applied, as for real data (described in chapter 3). Electronic PMT dark noise is simulated at 5.8kHz. When PMTs degrade and are disabled in the detector (due to becoming flashers, or suspiciously high or low hit rate, etc.), they are masked in the simulation.

Chapter 6

Event Reconstruction

Event reconstruction refers to the process of starting with the charge and timing information received from the PMTs, and “reconstructing” this into useful physics properties which can be used for analysis. You may recall from chapter 2, neutrino oscillation probability is dependent on the energy E , and the distance travelled L of the neutrino. For any sort of oscillation analysis, it is crucial to know what flavour of neutrino we are observing - if this cannot be discerned, we cannot measure anything but total neutrino flux. To identify whether a particle track is entering the tank from outside, or has been generated in the centre of the tank by a neutrino interaction, it is necessary to have precise vertex fitting. Reconstruction of all these properties, and more, is discussed in this chapter. To understand the co-ordinate system used in SK, please see figure 6.1. The software library encompassing neutrino event reconstruction is named “APFit”.

6.1 Vertex Fitting

General vertex fitting of events is calculated in a three-step process. Firstly, the most basic fitting procedure, termed “Point-fit” is used. Point-fit assumes that all the PMT hits in an event come from a single point. Considering a test point, time of flight (ToF) is subtracted from the hit timing on each PMT, forming a distribution of the residual timings. This distribution is fit to a gaussian for each test point, and that which returns the maximum goodness-of-fit, is taken as the event vertex. Particle direction is then calculated by taking the average of the charge-weighted direction vectors, from this vertex to each hit PMT.

The second step, is to identify the primary Cherenkov ring, using this initial vertex. Using the direction calculated by Point-Fit as a starting point, various Cherenkov ring opening

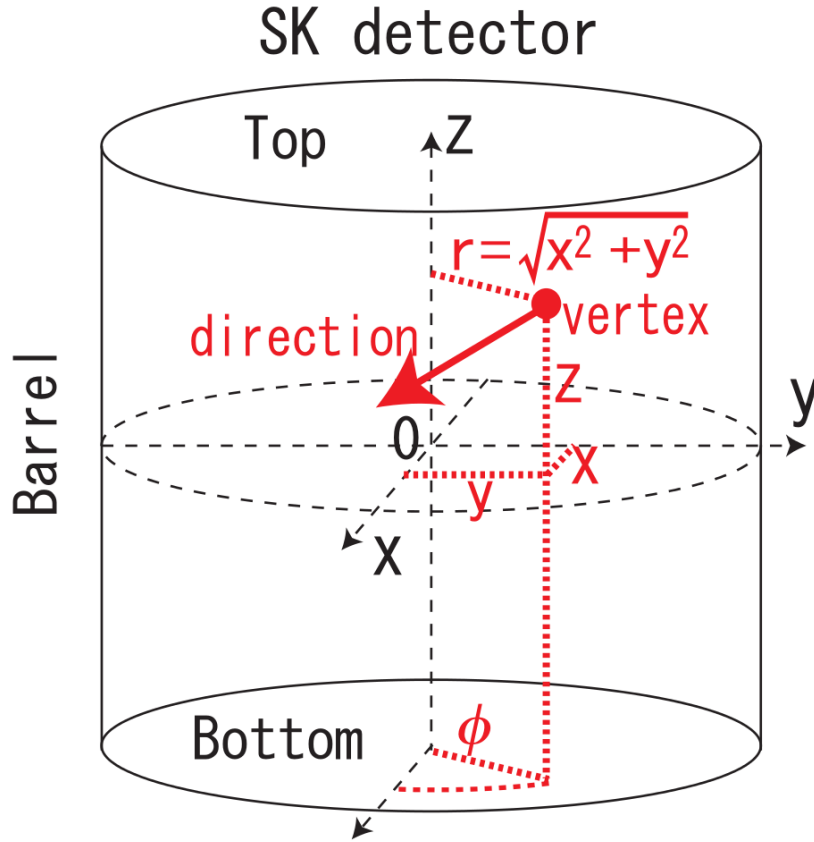


FIGURE 6.1: A depiction of the co-ordinate system used in SK. θ (zenith angle) is measured downwards from positive z.

angles θ are tested. The amount of charge collected in a ring is $q(\theta)$. The goodness-of-fit for a given opening angle θ_t is defined as

$$G = \frac{\int_0^{\theta_t} q(\theta) d\theta}{\sin\theta_t} \times e^{-\frac{(\theta_t - \theta_C)^2}{2\sigma^2}}, \quad (6.1)$$

where θ_C is the critical Cherenkov opening angle, and σ is the resolution of PMT hits around θ_t . Different directions and angles are tested, and the set with maximum G is chosen to be the first ring fit.

Following this, we attempt to refit the vertex, using only the PMT hits designated inside this chosen Cherenkov cone. The algorithm that performs this fit is called TDC-fit. In a similar fashion to Point-Fit, the timing residuals are computed, however this time they are allowed to come from any point along the particle track. Fixing the fitted Cherenkov ring, the vertex and direction of the particle are allowed to vary, then the fit with maximal goodness is selected.

For events with only a single Cherenkov ring, a more precise fitter is used, incorporating particle type information. This will be discussed in a later section.

6.1.1 Ring Counting

Once the primary ring has been determined, further rings are searched for using a Hough transformation[133] and likelihood technique. Ring searching is performed by assuming Cherenkov opening angle of 42° , and then for every hit PMT, a charge-weighted virtual-cone is drawn facing towards the vertex calculated by TDC-fit. Using a spherical coordinate system centred around this vertex, the weighted charge from each PMT is added up for every Θ and Φ . Directions identified with peaks of expected charge, are selected as ring candidates.

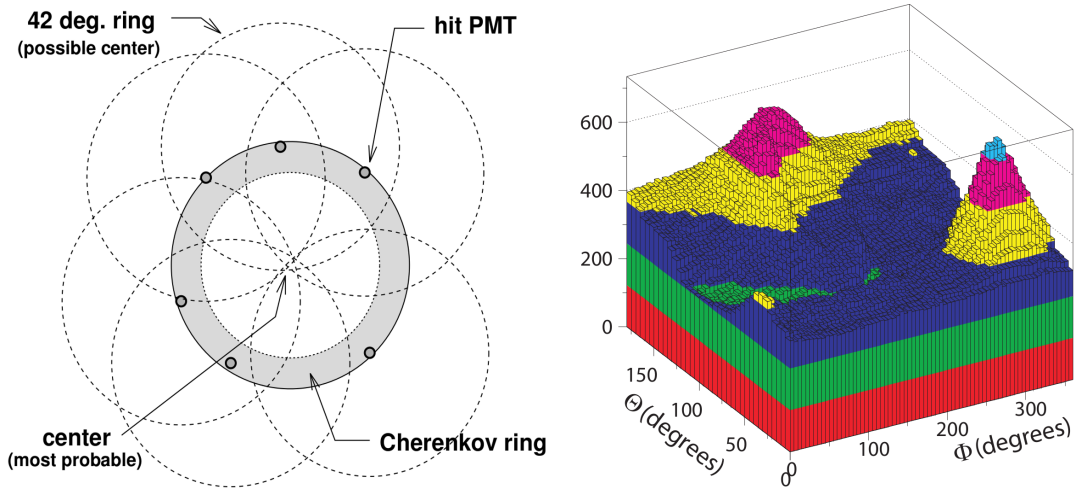


FIGURE 6.2: On the left, is a 2-d depiction of ring candidate searching. Each PMT has a charge-weighted cone drawn out from it at 42° , and the points with maximal charge are taken as ring candidates. The plot on the right is an example of the result of this, in a spherical co-ordinate system centred on the TDC-fit vertex. The angles with peaks of charge represent most probable rings.

Each ring is tested iteratively by a likelihood method, by comparing the $N + 1$ ring hypothesis to the N ring hypothesis. If $N + 1$ rings are found to be a better fit, $N + 2$ ring hypothesis is tested, and so forth, up to a maximum of 5 rings. The likelihood is calculated based on the probability of seeing observed charge q_i^{obs} in each PMT, compared to the expected charge q_i^{exp} given a hypothesis of N rings:

$$L_N = \sum_i \log(P(q_i^{obs}, \sum_{n=1}^N \alpha_n q_{i,n}^{exp})), \quad (6.2)$$

where α_n is a weight for ring n . The weights α_n are allowed to vary to find maximum likelihood. The probability function P is defined as

$$P(q_i^{obs}, q_i^{exp}) = \frac{1}{\sigma\sqrt{2\pi}} e^{-\frac{(q_i^{obs} - q_i^{exp})^2}{2\sigma^2}} \text{ for } q_i^{exp} > 20\text{p-e}, \quad (6.3)$$

where α is the resolution for q^{exp} . For PMTs with expected charge less than 20 photoelectrons, the probability is calculated from a convolution of the single p-e function with a Poisson distribution.

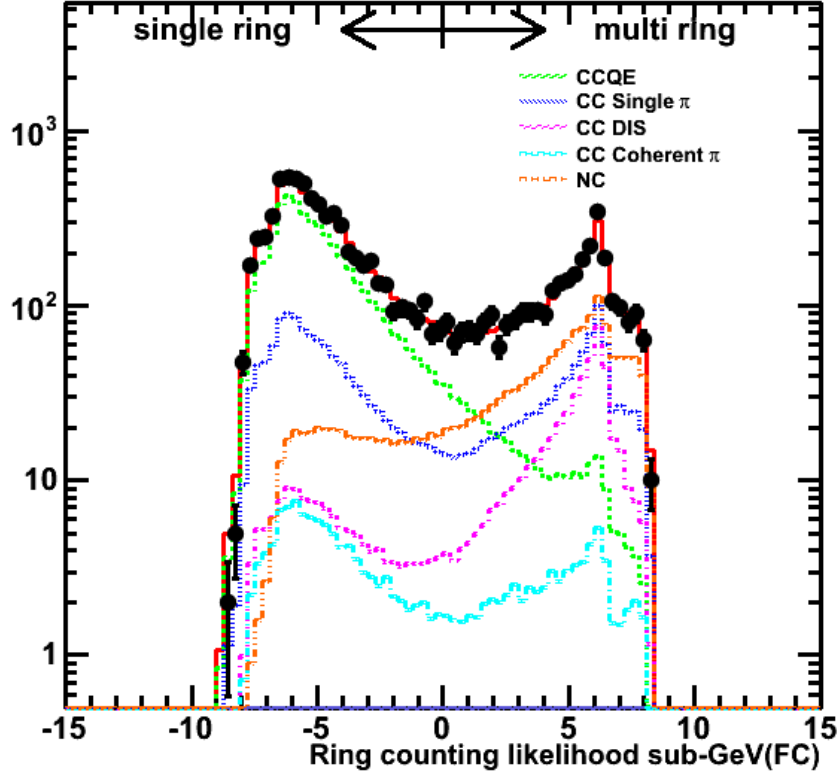


FIGURE 6.3: Output of $L(2 \text{ rings}) - L(1 \text{ ring})$ for SK-IV, $< 1330 \text{ MeV}$ neutrino events. The fraction of different event modes in each sample is shown by the coloured lines.

6.1.2 Precise Single Ring Fitting

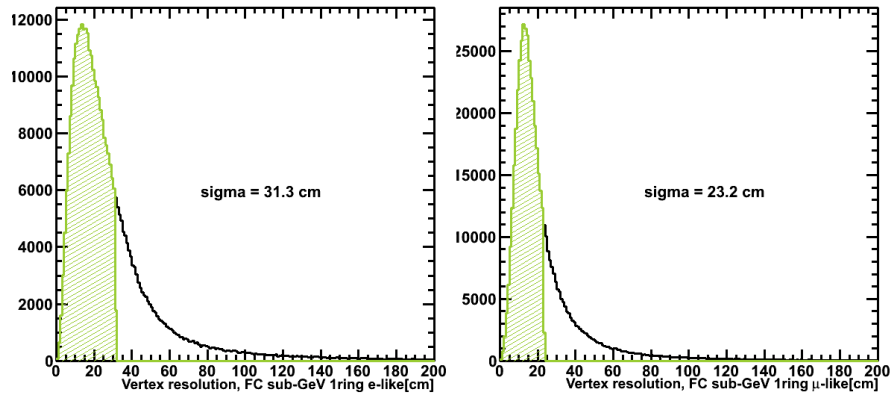
Fitting is further optimized for single ring events, by optimizing the vertex and direction based off the expected light pattern, given that the ring is either e-like or μ -like (determining this will be explained in the next section, please be patient). This algorithm is called MS-Fit.

To evaluate the performance of these fits, the Atmospheric Monte-Carlo sample described in chapter 5 is used. Distributions are made for the distance between true vertex and reconstructed vertex (and similarly for direction), then the fit resolution is defined as the width where 68% of events are included.

Single Ring Vertex Resolution (cm)				
	SK-I	SK-II	SK-III	SK-IV
< 1 GeV events				
e-like	31.2	35.6	31.1	31.3
μ -like	23.8	20.2	23.9	23.2
≥ 1 GeV events				
e-like	33.5	34.3	33.4	33.5
μ -like	24.8	26.9	25.1	23.7

Single Ring Angular Resolution ($^\circ$)				
	SK-I	SK-II	SK-III	SK-IV
< 1 GeV events				
e-like	3.1	3.2	3.0	3.0
μ -like	1.9	2.1	1.9	1.9
≥ 1 GeV events				
e-like	1.2	1.3	1.2	1.2
μ -like	0.8	1.0	0.9	0.9

TABLE 6.1: Vertex and angular resolutions for MS-Fit reconstruction of fully contained neutrino events.

FIGURE 6.4: Vertex resolution for SK-IV sub-GeV single-ring events, separated into μ -like and e-like.

6.2 Particle Identification

In CC neutrino interactions, the flavour of the neutrino corresponds to the flavour of lepton produced in the interaction. Therefore to perform any sort of oscillation analysis, we must have some sensitivity as to the particle type of, at least the most energetic ring (which usually corresponds to the initial lepton). Muon and electron Cherenkov ring patterns look very different, due to their respective interaction methods in water.

Electrons (or positrons) passing through water will generate an electro-magnetic shower, through the Bremsstrahlung ($e^- \rightarrow e^- \gamma$) and then photon pair production ($\gamma \rightarrow e^+ e^-$). As electrons and positrons produced in the shower go on to generate Cherenkov light

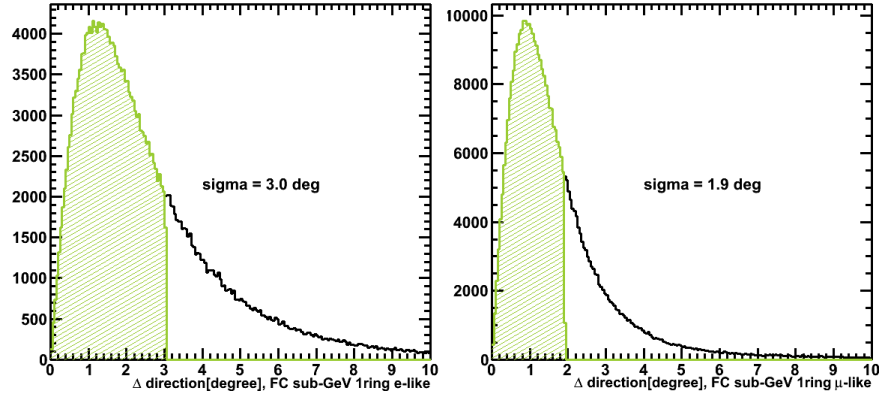


FIGURE 6.5: Angular resolution for SK-IV fully contained sub-GeV single-ring events, separated into μ -like and e-like.

of their own, the resulting ring pattern is very diffuse. High energy gamma rays also create electro-magnetic showers and are indistinguishable from electrons.

The cross section for Bremsstrahlung is $\propto \frac{1}{m^2}$, so for muons the primary energy loss is due to particle ionization. This means that scattering and showering effects are much less pronounced, and the muon tends to have a much sharper ring pattern.

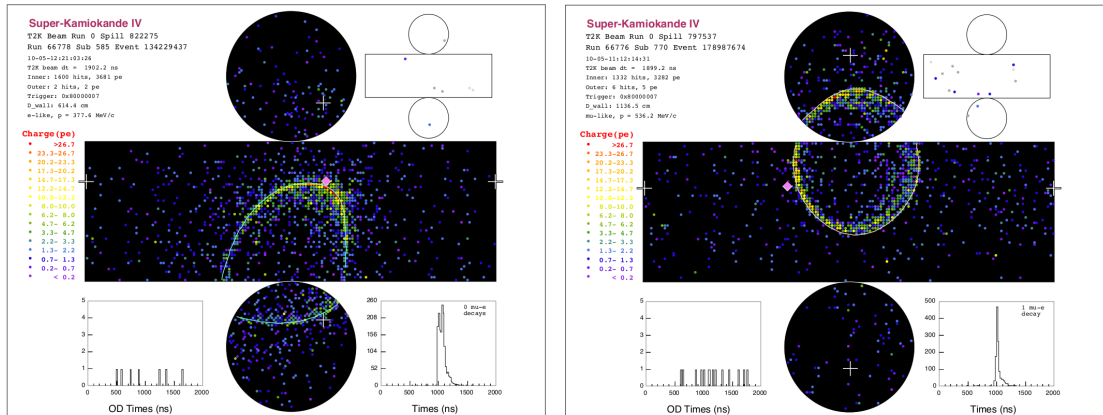


FIGURE 6.6: Example Cherenkov ring patterns for an electron (left), and a muon (right). The top and bottom circles represent the top and bottom of the SK tank, and the long rectangle represents the barrel. Auxiliary event information is provided around the edges (but it is not important to understand).

An additional distinguishing factor is the opening Cherenkov angle. Comparatively light electrons tend to have $\beta = v/c \sim 1$, resulting in an opening angle of 42° . In comparison the heavier muon has lower values of β at the same energy, resulting in a smaller opening angle.

Tau lepton interactions can occur in SK, but it is difficult to distinguish these from other ring types, as τ has a very short lifetime of 2.9×10^{-13} s, before which it decays to primarily pions and other leptons. Recently SK published work on using a neural

network analysis to make statistical measurements of τ appearance [75], however on an event by event basis we are still unable to distinguish these.

It is possible to identify π^0 . The main decay mode is $\pi^0 \rightarrow \gamma\gamma$. As γ rings shower similarly to e^\pm searching for event with two e-like rings, and further cuts on invariant mass can lead to pure samples of π^0 . These are useful to reduce neutral current background, much of which consists of $\nu + N \rightarrow \nu + N' + \pi^0$ type interactions. Charged pions π^\pm look very similar to muon rings, and thus cannot be separated. Protons from scattered nuclei can produce Cherenkov light, but they are heavy, and usually do not take a large fraction of the momentum in a neutrino interaction, so they produce little light and are hard to discern.

The primary type of particle identification computed in SK is the splitting of event samples into e-like and μ -like rings, so first this algorithm will be discussed.

6.2.1 Electron-like and Muon-like rings

Each ring in an event is categorized as either an electron-like (e-like) or muon-like (μ -like) ring. This is done by calculating expected charge on each PMT, for the assumption that the ring is e-like or μ -like, and then comparing to observed charge. Whichever of these fits to a maximal likelihood is taken as the Particle Identification (PID) of that ring.

The expected charge distribution for PMT i is calculated as

$$q_i^{exp}(e) = \alpha_e \times Q^{exp}(p_e, \theta_i) \times \left(\frac{R}{r_i}\right)^{1.5} \times \frac{1}{e^{r_i/L}} \times f(\Theta_i) + q_i^{scatt}, \quad (6.4)$$

where the variable definitions are as follows:

- α_e : a normalization factor
- r_i : the distance from fit vertex to i -th PMT
- θ_i : the opening angle between the i -th PMT and the ring direction
- L : the light attenuation length in water
- $f(\Theta_i)$: the i -th PMT acceptance as a function of incident photon angle
- R : the radius of the virtual sphere (16.9 m)
- $Q^{exp}(p_e, \theta_i)$: The expected charge distribution for an electron as a function of Cherenkov ring opening angle and momentum

- q_i^{scatt} : Expected charge on the i -th PMT due to scattered photons

The expected charge $Q^{exp}(p_e, \theta_i)$ and q_i^{scatt} are calculated using a MC simulation. The factor $(\frac{R}{L})^{1.5}$ is used to correct for the distance dependence of light intensity.

The equivalent predicted charge for muons is obtained as follows:

$$q_i^{exp}(\mu) = \left(\alpha_\mu \times \frac{\sin^2 \theta_{x_i}}{r_i(\sin \theta_{x_i} + r_i \frac{d\theta}{dx} |_{x=x_i})} + q_i^{knock} \right) \times \frac{1}{e^{r_i/L}} \times f(\Theta_i) + q_i^{scatt}, \quad (6.5)$$

where the additional variable definitions are:

- α_μ : a normalization factor
- x : muon track length
- x_i : the estimated track length of the muon at which Cherenkov photons received by PMT i were emitted.
- θ : the Cherenkov opening angle of the muon at track position x
- θ_i : the Cherenkov opening angle of the muon at track position x_i
- q_i^{knock} : Expected charge on the i -th PMT due to knock-on electrons

Knock-on electrons refer to electrons ionized by the passing muon. q_i^{knock} is calculated via MC simulation.

Electrons generate an electromagnetic shower, and expelling all of their energy in a very short distance, so the origin of Cherenkov photons is treated as point-like. For muons which can potentially travel all across the tank, the track length must be considered in calculation of expected charge. Hence the additional complication in the muon case.

Next, a likelihood distribution for the n -th ring is constructed as follows:

$$L_n(e \text{ or } \mu) = \prod_{\theta_i < (1.5 \times \theta_C)} P \left(q_i^{obs}, q_{i,n}^{exp}(e \text{ or } \mu) + \sum_{n' \neq n} q_{i,n'}^{exp} \right). \quad (6.6)$$

Function P is defined in equation 6.3. $q_{i,n'}^{exp}$ gives expected charge in PMT i due to other Cherenkov ring n' , without assuming particle type.

This is then combined with another estimator based on the Cherenkov opening angle. To use this combination we convert our likelihood value to a χ^2 parameter, and then a probability value.

$$\chi_n^2(e \text{ or } \mu) = -2 \log L_n(e \text{ or } \mu) + \text{constant} \quad (6.7)$$

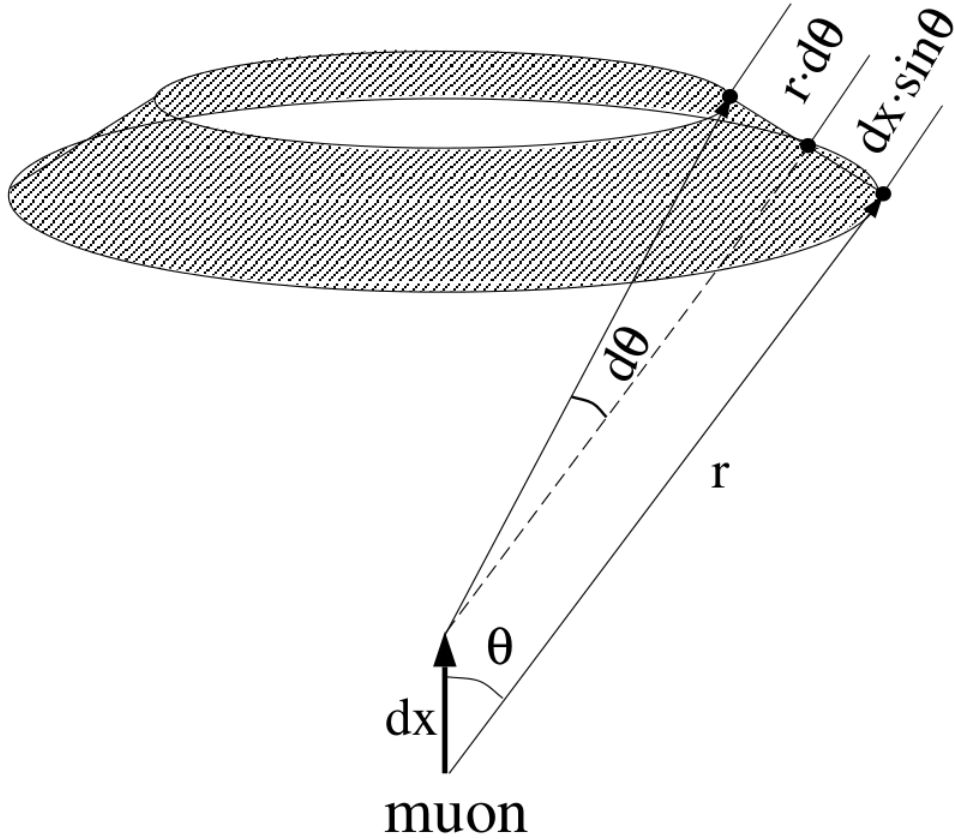


FIGURE 6.7: A depiction of how the muon track length is treated when calculating the expected charge. When a muon travels distance dx , Cherenkov photons are emitted to an area of $2\pi r \sin \theta(dx \sin \theta + r d\theta)$.

Then the probability of having an e-like or μ -like ring based on charge pattern is

$$P_n^{pattern}(e \text{ or } \mu) = \exp\left(-\frac{\chi_n^2(e \text{ or } \mu) - \min[\chi_n^2(e), \chi_n^2(\mu)]}{2\sigma_{\chi_n^2}^2}\right), \quad (6.8)$$

where $\sigma_{\chi_n^2}$ is the resolution of the χ^2 function, defined by $\sqrt{2N}$, where N is the number of PMTs included in the ring.

The second estimator using Cherenkov opening angle is calculated as:

$$P_n^{angle}(e \text{ or } \mu) = \exp\left(-\frac{(\theta_n^{obs} - \theta_n^{exp}(e \text{ or } \mu))^2}{2(\delta\theta_n)^2}\right). \quad (6.9)$$

Variables θ_n^{obs} and $\theta_n^{exp}(e \text{ or } \mu)$ are the observed and expected Cherenkov opening angles for ring n , with the latter being calculated from reconstructed momentum assuming either e-like or μ -like. $\delta\theta_n$ is the fitting error on the opening angle.

These estimators are then combined, to form the final probability functions, separately for single-ring and multi-ring events,

$$P_{1 \text{ ring}}(e, \mu) = P_{1 \text{ ring}}^{\text{pattern}}(e, \mu) \times P_{1 \text{ ring}}^{\text{angle}}(e, \mu) \quad (6.10)$$

$$P_{\text{multi-ring}}(e, \mu) = P_{\text{multi-ring}}^{\text{pattern}}(e, \mu). \quad (6.11)$$

Only the ring pattern estimator is used for multi-ring events, as it is difficult to estimate the opening angle precisely. The final PID likelihood is then taken to be

$$P_{PID} = \sqrt{-\log P(\mu)} - \sqrt{-\log P(e)}, \quad (6.12)$$

where P is taken from 6.10 or 6.11 depending on how many rings the event has.

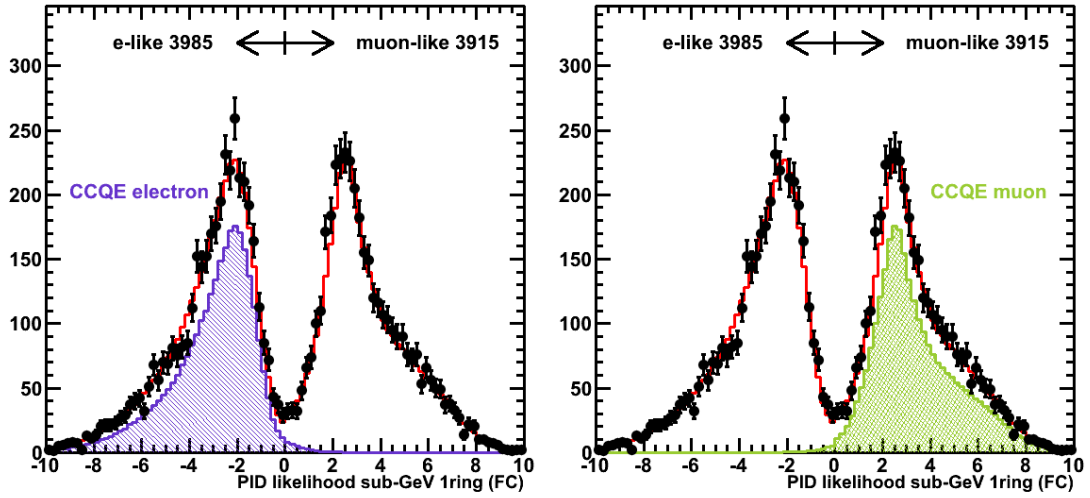


FIGURE 6.8: Output particle identification likelihoods (definition here 6.12) for SK-IV, sub-GeV fully contained single-ring events. The left and right plots show true CC-quasi elastic electron and muon events respectively.

6.3 Momentum Reconstruction

Particle momentum is reconstructed first by counting the number of p-e recorded in each ring, and then converting this value to a momentum using the absolute energy scale discussed in chapter 4. Firstly, for PMTs which contribute to multiple rings, the expected p-e from the n -th ring is calculated as:

$$q_{i,n}^{\text{obs}} = q_i^{\text{obs}} \times \frac{q_{i,n}^{\text{exp}}}{\sum_{n'} q_{i,n'}^{\text{exp}}}, \quad (6.13)$$

where $q_{i,n}^{\text{obs}}$ is the fraction of p-e expected to belong to the n -th ring in the i -th PMT. All p-e within a 70° half angle cone centred on the ring are taken to make up it's momentum.

The timing of the hits is also restricted to be within $-50 < t < +250$ ns surrounding the peak of ToF subtracted timing distribution. This is to avoid potential contamination from delayed hits such as decay electrons. When summing these p-e, we correct for water attenuation, PMT acceptance, and contribution from scattered light:

$$RTOT_n = \frac{G_{MC}}{G_{data}} \left(\alpha \times \sum_i^{N_{PMT}} \left(q_{i,n}^{obs} \times e^{\left(\frac{r_i}{L}\right)} \times \frac{\cos \Theta_i}{f(\Theta_i)} \right) - \sum_i^{N_{PMT}} S_i \right). \quad (6.14)$$

The variables are defined as:

- α : normalization factor
- $G_{data,MC}$: the relative PMT gain for data and MC
- $\theta_{i,n}$: half-angle for PMT i assuming it is a member of ring n .
- t_i : ToF subtracted hit timing for PMT i .
- N_{PMT} : Number of PMT hits which pass the cuts $\theta_{i,j} < 70^\circ$ and $-50 < t_i < +250$ ns
- L : light attenuation length in water
- r_i : distance from vertex position to i -th PMT
- $f(\Theta_i)$: PMT light acceptance as a function of incident angle Θ_i .
- S_i : expected p.e. for the i -th PMT from scattered photons

The calibration of $G_{data,MC}$ and L are discussed in chapter 4. RTOT is converted to a momentum value using the absolute energy scale calibration. The reconstructed momentum resolution for electron and muon events is estimated to be $1.7 + 0.7/\sqrt{P(\text{GeV}/c)}$ % and $0.6 + 2.6/\sqrt{P(\text{GeV}/c)}$ % respectively [134].

6.4 Reconstruction of Single Ring π^0 events

You may recall that π^0 almost always decay to $\gamma\gamma$, and this potentially gives us a nice method to distinguish these events. However, a common problem, especially for high energy π^0 , is that the Cherenkov rings of the two γ may be very overlapping, or the energy may be very asymmetric (that is, one ring with very high energy compared to the other). It is possible in these cases that only a single ring will be found, and thus the π^0 would be mis-classified as an electron. This is a problem, because a large number of NC events, which are undesirable in oscillation analysis, have interaction modes such as $\nu + N \rightarrow \nu + N + \pi^0$.

To try and identify these elusive π^0 events, an algorithm called POLfit was developed [135]. POLfit is applied to all single ring e-like events. Using the initial 1st ring, the best candidate for a second ring is searched for. Using these two rings, the invariant mass is calculated, and if this is similar to a π^0 ($m_{\pi^0} = 135$ MeV), the event will be classified as such.

Using the same vertex as is calculated during APfit, POLfit searches for an additional ring by varying three parameters - the direction of the new ring (θ, ϕ in the co-ordinate system of the first ring), and its energy fraction γ . For each step of these parameters, POLfit calculates the expected charge on every hit PMT, and compares to the observed charge. Then, a likelihood distribution is constructed, comparing the fits with a single electron assumption, and with the $\pi^0 \rightarrow \gamma\gamma$ assumption. The best fit second ring is calculated by maximizing the likelihood difference:

$$\Delta L(\theta, \phi, \gamma) = \log(L_{\pi^0}(\theta, \phi, \gamma)) - \log(L_{1e}(\theta, \phi, \gamma)). \quad (6.15)$$

Note that ΔL is not required to be positive, a second ring is always selected. When the new ring is chosen, its momentum is calculated using the more sophisticated APfit momentum reconstruction. The invariant mass is then calculated. For atmospheric neutrino analysis, if $m_{\pi^0} > 100$ MeV, and the 2-ring likelihood passes an energy dependent cut, the particle is classified as a π^0 .

6.5 Neutron Reconstructions

Two additional independent fitters are used in neutron-tagging analysis. Neutron-tagging refers to the algorithm that searches for 2.2 MeV γ -rays produced by neutron capture on hydrogen. 2.2 MeV γ -rays on average produce 7-8 PMT hits, and are difficult to reconstruct accurately. The vertex resolution of both of the neutron fitters is worse than the average distance the neutrons have travelled from the neutrino interaction before capture. Thus for best vertex resolution, the APfit reconstructed neutrino vertex should be used. However, as neutron capture events are known to not travel far from the neutrino vertex, these additional fits are valuable in reducing sources of background.

6.5.1 Bonsai Fit

The Bonsai (Branch Optimization Navigating Successive Annealing Iterations) fit is the primary fitting tool used in Low Energy analysis in SK. For a more detailed description, you may consult [136]. Bonsai is not optimized for fitting energy as low as 2.2MeV γ

rays - in fact the minimum amount of PMT hits supported to be fit by Bonsai is 10, which many 2.2 MeV gamma candidates do not have. So in the context of neutron tagging, all the PMT hits in a 1.3 μs window surrounding the 2.2 MeV γ candidate are given as input to Bonsai.

6.5.1.1 Bonsai Vertex Reconstruction

Low energy particles will only travel a short distance from their source before thermalization, so it is assumed that all the PMT hits come from a point source. The fit must be done entirely using hit timing information, as at low energy almost every PMT hit is a single photo-electron, and any charge variation is due to noise in the gain. The timing residuals of each hit are calculated for all potential vertices, and the accepted vertex is selected by maximizing a likelihood function based off these residuals. The timing residual of a hit is calculated by

$$t_{res} = t - t_{tof} - t_0, \quad (6.16)$$

where t is the raw PMT hit timing, t_{tof} is the time-of-flight from that PMT to the prospective vertex, and t_0 is the time of the interaction. The likelihood function is constructed as

$$L(\vec{x}, t_0) = \sum_i^{N_{hit}} \log(P(t_{res})), \quad (6.17)$$

where \vec{x} is the prospective vertex, and $P(t_{res})$ is the probability density function of the timing residuals, measured by LINAC calibration data (see figure 6.9). \vec{x} is then iteratively varied, until the maximum value of L is found.

6.5.1.2 Bonsai Energy Reconstruction

As the neutron capture gamma ray is mono-energetic (2.2 MeV), energy reconstruction is a potentially useful method of distinguishing signal from background.

As mentioned before, at low energy the charge collected by a PMT is not very useful information, so energy reconstruction is calculated based off variables N_{hit} and N_{eff} - the number, and effective number of hit PMTs in a 50ns time window. N_{eff} is defined

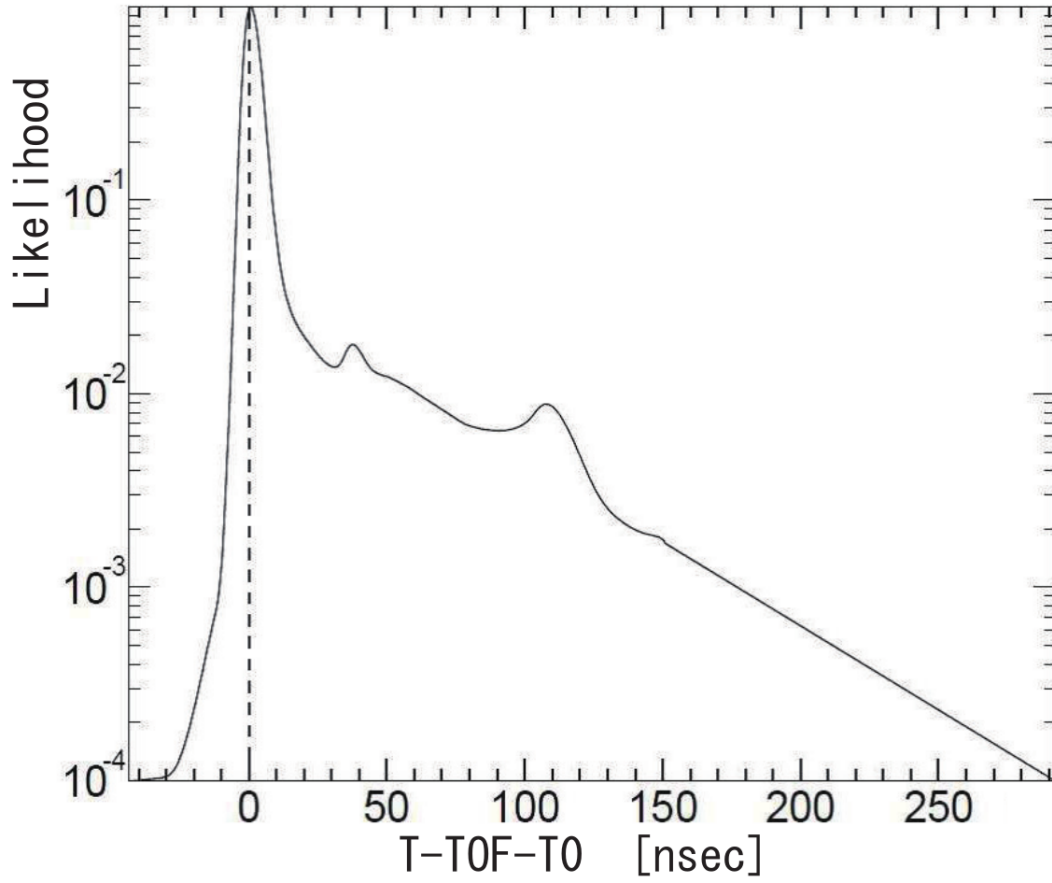


FIGURE 6.9: The timing residual probability density function measured by LINAC calibration data.

as:

$$N_{eff} = \sum_i^{N_{hit}} \left((X_i + \epsilon_{tail} - \epsilon_{dark}) \times \frac{N_{all}}{N_{alive}} \times \frac{1}{S(\theta_i, \phi_i)} \times e^{\frac{r_i}{\lambda_{eff}}} \times G_i(t) \right), \quad (6.18)$$

where the variables are as follows:

- X_i - a factor used to correct for PMTs which are likely to observe more than single photon. The definition differs depending on x_i = fraction of hit PMTs in a 3x3 patch around PMT i . If $x_i < 1$, $X_i = \frac{\log \frac{1}{1-x_i}}{x_i}$, and if $x_i = 1$, $X_i = 3$.
- ϵ_{tail} - accounts for hits that have scattered or reflected and thus fall outside the 50ns window:

$$\epsilon_{tail} = \frac{N_{100} - N_{50} - N_{alive} \times R_{dark} \times 50 \text{ ns}}{N_{50}}, \quad (6.19)$$

where N_j is the number of hits in j ns, N_{alive} is the number of functioning PMTs, and R_{dark} is the dark noise rate.

- ϵ_{dark} - correction applied due to dark noise:

$$\epsilon_{dark} = \frac{N_{alive} \times R_{dark} \times 50 \text{ ns}}{N_{50}}. \quad (6.20)$$

- N_{all}/N_{alive} - corrects for the number of dead PMTs.
- $S(\theta_i, \phi_i)$ - corrects for the acceptance of the i -th PMT, given an incident angle of θ_i, ϕ_i .
- r_i/λ_{eff} - r_i is the distance travelled from reconstructed vertex to the i -th PMT, and λ_{eff} is the water transparency, the measurement of which is described in chapter 4.
- $G_i(t)$ - this factor accounts for the 2-3% per year increase in PMT gain.

Using this calculated value of N_{eff} , the reconstructed energy can be calculated. The relationship between these two variables was precisely calibrated by LINAC and MC data.

$$E_{rec} = 0.82 + 0.13N_{eff} - 1.11 \times 10^{-4}N_{eff}^2 + 1.25 \times 10^{-6}N_{eff}^3 - 3.42 \times 10^{-9}N_{eff}^4 \quad (6.21)$$

Bonsai energy fit returns a failure state for event vertices reconstructed out of the inner detector.

6.5.2 Neut-Fit

Neutron Fit (Neut-Fit) is a simple vertex fitter designed to produce a vertex fit with very low numbers of PMT hits. As an input, it takes a neutron candidate (this will be described in detail in chapter 8), which consists of $N_{10} = 7 - 15$ hits in a 10 ns window. Each candidate is selected by ToF subtracting hits with respect to the APfit vertex, so a large bias exists towards this vertex. Using the initial N_{10} hits, a new vertex is searched for. For each prospective vertex, ToF subtraction for all the hits is recalculated. The best vertex is selected as the one with the minimum t_{rms} for all N_{10} hits:

$$t_{rms}(\vec{x}) = \sqrt{\frac{\sum_i^{N_{10}} (t_i - t_{mean})^2}{N_{10}}}, \quad (6.22)$$

where $t_{mean} = \sum_i^{N_{10}} t_i/N_{10}$, and t_i is the hit timing after ToF subtraction to vertex \vec{x} . This process is then repeated with an increasingly fine grid search, until the best fit is determined to within 0.5 cm.

6.6 Upward-going Muon Reconstruction

The upward-going muon event sample is broken down into two sub-samples: stopping muons, which use up all their energy before leaving the inner detector, and through-going muons, which pass through the inner detector, and exit through the top of the detector. Through-going muons are further divided into those which produce electro-magnetic showers, and those which do not, the former having a higher energy spectrum.

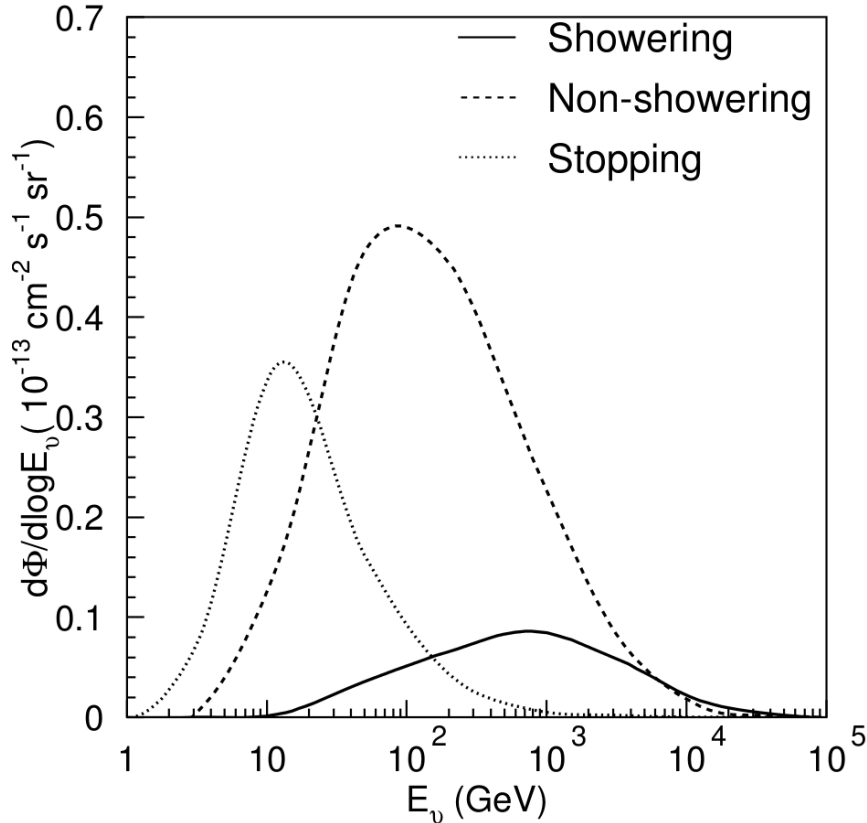


FIGURE 6.10: The energy distributions of upward-going muon showering, non-showering, and stopping events.

The re-construction of these events is done using a hybrid-fitter, named *Precise-fit*. *Precise-fit* is only applied to events with greater than 8000 p.e., below which there is too little light for a precise fit, and less than 175,000 p.e., above which the ID PMTs become saturated.

Precise fit uses adaptations of *MS-fit* and *TDC-fit*, as well as a third package, *OD-fit*. *OD-fit* is used for high energy showering muons, where it is difficult to reconstruct a Cherenkov ring due to a very large amount of energy being deposited in the ID. In these cases, an OD cluster finding algorithm is used, and then the particle vertex and direction are estimated based on clusters at the presumed entrance and exit positions

of the particle. The result from the most appropriate of these three fitters, is output by precise-fit.

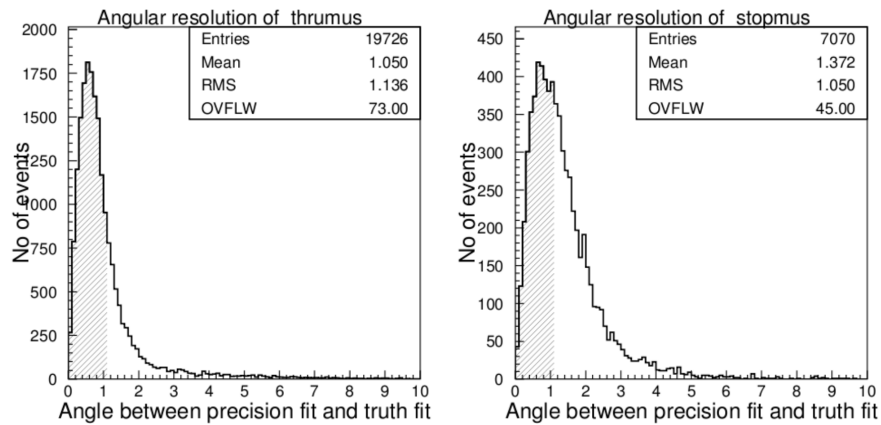


FIGURE 6.11: The vertex resolution of upward-going muon fitter precise-fit, based off a 40 year MC study.

The track length of upward going muons is calculated by monitoring dE/dx , along the muon track. The end of the muon track is defined as the point where the energy loss in a 1 m interval drops to below 40% of the average value from the first 1.5 m of the track.

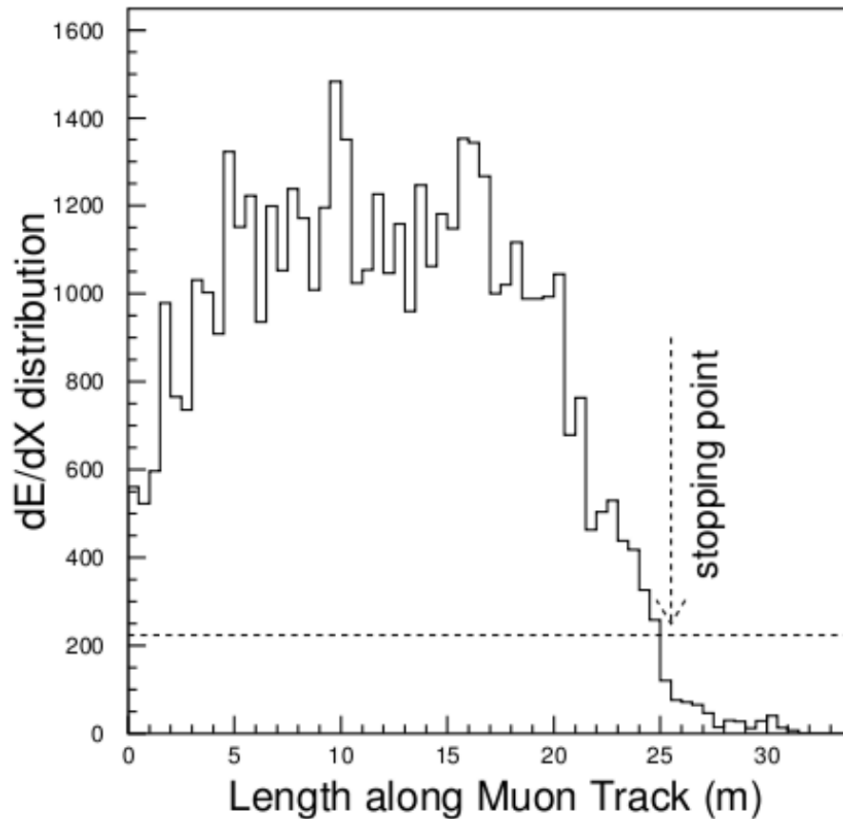


FIGURE 6.12: The calculation of the end-point of a stopping muon track. The dotted line shows the 40% of the average value in the first 1.5 m of the track.

Chapter 7

Data Reduction

The Super-Kamiokande inner detector high energy trigger fires $\sim 10^6$ times each day. The vast majority of these events are background - cosmic ray muons, radioactive gammas from radon contamination, spallation events, PMT flasher events and more. The goal of the reduction process is to remove these background events, and leave behind a pure sample of atmospheric neutrinos.

There are three main reduction processes, depending on the topology of the events. Fully Contained (FC) reduction relates to events that are fully contained within the inner volume of the detector. That is, the neutrinos interact somewhere in the ID, and the produced lepton does not have enough energy to travel outside. Partially Contained (PC) reduction searches for events which have a vertex inside the inner detector, but some of the produced particles have crossed over into the outer detector. These are generally higher energy muon events, as the electron deposits all its energy in a very short distance.

The final sample of atmospheric neutrinos is named UPMU, a shorthand for “UPward-going MUons”. This sample is comprised of muons, which enter from the bottom of the tank. As there is no feasible chance a cosmic ray muon could pass all the way through the Earth and interact with SK, these muon events must have been produced by neutrino interactions in the rock, shortly before entering the SK tank. This is limited to upward going muons, because similar events going downwards cannot be distinguished from cosmic ray background. The UPMU sample is further split into through-going and stopping muons, indicating whether the muon stopped in the tank (having deposited all its energy), or passed through. The highest energy events we observe are in the UPMU through-going sample.

A graphical depiction of each of these event types is shown in figure 7.1. The neutrino energy spectrums of each of these event categories can be seen in figure 7.2.

In some cases the reduction process is different, depending on the SK generation. The primary reasons for this are the reduced number of ID PMTs installed in SK-II (after the accident), and the improved front-end electronics in SK-IV.

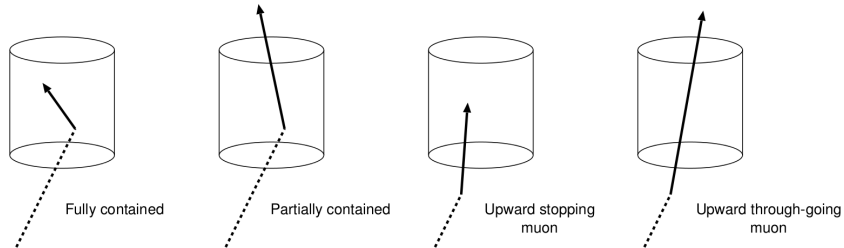


FIGURE 7.1: The different reduction types for selecting atmospheric neutrino events

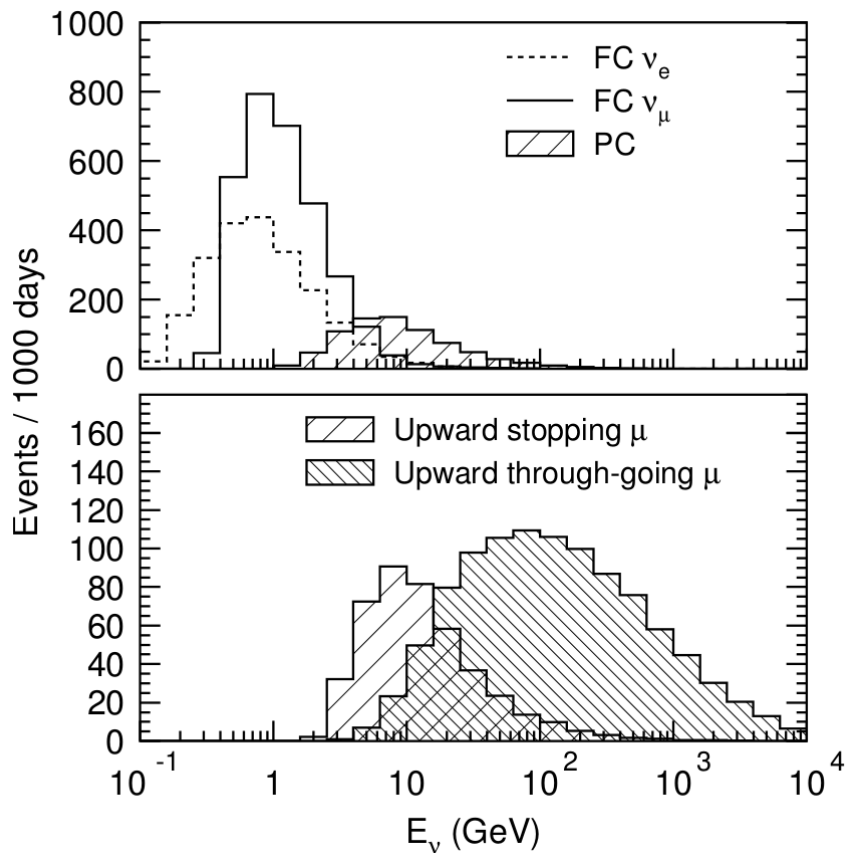


FIGURE 7.2: The energy spectrum for each sample of events, after reduction.

7.1 Fully Contained Reduction

The fully contained reduction is split up into 5 steps, each effective at removing a different category of background events.

7.1.1 1st Reduction (FC1)

This reduction step is designed to filter out most of the obvious low energy and cosmic ray muon backgrounds. The requirements to pass this stage are as follows:

- $PE_{total} > 200$ p-e (100 p-e for SK-II). PE_{total} represents the total charge collected by ID PMTs inside a 300 ns time window surrounding the trigger time.
- $NHITA_{800} \leq 50$. $NHITA_{800}$ is the total number of OD hits within an 800 ns window surrounding the trigger time. Many OD variables are labelled with “A”, which stands for “anti-detector”.

A 200 p-e event is roughly equivalent to a 22 MeV/c electron, so this cut removes all solar neutrinos, reactor neutrinos, and many other low energy backgrounds. The lowest energy atmospheric neutrinos may produce around 30 MeV/c electrons, due to the flux rigidity cut off.

The output of FC1 is typically ~ 1500 events/day.

7.1.2 2nd Reduction (FC2)

The reduction criteria for the second step are:

- $NHITA_{800} \leq 25$, for events where $PE_{total} < 100,000$ p-e (50,000 p-e for SK-II).
- $PE_{max}/PE_{300} < 0.5$ - PE_{max} is the maximum p-e observed in a single PMT within a 300 ns timing window around the event, and PE_{300} is the total p-e from all PMTs in this period.

The first of these cuts removes further cosmic ray muon events, which may have been too low energy to be identified by FC1. The second cut removes events where the majority of the charge in the event is coming from a single PMT. These type of events are likely to be due to flashing PMTs, or electronics noise.

The output for FC2 is ~ 200 events/day.

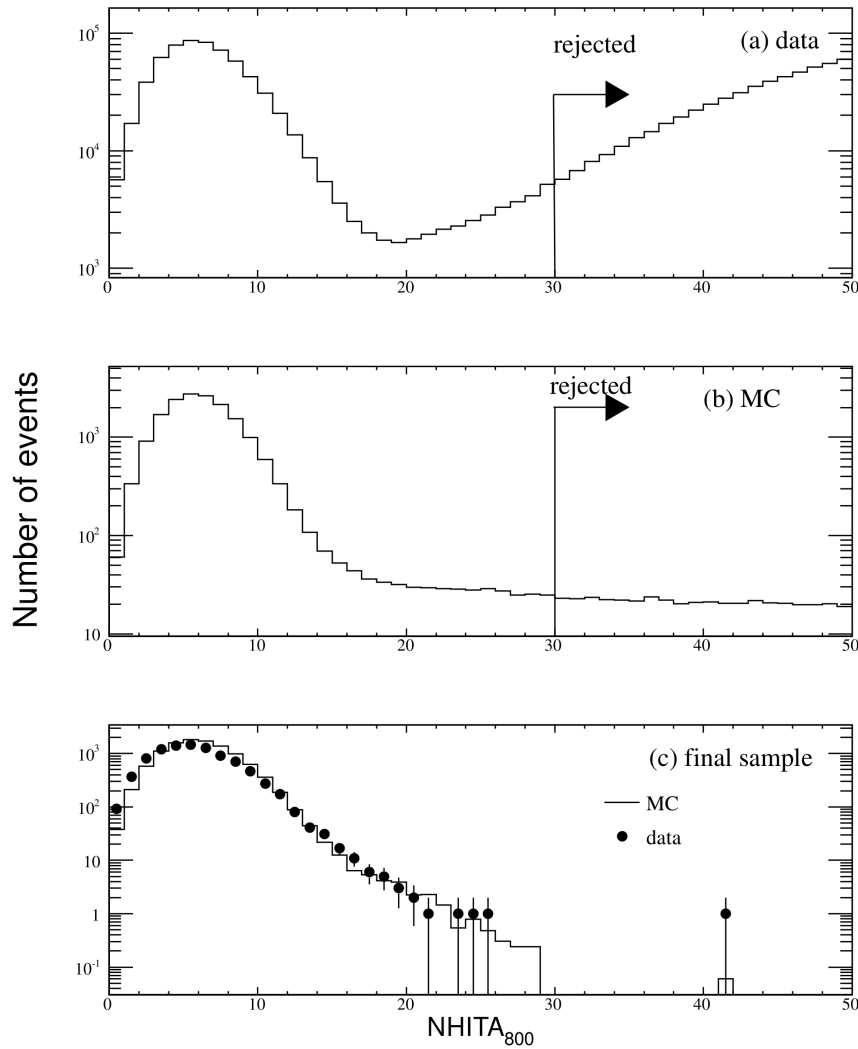


FIGURE 7.3: FC2 distributions of NHITA_{800} , for data, MC, and then the final selection with data and MC superimposed. The MC is a pure atmospheric neutrino sample, so the second plot shows the efficiency of this cut. In the final sample the events which remain in the cut region have either $\text{PE}_{\text{total}} > 100,000$, or the OD trigger did not fire.

7.1.3 3rd Reduction (FC3)

The third reduction consists of a series of more specifically targeted cuts, focusing on removal of cosmic ray muon events that have little OD activity, and further reductions of electronic noise events. After FC3 has been applied, ~ 45 events/day remain.

7.1.3.1 Through-going muon cut

Muons events that go through the tank without depositing much energy in the OD may be rejected here. These are generally high energy events, so the pre-criteria for this cut to be considered is that at least 1000 ID PMTs are hit, with each detecting more than

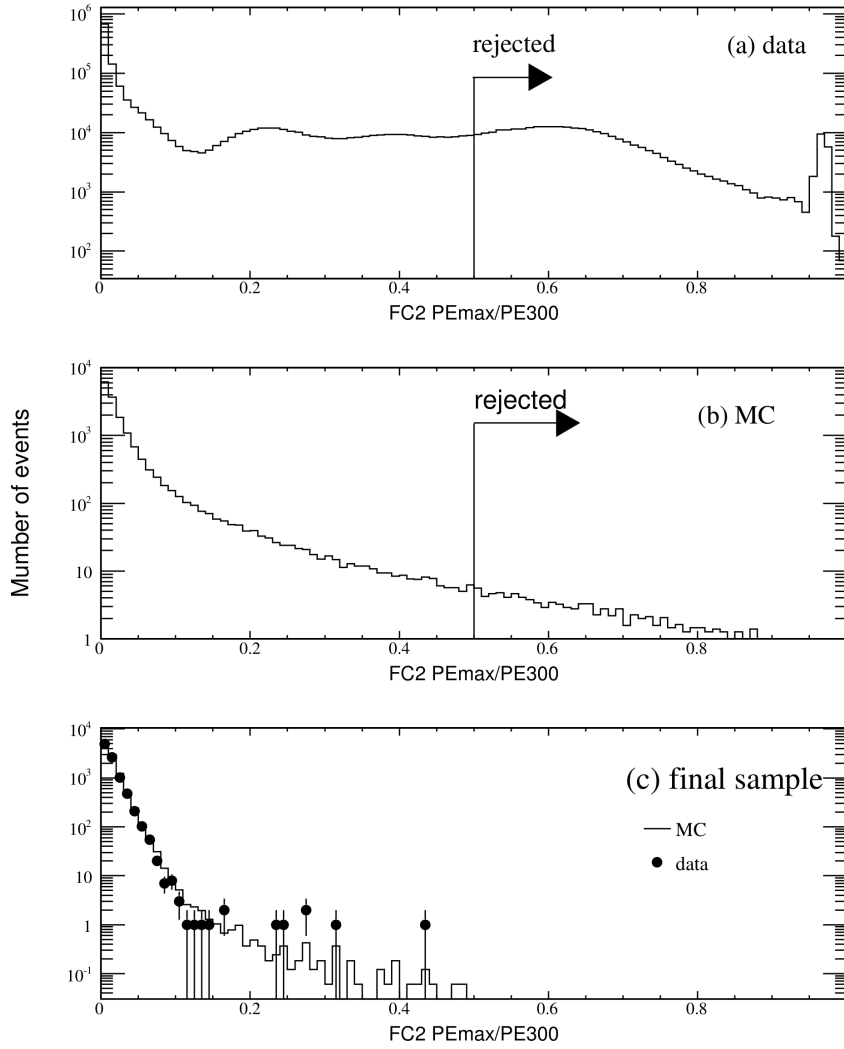


FIGURE 7.4: FC2 distributions of PE_{max}/PE_{300} . Plots of data, MC and then the final selection with data and MC superimposed are shown. The MC consists of pure atmospheric neutrino events.

230 p-e. If this condition is met, a through- μ fitter is applied. The fit assumes that the event is a through-going muon, setting the entrance point as the first hit PMT in the entrance cluster, and the exit point as the PMT at the centre of the exit cluster. For these entrance and exit points, the expected hit timing T_i for each PMT is calculated using a MC simulation. From this a goodness-of-fit parameter is given by:

$$\text{goodness} = \frac{1}{\sum_i \frac{1}{\sigma_i^2}} \times \sum_i \left(\frac{1}{\sigma_i^2} \exp \left(-\frac{(t_i - T_i)^2}{3\sigma_i^2} \right) \right), \quad (7.1)$$

where t_i and σ_i are the i -th PMT timing and timing resolution respectively. The requirements to pass this cut are:

- goodness > 0.75

- $\text{NHITA}_{in} \geq 10$ or $\text{NHIT}_{out} \geq 10$

where NHITA_{in} and NHITA_{out} are the numbers of hit OD PMTs in 800 ns, within 8 m of the entrance and exit PMTs respectively.

7.1.3.2 Stopping-muon cut

Stopping muons are cut in almost the same way as the through-going muons, except they do not have an exit point. To perform the fit this time, we must reconstruct the muon direction, which is found by maximizing the number of p-e observed by PMTs in a 42° Cherenkov opening angle from the entrance point. The goodness of fit is calculated again by equation 7.1. If either of the following cut criteria are met, the event is discarded as a stopping muon:

- goodness of stopping muon fit ≥ 0 and $\text{NHITA}_{in} \geq 10$
- goodness of stopping muon fit > 0.5 and $\text{NHITA}_{in} \geq 5$

7.1.3.3 Cable Hole Muons

To connect to the PMTs around the tank, SK has twelve holes through which cabling is thread. OD PMTs cannot be installed in these positions, so it is possible for cosmic ray muons to pass into the inner detector without interacting with enough PMTs in the OD to be vetoed. To circumvent this, plastic scintillator detectors are installed in four of the twelve cable holes. The event is cut if:

- Cable hole veto counter is hit
- Vertex reconstruction is within 4m of the cable hole counter.

To account for the holes where no veto counters are installed, an alternative set of cuts was introduced in SK-IV:

- goodness ≥ 0.4 (as defined by 7.1)
- $\text{PE}_{total} > 4000$ p-e
- reconstructed as downward going ($\cos \theta < -0.6$)
- distance from reconstructed vertex to cable hole < 2.5 m

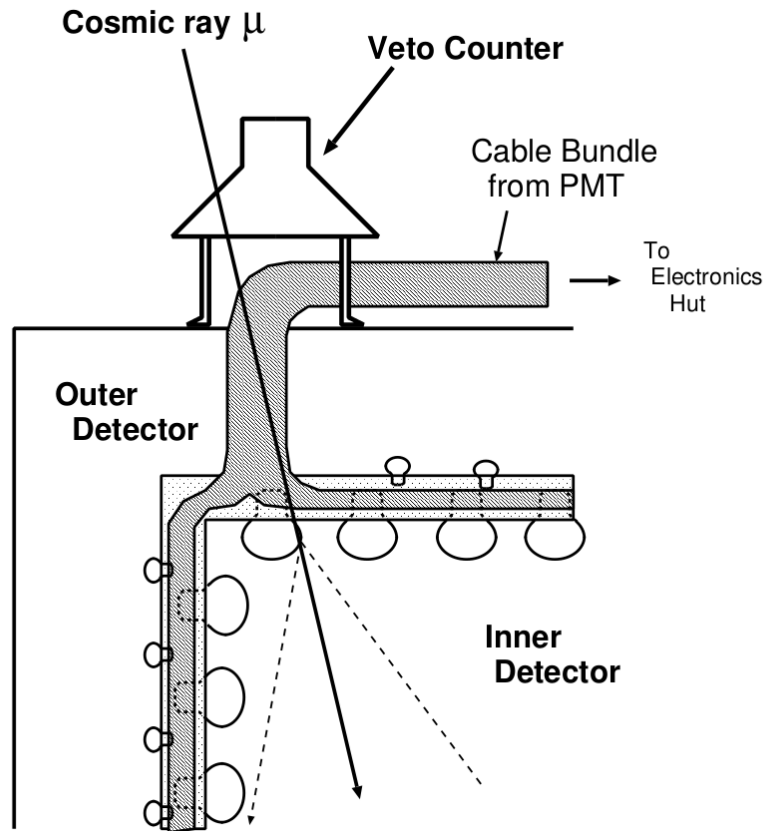


FIGURE 7.5: A schematic of the cable hole veto counters in SK

7.1.3.4 Flashers

Flasher refers to the phenomena where a PMT may misfire and result in many repetitive internal discharges, of both itself and nearby PMTs. Flasher events tend to have a broader hit timing distribution than neutrino events, so the cut to remove these is:

- SK-I: $N_{MIN_{100}} \geq 15$ or $N_{MIN_{100}} \geq 10$ if $N_{hit} \leq 800$
- SK-II to SK-IV: $N_{MIN_{100}} \geq 20$

where $N_{MIN_{100}}$ is the minimum number of hits in a 100 ns sliding time window from +300 to +800 ns after the trigger. N_{hit} is the number of ID PMT hits. Later reduction steps have other, more specific cuts for removing flashers.

7.1.3.5 Coincidence Muon

Sometimes, an event will trigger from a low energy event, but then shortly afterwards a cosmic ray muon will also pass through the tank. These events are referred to as

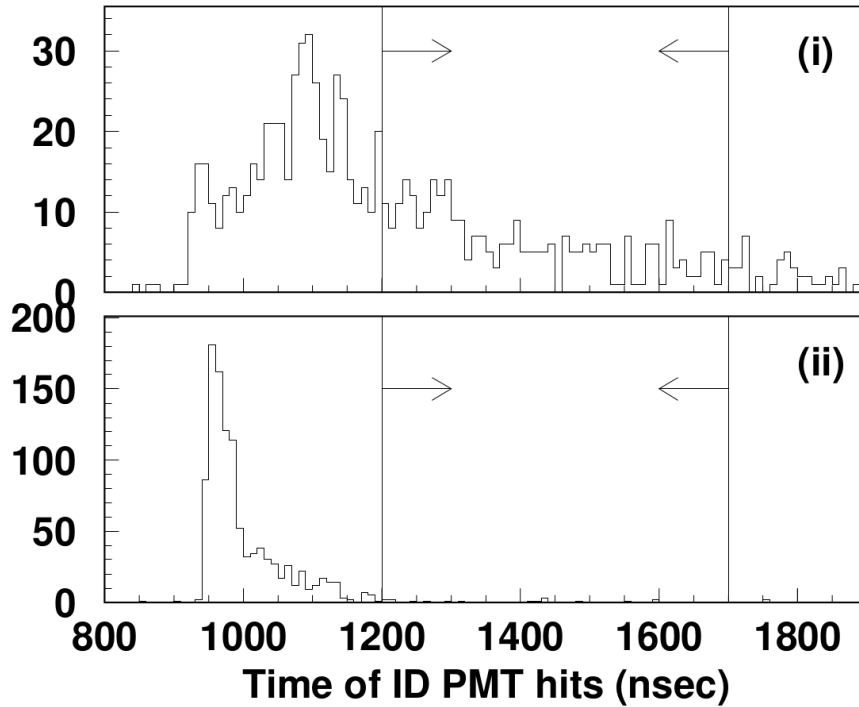


FIGURE 7.6: ID timing distributions of a typical flasher (i), and a typical neutrino (ii) event. The two lines indicate the timing region scanned in calculating $NMIN_{100}$.

coincidence muons. They avoid the previous low energy cuts, as the muon contributes a large amount of charge to the ID, but also the OD veto cut is circumvented, because the muon arrives later, outside of the cut timing window. The cuts to remove these events are:

- $NHITA_{off} \geq 20$
- $PE_{off} > 5000$ p-e (2500 for SK-II)

where $NHITA_{off}$ is the number of OD hit PMTs in the off-timing window, +400 to +900 ns after the trigger time. PE_{off} is the total ID hit PMTs in the same off-timing window.

7.1.3.6 Low Energy Events

This is a more tight cut to remove low energy events than we saw previously. Firstly hits are ToF corrected to a reconstructed vertex. Using a 50 ns scanning time window, the largest value of $NHIT_{50}$ is recorded. Cut the event if:

- $NHIT_{50} < 50$ (25 for SK-II)

7.1.4 4th Reduction (FC4)

Even after FC3, a significant amount of PMT flasher events remain in the data-sample. Often after a PMT becomes a flasher, it will continue to produce flashing events which have a highly correlated charge pattern, over a short space of time. FC4 attempts to reduce these, by using a pattern matching algorithm. This algorithm is run as follows:

1. The ID tank wall is divided up into 1450 partitions, containing between 6 and 9 PMTs each.
2. Correlation r between two events is calculated for each patch, by

$$r = \frac{1}{N} \sum_i \frac{(Q_i^A - \langle Q^A \rangle) \times (Q_i^B - \langle Q^B \rangle)}{\sigma_A \times \sigma_B}, \quad (7.2)$$

where N is the total number of patches. A and B are the two events being compared. $\langle Q \rangle$ is the average charge, and σ is the charge resolution.

3. The distance DIST_{max} between the PMT with the maximum charge in each event is calculated. If $\text{DIST}_{max} < 0.75$ m then an offset is applied to $r = r + 0.15$.
4. If $r > r_{th}$, the two events are marked as a match. r_{th} is a variable quantity based on the total ID charge for each event.

This procedure is carried out attempting to match with 10,000 events surrounding the target event. Events are cut depending on the number of total matches N_{match} , and correlation r . After FC4, an average of ~ 18 events/day remain.

7.1.5 5th Reduction (FC5)

FC5 removes a final set of very specific background types - invisible muons, coincidence muons, and long tail flashers. After FC5 has been applied, ~ 16 events/day remain.

7.1.5.1 Invisible Muons

Invisible muons refer to muons which have entered the detector some time before the trigger, and decayed to an electron. SK triggers on the signal from the decay electron, without being aware of the initial muon. These events can be identified as there is likely to be a signal in the OD from the muon, before the primary trigger. The cuts are as follows:

- $PE_{tot} < 1000$ p-e (500 for SK-II). PE_{tot} is the total number of p-e in the ID.
- $NHITAC_{early} + NHITAC_{500} \geq 10$ if $DIST_{clust} < 500$ cm.
 $NHITAC_{early} > 9$ otherwise.

$NHITAC$ is the number of hit OD PMTs in the largest cluster, and $NHITAC_{early}$ is calculated in a sliding 200 ns time window between -8800 ns and -100 ns relative to the primary trigger. $NHITAC_{500}$ is the largest number of hits in an OD cluster from -100 to +400 ns. $DIST_{clust}$ is the distance (cm) between these two OD hit clusters.

7.1.5.2 Coincidence Muons

This is a tighter cut for the same coincidence muons defined in FC3, that is, muons which pass through the detector in a late timing period after it has triggered off a low energy event. The cut criteria for the removal of these are

- $PE_{500} < 300$ p-e (150 for SK-II). PE_{500} is the total of ID p-e in the time interval -100 to +400 ns.
- $PE_{late} \geq 20$ p-e. PE_{late} is the maximum amount of p-e recorded in the OD, using a 200 ns scanning time window from +400 to +1600 ns.

7.1.5.3 Long Tail Flashers

Similar to the flasher cut in FC3, but with tighter criteria. The simple vertex fitter Point-Fit's (as described in chapter 6) goodness output is used - a well fit Cherenkov ring is unlikely to be a flasher event. The criteria are as follows:

- $NMIN_{100} \geq 6$ if the goodness of Point Fit is < 0.4 . As before, $NMIN_{100}$ is the minimum number of ID PMT hits in a 100 ns scanning time window between +300 and +800 ns.
- SK-II to SK-IV only: $NMIN_{100} \leq 5$ if the goodness of Point Fit < 0.3 .

7.1.6 Fiducial Volume Selection

There are three final cuts applied to the FC sample, to ensure our neutrino sample is as pure as possible:

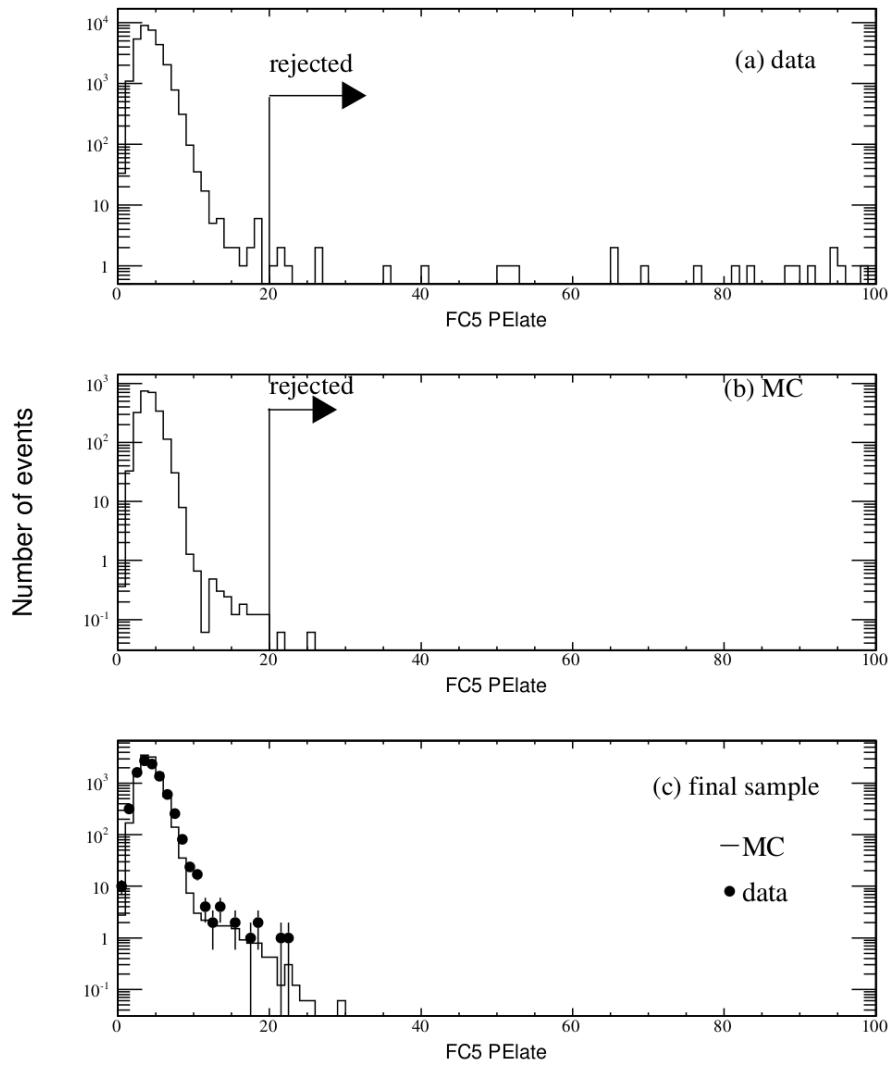


FIGURE 7.7: FC5 Coincidence muon cut variable PE_{late} . From top to bottom, the plots show the data, atmospheric neutrino MC, and then the final selection of events with data and MC superimposed. It is also required that $PE_{500} < 300$ p-e, so there are a few events remaining in the final sample that have $PE_{late} > 20$.

- $dWall > 200$ cm, where $dWall$ is the distance from the reconstructed vertex to the closest tank wall. This is to further veto events which have entered from outside the tank, and events due to radioactive impurities in the tank wall.
- $NHITAC < 16$ (10 for SK-I). $NHITAC$ is the number of hits in the largest charge cluster in the OD. Again, the purpose is to remove any events entering from outside the tank.
- $E_{vis} > 30$ MeV, where E_{vis} is the sum of the reconstructed momentum of all rings, assuming they are produced by electrons.

After this final selection, the remaining event rate is around 8 atmospheric neutrinos / day. This sample is known as the FCFV (fully-contained fiducial volume) sample.

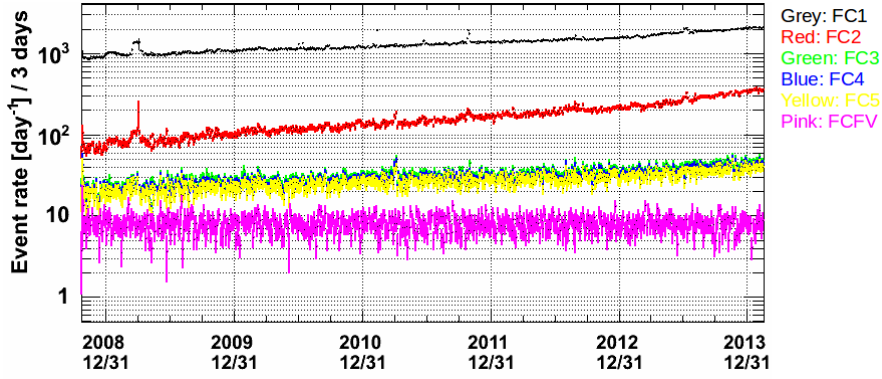


FIGURE 7.8: The event rate for each of FC1-5, and FCFV reductions, for all of SK-IV. The increasing event rate is due to the PMT degradation causing gain increase of 2% per year, and is accounted for in analysis. The event rate spike around March 2009 is due to faults in the HV system.

7.1.7 FC Reduction Summary

The efficiency of each reduction step is calculated by applying the procedure to a purely atmospheric neutrino MC, as described in a chapter 5. The systematic error for the reduction efficiency is estimated by comparing distributions of data vs MC for each reduction step. These errors are 0.2%, 0.2%, 0.8% and 0.3% for SK I-IV respectively.

The background in the final sample is determined by eye-scanning all of the selected events. The primary sources of background are flasher events remaining in the e-like samples, and cosmic ray muon events remaining in the μ -like samples. These samples are further split into sub-GeV, where $E_{vis} < 1330$ MeV, and multi-GeV, where $E_{vis} \geq 1330$ MeV.

A summary of the FC reduction process can be seen in table 7.1.

7.2 Partially Contained Reduction

The partially contained sample consists of neutrino events, whose vertex is reconstructed in the ID, but also have some activity in the OD that prevents them from being fully contained. OD segmentation was installed after SK-II, so there are some differences in the reduction from SK-III onwards. Cosmic ray muon and upward-going muon background is significantly more difficult to remove in PC, as there are expected to be some hits in the OD. This is reflected in the complexity of the reduction steps.

FC	SK-I	SK-II	SK-III	SK-IV
Reduction	Selection Efficiency (%)			
FC1	100.0	99.97	100.0	100.0
FC2	100.0	99.92	99.98	99.99
FC3	99.93	99.78	99.81	99.82
FC4	99.29	99.38	99.30	99.00
FC5	99.26	99.30	99.24	98.95
FCFV	99.25	99.95	99.62	99.19
	Final Sample Background (%)			
Sub-GeV e-like	0.1	0.4	0.1	0.1
Sub-GeV μ -like	0.2	0.2	0.3	0.1
Multi-GeV e-like	0.5	0.2	0.2	0.1
Multi-GeV μ -like	0.3	0.2	0.3	0.1
	Total Number of Events			
Livetime (days)	1489.2	798.6	518.2	1775.6
MC Prediction	11878.7	6407.6	4198.5	14251.2
Data	12299	6610	4355	14444
Events / day	8.26 ± 0.07	8.28 ± 0.10	8.41 ± 0.13	8.13 ± 0.07

TABLE 7.1: Summary of the efficiencies, remaining background, and number of events remaining after the FC reduction process.

7.2.1 1st Reduction (PC1)

Similarly to FC1, PC1 rejects through going cosmic ray muon events, and low energy events. For SK-I and II the criteria are as follows:

- $PE_{tot} \geq 1000$ p-e (500 for SK-II)
- $TWIDA \leq 260$ ns (170 for SK-II)
- $NCLSTA \leq 1$ (SK-I only)

PE_{tot} is the total charge in the ID, which for a muon is equivalent to a track length of ~ 2 m. $TWIDA$ is the width of the hit timing distribution in the OD PMTs. This is used to reject events which have entered the tank through the OD, and subsequently exited, which will have a broader timing distribution. This criteria is tightened in SK-II due to the increased quantum efficiencies of OD PMTs at this time. $NCLSTA$ is the number of clusters of hits in the OD, an additional cut to reject through-going cosmic rays.

From SK-III onwards, the OD segmentation made through going particle rejection more efficient, so the cut criteria were altered:

- $PE_{tot} \geq 1000$ p-e

- $\text{NHITA}_{top} < 10$ or $\text{NHITA}_{bottom} < 10$
- $\text{NHITA}_{endcap} < 25$ or $\text{NHITA}_{side} < 70$
- $\text{ODR}_{mean} < 2100$ cm, if $\text{NHITA} < 20$ in a 500 ns time window.

$\text{NHITA}_{location}$ is the number of hits in that area of the OD. “Endcap” refers to the top + bottom segments. Thus the NHITA_x cuts are used to remove muons that travel through the top and bottom of the tank, and also muons which travel through the top or bottom and side of the tank (referred to as through-going muons and corner-clipping muons respectively).

The final cut variable, ODR_{mean} is the average distance between every pair of hits in the OD.

$$\text{ODR}_{mean} = \frac{1}{N_{pair}} \sum_i^{\text{NHITA}-1} \sum_{j=i}^{\text{NHITA}} |\vec{x}_i - \vec{x}_j| \quad (7.3)$$

This is another measure of the spatial spreading of the PMT hits, specifically useful for events with less deposited energy.

7.2.2 2nd Reduction (PC2)

PC2 is used in combination with a clustering algorithm, using the number of hit clusters to reject through-going, corner clipping and stopping muons. The OD walls are divided into 11×11 patches, and for each of these the total charge is added up. Clusters of hits are selected based on the charge gradient between neighbouring patches. This is also defined for the ID, with 21×21 patches. A graphical depiction of this algorithm can be seen here [7.9](#).

These cuts are fairly involved, so the variables relevant for these reduction cuts will be described first, as follows:

- $\text{NCLSTA2}[x]$ - the number of clusters including $> x$ PMTs.
- $\text{NCLSTA2}(2)[x]$ - the number of hits in the 2nd OD hit cluster requiring $> x$ PMTs.
- NHITAC_{min} - the minimum number of clustered hit PMTs in the top or bottom, and side regions of the OD.

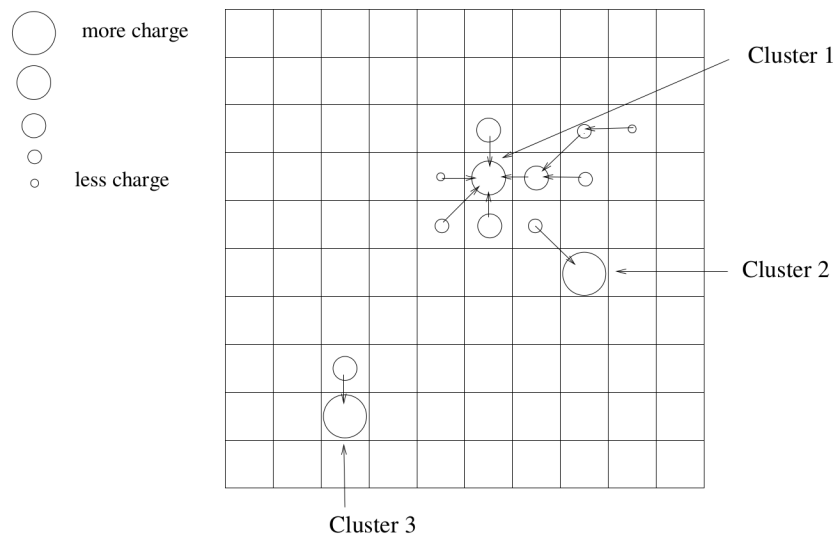


FIGURE 7.9: Explanation of OD clustering algorithm. The charge in each patch is proportional to the size of the circle. The charge is added to a cluster in the direction of the largest charge gradient.

- PE_{200} - the number of p-e within 200 cm of the highest charge PMT, in the ID hit cluster which is closest to the OD hit cluster.
- $NHITA_{location}$ - the number of OD PMT hits in that region.
- $MAX(NHITA_{side}) = \exp(a - b \times NHITA_{side})$. If $NHITA_{side} < 75$, $a = 5.8$, $b = 0.023$. If $NHITA_{side} \geq 75$, $a = 4.675$, $b = 0.008$.
- $NHITAC2$ - the number of OD hit PMTs in the 2nd cluster.

The exact cut criteria are quite different across the SK generations, so will be described separately.

7.2.2.1 PC2: SK-I

- $NCLSTA2[6] \leq 1$
- $NCLSTA2(2)[6] \leq 1$
- $NHITAC_{min} < 7$
- If $NCLSTA2[6] = 1$, require that $PE_{200} > 1000$ p-e

7.2.2.2 PC2: SK-II

- $NCLSTA2[6] \leq 1$

- $NCLSTA2(2)[10] \leq 1$
- $NHITA_{endcap} < \min[20, \text{MAX}(NHITA_{side})]$
- $NHITAC2 < 12 + 0.085 \times PE_{200}$

7.2.2.3 PC2: SK-III and SK-IV

- $NCLSTA2(2)[10] \leq 1$
- $NHITA_{endcap} < \min[20, \text{MAX}(NHITA_{side})]$

For SK-III and IV, OD segmentation makes PC1 very efficient, so the PC2 cuts can be somewhat relaxed.

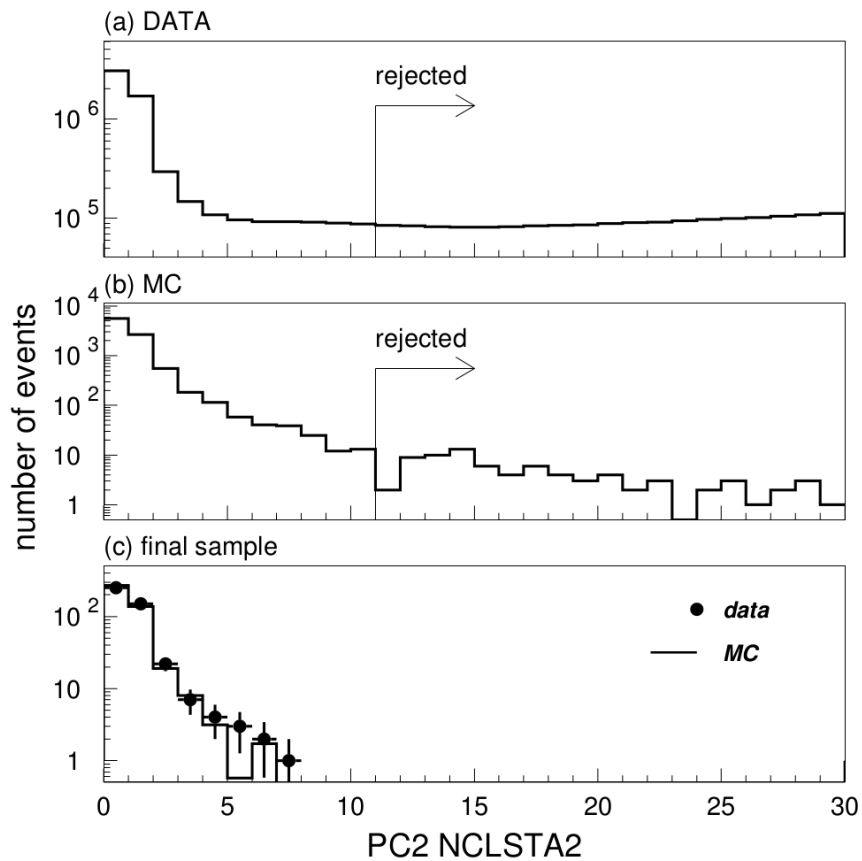


FIGURE 7.10: The number of hits in the 2nd largest OD charge cluster. If there are two large clusters, they likely represent entrance and exit points in an event. As PC events must originate in the ID, these events may be cut. The MC shows a simulated pure atmospheric neutrino sample, and the final sample is the agreement between data and MC for this variable after the final PC selection.

7.2.3 3rd Reduction (PC3)

PC3 consists of two specific cuts. Similar to FC3, the first is to remove PMT flashers from the data sample. Flasher events tend to have a more broad timing distribution than neutrino events. The second cut, applied only for SK-I and II, is used to reject stopping muon events. For SK-III and IV, this cut has been moved into PC5. Thus, the criteria for rejection at this stage is:

- $NMIN_{100} > 14$ or, if the number of hit ID PMTs < 800 , $NMIN_{100} > 9$.
 $NMIN_{100}$ is defined as the minimum number of ID PMTs hit in a 100 ns scanning window from +300 ns to +800 ns after the primary trigger.
- $NHITA_{in} > 10$ (SK-I and II only)
 $NHITA_{in}$ is defined as the number of hit OD PMTs within 8 m and 500 ns of the fitted ID vertex (as fitted by Point-fit).

7.2.4 4th Reduction (PC4)

PC4 has two very different versions for SK-I and II, and SK-III and IV. They will be described separately.

7.2.4.1 PC4: SK-I and II

Despite many efforts so far to remove them, there are still persistent stop, through-going and corner-clipping muons contaminating this sample, typically with relatively little OD activity. This reduction step uses information from multiple fit programs to try and extract these events from the PC neutrino sample. The through-going muon fitter is applied, with the expectation that the fit result will be sub-optimal and have lower goodness for true PC events, as their vertices are not necessarily at the tank wall. Point-fit is also used, which gives a reasonable estimate for the vertex of both through-going muons and PC events. Events may criteria are as follows:

- $\vec{d}_{pfit} \cdot \vec{d}_{PMT} > -0.8$,
 where \vec{d}_{pfit} is the direction as reconstructed by Point-fit, and \vec{d}_{PMT} is the direction from the reconstructed vertex, to the earliest saturated PMT. This cut removes events where the earliest hit PMT is in the opposite direction to that the primary Cherenkov cone is pointing in, implying the particle may have entered from outside the tank.

- $DCORN < 150$ cm.

DCORN is the distance between the Point-fit vertex, and the nearest tank corner. This aims to reject corner-clipping muons.

- $TLMU > 30$ m, and goodness of the through-muon fit > 0.85 .

TLMU is the estimated track length of the event, when modelling it as a through-going muon. Events with long track lengths are rejected.

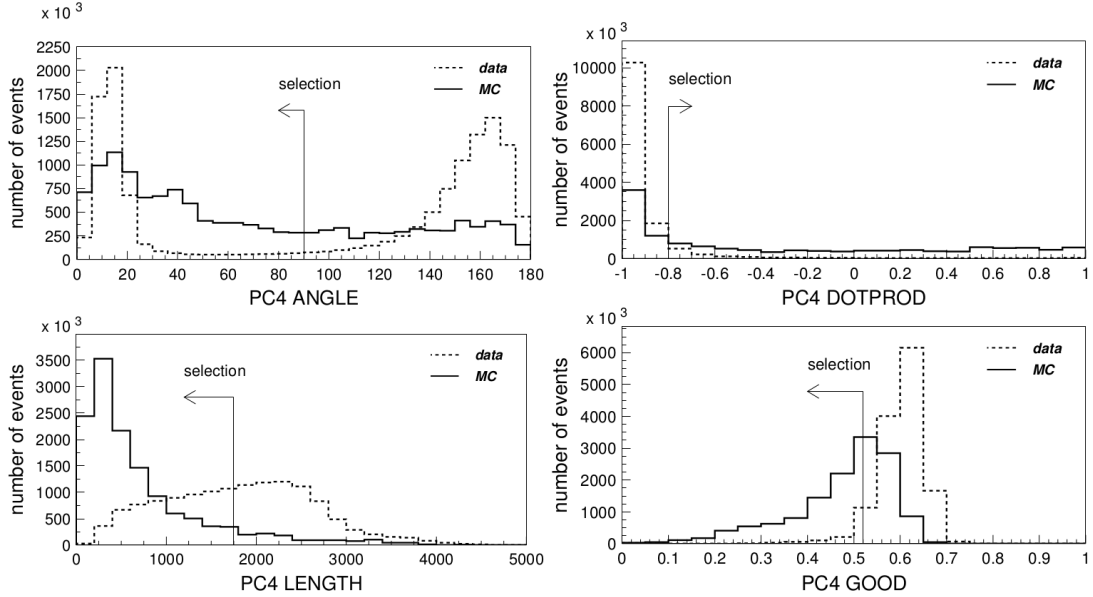


FIGURE 7.11: These are the selection criteria in PC4 for SK-III and IV, used to reject muon events that originated outside the inner detector. The dotted line shows the data, after the output of PC3. The solid line shows MC, which may be thought of as the expectation for a pure PC neutrino sample.

7.2.4.2 PC4: SK-III and IV

Here a new muon fitting program is used, which attempts to classify muon events as one of: stopping muon, through-going muon, corner-clipping muon, or multiple muons. To this end, five selection criteria are calculated:

1. $angle_{\mu} < 90^{\circ}$.

This is the angle between the fitted direction, and the direction between Point-fit vertex and the centre of the largest OD charge cluster.

2. $dotprod_{\mu} > -0.8$.

The dot product of the fitted direction, with the direction between Point-fit vertex and the earliest saturated ID PMT.

3. $\text{length}_\mu < 1750$ cm.
The length of the fitted muon track.
4. $\text{goodness}_\mu < 0.52$.
The goodness of fit returned by the muon fitter.
5. $\text{corner}_\mu \geq 300$ cm.
Distance between the fitted entrance point and the tank corner.

An additional selection criteria applies for only stopping muon events:

- $\text{goodness}_\mu < 0.5$ or $\text{ehit}_\mu < 10$,
where ehit_μ is the number of OD hits within 8 m and 500 ns of the fitted muon ID entrance point.

For classification as a through-going muon, the event must pass 4/5 of these selections. For stopping muon classification, 4/5 passes are still required, however these must include selection 2), and also the additional stopping-muon selection. Corner-clipping and multiple muon classifications require only 2/5 of the above criteria to be passed. If an event passes the selection for any of these types of muon events, it is rejected from the PC sample.

An additional cut imposed in PC4 is the following:

- $\text{PE}_{tot} < 2900$ p-e,
where PE_{tot} is the total number of p-e in the ID.

This corresponds to a ~ 500 MeV/c muon, and serves to reduce more low energy background events. In a true PC event, the muon must have a minimum momentum of ~ 700 MeV/c to even reach the OD, so there is not much efficiency loss by this cut.

7.2.5 5th Reduction (PC5)

In PC5, further cuts are imposed to reduce specific subsets of each background which have failed to be removed thus far. Again, these cuts are quite different for SK-I and II, compared to SK-III and IV, so they will be discussed in separate sections.

7.2.5.1 PC5: SK-I and SK-II

Low energy event cut

Reduction of low energy background that was not performed in PC4.

- $PE_{tot} < 3000$ p-e,
where PE_{tot} is the total number of p-e in the ID.

Through-going muon cut A

Events satisfying these additional criteria are removed as through-going muons. The OD cluster finding algorithm from PC2 is used except this time the OD is divided into 6×6 patches instead of 11×11 .

- $DIST_{clust} > 20$ m,
where $DIST_{clust}$ is the distance between the two OD clusters with the highest charge.
- $PEAC_{2nd} \geq 10$ p-e,
where $PEAC_{2nd}$ is the number of p-e in the 2nd largest OD hit cluster.
- $NCLSTA5 \geq 2$,
where $NCLSTA5$ is the number of clusters in the OD with more than 9 hits.

For events that have passed all cuts up until now, a full reconstruction is performed, so final rejections can be calculated from variables output from this.

Through-going muon cut B

This cut is to reject cosmic ray muon events which travel from the top of the tank to the bottom, staying close to the ID wall for the whole journey. The light collection for events near the tank wall is poor, so they often escape previous reductions. If all the following criteria are satisfied, the event is rejected:

- $NHITA_{top} \geq 7$ and $NHITA_{bottom} \geq 7$,
where $NHITA_{location}$ is the number of OD PMTs hit within an 8 m radius sphere of that location.
- $PEA_{top} \geq 10$ p-e and $PEA_{bottom} \geq 10$ p-e.
 $PEA_{location}$ is defined the same as $NHITA_{location}$, but counts the total p-e instead of the number of hits.

- $0.75 < \text{TDIFFA} \times c/40 \text{ m} < 1.5$,
where TDIFFA is the difference between the average hit time for the two spheres defined by $\text{NHITA}_{location}$.

Through-going muon cut C

The final cut for through-going muons, is still looking for charge clusters near the entrance and exit points, but now the event reconstruction is based off the MS-fit result. The entrance and exit points for the muon are found by extrapolation from the MS-fit vertex and direction. If both of the following conditions are met, the event is cut:

- $\text{NHITA}_{in} \geq 5$ and $\text{NHITA}_{out} \geq 5$.
 $\text{NHITA}_{in,out}$ gives the number of hit OD PMTs within an 8 m radius sphere of the entrance or exit point.
- $0.75 < \text{TDIFFA} \times c/\text{TRACK} < 1.5$. TRACK is the distance between the entrance and exit points, by MS-fit calculation.

Stopping muon cut A

The entrance point is reconstructed by extrapolating from the MS-fit vertex and direction. Any event satisfying the following criteria is rejected as a stopping muon.

- $\text{NHITA}_{in} \geq 10$.
 NHITA_{in} gives the number of hit OD PMTs within an 8 m radius sphere of the entrance point.

Stopping muon cut B

Using both TDC-fit, and MS-fit, the Cherenkov opening angle is calculated. Stopping muon events are expected to have higher energy, thus a larger opening angle than PC events. If the event passes this cut, it is rejected:

- $\theta_{TDC} > 90^\circ$ or $\theta_{MS} > 90^\circ$,
where θ_x is the Cherenkov opening angle as calculated by fit x .

Stopping muon cut C

The stopping muon fitter is used to try and fit the event. As PC event vertices are significantly displaced from the tank wall, but stopping muons require that the vertex is on the wall, the fit will be more likely to reconstruct incorrectly for PC events. If the following criteria are all satisfied, the event is rejected as a stopping muon:

- stopping muon fit goodness > 0

- $PE_{cone}/PE_{tot} \geq 0.6$,

where PE_{cone} is the total p-e count within a 42° Cherenkov cone from the stopping muon fit vertex. PE_{tot} is the total ID p-e. If the Cherenkov cone contains a large amount of the total charge, the event is more likely to be a stopping muon.

- $NHITA_{in} > 6$,

where $NHITA_{in}$ is the number of hit OD PMTs within 8 m of the fit vertex.

Cable hole muon cut

If a cable hole veto counter is hit, and the event reconstruction matches the direction of the cable hole, the event is rejected:

- a veto counter is hit

- $\vec{d}_{TDC} \cdot \vec{d}_{veto-vertex} > -0.8$,

where \vec{d}_{TDC} is the reconstructed ring direction by TDC fit, and $\vec{d}_{veto-vertex}$ is the direction from the hit veto counter to the reconstructed vertex.

Corner clipping muon cut A

Corner clipping muons typically only have a small cluster of charge in the ID, before they exit through the tank wall. Thus the vertex reconstruction assuming it is a primarily ID event, will often be very poor. This cut compares the predicted track length using the MS-fit reconstruction, to the predicted track length by visible energy (recall that muons lose ~ 2 MeV/cm. Thus the cut criteria to reject these events is:

- if $(TRACK > 1500 \text{ cm})$ and $E_{vis}/2 < TRACK - 1500$,

where $TRACK$ is the track length estimated as the distance from MS-fit vertex to extrapolated exit point, and $E_{vis}/2$ is an approximation for the track length in cm.

7.2.5.2 PC5: SK-III and SK-IV

The final PC reduction for SK-III and IV consists of two types of cuts - ‘‘hard’’ cut and ‘‘soft’’ cuts. All events are required to pass all of the hard cuts. If events fail > 1 soft cut, they will be removed from the sample. The hard cuts are as follows:

1. Through-going muon cut A

2. Through-going muon cut B
3. Stopping muon cut B
4. Cable hole muon cut
5. Corner-clipping muon cut B

The first four of these are identical to those described in the SK-I and II reductions. The final cut is specific to SK-III and IV. The soft cuts are:

1. Through-going muon cut C
2. Through-going muon cut D
3. Stopping muon cut A
4. Stopping muon cut C
5. Stopping muon cut D
6. Stopping muon cut E
7. Corner clipping muon cut A
8. Decay electron cut

of which if two or more are failed, the event is cut. Soft cuts (1), (3), (4) and (7) have already been covered in the SK-I and II PC5 reduction. The hard and soft cuts which have not yet been introduced will be defined below.

Corner clipping muon cut B

This corner clipping cut is used to remove muons which just tag the corner of the tank. This is a hard cut, and must be passed for the event to be accepted.

- $DCORN > 150$ cm,

where $DCORN$ is the distance between the vertex reconstructed by point-fit, and the nearest tank corner.

Through-going muon cut D

This cut removes through-going muons with two large clusters of charge in the OD.

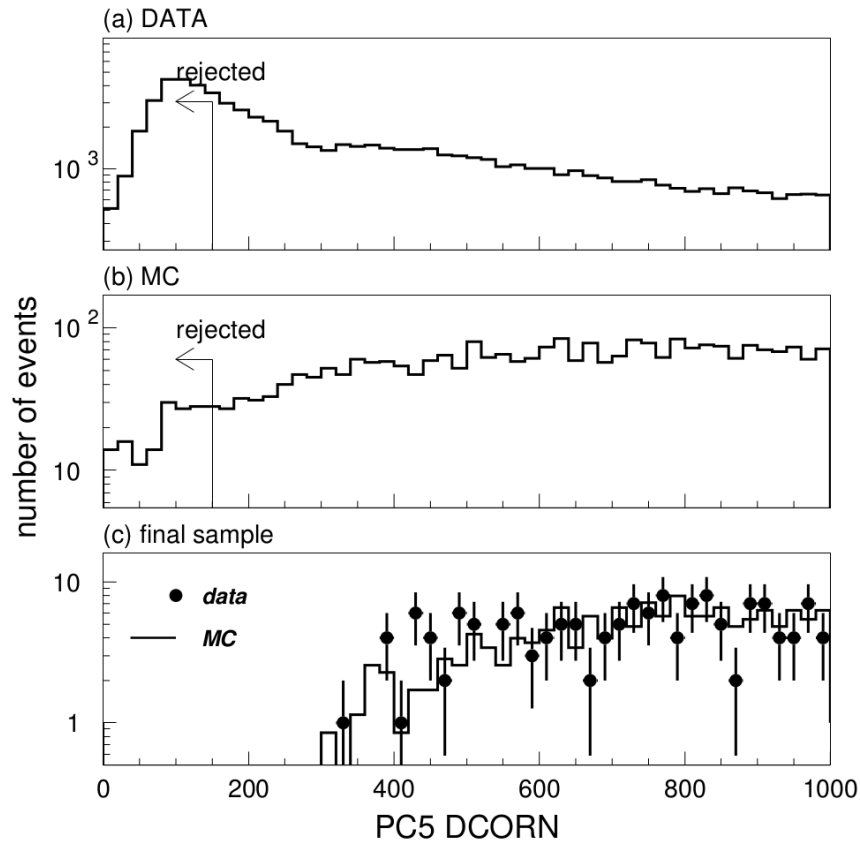


FIGURE 7.12: These plots show the distance from the reconstructed muon vertex to the nearest corner of the tank. MC is a sample of pure atmospheric neutrino. This cut is used to remove corner-clipping muons. The bottom plot shows data-MC agreement after the final selection of PC events.

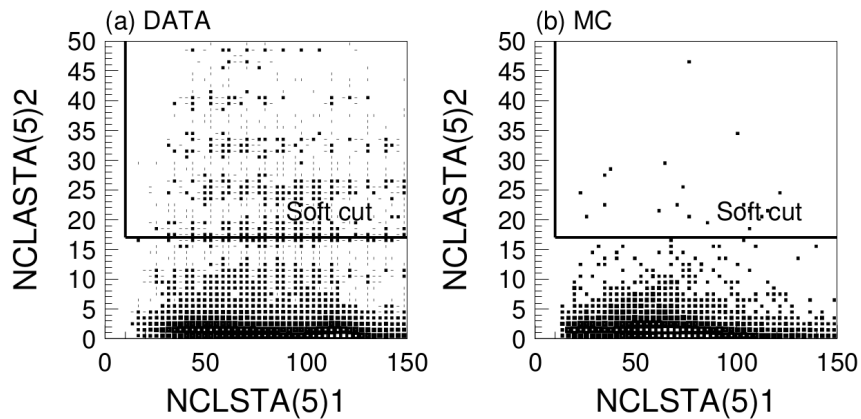


FIGURE 7.13: $NCLSTA5(x)$ gives the number of OD PMTs inside the x -th highest charge cluster. Large values for two clusters suggests a through-going muon event, which is then cut.

- $NCLSTA5(1) \geq 10$ and $NCLSTA5(2) \geq 17$,
where $NCLSTA5(x)$ is the number of OD PMTs inside the x -th highest charge cluster.

Stopping muon cut D

Stopping muon cut D is similar to that used in PC3 for SK-I and II events, but has been moved to PC5 for SK-III and IV. This is because MS-fit information is needed, and the full reconstruction is not applied until PC5. Stopping muons are removed if there are enough hits surrounding the entrance point of the particle in the OD, but only if point-fit and MS-fit vertex positions are in agreement.

- $\text{NHITA}_{in} > 6$, applied only if $|\vec{P}_{\text{ffit}} - \vec{P}_{\text{MS}}| < 1500$ cm, where NHITA_{in} is the number of hit OD PMTs within 8 m from the particle entrance point. \vec{P}_{ffit} and \vec{P}_{MS} are the vertices from point-fit and MS-fit respectively.

Stopping muon cut E

This is identical to a selection criteria used in PC4 to remove upward-going muon events. It was not necessary to pass in PC4, and it is included again here as a soft cut. A muon fitter result is compared to the assumption that the muon originated from an OD charge cluster. If the directions of the two vectors match well, the event is removed.

- $\text{angle}_{\mu} < 90^{\circ}$, where angle_{μ} is the difference between the fitted direction from the μ -fitter described in PC4, and the vector between the point-fit vertex and the highest OD charge cluster.

Decay electron cut

If a neutrino is very high energy ($E_{vis} > 25$ GeV), it is very likely to produce a decay electron, via pions ejected in the initial interaction. If no decay electron is detected, the event is cut, as it is likely that the interaction producing the observed event occurred outside of the inner detector.

7.2.6 Fiducial Volume Selection

A final set of cuts are performed on the remaining PC sample:

- $\text{dWall} > 200$ cm, where dWall is the distance from the reconstructed vertex to the closest tank wall. This is to further veto events which have entered from outside the tank, and events due to radioactive impurities in the tank wall.
- $\text{NHITAC} \geq 16$ (10 for SK-I). NHITAC is the number of hits in the largest charge cluster in the OD. This cut ensures there is no overlap of events between the PC sample and the FC sample (which requires $\text{NHITAC} < 16$).

- $E_{vis} > 350$ MeV, where E_{vis} is the sum of the reconstructed momentum of all rings, assuming they are e-like. This cut is higher than the equivalent FC cut, because the particles need this minimum amount of energy to reach and pass through the ID-OD tank wall.

7.2.7 PC Reduction Summary

The efficiency of each reduction step is determined by performing the reduction on an atmospheric neutrino MC. The systematic error on these reduction efficiencies is calculated by comparing data-MC distributions for each cut variable, and is determined to be 2.4%, 4.8%, 0.5% and 1.0% for SK-I to IV respectively.

Background in for final PC reduction comprises predominantly of cosmic ray muon events. The background rate is estimated by eye-scanning the final sample. A table containing the reduction efficiencies, backgrounds, and final event rates is shown in 7.2.

PC	SK-I	SK-II	SK-III	SK-IV
Reduction	Selection Efficiency (%)			
PC1	98.98	98.58	99.09	99.63
PC2	96.74	93.43	98.52	98.73
PC3	95.69	92.32	98.51	98.68
PC4	89.86	84.60	97.87	97.42
PC5	88.66	82.63	96.61	96.15
PCFV	80.98	74.80	88.80	86.30
	Final Sample Background (%)			
Background in PCFV	0.2%	0.7%	1.1%	0.5%
	Number of Events			
Livetime (days)	1489.2	798.6	518.2	1775.6
MC Prediction	913.8	448.6	356.0	1206.3
Data	902	427	344	1105
Events / day	0.66 ± 0.04	0.65 ± 0.04	0.62 ± 0.03	0.62 ± 0.02

TABLE 7.2: PC Summary Table

7.3 Upward-going Muon Reduction

Upward-going muons (UPMU) are muons which enter the detector tank from below the horizon. These muons are created by neutrino interactions in the rock below SK. There are analogous downward going muons generated from neutrino events, but these are impossible to separate from cosmic-ray muon background, so are not considered in neutrino analyses. Each UPMU event may be classified as a stopping muon (stop-mu), which stops inside the SK tank, or a through-going muon (thru-mu), which has

not stopped before it exits through the top of the detector. Through-going muons are further split into showering (produces Bremsstrahlung and electro-magnetic showers), and non-showering events.

The main aim for UPMU reduction is to remove cosmic ray muons and other backgrounds, then separate the remaining sample into one of the three event categories. The reduction steps will be covered briefly here, for more details see [137].

7.3.1 1st Reduction (UPMU1)

Firstly, a low energy cut, and a very high energy cut are applied:

- $PE_{tot} > 8000$ p-e (3000 for SK-II)
- $PE_{tot} < 1.75 \times 10^6$ p-e (8×10^5 for SK-II)

PE_{tot} is the total number of photo-electrons recorded in the ID. At energies above 1.75×10^6 p-e, the tank PMTs become saturated, and thus the event is difficult to reconstruct. These high energy events are very rare - only one was observed in all of SK-I. The low energy cut corresponds to a minimum track length of ~ 7 m.

An OD cluster finding algorithm is used to broadly categorize events as either stop-mu or thru-mu, as well as eliminating some other backgrounds such as calibration events. An UPMU fitter is then used, to estimate the vertex, direction and track length of all remaining events. Further cuts are made based on the output of this fit.

- fit goodness > 0.3
- fit direction $\cos \theta > 0$,
where θ is the zenith angle.

The latter criteria rejects events that are not going upwards. The output of this reduction step is $\sim 9,000$ events/day.

7.3.2 2nd Reduction (UPMU2)

The remaining events are fit again, with three separate fitters. The first attempts to fit the event as a stop-mu, the second a non-showering thru-mu, and the third attempts to fit as a showering thru-mu or multiple muon event. Based on the goodness of these fits, a decision is made as to whether the event is a stop-mu or thru-mu. The fit results also categorize the event as one of six types:

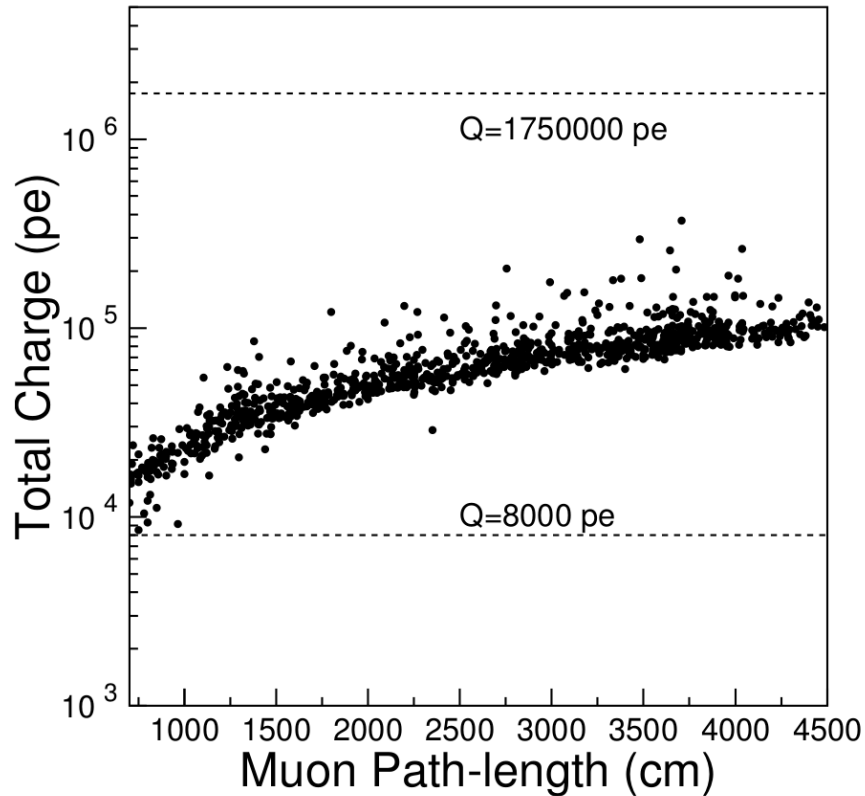


FIGURE 7.14: Total ID p-e as a function of track length. Data taken with down-going cosmic ray muon calibration sample.

- failed fit
- down-going ($\cos \theta < -0.12$)
- near-horizontal ($-0.12 \leq \cos \theta < 0$)
- down-going, entry from top of tank
- near-horizontal, entry from top of tank
- up-mu

After combining the results from all the fits, any events recorded as down-going or failed are removed. Horizontal and up-mu events continue onto the next reduction, comprising of ~ 250 events/day.

7.3.3 Interlude

After the second reduction, the most precise muon fitter is applied, aptly named precise-fit and described in chapter 6. As a subroutine of the precise-fit, a showering algorithm is

run, to determine whether the event should be labelled as showering, or non-showering, which shall be briefly described here.

7.3.3.1 Showering Algorithm

The showering algorithm is applied to through-going muons, and aims to identify events which primarily lose their energy via an electromagnetic shower, rather than ionization. An electromagnetic shower occurs as a result of Bremsstrahlung interactions along the muon track, which produce photons that create EM showers. Of course the muon is also producing Cherenkov photons all the time, but these are too low energy to induce a showering effect. The switch from energy loss by ionization to energy loss by Bremsstrahlung occurs around 1 TeV [138].

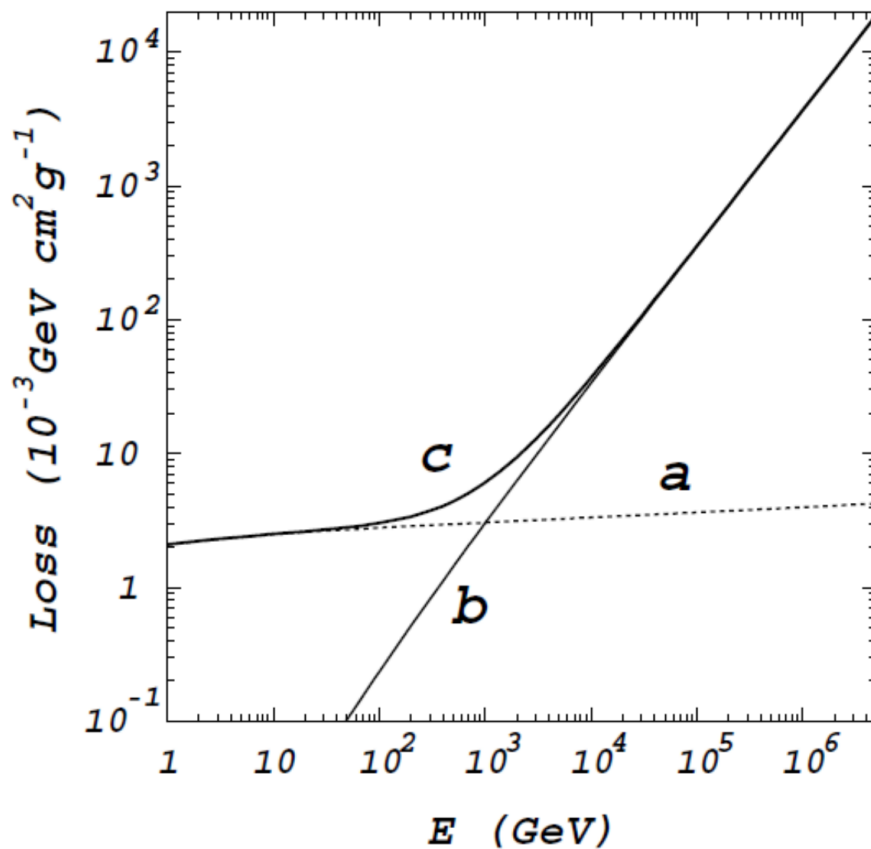


FIGURE 7.15: Primary methods of muon energy loss, when travelling through water. The line (a) shows energy loss via ionization, (b) shows energy loss via Bremsstrahlung, and (c) is the total.

Energy loss by ionization occurs at a relatively constant rate of 2.2 MeV/cm. Showering muons can be distinguished from this, as their energy loss is much faster, as can be seen in figure 7.15.

The muon track is broken up into segments of 50 cm, and for each segment i , the observed charge Q_{corr}^i is compared to the average charge observed in all segments $\langle Q_{corr} \rangle$ (to judge if the rate of energy loss is changing). In addition, the average observed charge is compared to the expectation for a non-showering event $\langle Q_{exp} \rangle$. The *corr* subscripts for these variables refer to the charge correction performed for every PMT hit to account for attenuation in water, and acceptance for a given incident angle.

Two values are calculated based on these parameters:

$$\chi^2 = \sum_{i=3}^{N-2} \left(\frac{(Q_{corr}^i - \langle Q_{corr} \rangle)^2}{\sigma_{Q_{corr}^i}^2} + \frac{(\langle Q_{corr} \rangle - \langle Q_{exp} \rangle)^2}{\sigma_{\langle Q_{exp} \rangle}^2} \right) \quad (7.4)$$

$$\Delta = \langle Q_{corr} \rangle - \langle Q_{exp} \rangle - \delta Q, \quad (7.5)$$

where σ_x is the resolution of quantity x . Track segments near the edges of the detector are ignored ($i = 1, 2, N - 1, N$), as it is difficult to calculate the corrected charge accurately here. δQ is a tuning parameter calibrated in each SK period, to set the peak value of Δ to 0 for the MC.

Using these two variables, showering muons are selected if the following criteria are satisfied:

- $\Delta > 0.5$, for $\chi^2 > 50.0$
- $\Delta > 4.5 - 0.08\chi^2$, for $\chi^2 \leq 50.0$

The separation between showering and non-showering events can be seen in figure [7.16](#)

7.3.4 3rd Reduction (UPMU3)

From here, separate cuts will be applied to stop-mu and thru-mu events. The cuts are based on the output of precise-fit, which was performed on every candidate before beginning this reduction step. For through going events, the requirements are as follows:

- $UM_EHIT8M > 10$ (16 for SK-II),
where UM_EHIT8M is the number of OD PMTs hit within 8 m of the tank entrance point.
- $UM_OHIT8M > 10$ (16 for SK-II),
where UM_OHIT8M is the number of OD PMTs hit within 8 m of the tank exit point.

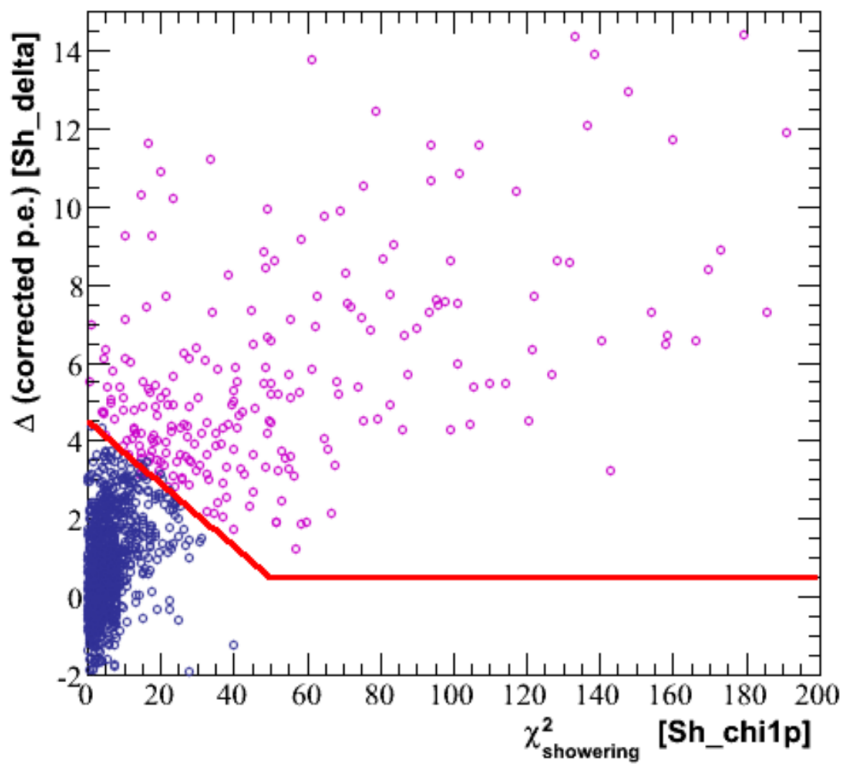


FIGURE 7.16: The thru-mu showering vs non-showering selection criteria, shown here with SK-IV dataset. Events above the red line are classified as showering, and below are classified as non-showering.

- Track length ≥ 700 cm (precise-fit)
- Fit direction $\cos\theta \geq 0$ (precise-fit),
where θ is the zenith angle.

For stopping muon events, the criteria are:

- UM_EHIT8M > 10 (16 for SK-II),
where UM_EHIT8M is the number of OD PMTs hit within 8 m of the tank entrance point.
- UM_OHIT8M < 10 (16 for SK-II),
where UM_OHIT8M is the number of OD PMTs hit within 8 m of the tank exit point.
- Fit momentum ≥ 1.6 GeV/c (precise-fit)
- Fit direction $\cos\theta \geq 0$ (precise-fit),
where θ is the zenith angle.

Track length is used in the through-going muon case, as it is simple to calculate between the entrance and exit points, and is analogous to a momentum requirement. For stopping muons, reconstructed momentum of 1.6 GeV/c corresponds to a track length ~ 700 cm.

7.3.5 4th Reduction (UPMU4)

By this stage almost all of the cosmic ray muon background in these samples has been removed, however still remaining are events where cosmic ray muons brush the corner of the inner detector, so called "corner-clipping" muons. These events are difficult to fit, as the two OD clusters are close together, and the ID track is very short.

From SK-III, after the optical segmentation of the ID and OD was introduced, an improved OD cluster-fitting algorithm was developed. If 2 or more clusters are found using this algorithm, and Precise-fit is found to perform poorly compared to a simple fit based on clusters of ID PMT charge, the event is classified as a corner-clipper and removed from the sample.

All remaining UPMU events are eye-scanned by experts, to remove remaining corner clipper and cosmic ray background.

7.3.6 Background Subtraction

Mt. Ikenoyama above SK reduces much cosmic-ray background, however for cosmic-rays entering from a horizontal direction, the amount of rock shielding has azimuthal dependence, and thus the background rate varies depending on the thickness of surrounding rock. This effect can be seen in figure 7.17, and the 1-d projection in figure 7.18.

From the plots we can see that the tank may be roughly split up into two regions - region 1, where little additional background is expected due to significant shielding, and region 2, where the rock is thin, and additional cosmic ray muons are likely to enter the sample. For stopping muons

Region 1 : $\phi < 60^\circ$ and $\phi > 310^\circ$

Region 2 : $60^\circ < \phi < 310^\circ$

and for through-going muons

Region 1 : $\phi < 60^\circ$ and $\phi > 240^\circ$

Region 2 : $60^\circ < \phi < 240^\circ$,

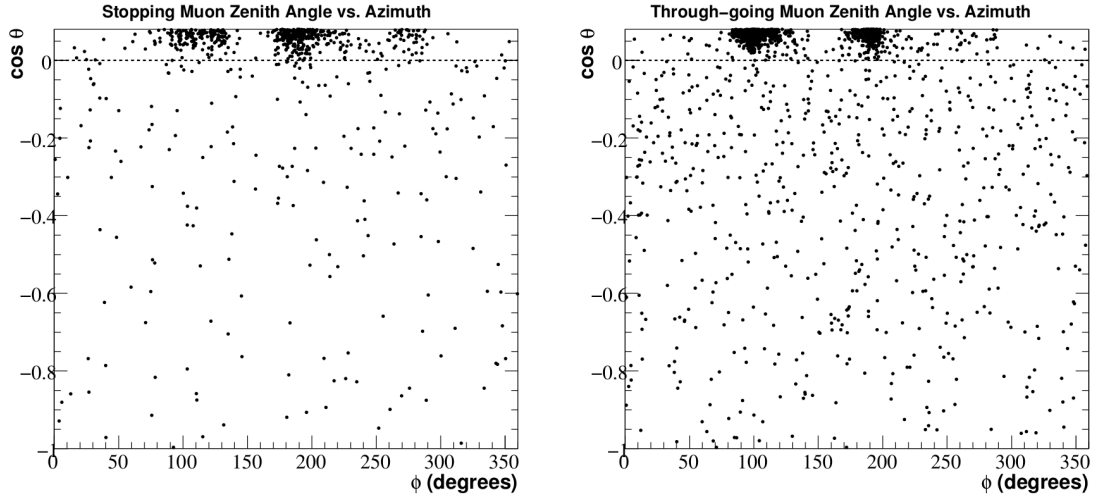


FIGURE 7.17: The zenith and azimuthal dependence of Stopping and through-going muons for SK-III. Some above horizon events have been included for demonstration of this effect.

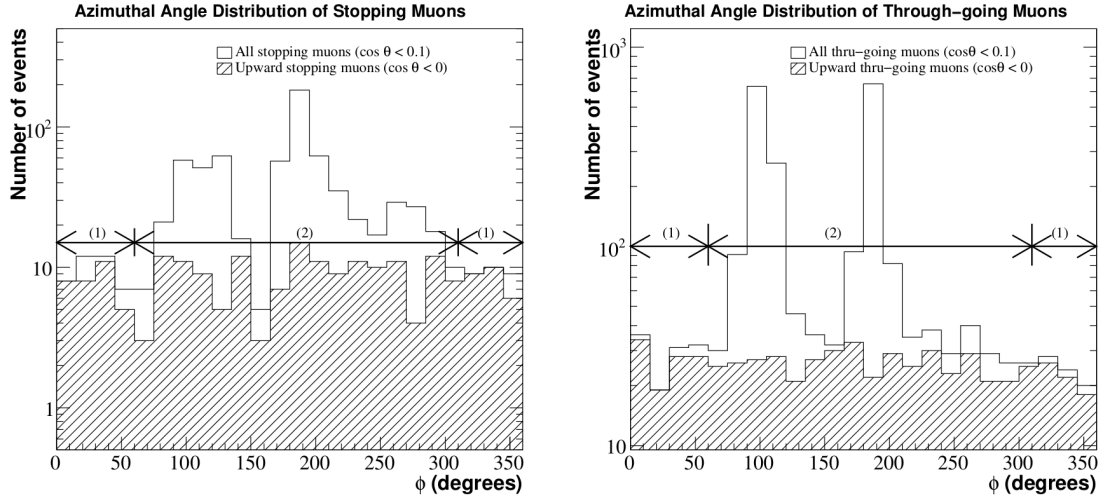


FIGURE 7.18: The 1-dimensional projection of the azimuthal dependence of UPMU background. Events coming from above the horizon are shown with no fill, and upward-going muons are shown with hashed fill.

where ϕ is the azimuthal angle. For region 2, the event distributions may be modelled using an exponential function of zenith angle:

$$F(\cos \theta) = P_0 + e^{P_1 + P_2 \cos \theta}. \quad (7.6)$$

The results of this fit can be seen in figure 7.19.

For atmospheric neutrino oscillation analysis, for which event-by-event discrimination is less important, a correction for the extra expected background in near-horizontal zenith bins is made:

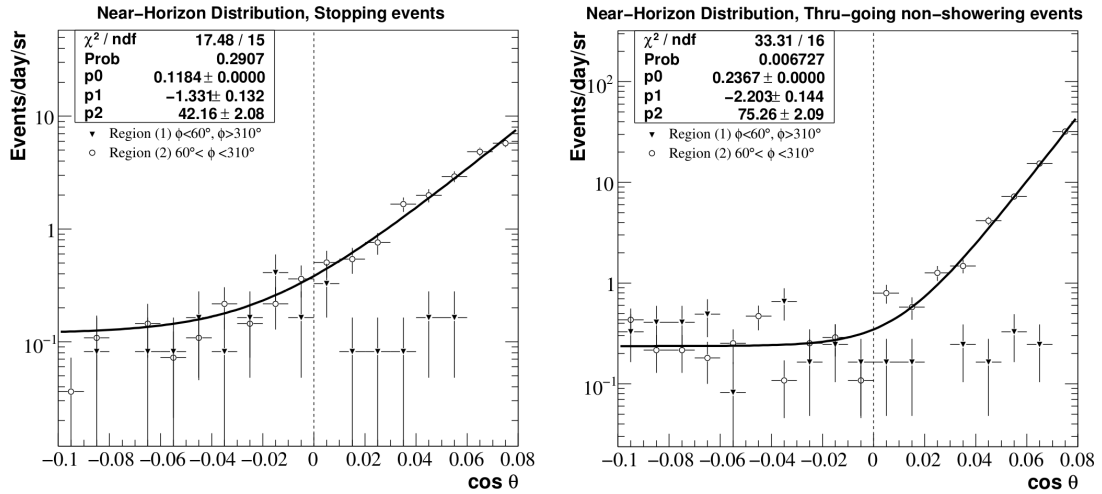


FIGURE 7.19: Extra background contamination in stop-mu and thru-mu samples, fitted to a constant + exponential function of zenith angle. The triangles represent the approximately constant background in azimuthal region 1, and the circles are the exponentially increasing background in region 2.

$$N_{BG} = \int_{\cos \theta_1}^{\cos \theta_2} e^{P_1 + P_2 \cos \theta} d(\cos \theta), \quad (7.7)$$

where θ_1 and θ_2 represent the edges of the zenith bin to be corrected. This correction is performed for through-going muons where $-0.1 < \cos \theta < 0.0$, and for stopping muons where $-0.2 < \cos \theta < 0.0$.

7.3.7 UPMU Reduction Summary

A summary of the event rates after each reduction (data shown for SK-III period), can be seen below (7.3).

Reduction Step	Events/day
UPMU1	9,900
UPMU2	244
UPMU3	3.7
UPMU4	1.9
Eyescan	1.5

TABLE 7.3: Approximate events remaining after each UPMU reduction step.

The final samples, event rates and expected background for SK-I to IV UPMU reduction are shown in table 7.4.

UPMU	SK-I	SK-II	SK-III	SK-IV
	Number of Events			
Stop-mu	462	214	210	480
Thru-mu	1866	888	735	2097
Livetime (days)	1645.9	827.7	635.6	1775.6
Total Events/day	1.41 ± 0.03	1.33 ± 0.04	1.49 ± 0.05	1.45 ± 0.03
	Background Subtraction			
Stop-mu	36.0	13.0	17.0	35.0
Thru-mu	30.4	37.6	12.1	14.1

TABLE 7.4: Summary of the remaining events, and background subtraction for the data sample remaining after UPMU reduction

Chapter 8

Neutron Tagging

Free neutrons travelling through water are quickly thermalized, and then captured by an oxygen or hydrogen nucleus. The cross sections for these capture processes are 0.19 milli-barns and 0.33 barns respectively, so it is safe to assume $\sim 100\%$ of neutrons are captured by hydrogen, in the interaction

$$n + p \rightarrow d + \gamma \text{ (2.2 MeV)}. \quad (8.1)$$

Neutron tagging refers to the process by which these 2.2 MeV γ -rays are identified, thus the number of neutrons produced by the neutrino interaction may be inferred.

Detecting neutrons provides a method by which water Cherenkov detectors can distinguish anti-neutrinos from neutrinos, since the charged-current quasi-elastic interaction $\bar{\nu}_e + p \rightarrow e^+ + n$ is prohibited by charge conservation and lepton number for neutrinos. At energies $E_\nu > 1$ GeV, few interactions are pure CCQE, and often additional neutrons are liberated by secondary hadronic interactions. However it is still possible to produce anti-neutrino enriched samples.

The neutron capture lifetime is measured to be $204.8\mu\text{s}$ [139]. To encompass this time range, an additional trigger “AFT” was introduced at the start of SK-IV, triggering automatically if a SHE trigger is issued without an OD trigger. The AFT trigger saves an additional $500\mu\text{s}$ of data following the $35\mu\text{s}$ saved by SHE, to allow a total of $\sim 92\%$ of neutron capture signals to be saved in the data.

The neutron tagging study was first introduced to SK in 2009 by H. Watanabe and H. Zhang [140] with the intention of reducing the background from a primarily anti-neutrino based supernova relic neutrino signal. This thesis presents the development of neutron tagging for use in high energy atmospheric neutrino interactions.

8.1 Neutron Simulation

The primary event simulation methods for atmospheric neutrinos are discussed in chapter 5. Some additional modifications have been made to this MC to enable neutron study.

- To enable production of neutron capture gamma rays, the low energy cut off for simulating neutral hadrons is reduced to 0.1×10^{-4} eV.
- The simulation time is extended to $535\mu\text{s}$ to match the SHE+AFT trigger length.
- PMT dark noise is simulated only up until $18\mu\text{s}$, after which dummy trigger data was used instead (figure 8.1). Dummy trigger data simply refers to real data recorded in SK after a random trigger. Using this circumvents the need to simulate all possible low energy backgrounds.

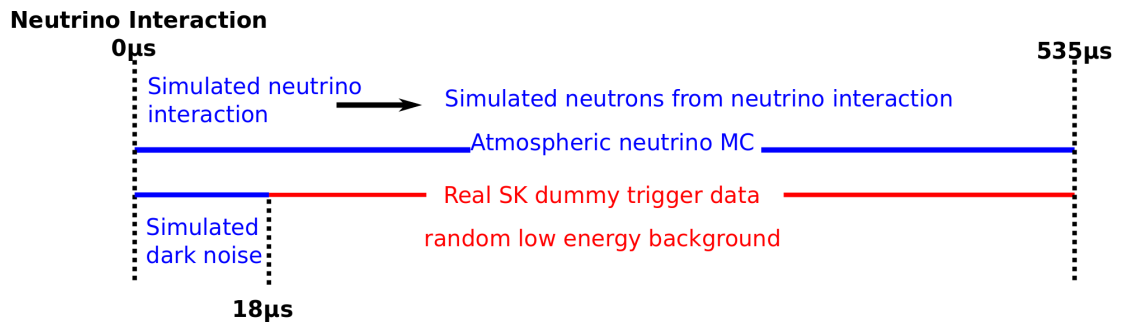


FIGURE 8.1: Construction of neutron MC. After $18\mu\text{s}$ dummy trigger data is convoluted with simulated neutrons produced by an atmospheric neutrino interaction.

The last point is necessary as low energy backgrounds, such as radioactive decay products, are not simulated by the MC. Simulated PMT dark noise is used up until $18\mu\text{s}$ after primary trigger time, to negate any effect on the existing atmospheric neutrino analysis. The dummy trigger data used was taken in 2009 near the start of SK-IV. Due to the increasing PMT gain of 2% per year, the average number of 2.2 MeV γ candidates in the dummy trigger period - 5.34/event, is 4% less than the average for all of SK-IV - 5.54/event (figure 8.2). This difference is accounted for in the background estimation.

Following high energy neutrino interactions, it is common for neutrons to be ejected with momentum over 100 MeV/c. This means the neutron capture vertex is often displaced by some metres from the neutrino interaction vertex (figure 8.3). This causes a larger spread in the 2.2 MeV γ timing distribution after Time-of-Flight (ToF) subtraction, reducing the efficiency of detection at high energies.

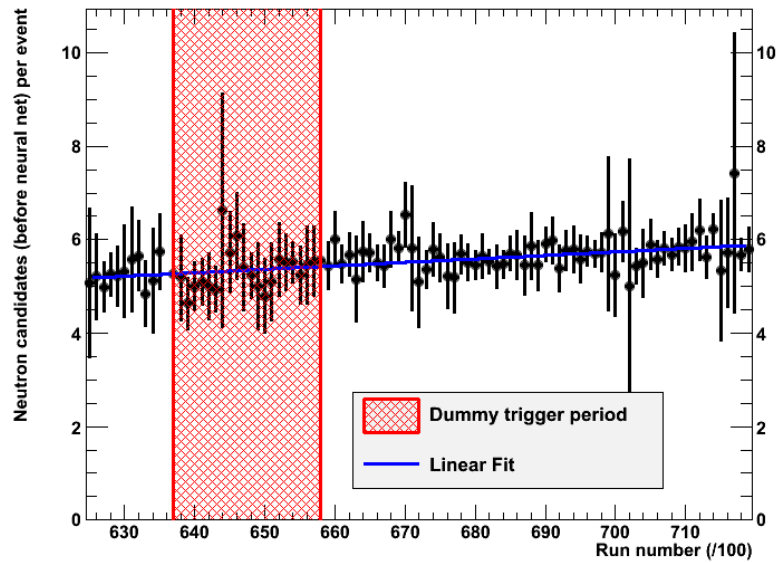


FIGURE 8.2: Number of 2.2 MeV γ candidates (before neural network selection) per day, as a function of run number in SK-IV. The dummy trigger data taking period is shaded in red. The average candidates per event for the dummy trigger period is 5.34/event, and the average for all of SK-IV is 5.54/event. The gradient is consistent with a 2% increase in PMT gain per year.

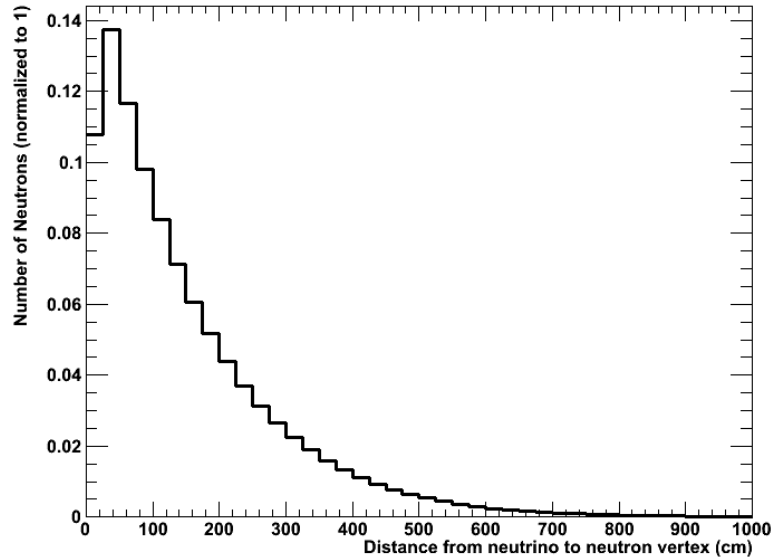


FIGURE 8.3: Neutron travel distance from the initial neutrino interaction vertex, according to the atmospheric neutrino MC simulation.

The efficiency and background of the neutron tagging algorithm are evaluated using the atmospheric neutrino MC by the following criteria:

$$\delta t_{min} < 100 \text{ ns: True } 2.2 \text{ MeV } \gamma$$

$$\delta t_{min} > 100 \text{ ns: Background,}$$

where t_{min} is defined as

$$\delta t_{min} = \min[|t_{rec} - t_{true}^i|] \quad (8.2)$$

the minimum time interval between a true neutron capture at t_{true}^i and the reconstructed neutron capture time t_{rec} (figure 8.4).

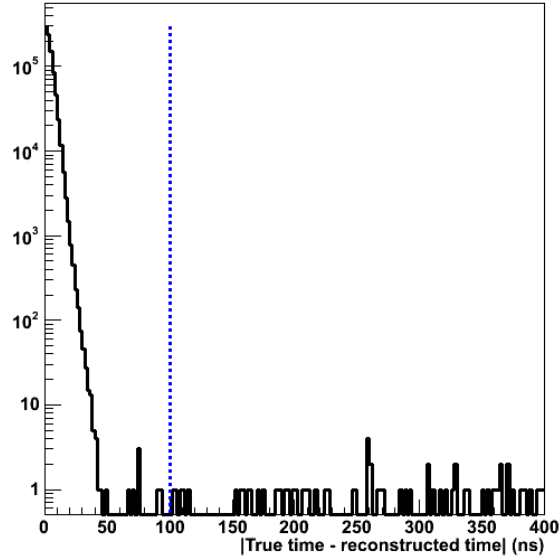


FIGURE 8.4: Showing the time resolution of final selection of neutrons in 500 years of MC. The blue line shows the cut for calculating efficiency and background of the neutron tagging algorithm.

The secondary particle information storage bank for the MC is limited to 1000 particles. For events with more particles, all secondary particles and gamma rays are still simulated and generate signals on PMTs, but information about the timing, particle type and so on is not stored. Therefore MC events with 1000 or more secondary particles are ignored when calculating efficiency and background of the neutron tagging algorithm.

8.2 Neutron Tagging Algorithm

To distinguish a 2.2 MeV γ signal, we must first consider its characteristics. The 2.2 MeV γ ray is expected to produce all its PMT hits in a narrow timing distribution, and these are expected to be anisotropic. The neutron capture point is expected to be <200 cm from the neutrino vertex, and the energy of the hits should correspond to ~ 2.2 MeV. Prominent backgrounds at this energy range include radioactive decays from the surrounding rock and detector material, radon contamination in the water, PMT dark noise and others. Each background source has different characteristics - some produce isotropic, seemingly random hit patterns, and others produce very tight clusters of hits.

Many background sources are located along the tank wall, and some have a more spread out timing signature than 2.2 MeV γ . With this in mind, an algorithm to pick out true 2.2 MeV γ signal from its background was devised.

The identification of 2.2 MeV γ -rays is split up into two stages. The first looks for peaks in the PMT hit timing distribution to select initial 2.2 MeV γ candidates. Afterwards a set of 16 variables is calculated for each γ candidate, and input into a neural network. The final selection of neutron capture γ -rays is based on the output of this neural network.

8.2.1 Initial Candidate Selection

First, all PMT hits are Time-of-Flight (ToF) subtracted to the neutrino vertex, as calculated by APfit, described in chapter 6. A 10 ns sliding time window from $18\mu\text{s}$ until $535\mu\text{s}$ is then used, to select 2.2 MeV γ candidates, where time is defined relative to the primary trigger. Though particle backgrounds from the initial neutrino interaction mostly subside during the first $5\mu\text{s}$ after the event (with the exception of muon decay electrons), from $12\text{-}18\mu\text{s}$ the PMTs experience an after pulse, which contributes significant background to neutron-tagging (figure 8.5). This gives the lower bound of $18\mu\text{s}$.

A cluster of PMT hits is selected as a 2.2 MeV γ candidate if

$$N_{10} \geq 7, \tag{8.3}$$

where N_{10} is the number of hits in the 10 ns window (figure 8.6). The candidate time, t_0 , is defined as the timing of the first hit of N_{10} . To avoid multiple counting of a single neutron capture event, once a candidate is found searching continues until $t_0 + 20$ ns. The peak value of N_{10} from this 20 ns window is taken as the 2.2 MeV γ candidate. Peaks found after $t_0 + 20$ ns are treated as separate candidates.

Additional requirements for the initial selection of neutron capture candidates are

$$\begin{aligned} N_{10} &\leq 50 \\ N_{200} &\leq 200, \end{aligned}$$

where N_{200} is the number of hits in 200 ns surrounding the candidate at t_0 . These cuts are to remove high energy backgrounds such as cosmic ray muons. After all these selections are applied 33.2% of neutron capture events are still remaining, with an expected 4.5 mis-tagged background events per neutrino event in $535\mu\text{s}$.

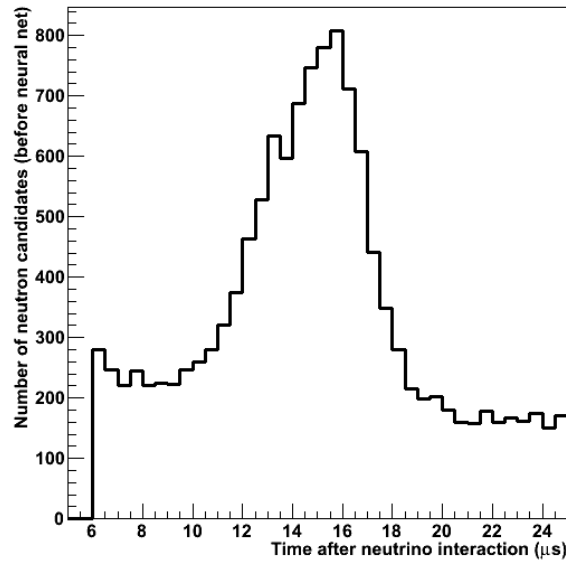


FIGURE 8.5: The increase in number of γ candidates due to the PMT after-pulse. Scanning is performed after $18\mu\text{s}$.

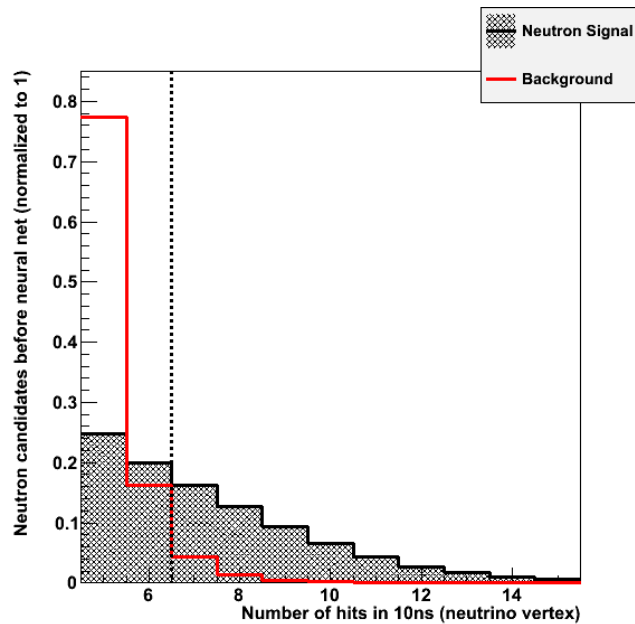


FIGURE 8.6: Values of N_{10} used to select initial 2.2 MeV candidates. Background increases exponentially as the required N_{10} is reduced.

8.2.2 Final Candidate Selection

Following this initial selection 16 variables with power to distinguish between 2.2 MeV γ signals and backgrounds are calculated and input to a neural network. Plots for each of these variables will be shown - including data comparison with MC, and signal-background figures. The signal and background histograms, shaded in green and blue respectively, are both normalized to the integral of the data histogram/4 to make reading

easier (on log scale plots, this normalization factor is reduced to 1/40) . In the data-MC comparison, the MC (red line) is normalized by

$$(MC_{sig} + 1.04 \times MC_{bg}) \frac{LT_{data}}{LT_{MC}}, \quad (8.4)$$

where MC_{sig} is the number of tagged candidates corresponding to a true neutron event, MC_{bg} is the number of tagged candidates which do not correspond to a neutron-capture event, as defined in section 8.1. LT_x is the livetime of sample x . The coefficient 1.04 is a correction for the dummy trigger data period's PMT gain not matching the average of SK-IV. This is a somewhat crude correction, as increased gain will lead to a proportional increase in some background sources, such as PMT dark noise, but for real particle backgrounds such as radioactive decay products, the frequency will not increase but the shape of the signal may change. This may lead to discrepancies in some variables which are not easy to compensate for.

8.2.2.1 Number of Hits in 10 ns: N_{10}

This is the same variable that is used to make the initial selection of 2.2 MeV γ candidates. This variable has already been cut, requiring $N_{10} \geq 7$, but the remaining distribution's shape still holds discriminatory power, so it is used in the neural network (figure 8.7). The background increases exponentially for smaller values of N_{10} .

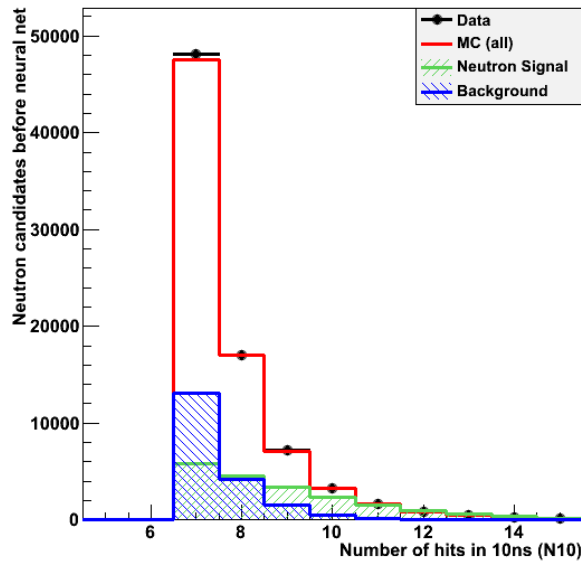


FIGURE 8.7: N_{10} variable as a neural network input. The plot shows a comparison of neutron capture signal (green), background (blue), data (black dots) and MC total (red line). The normalization is explained in section 8.2.2

8.2.2.2 Number of Clustered Hits: N_c

Many background events are found to have a clustered hit pattern, both in time and space. This may be due to backgrounds which originate close to the PMTs themselves, for instance due to radioactive contaminants in the PMT glass or to PMT flashing. A requirement of atmospheric neutrino events is that the event vertex lies > 2 m from the tank wall, so it is rare for neutron capture to occur so close to the PMTs as to cause this type of hit pattern.

To search for clustered hits, the angle between each of the N_{10} hit vectors is calculated. These are unit vectors between each hit PMT, and the APfit neutrino vertex. If a pair of hit vectors is less than 14.1° apart, they are considered a cluster. If additional hits are within 14.1° of any hit contained in a cluster, they are added to it. This process is iterated until all N_{10} hits have been considered and the total number of hits in clusters is counted as N_c .

As N_{10} for 2.2 MeV γ signal is likely to be larger than for background events, this may unfairly increase the number of clusters in the signal sample. Hence the variable input to the neural network is taken as $N_{10} - N_c$ (figure 8.8).

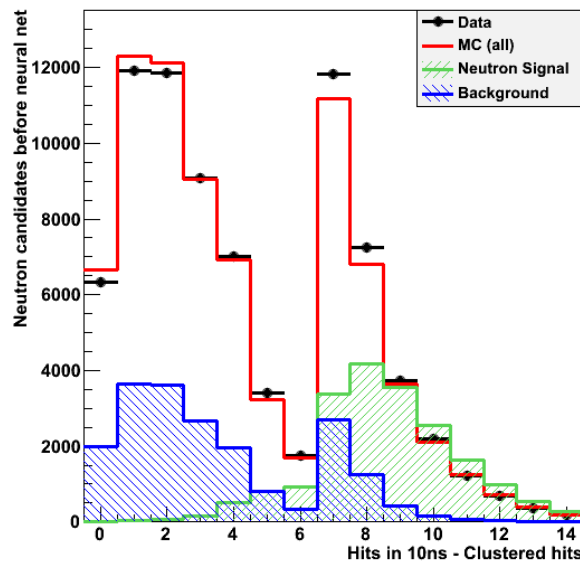


FIGURE 8.8: Clusters of hits variable, $N_{10} - N_c$. The plot shows a comparison of neutron capture signal (green), background (blue), data (black dots) and MC total (red line). The normalization is explained in section 8.2.2

8.2.2.3 Number of Hits on Low Probability PMTs: N_{low}

For a given neutrino event, most neutron captures occur < 200 cm from the neutrino interaction point (see figure 8.3). Therefore PMTs which are closer to the neutrino interaction vertex have a higher chance of being hit by the neutron capture γ -ray. In contrast, background events may originate from anywhere in the tank. There is very little spatial bias in the background towards the neutrino vertex, as after cutting $\delta t > 18\mu s$ most related particles have already decayed.

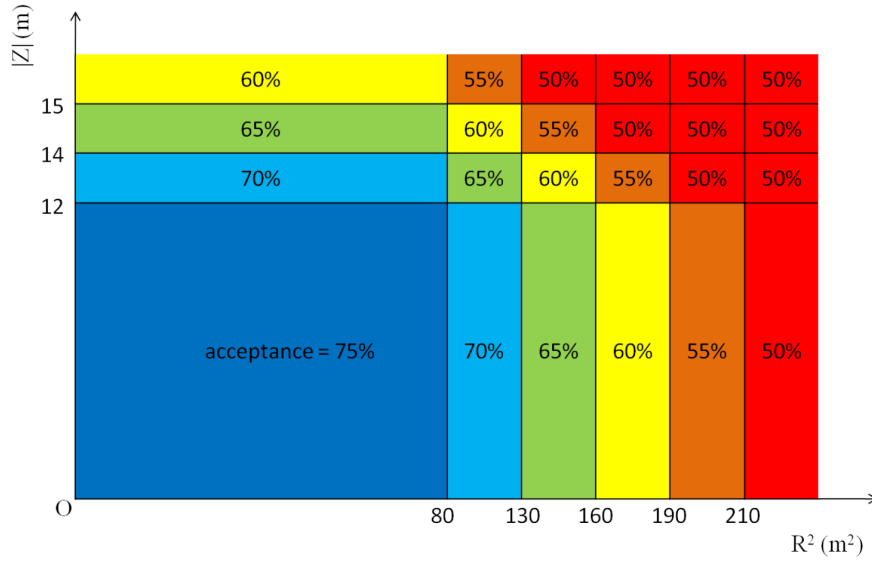


FIGURE 8.9: The varying acceptance requirements for the N_{low} cut, shown as a function of tank coordinates.

The probability to be hit (termed acceptance) for the i -th PMT is defined as

$$A_i \propto \frac{F(\theta_i)}{R_i^2} e^{R_i/L}, \quad (8.5)$$

where $F(\theta_i)$ is the PMT angular dependence for incident angle θ_i , R_i is the distance from the neutrino interaction vertex to PMT i , and L is the light attenuation length in water.

To calculate N_{low} , an area of high probability PMTs is defined for each neutrino event, which contains PMTs totalling $x\%$ of the acceptance for all PMTs. If a PMT hit occurs outside of this area, it is counted towards N_{low} . For neutrino events occurring near the wall this cut is very strict, as a very focused signal on a small number of PMTs. In contrast, for neutrino vertices near the tank centre, all PMTs are assigned a similar hit probability. To compensate for this bias, the total hit probability required, $x\%$, is altered throughout the tank, as shown in figure 8.9.

The variable input to the neural network is in fact $N_{10} - N_{low}$ (figure 8.10).

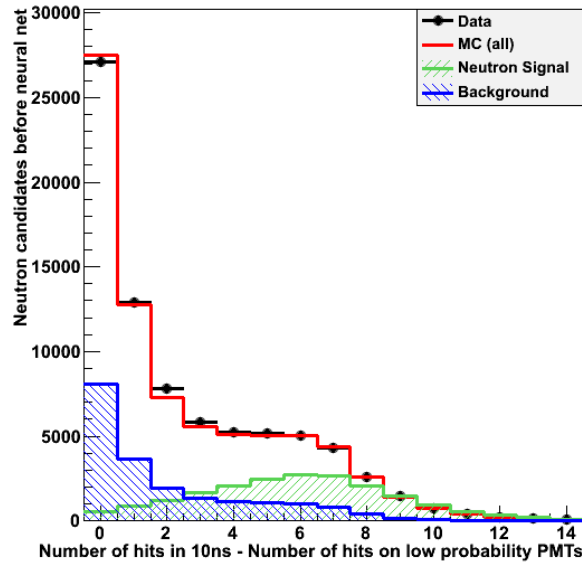


FIGURE 8.10: Hits on low probability PMTs, $N_{10} - N_{low}$. The plot shows a comparison of neutron capture signal (green), background (blue), data (black dots) and MC total (red line). The normalization is explained in section 8.2.2

8.2.2.4 Number of Hits in 300 ns: N_{300}

A true neutron capture event will have a sharp timing peak, almost all of which will be contained within a 10 ns window after ToF subtraction. Some background events (for example PMT flashing) may mimic a 2.2 MeV γ signal in 10 ns but in fact be part of a larger, more disperse signal (for an example see figure 8.11). N_{300} is sensitive to these types of background, and looks for broader scale timing peaks in the 300 ns surrounding a 2.2 MeV γ candidate. Again, to compensate for γ signals with large values of N_{10} , the value input to the neural network is $N_{300} - N_{10}$ (figure 8.12).

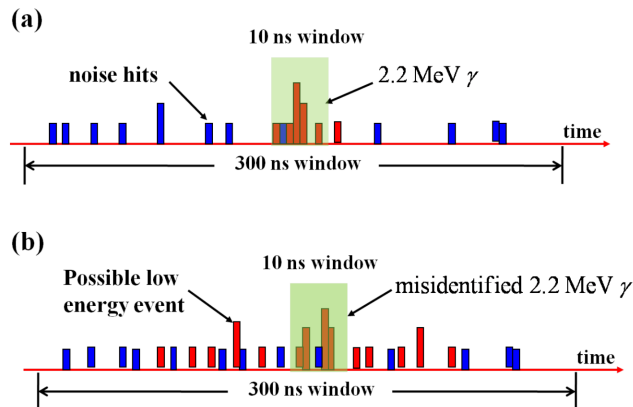


FIGURE 8.11: The utility of the N_{300} cut. Figure (a) shows a typical neutron capture event, and figure (b) shows a hypothetical background signal to be rejected. The blue lines correspond to PMT dark noise, and the red is some signal.

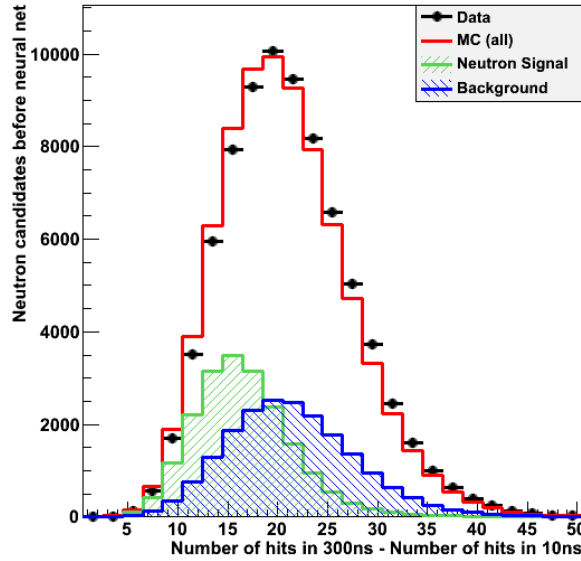


FIGURE 8.12: Number of hits in 300 ns, $N_{300} - N_{10}$. The plot shows a comparison of neutron capture signal (green), background (blue), data (black dots) and MC total (red line). The normalization is explained in section 8.2.2

8.2.2.5 Hit Vector RMS: ϕ_{rms}

The signal from a neutron capture event is a single 2.2 MeV γ -ray, which is expected to deposit most of its energy in a single direction. Some sources of background, such as PMT dark noise, are likely to have a more random hit pattern. ϕ_{rms} calculates the root-mean-square of the azimuthal angle (with respect to the average hit vector direction) of the hit vectors for each of the N_{10} candidate hits (figure 8.13). This information helps to effectively remove these types of random background.

8.2.2.6 Mean Opening angle: θ_{mean}

An angle θ_i is defined as the angle between the fitted direction (average of all hit vectors), and each individual PMT hit i that makes up the candidate event. Compared to a 2.2 MeV γ -ray, background events are more likely to have clustered hit patterns. θ_{mean} is the mean value of the opening angle θ_i (figure 8.14).

8.2.2.7 Root-mean-square of hit timing: t_{rms}

A distinguishing feature of the 2.2 MeV γ signal is its narrow hit timing distribution. The PMT timing resolution is ~ 3 ns [141], so even within a 10 ns window, it is possible

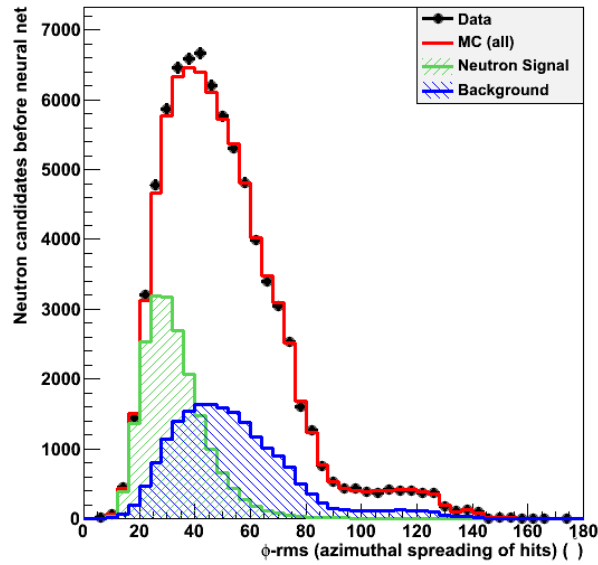


FIGURE 8.13: Root-mean-square of the azimuthal angle of 2.2 MeV candidate hit vectors ϕ_{rms} . The plot shows a comparison of neutron capture signal (green), background (blue), data (black dots) and MC total (red line). The normalization is explained in section 8.2.2

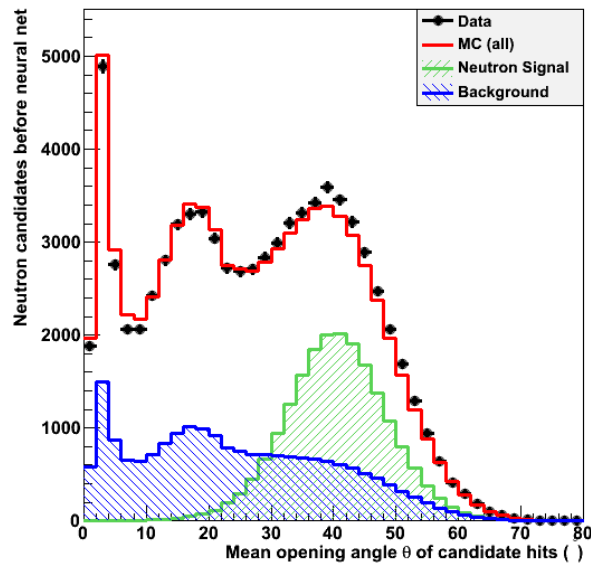


FIGURE 8.14: Mean value of hit opening angles, θ_{mean} . The plot shows a comparison of neutron capture signal (green), background (blue), data (black dots) and MC total (red line). The normalization is explained in section 8.2.2

to pick out particularly sharp concentrations of PMT hits. Variable t_{rms} is the root-mean-square of the timing of all N_{10} hits (figure 8.15).

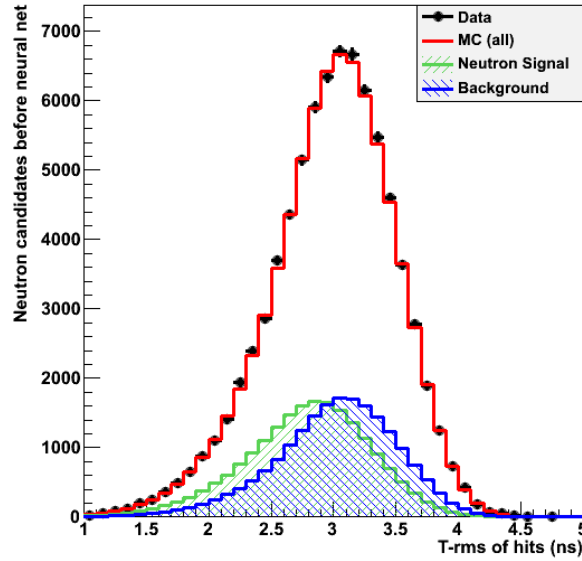


FIGURE 8.15: The root-mean-square of the timing of candidate hits, t_{rms} . The plot shows a comparison of neutron capture signal (green), background (blue), data (black dots) and MC total (red line). The normalization is explained 8.2.2

8.2.2.8 Minimum Root-mean-square of hit timing: $min - t_{rms}$

Ideally, for a 2.2 MeV γ event all of the hits in the 10 ns timing window will be due to the gamma-ray. However many candidates are selected which consist of only a few hits from the 2.2 MeV γ , and then the rest are contributed by dark noise or other backgrounds. To account for these events, $min - t_{rms}$ calculates the minimum value of t_{rms} when considering a cluster of x hits out of the total N_{10} . All possible combinations of x hits are considered, to find the tightest cluster. A depiction of this method is shown in figure 8.16. Two variables are constructed, for $x = 3$ and $x = 6$, and used as neural network inputs (figure 8.17).

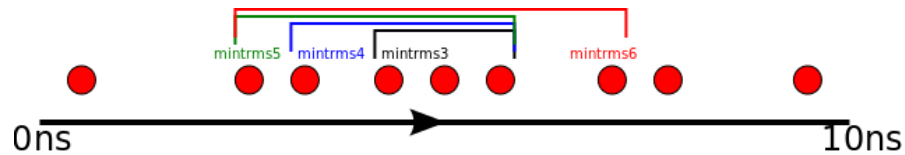


FIGURE 8.16: The selection of $min - t_{rms}$ hit clusters. Optimal selections for clusters of 3-6 hits are shown, for an example candidate where $N_{10} = 9$. Possible background hits on the fringes of the candidate time are ignored.

8.2.2.9 Bonsai Fit Variables: BS_{energy} and BS_{wall}

The Bonsai fit is an unbiased low energy fitter described in chapter 6. For each 2.2 MeV γ candidate, Bonsai fit is performed on the surrounding $1.3\mu s$ of data. BS_{wall} gives

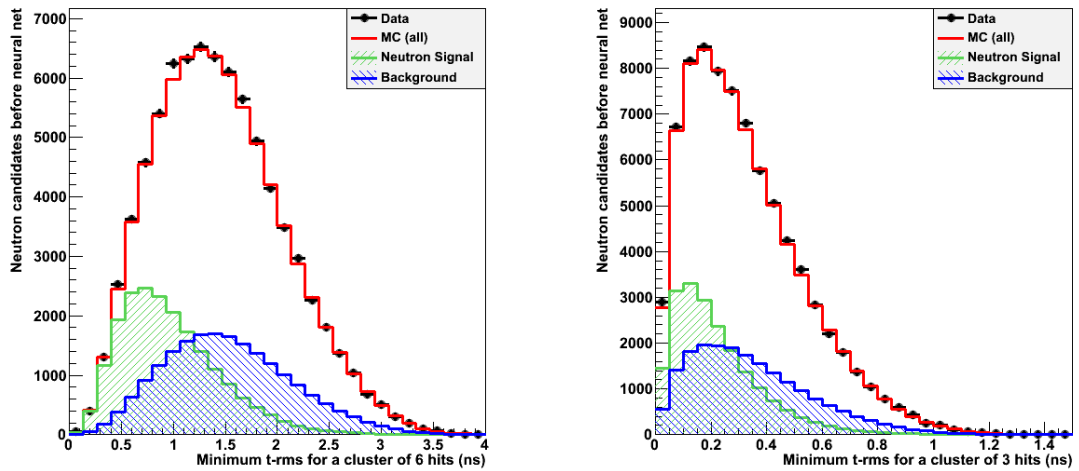


FIGURE 8.17: $\min - t_{rms}$ of clusters of 6 hits (left) and 3 hits (right). The plot shows a comparison of neutron capture signal (green), background (blue), data (black dots) and MC total (red line) comparison. The normalization is explained 8.2.2

the distance from the reconstructed Bonsai vertex to the nearest ID tank wall. Many background sources originate from the walls of the tank, such as those from radioactive decay in the detector material, and these events can be removed by the BS_{wall} variable (figure 8.18). BS_{energy} is the reconstructed energy of the candidate event. Since the 2.2 MeV γ -ray is mono-energetic, so its energy distribution is expected to peak more sharply at 2.2 MeV (figure 8.18).

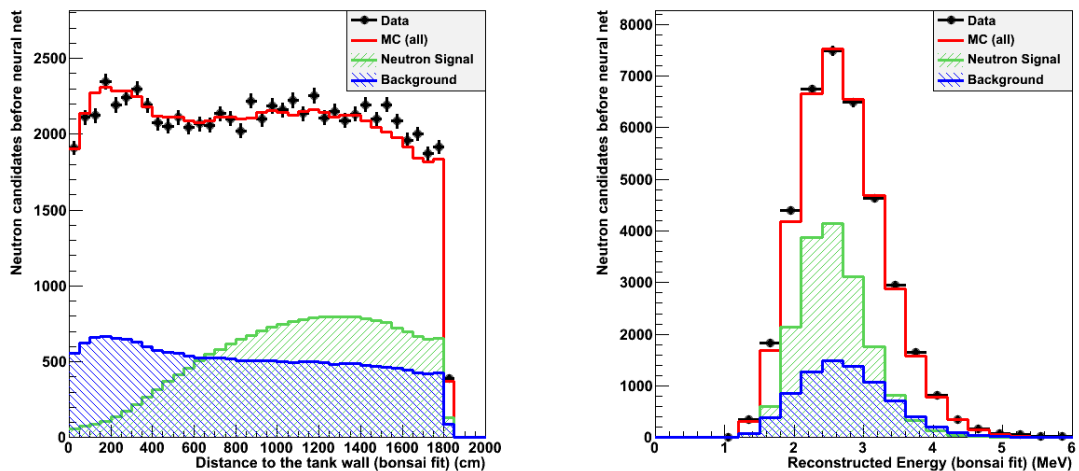


FIGURE 8.18: Distributions of BS_{wall} and BS_{energy} for 2.2 MeV γ candidate events. The normalization of BS_{energy} is different for signal and background, as many background events fail to reconstruct at this stage. The plots show a comparison of neutron capture signal (green), background (blue), data (black dots) and MC total (red line).

The normalization is explained in section 8.2.2

8.2.2.10 Neut-Fit Variables: NF_{wall} , ΔN_{10} , Δt_{rms}

These variables relate to Neut-Fit, as described in chapter 6. Neut-Fit acts only on the N_{10} hits already selected by ToF-subtraction to the APFit vertex, so it has substantial bias towards this point. NF_{wall} is the distance between the Neut-Fit vertex and the nearest tank wall. As Neut-Fit is biased towards the APFit vertex, and the atmospheric neutrino FC reduction requires that the APFit vertex be $> 200cm$ from the tank wall, Neut-Fit is unlikely to reconstruct any true neutron events in this region (figure 8.19).

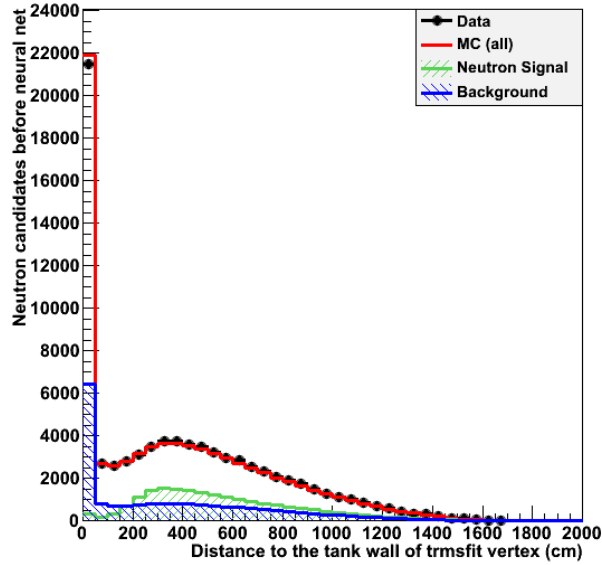


FIGURE 8.19: The distance to the wall from Neut-Fit vertex, NF_{wall} . The plot shows a comparison of neutron capture signal (green), background (blue), data (black dots) and MC total (red line). The normalization is explained in section 8.2.2

Neut-Fit functions by searching for the point in the SK tank with the minimum value of t_{rms} for all the hits. For neutron capture signal events, an optimal neutron capture vertex is expected to be found with a small value of t_{rms} . Many background events do not come from a single source (like PMT dark noise), or may come from a source where the vertex reconstruction is outside the inner detector so the improvement of t_{rms} will be less for these backgrounds than for a true neutron capture signal. Thus Δt_{rms} examines the difference between t_{rms} as calculated with the APFit vertex, and t_{rms} when calculated using the Neut-Fit vertex (figure 8.20).

The final Neut-Fit related variable is ΔN_{10} . For 2.2 MeV γ candidates, $\sim 90\%$ of PMT hits are recorded inside 10 ns, but due to the imperfect reconstruction of the APFit vertex, some hits may be spread outside this window. Using the Neut-Fit vertex, ToF subtraction is performed again on 40 ns of hits surrounding the gamma candidate, and a new value of N_{10} is calculated. If the candidate is a true 2.2 MeV γ , some of these

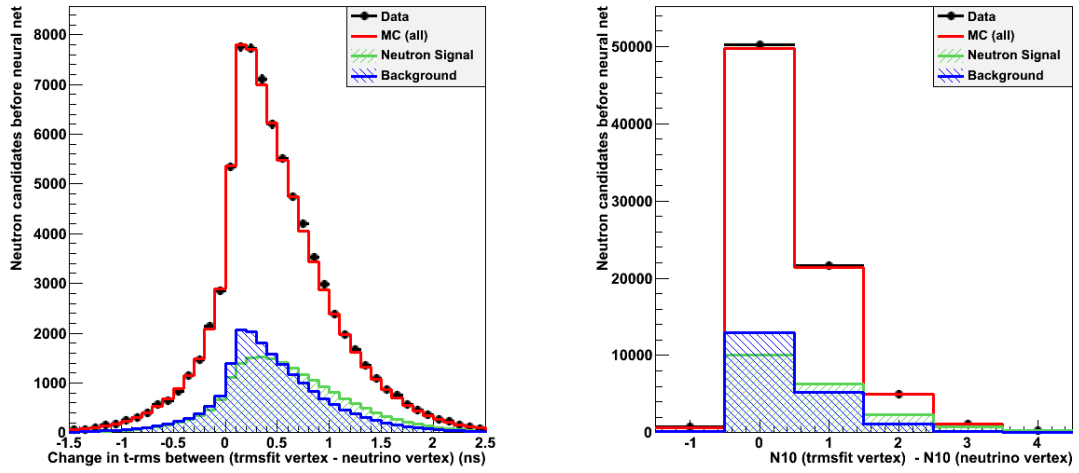


FIGURE 8.20: The variables Δt_{rms} and ΔN_{10} are shown in the left and right figures, respectively. The plots show a comparison of neutron capture signal (green), background (blue), data (black dots) and MC total (red line). The normalization is explained in section 8.2.2

outside hits may be brought into the 10 ns window. The variable ΔN_{10} is the difference in N_{10} when calculated using APFit vertex, and Neut-Fit vertex.

8.2.2.11 Fit Agreement variables: $(NF - BS)_{dis}$, $(NF - AP)_{dis}$

The final two variables are the distance between the vertex reconstructions of the different neutron fitters. $(NF - AP)_{dis}$ gives the distance between the Neut-Fit, and the APFit vertex. This is a powerful variable, as we know that neutrons do not travel far (see figure 8.3) from the neutrino interaction point before capture. Thus when Neut-Fit reconstructs close to the APFit vertex, the candidate is more likely to be a true 2.2 MeV γ (figure 8.21).

The distance between Bonsai fit and Neut-Fit, $(NF - BS)_{dis}$ is also used. Bonsai decides the vertex based on all hits within $1.3\mu s$ of the candidate event, however Neut-Fit uses only 10 ns surrounding the candidate. Thus, if the reconstructions are very different, it suggests that the candidate is a part some larger scale background spread out over $1.3\mu s$ that Neut-Fit is not sensitive to (figure 8.21).

8.2.3 Neural Network

Neural networks are a machine-learning based tool, primarily used for pattern recognition in fields such as stock market prediction, image analysis, remote sensing, as well

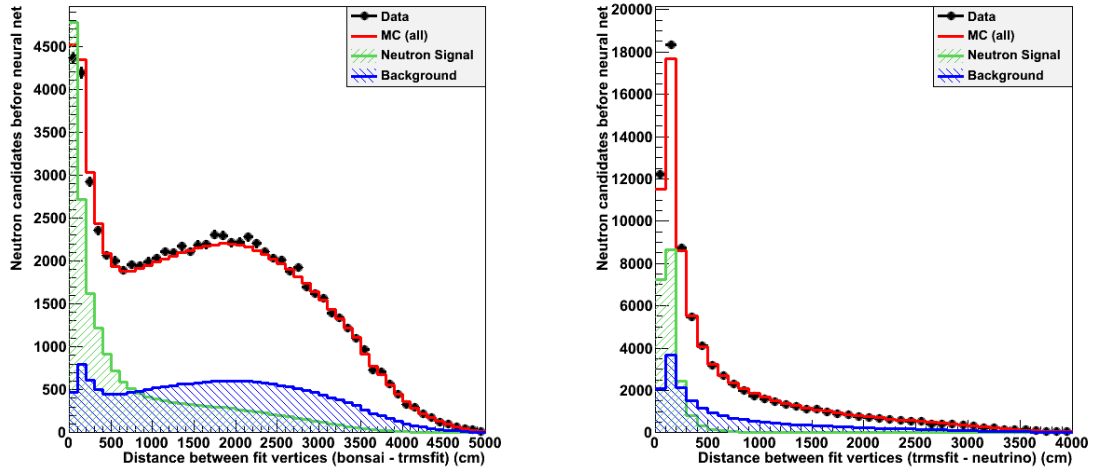


FIGURE 8.21: The variables $(NF - BS)_{dis}$ (distance between Bonsai reconstructed candidate vertex, and Neut-Fit reconstructed candidate vertex) and $(NF - AP)_{dis}$ (distance between Neut-Fit reconstructed candidate vertex, and APFit vertex), are shown in the left and right figures, respectively. The plots show a comparison of neutron capture signal (green), background (blue), data (black dots) and MC total (red line).

The normalization is explained in section 8.2.2

as signal-background classifications in particle physics. Here a feed-forward Multi-Layer Perceptron is used based on the ROOT class TMLP. The network was trained using 500 years of Atmospheric Neutrino MC, which comprised of 1,721,004 true 2.2 MeV candidates, and 15,578,057 background candidates after the initial selection process. This sample was split into a training sample and a testing sample to avoid overtraining of the network. The network was trained using the Broyden, Fletcher, Goldfarb, Shanno (BFGS) method [142], for 1000 iterations over the training data.

Deciding the structure and number of nodes in a neural network is a difficult problem, typically only solved experimentally [143]. The node pattern is chosen as 16:14:7:1, where 16 represents the number of input nodes, 14 and 7 are the number of nodes in two hidden layers, and 1 is the output node: 2.2 MeV γ signal or background. A single hidden-layer network was tested using a proposed optimal number of nodes $\log T$ where T is the number of events in the training sample [144]. For this analysis, the architecture becomes 16:17:1. This was found to give inferior performance (-11% efficiency), so a 2 hidden-layer network is deemed necessary for this analysis. Three configurations of networks with 2 hidden-layer networks were tested - 16:8:4:1 and 16:17:16:1, in addition to the aforementioned 16:14:7:1.

A summary of the results from these is shown in table 8.1. Methods are evaluated by their efficiency relative to the 16:14:7:1 architecture. The output of the networks is cut automatically to retain a signal efficiency (%) to background per neutrino event ratio

Network Architecture	Relative Efficiency	Training time
16:14:7:1	n/a	10 days
16:17:16:1	+0.3%	13 days
16:8:4:1	-3.7%	8 days
16:17:1	-14.8%	1 day

TABLE 8.1: The differences in neutron tagging efficiency, and training time, for each neural network layout that was tested. The efficiencies shown are relative to the result given by the 16:14:7:1 architecture.

of 14:1. The 16:14:7:1 architecture appears to be close to the optimal solution, and was chosen for this analysis. For this network structure, the neural network cut position is determined to be at 0.832, as shown in figure 8.22. This cut position is chosen to achieve $\text{tagging efficiency}/\text{background per event} = 14$.

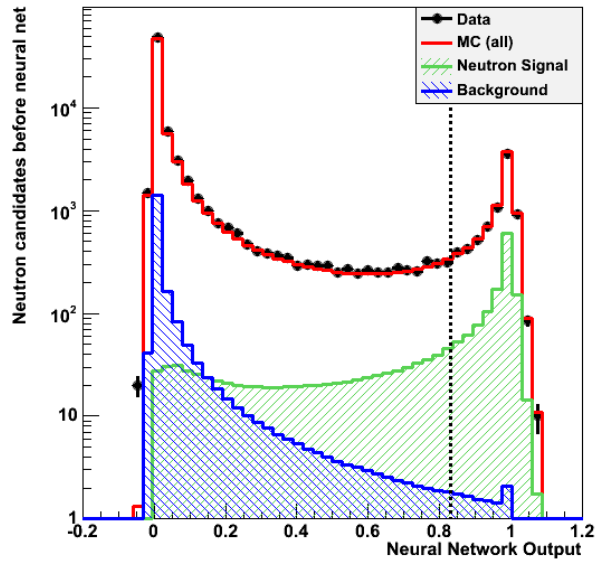


FIGURE 8.22: The neural network output for selecting final neutron candidates. Everything to the right of the dotted cut line is selected as a neutron capture event. The small peak in the background histogram at NN output ~ 1 is due to events where the secondary particle bank is overfilled. For these events some true neutron capture information is not stored, and some candidates are mis-classified as background. The data-MC discrepancy in the far left bin looks drastic on a log-scale plot, but this represents $< 0.1\%$ of total background events. The plot shows a comparison of neutron capture signal (green), background (blue), data (black dots) and MC total (red line).

The normalization is explained in section 8.2.2

8.2.4 Results

The efficiency of 2.2 MeV γ -ray selection is defined to be

$$\frac{\text{Candidates selected which are true neutrons (see 8.1)}}{\text{All true neutron captures}}. \quad (8.6)$$

The background is defined by

$$\frac{\text{Candidates selected which are background events (see 8.1)}}{\text{Total Neutrino Events}}. \quad (8.7)$$

Events where the secondary particle storage banks are filled are discarded in this calculation, as some true neutron information may be missed. The calculated efficiency and accidental background values are shown in table 8.2.

Selection stage	Efficiency	Background / Event
Initial Selection	33.2%	4.45
After Neural Net	20.5%	0.018

TABLE 8.2: Final efficiency and background rate of the neutron tag algorithm, after each stage of selection

If we consider only neutron captures which fall within the selected timing range, $18 \rightarrow 535\mu s$, the efficiency becomes 24.6%. Compensating for increasing PMT gain, the background changes from 1.77% \rightarrow 1.84%. The efficiency is heavily dependent on the distance travelled from the neutrino interaction by the neutron (see figure 8.23). For high energy neutrino events, the average multiplicity of neutrons increases, which results in many low energy neutrons that do not travel very far. Therefore, the average efficiency does not change much (figure 8.23).

The efficiency is also dependent on the position of the neutron in the tank. γ -rays from neutron capture close to the centre of the tank are attenuated more before reaching the PMTs on the tank wall so the detection efficiency is reduced in this region. For capture events very close to the wall the acceptance of the PMTs is reduced, resulting in lower efficiency. The 2-dimensional efficiency profile can be seen in figure 8.24.

8.3 Atmospheric Neutrinos

Neutron tagging was applied to the SK-IV atmospheric neutrino fully-contained sample, as selected by the FC reduction process described in chapter 7, and the atmospheric neutrino MC from chapter 5 (with neutron modifications mentioned in section 8.1). The MC was normalized to the livetime of the data, 1775.6 days. The MC is oscillated using a 2-flavour oscillation approximation with $\Delta m^2 = 2.5 \times 10^{-3} \text{eV}^2$ and $\sin^2 2\theta = 1.0$. At

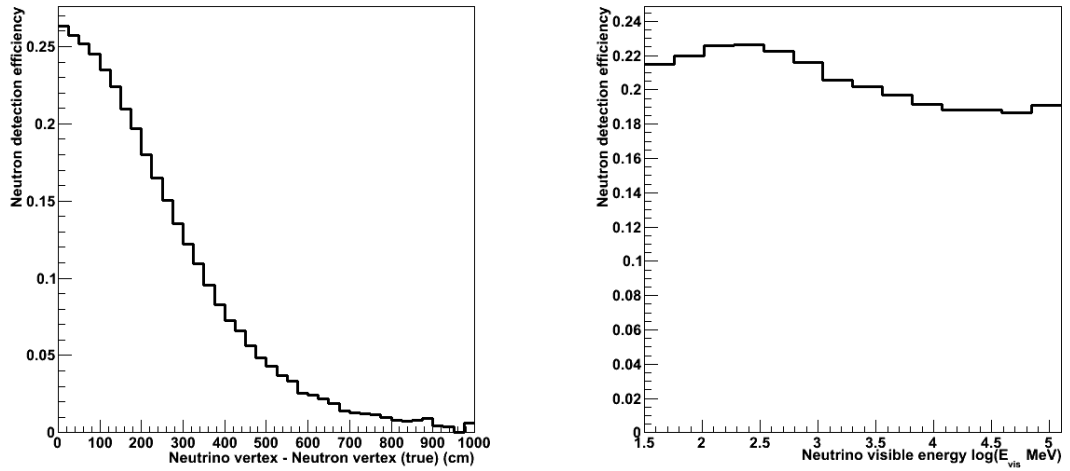


FIGURE 8.23: The dependence of 2.2 MeV detection efficiency on the distance travelled by the neutron (left), and the visible energy from the neutrino interaction (right). Efficiency is defined as the number of selected candidates corresponding to true neutrons, per number of true neutron capture events in each bin.

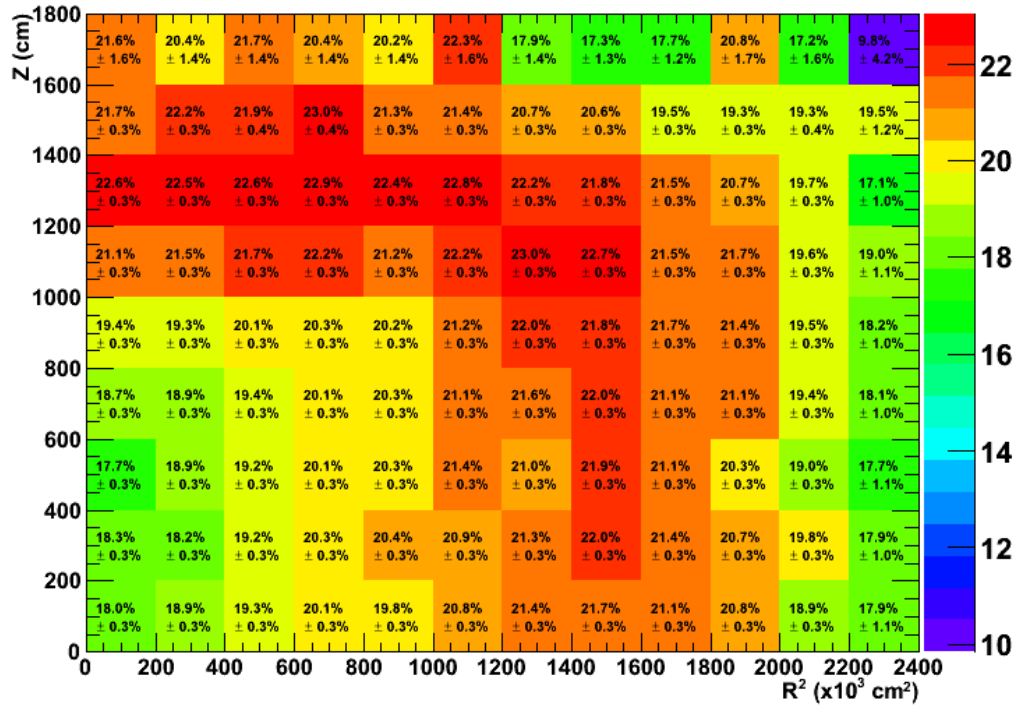


FIGURE 8.24: The efficiency of detecting neutrons as a function of neutrino (APFit) vertex position throughout the ID. Only neutrino events passing the fiducial volume cut ($dWall > 200$ cm) are considered.

energies $E_\nu > 30$ GeV, significant data-MC discrepancy is present, however this energy range comprises a relatively small number of events and has little effect on the neutrino

oscillation analysis in chapter 9. A summary of the data-MC agreement can be seen in table 8.3.

Sample	SK-IV Data (1775.6 days)	MC
Total Neutrons	8125	8589.9
Events with any neutrons	4511	4391.8
Events with only one neutron	2900	2721.0

TABLE 8.3: A comparison of the expected and measured neutron capture events in the atmospheric neutrino SK-IV data-set (1775.6 days). Most of the data-MC discrepancy is from very high energy (>30 GeV events). The MC is normalized by data livetime, and oscillated under a 2 flavour approximation: $\Delta m^2 = 2.5 \times 10^{-3}$ and $\sin^2 2\theta = 1.0$.

The neutron lifetime is fit to $205.2 \pm 3.7 \mu\text{s}$, as shown in figure 8.25. This agrees with a previous measurement of $204.8 \mu\text{s}$ [139]. The total number of events with neutrons, the average multiplicity, and the neutron multiplicity split into Sub-GeV and Multi-GeV samples can be seen in figure 8.26.

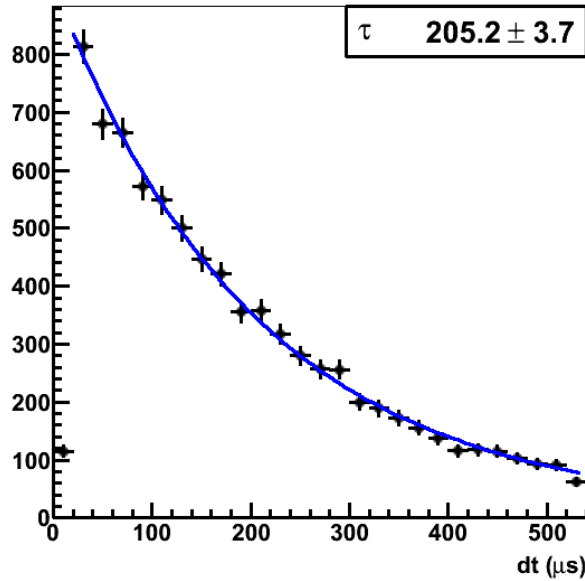


FIGURE 8.25: Final selected 2.2 MeV gamma candidates timing distribution. The primary trigger is at $t = 0$. Blue curve is a best exponential fit using chi-squared method. The neutron capture lifetime is calculated to be $205.2 \pm 3.7 \mu\text{s}$. The background rate is set to $0.0184 / \text{neutrino event}$. Data is taken from all of SK-IV (1775.6 days)

8.4 Americium-Beryllium Systematic Error Study

To study the efficiency of neutron tagging, an Americium-Beryllium (Am-Be) source is used. This study was first performed in SK-III [140], and then again at the start of SK-IV to take advantage of the upgraded electronics.

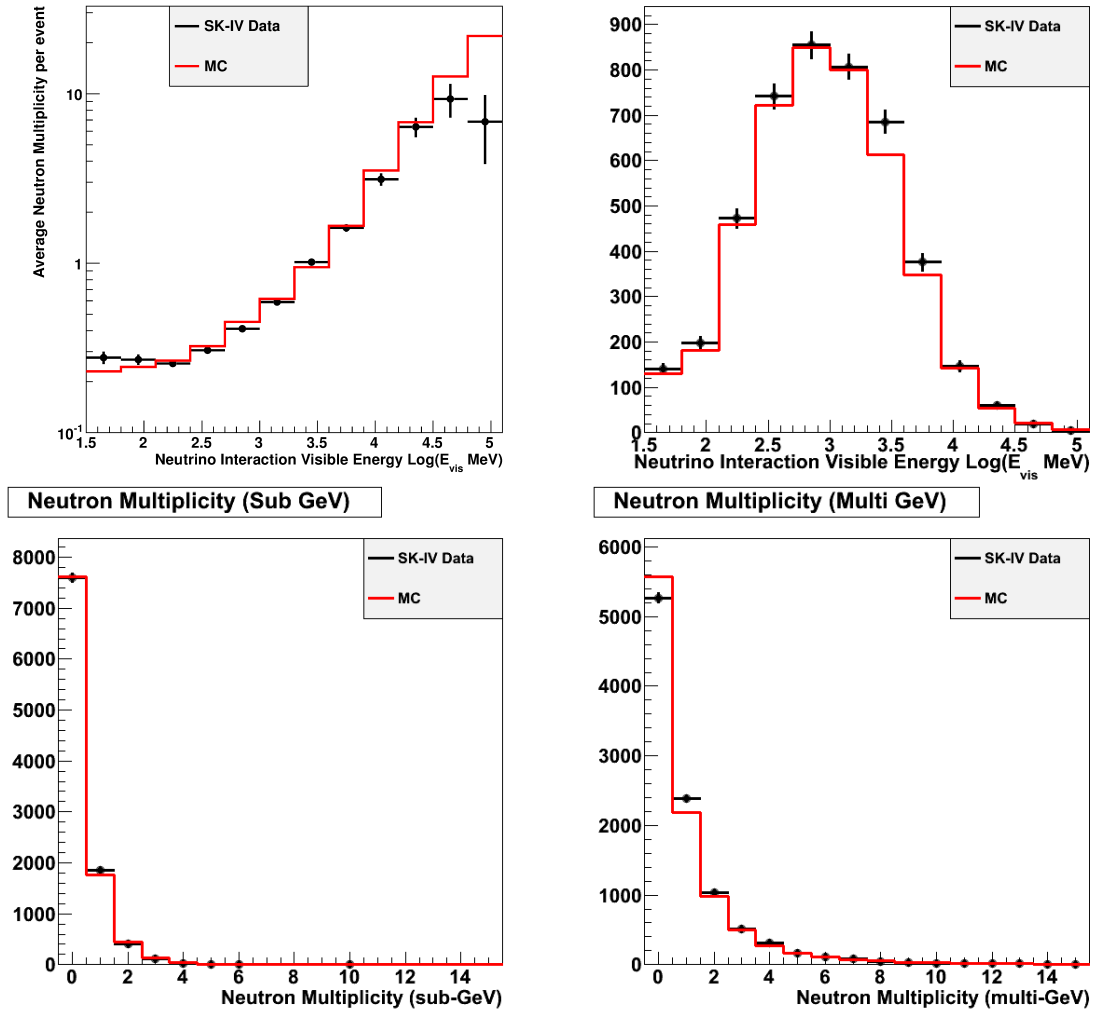
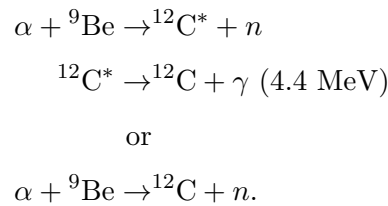


FIGURE 8.26: These plots show data-MC comparisons for neutrons tagged in the SK-IV 1775.6 days dataset. The top left plot shows the average multiplicity of neutrons, the top right plot shows the number of neutrino events with ≥ 1 neutrons, the bottom left plot shows the neutron multiplicity in Sub-GeV events ($E_{vis} < 1330$ MeV), and the bottom right plot shows neutron multiplicity in Multi-GeV events ($E_{vis} \geq 1330$ MeV). The multiplicity plots are normalized to the number of neutrino events. The number of events plot (top right) is normalized to data livetime and oscillated under a 2 flavour approximation: $\Delta m^2 = 2.5 \times 10^{-3}$ and $\sin^2 2\theta = 1.0$.

The ^{241}Am nucleus emits α -particles, which then interact with ^9Be , and produce a neutron in the following fashion:



The ^{241}Am source intensity for this experiment is $97\ \mu\text{Ci}$, which corresponds to 87 Hz of 4.4 MeV γ -ray emission interaction, and 76 Hz of the direct transition to ground-state. The 4.4 MeV γ -ray is used to trigger the detector, and then subsequent neutron capture signals are searched for. The ground-state transition produces an irreducible constant background of neutrons, since there is no way for it to produce a primary trigger in the detector.

8.4.1 Experimental Setup

The Am-Be source is embedded in a 5 cm cube of BGO scintillator (see figure 8.27) to amplify the light released by the 4.4 MeV γ -ray, such that it will activate the SHE trigger in the detector. Upon triggering SHE stores $35\ \mu\text{s}$ of data, and then an extended AFT trigger is activated to store an additional $800\ \mu\text{s}$, and grant a more complete view the neutron capture time spectrum.

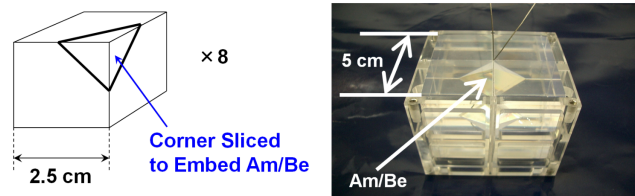


FIGURE 8.27: Am-Be crystal embedded in a 5 cm cube of BGO scintillator. This is held in an acrylic case.

This configuration was set up in 3 different locations around the tank: the centre (35.3, -70.7, 0) cm (Centre), near the side of the barrel (35.3, -1201.9, 0) cm (Y12), and near the top of the tank (35.3, -70.7, 1500.0) cm (Z15). Random data was also taken with the apparatus in the centre, using a 10Hz trigger, to study the irreducible background from the ground-state transition.

8.4.2 Data Selection

The primary selection criteria for 4.4 MeV γ -ray events is based on the number of photo-electrons (p-e) recorded in the ID. The exact criteria varies dependent on the source position, as follows:

$$\text{Centre: } 750 < \text{p-e} < 1050$$

$$\text{Y12: } 850 < \text{p-e} < 1150$$

$$\text{Z15: } 900 < \text{p-e} < 1150.$$

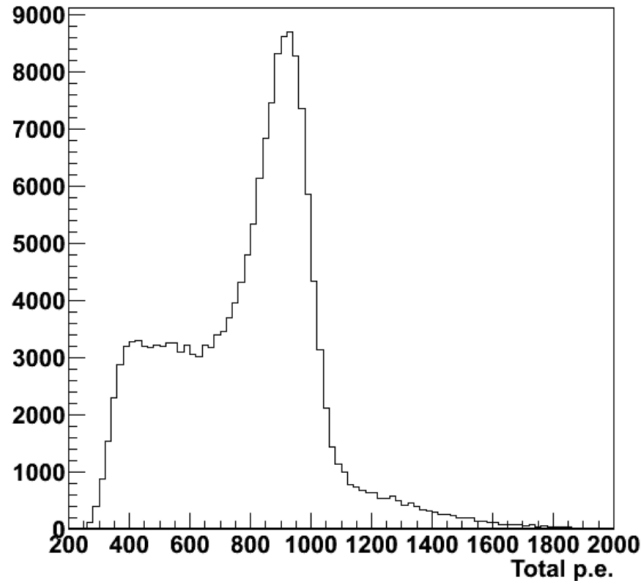


FIGURE 8.28: The total p-e from 4.4 MeV γ scintillation events, with the Am-Be source positioned at the centre of the tank. Events with $750 < \text{p-e} < 1050$ are selected.

After this two further cuts are made. First, to avoid neutron signal contamination from a previous scintillation event

- The time to the previous trigger must be > 1.5 ms,

Additionally, events where a second scintillation event has occurred shortly after the first must be rejected. A 200 ns sliding time window is used to search through the $835\mu\text{s}$ of data following a trigger. The maximum number of hits recorded by this window is saved as N_{200}^{max} . If

- $N_{200}^{max} < 50$

is not satisfied, the event is rejected.

8.4.3 Data Analysis

Neutron tagging is then performed on the remaining Am-Be dataset, and a 2.2 MeV γ -ray MC. There are some differences between this study and the atmospheric neutrino study discussed up until now. Neutrons released by Beryllium have an energy ranging from 2-10 MeV, much less than the average neutron energy following atmospheric neutrino interactions. Thus, we can make the assumption that the location of the Am-Be apparatus is roughly the same as the neutron capture vertex. This raises the expected neutron detection efficiency in accordance with figure 8.23. In addition,

the PMT after-pulse observed following high energy atmospheric neutrino events (figure 8.5) is not produced to the same extent after Am-Be events, so neutron searching is started at $5\mu\text{s}$ (previously $> 18\mu\text{s}$) after the primary trigger. The AFT trigger for Am-Be is also extended, allowing neutron-searching until $835\mu\text{s}$ after the initial trigger. The efficiency is calculated by fitting the timing distribution of neutron candidates to a constant background + exponentially decaying signal representing the neutron capture lifetime.

To predict the neutron tagging efficiency for the Am-Be study, a MC of pure 2.2 MeV γ interactions was created, with 50,000 events at each of the three Am-Be crystal locations. Only $2\mu\text{s}$ of data surrounding the gamma-ray is analysed, so the effect from mis-tagging is assumed to be negligible (< 3.4 mis-tagged events expected in 50,000 MC events). The true vertex of γ -ray production was used to perform ToF-subtraction in neutron tagging algorithm. The efficiency is calculated simply by counting the number of successfully identified 2.2 MeV γ -rays.

The fitted neutron lifetimes are $206.3 \pm 5.3\mu\text{s}$, $201.7 \pm 8.2\mu\text{s}$ and $207.7 \pm 9.5\mu\text{s}$ for the centre, Y12 and Z15 positions respectively (see figure 8.29). This is consistent with $204.8\mu\text{s}$ found in previous works [139].

The efficiency of neutron-tagging in Am-Be data compared to the 2.2 MeV γ -ray MC can be seen in table 8.4.

Sample	Am-Be Efficiency	MC Efficiency
Centre	$25.6 \pm 0.5\%$	$26.9 \pm 0.2\%$
Y12	$30.9 \pm 0.9\%$	$33.5 \pm 0.3\%$
Z15	$33.6 \pm 1.1\%$	$36.8 \pm 0.3\%$

TABLE 8.4: Estimated efficiency of neutron tagging, using Am-Be data, compared to the expectation from a 2.2 MeV γ -ray MC. The efficiencies here are higher than those quoted previously, as the neutron capture vertex is now known to $< 20\text{ cm}$.

The data-MC discrepancy here is larger than previous studies which were conducted with a combined cuts and likelihood tagging algorithm [145]. The reason for this may be that the presence of BGO scintillator is affecting the 2.2 MeV γ signal, and the more finely tuned multi-variate analysis techniques presented here are more sensitive to this difference.

The largest discrepancy, from the Z15 data is found to be 9.5%. Therefore 10% is taken as the systematic error on neutron-tagging efficiency in the following neutrino oscillation analysis.

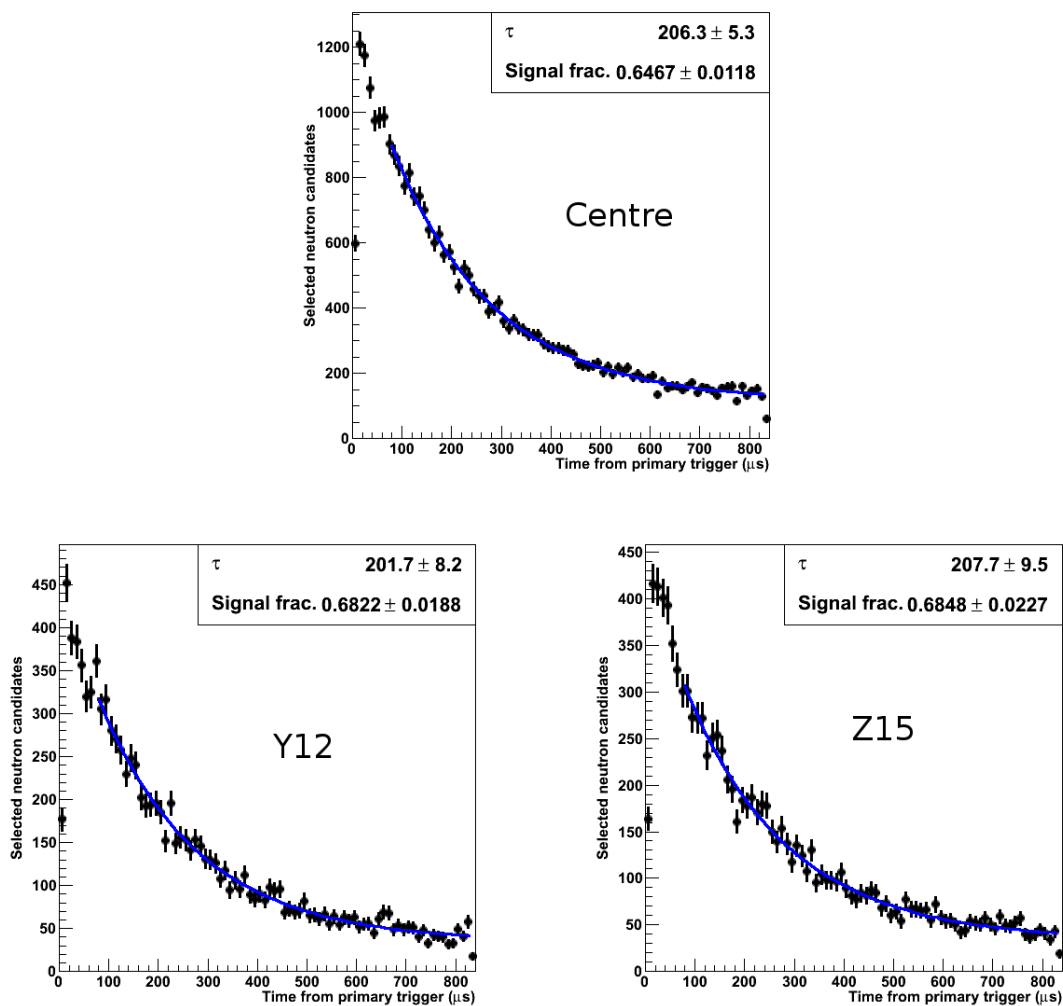


FIGURE 8.29: The timing distribution of tagged 2.2 MeV γ candidates, after triggering on a prompt 4.4 MeV γ ray from the Am-Be neutron source. The dots are data-points, and the blue line is a best fit to a constant background + exponential decay, where τ is the neutron capture lifetime in μs , and signal fraction is the fraction of all tagged events expected to be neutrons.

Chapter 9

Oscillation Analysis

Once the reduction, reconstruction, and neutron-tagging processes have been performed on the data-sets and corresponding MC for each of SK-I to SK-IV, neutrino oscillation analysis may begin. This analysis specifies a set of oscillation parameters for the MC, which is oscillated accordingly to calculate the expected number of events in each of 580 analysis bins. A goodness of fit is defined using a χ^2 method, to judge the agreement between the oscillated MC and data. The systematic errors are included in this calculation via a pull method. This χ^2 value is calculated over a parameter space of 37,638 different sets of oscillation parameters. The smallest value of χ^2 in this parameter space is defined as the best fit point. The whole parameter space is calculated twice - once assuming the normal hierarchy, and then assuming the inverted hierarchy (referring to the mass hierarchy of the neutrinos, as explained in chapter 2). The mass hierarchy preference is calculated by the difference in χ^2 at the best fit points for each of the hierarchies.

In this thesis only variation in atmospheric neutrino oscillation parameters is considered, across a linear parameter space of

$$\begin{aligned}\Delta m_{23}^2: 1.0 \times 10^{-3} \rightarrow 5.0 \times 10^{-3} \text{eV}^2 & \quad (41 \text{ points}) \\ \sin^2 \theta_{23}: 0.2 \rightarrow 0.7 & \quad (51 \text{ points}) \\ \delta CP: 0 \rightarrow 360^\circ & \quad (18 \text{ points})\end{aligned}$$

The remaining oscillation parameters are fixed by values set by other experiments: $\sin^2 \theta_{13} = 0.025$ [65], $\Delta m_{12}^2 = 7.5 \times 10^{-5} \text{eV}^2$, and $\sin^2 \theta_{12} = 0.31$ [146]. Their uncertainties are included as systematic errors.

This section will explain the calculation of χ^2 , the systematic errors used in the analysis, the updated analysis binning using neutron information, the sensitivity of the analysis to the neutrino mass hierarchy, and finally the analysis results.

9.1 Calculation of χ^2

The χ^2 value for each point in the oscillation parameter space is calculated using a Poisson likelihood function, given by:

$$L(N^{exp}, N^{obs}) = \prod_i^{nBins} \frac{e^{-N_i^{exp}} N_i^{exp N_i^{obs}}}{N_i^{obs}!}, \quad (9.1)$$

where N_i^{obs} and N_i^{exp} are the observed and expected events in the i -th bin, and $nBins$ is the total number of analysis bins. The χ^2 value is defined as the log likelihood ratio:

$$\chi^2 = -2 \ln \frac{L(N^{exp}, N^{obs})}{L(N^{obs}, N^{obs})} = 2 \sum_i^{nBins} \left(N_i^{exp} - N_i^{obs} + N_i^{obs} \ln \frac{N_i^{obs}}{N_i^{exp}} \right). \quad (9.2)$$

At this stage we must also take into account the systematic errors, which are included in each bin utilizing the ‘‘pull’’ method [147]. This involves allowing the expected value of each bin to vary depending on each independent error relevant to that bin:

$$N_i^{exp} \rightarrow N_i^{exp} \left(1 + \sum_j^{nErr} f_j^i \epsilon_j \right), \quad (9.3)$$

where $nErr$ is the total number of systematic errors, and f_j^i is the fractional change of the number of events in the i -th bin, due to a 1σ variation of the j -th systematic error, defined as:

$$f_j^i = \frac{(N_i^{exp})_{j(+\sigma)} - (N_i^{exp})_{j(-\sigma)}}{2(N_i^{exp})_{j(0)}}. \quad (9.4)$$

The values ϵ_j are fit parameters that are allowed to vary. At every point in the oscillation parameter space, a fit is performed to find the values of ϵ_j that give the minimum χ^2 at that point.

If the ϵ values are allowed to move freely, a near perfect fit could be achieved every time, so the range of epsilons must be constrained. This is done by adding a penalty term to

the χ^2 calculation, assuming gaussian systematic error:

$$\sum_j^{nErr} \left(\frac{\epsilon_j}{\sigma_j} \right)^2, \quad (9.5)$$

where σ_j is the estimated 1σ error size of the j -th systematic error. Thus, the final value of χ^2 to be minimized is given by:

$$\chi^2 = 2 \sum_i^{nBins} \left(N_i^{exp} \left(1 + \sum_j^{nErr} f_j^i \epsilon_j \right) - N_i^{obs} + N_i^{obs} \ln \frac{N_i^{obs}}{N_i^{exp} \left(1 + \sum_j^{nErr} f_j^i \epsilon_j \right)} \right) + \sum_j^{nErr} \left(\frac{\epsilon_j}{\sigma_j} \right)^2. \quad (9.6)$$

The minimum value of χ^2 is then obtained by requiring $\delta\chi^2/\delta\epsilon_j = 0$ for each of the $nErr$ errors.

9.2 Analysis Binning

Before the oscillation analysis is performed the data sample and MC are divided into bins to improve sensitivity to the oscillation parameters. First the data is separated into Upward-going muons (UPMU), Fully Contained (FC) and Partially Contained (PC) events, as selected by their respective reduction processes (these are all samples of neutrino events, as described in chapter 7).

Recall that oscillations are dependent on the fraction $\frac{L}{E}$, where E is the energy and L is the distance travelled of the neutrino. The reconstructed energy and zenith angle $\cos\theta$ (different value of $\cos\theta$ correspond to different neutrino path lengths through the Earth) are therefore used to bin each event.

The FC event sample undergoes additional separation. As ν_e and ν_μ are constructed from different fractions of neutrino mass states, the oscillation profiles of these flavours will be different. To best observe this, the FC sample is split up into μ -like and e -like, referring to the reconstructed identity of the most energetic ring. The events of interest to us in neutrino oscillation analysis are primarily CC (charge current) events, as NC interactions are insensitive to neutrino flavour. To select more pure CC samples, some of the samples are further split up into single-ring, and multi-ring samples; the former are more likely to be pure CC quasi-elastic interactions. The Multi-GeV Multi-Ring electron-like sample has a large contamination of NC events, so an additional likelihood to improve the sample's CC ν_e purity is applied. Events which fail this likelihood selection are placed

into the Multi-Ring Other category. For more details on this likelihood selection see [148].

In Sub-GeV interactions, additional cuts are made to remove single π^0 events, which comprise a significant neutral current background. The π^0 almost always decays to $\gamma\gamma$, each of which creates a Cherenkov ring pattern similar to an electron. Thus events with 2 e-like rings and no decay electron are labelled as π^0 -like. These events are often reconstructed as single-ring events, so an additional likelihood is constructed to select out these events. More details of this selection can be found in chapter 6 (POLFIT), and in [148]. A summary of the FC sub-GeV event sample selections is shown below, in table 9.1.

The final FC sample splitting, and focus of this thesis, is the separation of anti-neutrino and neutrino interactions in multi-GeV events. While event-by-event separation is not possible, statistically enriched samples can be produced. This is the region most sensitive to neutrino mass hierarchy, which causes an enhancement in upward going electron-neutrino, or electron-antineutrino event rate depending on whether it is normal or inverted. In this analysis improved separation is achieved using information from the neutron-tagging procedure, and a neural network method. Separation of μ -like events is also introduced, which may provide some sensitivity through a deficit in events corresponding to the ν_e excess. A summary of the FC Multi-GeV event samples (prior to ν - $\bar{\nu}$ selection), can be seen in table 9.2.

Sub-GeV				
Sample Name	Cherenkov Rings	Particle ID	Decay-electrons	Other Criteria
e-like 0 dcy	1	e-like	0	$p_e > 100$ MeV/c
e-like 1 dcy	1	e-like	≥ 1	$p_e > 100$ MeV/c
1-Ring π^0 -like	1	e-like	0	passes π^0 likelihood selection
2-Ring π^0 -like	2	e-like	0	$85 < \pi^0$ mass < 215 MeV
μ -like 0 dcy	1	μ -like	0	$p_\mu > 200$ MeV/c
μ -like 1 dcy	1	μ -like	1	$p_\mu > 200$ MeV/c
μ -like 2 dcy	1	μ -like	≥ 2	$p_\mu > 200$ MeV/c

TABLE 9.1: Summary for selection of Fully Contained Sub-GeV event samples

In tables 9.1 and 9.2, p_x refers to the momentum of the most energetic ring (MER), reconstructed assuming it was created by lepton x . Sub-GeV refers events with energy $E_{vis} < 1.33$ GeV, and events exceeding this energy are labelled as Multi-GeV.

Excluding the Multi-Ring Other sample, all of the Multi-GeV samples are further split into ν -like and $\bar{\nu}$ -like, using methods discussed in the following section.

Multi-GeV		
Sample Name	Cherenkov Rings	Other Criteria
e-like 1-Ring (M1E)	1, e-like	
e-like Multi-Ring (MME)	≥ 2 , MER e-like	Pass MultiRing likelihood
Multi-Ring Other	≥ 2 , MER e-like	Fail MultiRing likelihood
μ -like 1-Ring (M1M)	1, μ -like	
μ -like Multi-Ring (MMM)	≥ 2 , MER μ -like	If $p_\mu > 600$ MeV/c $E_{vis} < 1.33$ GeV is allowed

TABLE 9.2: Summary for selection of Fully Contained Multi-GeV event samples

The PC event sample is split up into two samples: PC stopping, which come to a halt within SK's outer detector, and PC-through-going, which pass through the OD and leave the tank. The PC-through events generally have a higher energy, but also more reconstruction uncertainty. Similarly the UPMU samples are categorized into stopping muons, which stop within the tank, and through-going non-showering, and showering events (referring to the production of an electro-magnetic shower). Again the energy of these events is progressively higher and more uncertain. The selection of the UPMU and PC samples is described in detail in chapter 7.

Thus, the entire data-set is split up into 21 sub-samples, for each of SK-I to SK-IV. Each of these sub-samples is split further into zenith and energy bins for the oscillation analysis. The bins in each SK period are then merged, after evaluating the systematic errors:

$$N_i^{obs} \rightarrow \sum_{skx}^4 N_{i,skx}^{obs}$$

$$N_i^{exp} (1 + \sum_j^{nErr} f_j^i \epsilon_j) \rightarrow \sum_{skx}^4 N_{i,skx}^{exp} (1 + \sum_j^{nErr} f_j^i \epsilon_j)$$

This results in a total of 580 analysis bins, of which 60 come from PC events, 50 from UPMU events, and 470 from FC events.

9.2.1 Neutrino and Anti-neutrino separation

Distinguishing between neutrino and anti-neutrino is a difficult task for pure water Cherenkov detectors. Applying a magnetic field and observing the lepton tracks curving in different directions depending on their charge is not viable here, as for consistent PMT operation very low magnetic fields are required. Even if we could apply a magnetic field, this would only help to distinguish μ^+ and μ^- tracks, as both e^+ and e^- quickly produce

an electromagnetic shower, which causes the same Cherenkov light pattern regardless of the initial particle charge.

Thus, we must look for other means of distinguishing ν and $\bar{\nu}$. This thesis focuses on using neutron tagging to achieve this goal. Charged current quasi-elastic interactions are represented as

$$\begin{aligned}\nu_l + n &\rightarrow l^- + p \\ \bar{\nu}_l + p &\rightarrow l^+ + n,\end{aligned}$$

where l is a lepton flavour. In high energy interactions, the protons can produce a small amount of Cherenkov light, but it is difficult to distinguish this from other low energy charged particles. As discussed in chapter 8, the delayed neutron-capture γ -ray allows us to observe 20.5% of all neutrons. Unfortunately, for mass hierarchy sensitivity we are interested mostly in $E_{vis} = 2$ -10 GeV events, where pure CCQE interactions are more rare. In addition, many neutrino interactions produce more than just a single neutron, either through secondary hadronic processes in the water, or multi-nucleon production within the interaction nucleus. Thus it cannot be said simply that neutron observation directly implies presence of an anti-neutrino. However neutrons still have significant discriminating power in the CCQE-enhanced single Cherenkov ring samples.

- More neutrons are produced following anti-neutrino interactions (figure 9.1).

Aside from neutrons, there are other clues we can use to determine the neutrino type. In high energy neutrino interactions, it is typical for many pions to be produced. We may write these interactions as:

$$\begin{aligned}\nu_l + n &\rightarrow l^- + N' + \text{pions} && (\text{total hadronic charge} = +1) \\ \nu_l + p &\rightarrow l^- + N' + \text{pions} && (\text{total hadronic charge} = +2) \\ \bar{\nu}_l + p &\rightarrow l^+ + N' + \text{pions} && (\text{total hadronic charge} = 0) \\ \bar{\nu}_l + n &\rightarrow l^+ + N' + \text{pions} && (\text{total hadronic charge} = -1).\end{aligned}$$

Thus we can expect an excess (deficit) in the number of charged hadrons, and in particular positively charged pions following a neutrino (anti-neutrino) interactions. These positively charged pions will decay to muons and produce decay electrons:

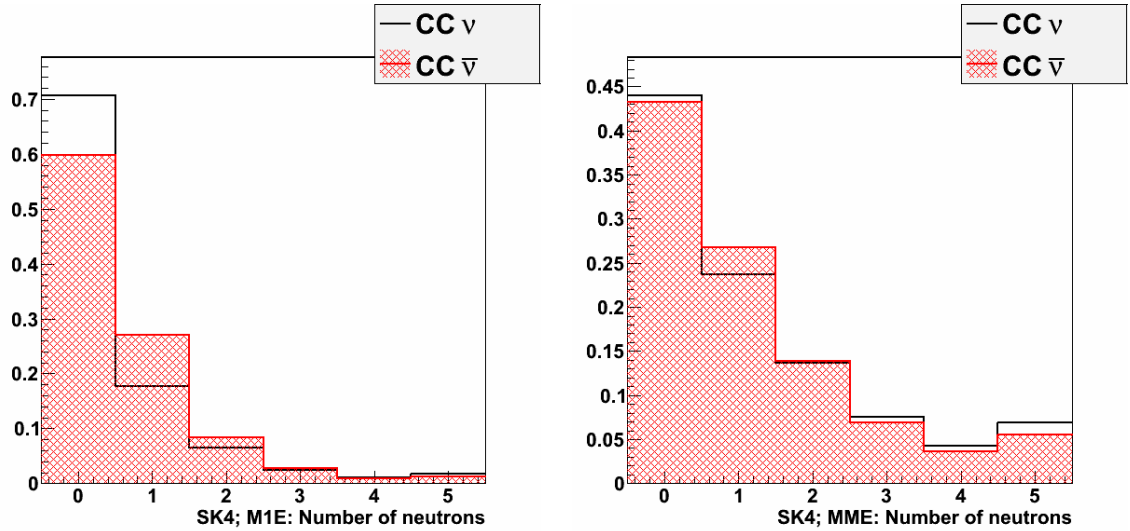
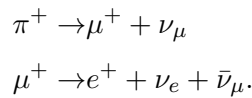


FIGURE 9.1: The multiplicity of neutrons following neutrino interactions in the Multi-GeV 1-ring electron-like sample (left) and Multi-GeV Multi-ring electron-like sample (right). The multi-ring sample consists of more deep inelastic scattering events, so neutrons are significantly less useful in this sample. However the excess in anti-neutrino 1-neutron events from CCQE interactions is still apparent. Only CC events corresponding to sample type are shown (i.e. for e-like samples, only CC ν_e and CC $\bar{\nu}_e$), and all histograms are normalized to 1. For use in analysis, any events producing >5 neutrons are added into the 5 neutron bin.



In water, most negatively charged pions will be absorbed, without producing a decay electron. Therefore a neutrino interaction will tend to produce more decay electrons than an anti-neutrino interaction. Any events containing > 5 decay-electrons are added into the 5 decay-electron bin.

- More (fewer) decay electrons are produced following CC ν ($\bar{\nu}$) interactions (figure 9.2).
- More (fewer) Cherenkov rings are observed following CC ν ($\bar{\nu}$) interactions (figure 9.3).

The additional hadrons produced in a neutrino interaction, also have the effect of spreading the interaction energy over a larger number of particles, so we may expect the primary lepton to be less energetic.

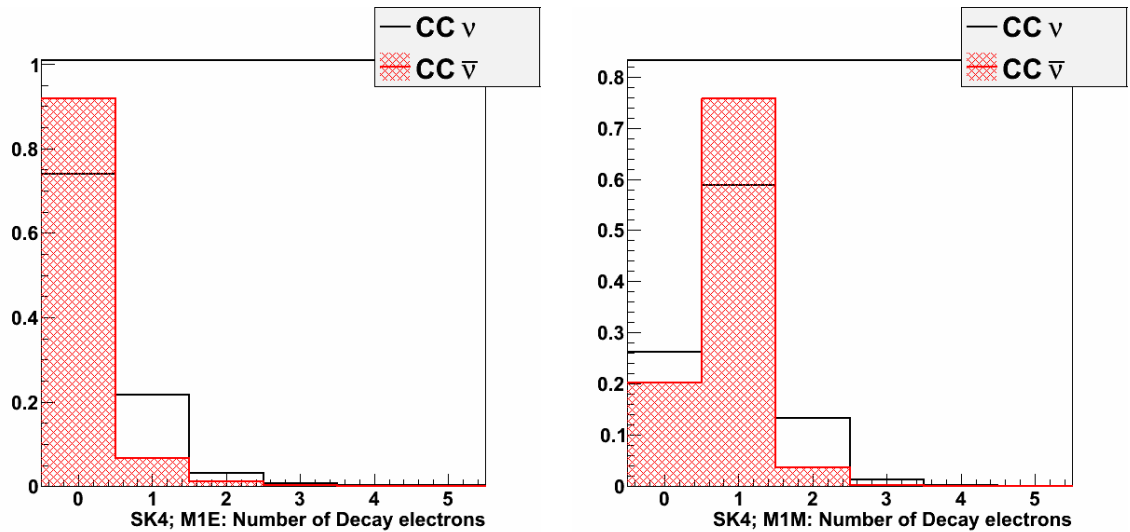


FIGURE 9.2: The number of decay electrons, following neutrino interactions in the MultiGeV 1-ring electron-like sample (left) and MultiGeV 1-ring muon-like sample (right). In the muon sample, many more decay-electrons are produced in general, however the excess in the neutrino sample is still apparent. Only CC events corresponding to sample type are shown (i.e. for e-like samples, only CC ν_e and CC $\bar{\nu}_e$), and all histograms are normalized to 1.

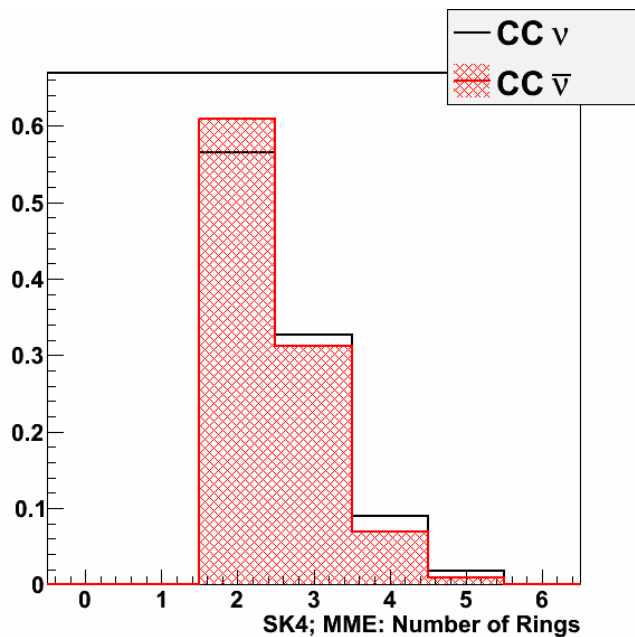


FIGURE 9.3: The number of Cherenkov rings, following neutrino interactions in the MultiGeV Multi-ring electron-like sample. There is some excess in the true CC ν sample, due to the additional charged hadrons produced in this interaction. Only CC events corresponding to sample type are shown (i.e. for e-like samples, only CC ν_e and CC $\bar{\nu}_e$), and all histograms are normalized to 1.

- In CC ν ($\bar{\nu}$) interactions the energy fraction of the most energetic Cherenkov ring will be smaller (larger) (figure 9.5).

- In CC ν ($\bar{\nu}$) interactions the farthest decay electron will be reconstructed closer to (farther from) the interaction vertex (“farthest” decay-electron means the reconstructed candidate vertex farthest from the reconstructed neutrino interaction point. This is chosen as it is most likely to correspond to the decay electron from primary lepton) (figure 9.4).

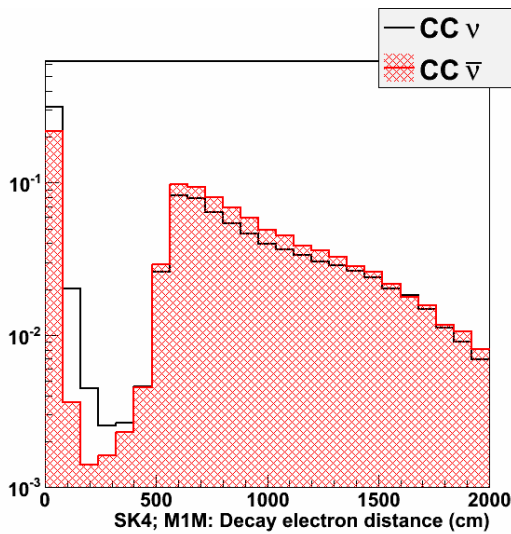


FIGURE 9.4: This plot shows the farthest decay-electron travel distance $|\text{neutrino vertex} - \text{decay electron vertex}|$, in the Multi-GeV 1-ring μ -like sample. Only CC events corresponding to sample type are shown (i.e. for e-like samples, only CC ν_e and CC $\bar{\nu}_e$). All histograms are normalized to 1.

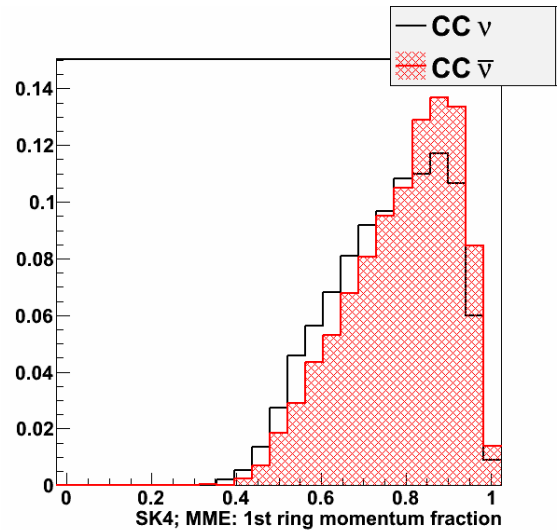


FIGURE 9.5: This plot depicts the fraction of reconstructed energy in the first ring divided by the total energy in the event for the Multi-GeV Multi-Ring e-like sample. Only CC events corresponding to sample type are shown (i.e. for e-like samples, only CC ν_e and CC $\bar{\nu}_e$) and all histograms are normalized to 1.

Charged pions and other hadrons are not always perfectly re-constructed into their own Cherenkov rings. Many times these particles will not produce enough Cherenkov light to be re-constructed, or their rings may overlap with the light pattern from the primary lepton, and be mis-reconstructed as a single ring. In these instances, the mis-fitted Cherenkov ring is more likely to deviate from the expected charge pattern of an electron or muon. Thus, for CC ν ($\bar{\nu}$) events, the particle identification algorithm may identify these events as “less (more) e-like” or “less (more) μ -like”.

- In CC ν ($\bar{\nu}$) interactions, the particle identification of the most energetic ring is “less (more) e-like” or “less (more) μ -like” (figure 9.6).

There is one final discriminating variable, which can only be applied to muon-neutrino events. We know that μ^- may be captured by an oxygen nucleus whereas μ^+ may not.

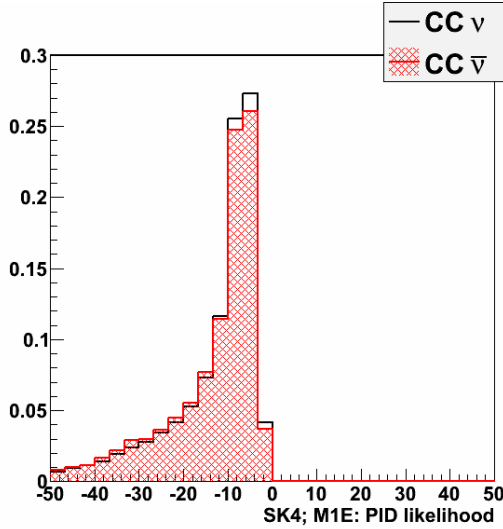


FIGURE 9.6: The particle identification likelihood output, for the Multi-GeV 1-ring e-like sample. $\text{PID} < 0$ is required to classify the ring as e-like. Only CC events corresponding to sample type are shown (i.e. for e-like samples, only CC ν_e and CC $\bar{\nu}_e$), and all histograms are normalized to 1.

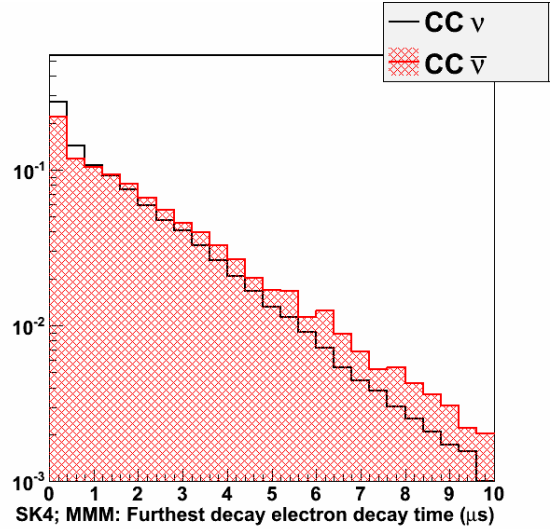


FIGURE 9.7: The decay time of the decay-electron reconstructed farthest from the neutrino interaction, for the Multi-GeV Multi-Ring μ -like sample. Only CC events corresponding to sample type are shown (i.e. for e-like samples, only CC ν_e and CC $\bar{\nu}_e$), and all histograms are normalized to 1.

This is due to its negative charge allowing it to orbit very close to the nucleus, similar to an electron. Hence the effective decay time for the μ^- events is reduced.

- After CC ν_μ interactions, the time between the neutrino interaction, and detection of the farthest decay electron will be shorter relative to a CC $\bar{\nu}_\mu$ -produced decay electron (figure 9.7).

9.2.2 Multi-Variate Analysis

Multi-variate analysis is then performed using these variables to separate each sample into ν -like and $\bar{\nu}$ -like. Different sets of variables are applicable to different samples, so they are described individually here. Neutron tagging is only available in SK-IV, so is not used in the analysis of SK-I to III. The improved trigger logic of SK-IV also increases our decay electron tagging efficiency, so generally the ν - $\bar{\nu}$ separation is better in this period.

Most of the neutrino type sensitivity in the Multi-GeV 1-ring electron-like sample comes from decay-electron and neutron counting, which are both discrete variables, so a simple cut-based analysis was used in this case. The MultiRing e-like sample, and the μ -like samples are separated via a neural network. This is implemented using ROOT's

TMVA (Multi-Variate Analysis) framework, trained using the BFGS method (ROOT option MLPBNN)[149]. One hidden layer of size $N + 5$ for each network was used, where N is the number of input variables. Separate networks were trained for each SK generation. Alternate multi-variate analysis tools were also considered: a likelihood method, which was found to have worse performance, and a boosted decision tree, which had slightly increased performance, but significant over-training (that is, significantly better performance was found using the training sample than the testing sample).

The cut position on the neural network output is determined automatically in each case to maximize the value

$$\text{efficiency}_{\nu\text{-like}} \times \text{purity}_{\nu\text{-like}} \times \text{efficiency}_{\bar{\nu}\text{-like}} \times \text{purity}_{\bar{\nu}\text{-like}}. \quad (9.7)$$

Efficiency is the number of neutrinos (anti-neutrinos) in the ν ($\bar{\nu}$)-like sample, divided by the total number of neutrinos (anti-neutrinos) in both samples. Purity is the fraction of the the ν ($\bar{\nu}$)-like sample which comprises of ν ($\bar{\nu}$) events.

Determining the optimal cut position in regards to mass hierarchy sensitivity for these separations is an interesting problem. It is unclear whether two equally sized samples, or a small but pure sample and a large impure sample is ideal. If using a small and pure sample is optimal, then we must consider how small it can be made before the reduction in hierarchy sensitivity from lower statistics outweighs the improvement from increased purity. Of course, the optimal way to determine cut position would be to re-calculate mass hierarchy sensitivity for every possible cut position. However this method was not used here as the required computing power was prohibitive.

9.2.2.1 Multi-GeV, Single-Ring, e-like sample

The Multi-GeV Single-Ring e-like sample is split using a cut on two variables: decay-electron number, and neutron multiplicity. Neutron multiplicity is only used in SK-IV. An event is selected as ν -like, if it satisfies the following:

- ≥ 1 decay electron
- No neutrons (SK-IV only)

Otherwise it is classified as an anti-neutrino. This results in a very small and pure ν_e -like sample, and a large, impure $\bar{\nu}_e$ -like sample. This cut position was chosen in SK-I to III as any other cut position results in an un-usably small neutrino sample. In SK-IV neutron cut was added to increase the purity of the ν_e -like sample, whilst maintaining a

consistent sample size with SK-I to III. The sample breakdown and data-MC agreement is shown in table 9.3, and figure 9.8.

Interaction type	Total	ν_e -like	$\bar{\nu}_e$ -like
True CC ν_e	1409.5	246.4	1163.2
True CC $\bar{\nu}_e$	752.5	38.2	714.3
True CC ν_μ	67.8	35.7	32.1
True CC $\bar{\nu}_\mu$	14.3	7.5	6.8
True NC	224.3	59.2	165.1
Total MC	2468.4	387.0	2081.4
Data (All SK, 4581.5 days)	2463	455	2008

TABLE 9.3: Multi-GeV 1-ring e-like sample, split into ν_e -like and $\bar{\nu}_e$ -like. The top half of the table shows the estimated event breakdown of each sample, constructed with MC information. The bottom half shows a total data-MC comparison. The data used is all of SK-I to IV.

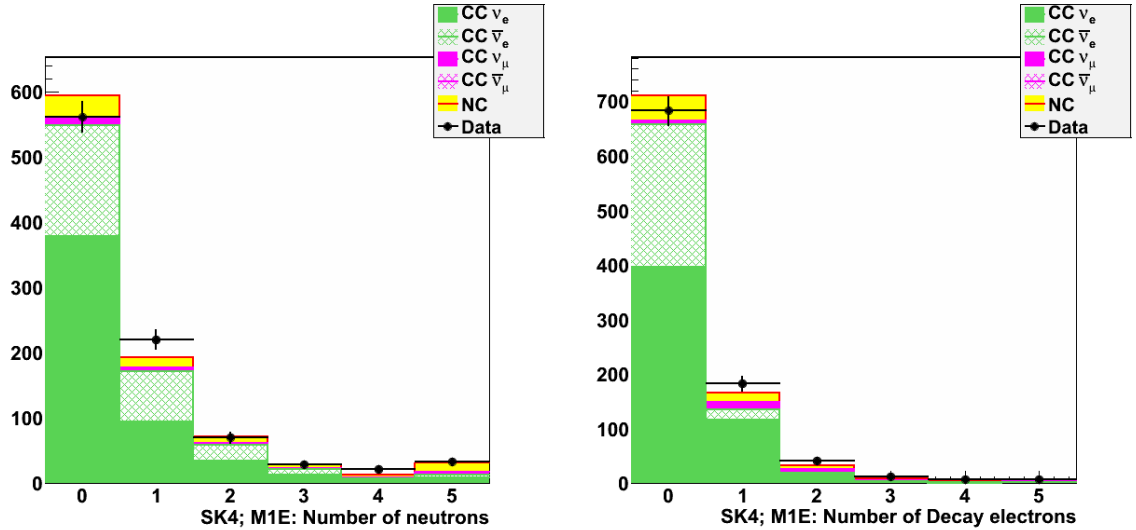


FIGURE 9.8: These plots show the data-MC agreement in SK-IV for the number of neutrons and number of decay-electrons in the MultiGeV 1 ring e-like sample. The colours represent the different event types each sample consists of: green and green-hatched are ν_e and $\bar{\nu}_e$ respectively. Purple is true ν_μ events, and yellow is neutral current events. The MC events are normalized to the livetime of the dataset, and oscillated in a 2 flavour framework with $\sin^2 2\theta = 1.0$, and $\Delta m^2 = 2.5 \times 10^{-3} eV^2$. Systematic errors are not included here.

9.2.2.2 Multi-GeV, Multi-Ring, e-like samples

The Multi-GeV Multi-Ring e-like sample separation is done using a neural network analysis, taking the following variables as input:

- Number of decay electrons

- Number of rings
- The most energetic ring's visible energy fraction
- Particle identification likelihood
- Number of neutrons (SK-IV only)

This sample consists only of events selected after a likelihood function was applied to remove neutral current events, but there is still a relatively large neutral current contamination. The NC events are more often classified as ν -like rather than $\bar{\nu}$ -like, as these events are often multiple-pion ejection, a feature shared by neutrino events (as described in the previous section). Figure 9.9 shows the multivariate analysis output for this sample. Table 9.4 shows the event breakdown.

Interaction type	Total	ν_e -like	$\bar{\nu}_e$ -like
True CC ν_e	777.1	453.4	323.7
True CC $\bar{\nu}_e$	267.8	102.6	165.2
True CC ν_μ	102.1	77.8	24.3
True CC $\bar{\nu}_\mu$	9.5	6.2	3.3
True NC	235.7	168.9	66.7
Total MC	1392.2	809.0	583.2
Data (All SK, 4581.5 days)	1435	862	573

TABLE 9.4: Multi-GeV Multi-ring e-like sample, split into ν_e -like and $\bar{\nu}_e$ -like. The top half of the table shows the estimated event breakdown of each sample, constructed with MC information. The bottom half shows a total data-MC comparison. The data used is all of SK-I to IV.

9.2.2.3 Multi-GeV, Single-Ring, μ -like samples

The Multi-GeV single-ring μ -like sample is sensitive to all the same variables as the e-like samples, with the addition of the decay electron distance, and decay electron time information. Compared to the single-ring e-like case, significant performance increase was seen using a neural network method rather than a cuts method in this sample. The variables employed are as follows:

- Number of decay electrons
- Particle identification likelihood
- Decay electron distance
- Decay electron time
- Number of neutrons (SK-IV only)

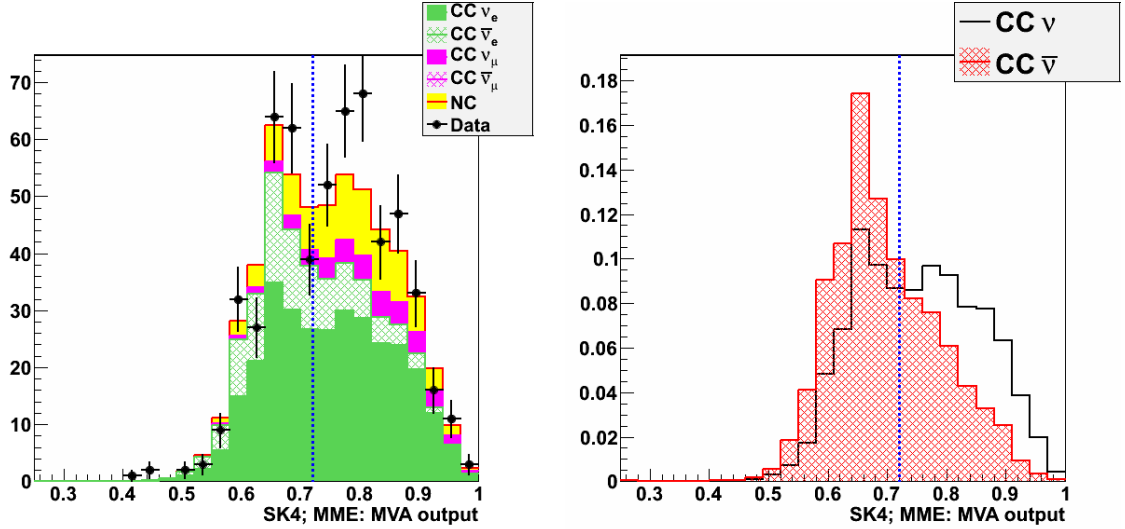


FIGURE 9.9: These plots show the data-MC agreement, and the ν_e - $\bar{\nu}_e$ separation in the multi-variate analysis output. The event sample is the MultiGeV Multi-ring e-like sample for SK-IV. The cut position is shown here as a dotted blue line at 0.72, chosen automatically (see 9.2.2). Events >0.72 are classified as ν_e -like, and <0.72 are $\bar{\nu}_e$ -like. For the right-hand plot, both histograms are normalized to 1. In the left-hand plot, the MC events are normalized to the livetime of the dataset, and oscillated in a 2 flavour framework with $\sin^2 2\theta = 1.0$, and $\Delta m^2 = 2.5 \times 10^{-3} eV^2$. Systematic errors are not included here.

The neural network output here is quite an unusual shape, as the variables with the most discriminating power - neutrons and decay electrons, are both discrete. This feature is common in both the data and MC. The data-MC agreement and ν - $\bar{\nu}$ separation can be seen in figure 9.10, and table 9.5.

Interaction type	Total	ν_μ -like	$\bar{\nu}_\mu$ -like
True CC ν_e	6.0	5.4	0.6
True CC $\bar{\nu}_e$	2.3	2.2	0.1
True CC ν_μ	1479.2	930.4	548.8
True CC $\bar{\nu}_\mu$	888.2	372.8	515.4
True NC	4.7	3.6	1.1
Total MC	2380.4	1314.3	1066.1
Data (All SK, 4581.5 days)	2210	1210	1000

TABLE 9.5: Multi-GeV 1-ring μ -like sample, split into ν_μ -like and $\bar{\nu}_\mu$ -like. The top half of the table shows the estimated event breakdown of each sample, constructed with MC information. The bottom half shows a total data-MC comparison. The data used is all of SK-I to IV.

9.2.2.4 Multi-GeV, Multi-Ring, μ -like samples

The Multi-GeV Multi-Ring μ -like sample uses the largest amount of input variables, combining those relevant to muons, and those relevant to multi-ring events:

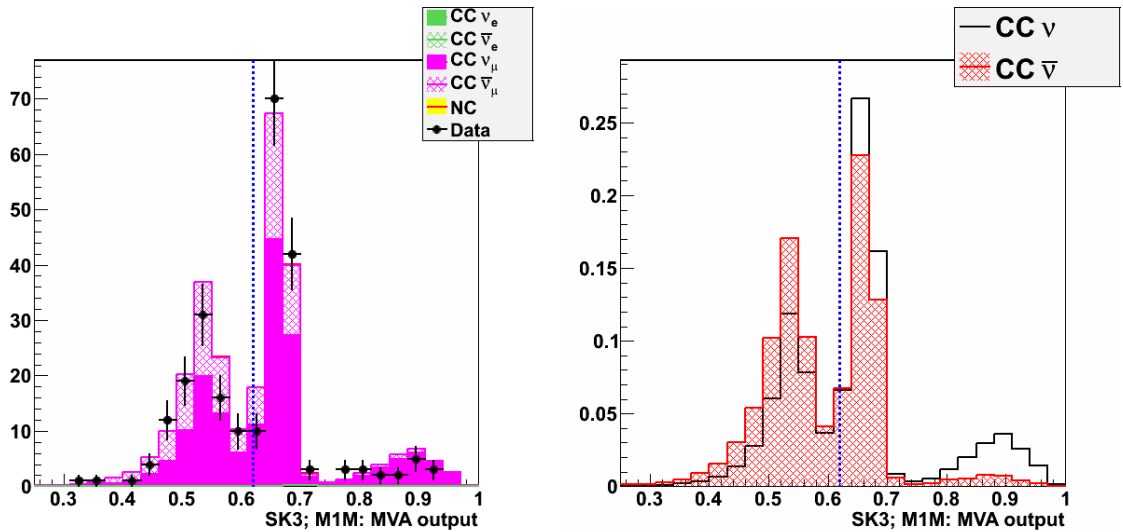


FIGURE 9.10: These plots show the data-MC agreement, and the ν_μ - $\bar{\nu}_\mu$ separation in the multi-variate analysis output. The event sample is Multi-GeV single-ring μ -like, for SK-III. The cut value is chosen automatically (described at 9.2.2), shown here as a dotted blue line at 0.62. Events >0.62 are classified as ν_μ -like, and <0.62 are $\bar{\nu}_\mu$ -like. For the right-hand plot, both histograms are normalized to 1. In the left-hand plot, the MC events are normalized to the livetime of the dataset, and oscillated in a 2 flavour framework with $\sin^2 2\theta = 1.0$, and $\Delta m^2 = 2.5 \times 10^{-3} eV^2$. Systematic errors are not included here.

- Number of decay electrons
- Particle identification likelihood
- Number of rings
- Most energetic ring's visible energy fraction
- Decay electron distance
- Decay electron time
- Number of neutrons (SK-IV only)

Similar to the multi-ring e-like case, this sample has some NC contamination, which has been mostly labelled as ν -like. The data-MC agreement and ν - $\bar{\nu}$ separation can be seen in figure 9.11, and table 9.6.

9.3 Systematic Errors

This analysis utilizes 185 independent systematic error parameters. Of these, 37 are common in SK-I to IV, and an additional 37 x 4 are calculated individually for each

Interaction type	Total	ν_μ -like	$\bar{\nu}_\mu$ -like
True CC ν_e	60.6	54.9	5.8
True CC $\bar{\nu}_e$	9.1	8.7	0.4
True CC ν_μ	1417.1	942.2	475.0
True CC $\bar{\nu}_\mu$	419.0	165.1	254.0
True NC	113.8	104.0	9.8
Total MC	2019.7	1274.8	744.9
Data (All SK, 4581.5 days)	1937	1146	791

TABLE 9.6: Multi-GeV Multi-ring μ -like sample, split into ν_μ -like and $\bar{\nu}_\mu$ -like. The top half of the table shows the estimated event breakdown of each sample, constructed with MC information. The bottom half shows a total data-MC comparison. The data used is all of SK-I to IV.

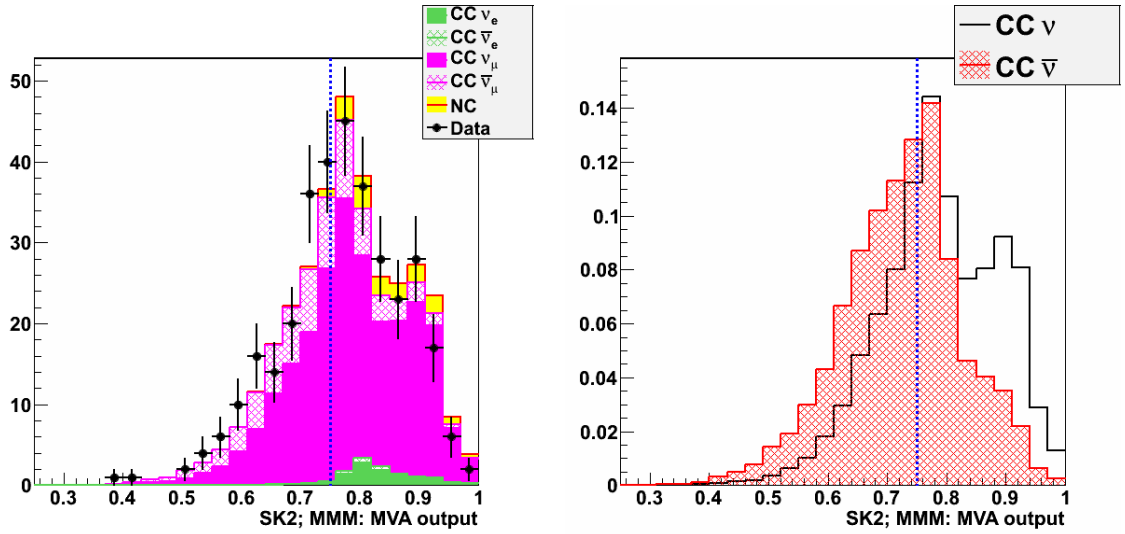


FIGURE 9.11: These plots show the data-MC agreement, and the ν_μ - $\bar{\nu}_\mu$ separation in the multi-variate analysis output. The event sample is Multi-GeV multi-ring μ -like, for SK-II. The cut value is chosen automatically (described at 9.2.2), shown here as a dotted blue line at 0.75. Events >0.75 are classified as ν_μ -like, and <0.75 are $\bar{\nu}_\mu$ -like. For the right-hand plot, both histograms are normalized to 1. In the left-hand plot the MC events are normalized to the livetime of the dataset, and oscillated in a 2 flavour framework with $\sin^2 2\theta = 1.0$, and $\Delta m^2 = 2.5 \times 10^{-3} eV^2$. Systematic errors are not included here.

SK generation. Each of these error sources contribute an additional fit parameter, ϵ_j , which is allowed to vary during the fit to the data. Most of the errors may be classified as either uncertainty in the neutrino flux, uncertainty in the neutrino interaction, or uncertainty in the event reconstruction and sample selection. The best fit values of ϵ_j , and estimated σ_j of each error are listed in the appendix.

9.3.1 Systematic Errors related to Neutrino Flux

This category of errors refers to any uncertainty on the neutrino flux. This includes uncertainty on the composition of the neutrino flux, and its angular dependence.

9.3.1.1 Flux Ratios

Various ratios of the incoming flux are examined. Firstly, the uncertainty in the neutrino flavour ratio $(\nu_\mu + \bar{\nu}_\mu)/(\nu_e + \bar{\nu}_e)$. This is estimated by comparing the result from the Honda flux used in SK [7], with other neutrino flux models, such as the FLUKA flux [96] and Bartol flux [97]. The flux models diverge at high energy so an energy dependent error is assigned here. The uncertainty is estimated as 2% for $E_\nu < 1$ GeV, 3% for $1 < E_\nu < 10$ GeV, and 5% for $10 < E_\nu < 30$ GeV. From $30 \text{ GeV} < E_\nu < 1 \text{ TeV}$ the error increases as a function of $\log E_\nu$. The deviation between flux models can be seen in figure 9.12.

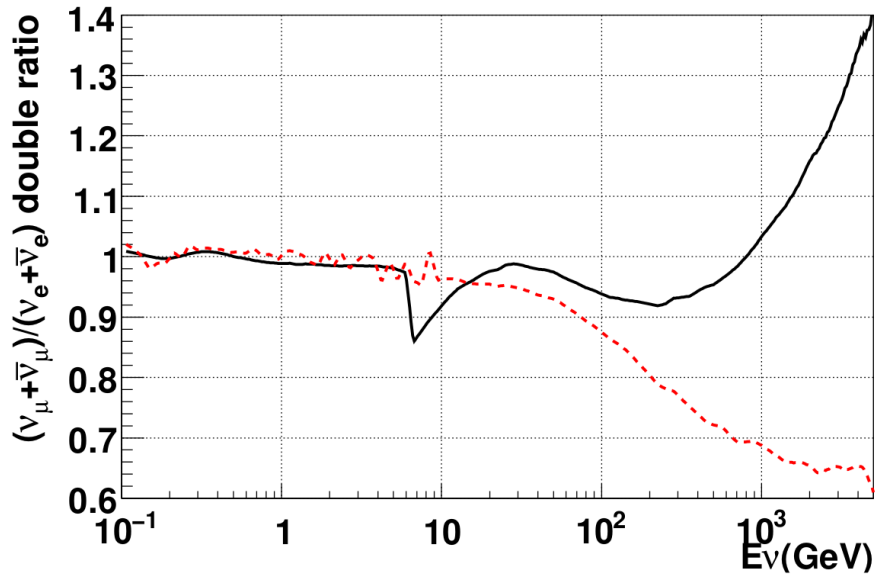


FIGURE 9.12: The flavour ratio between the Honda flux and competing flux models used for systematic error calculation. The solid black line shows the ratio FLUKA/Honda flux, and the dashed red line depicts the Bartol/Honda flux. The spike around 8 GeV in the FLUKA flux is due to a flux calculation technicality, and has been corrected for in the error evaluation.

In a similar fashion to the flavour ratio error, there is an error term accounting for uncertainty in the anti-neutrino/neutrino ratios, $\bar{\nu}_e/\nu_e$ and $\bar{\nu}_\mu/\nu_\mu$. Again the estimation is conducted by comparing the Honda flux, to the FLUKA and Bartol models.

The ratio of the flux models used to decide this error is shown in figure 9.13.

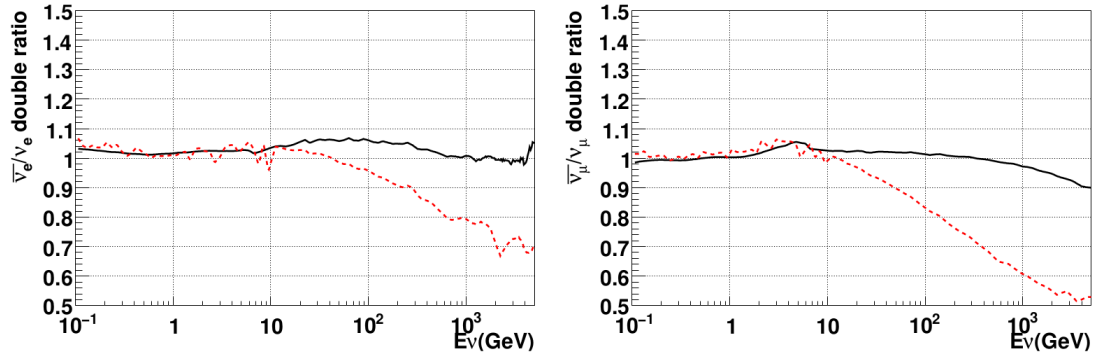


FIGURE 9.13: The anti-neutrino / neutrino double ratio between the Honda flux and competing flux models used for systematic error calculation. The solid black line shows the ratio FLUKA/Honda flux, and the dashed red line depicts the Bartol/Honda flux. The left plot shows the double ratio of $\bar{\nu}_e/\nu_e$ and the right plot shows $\bar{\nu}_\mu/\nu_\mu$

A further two flux ratio errors are the up/down error, and the horizontal/vertical error. As the names imply, these account for uncertainty in neutrino flux depending on the direction by which they enter the tank, which is important for zenith angle analysis. The main cause of uncertainty in these errors is the shape and rigidity cut-off of the Earth's geomagnetic field. Similarly, these errors are estimated using the difference between the Honda flux and the FLUKA and Bartol models.

9.3.1.2 K/ π ratio

At energies below 10 GeV, neutrino production is primarily due to pion decay, however as the cosmic ray energy increases, the production becomes more dominated by kaons. This error describes the uncertainty in the ratio of K to π based neutrino production. This error was estimated using data from the SPY experiment [150] to be 5% for $E_\nu < 100$ GeV, and then linearly increasing with energy until 20% at 1 TeV.

9.3.1.3 Solar Activity

The solar activity cycles over an 11 year period and the resultant magnetic field changes have some effect on the cosmic ray flux. The uncertainty of the solar cycle is taken to be ± 1 year, which corresponds to 20%, 50%, 20% and 10% errors for SK I-IV respectively.

9.3.1.4 Neutrino Production Height

An uncertainty in the neutrino production height will propagate through to uncertainty in the distance travelled by neutrinos, and thus the oscillation probability of the neutrinos. This error is negligible for upward-going neutrinos but represents a significant

uncertainty in downward-going and horizontal-going neutrinos. The root of this error is in the uncertainty of the atmospheric density structure, which is estimated to be 10% by comparison between the US-standard 76 and the MSISE90 experiment [151]. The atmospheric density is then changed by 10% in the neutrino flux model, and the change in neutrino path length is calculated. This change in path length is taken as the systematic uncertainty.

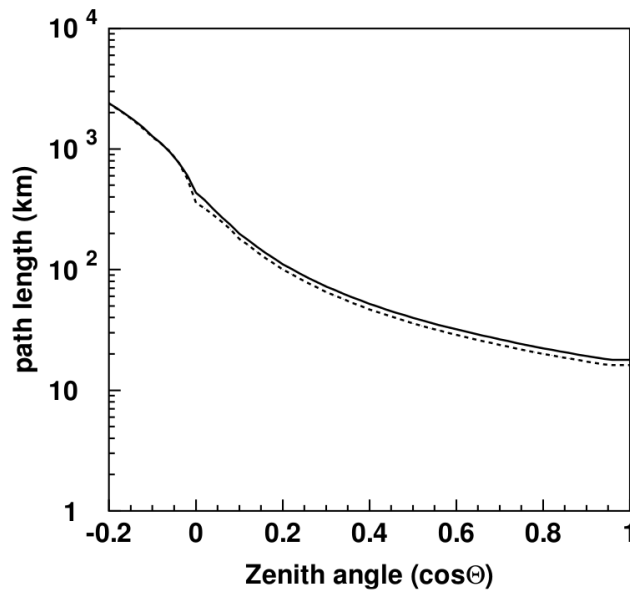


FIGURE 9.14: The neutrino path length, as a function of zenith angle. The solid line represents the path lengths provided in the default Honda flux model, and the dotted line shows the path-lengths after a 10% change in the atmospheric density.

9.3.1.5 Matter Effect

The neutrino oscillation probability in the Earth is dependent on the electron density in the Earth, and while the total matter density is well known [152], the electron density depends on the exact chemical composition, and has some uncertainty. The core is assumed to consist of iron and other heavy elements, which have $\sim 6.8\%$ reduced electron density compared to if it was constructed primarily of light elements. This difference is propagated to the oscillation probability uncertainty, and used as a systematic error source.

9.3.1.6 Absolute normalization

Finally we take a systematic error on the absolute normalization of the neutrino flux. This was estimated by Honda in [153], taking into account uncertainty in pion production, kaon production, hadronic interaction cross sections and the atmospheric density

profile, as shown in figure 9.15. The final uncertainty is calculated using the two dominant sources, pion production and the hadronic interaction errors. The kaon production and atmospheric density profile uncertainties are already accounted for in previously mentioned errors.

However above 10 GeV, this error is not sufficient to account for the differences between the flux models, Bartol, FLUKA and Honda. Thus, an additional normalization error of 5% is applied in the FC Multi-GeV, PC, and UPMU samples, whose energy spectra peak above 10 GeV.

9.3.2 Systematic Errors related to Neutrino Interactions

Systematic errors are applied to the simulation of neutrino interactions including those that affect the initial interaction, associated nuclear effects, and the secondary interactions in the water.

9.3.2.1 CCQE Cross Section

Similar to the neutrino flux systematics, the errors applied to the neutrino cross sections are in the form of an absolute error on ν_e and ν_μ , and the ratios $(\nu_\mu + \bar{\nu}_\mu)/(\nu_e + \bar{\nu}_e)$ and $\bar{\nu}/\nu$. The CCQE cross section model used in SK is based on the Smith and Moniz Fermi-gas model [108], and to estimate uncertainty this was compared to the model calculated by Nieves et al. [154]. The difference between these models for each error can be seen in figure 9.16.

9.3.2.2 Axial Mass

The axial mass used in the SK MC is set to $M_A = 1.21$ GeV, however there is some uncertainty on this value in recent experiments [155][156]. To account for this, the axial mass error is taken to be 10%.

9.3.2.3 Single Meson Production

Experimental measurements of the interaction $\nu_\mu p \rightarrow \mu^- p \pi^+$ are used to assess the single meson production cross section error, which is estimated to be 20%. There are fewer experimental results for π^0 production, so a comparison with the Hernandez model [157] was performed to calculate this error. Thus the π^0 production cross section is assigned an additional 40% error relative to the π^\pm uncertainty.

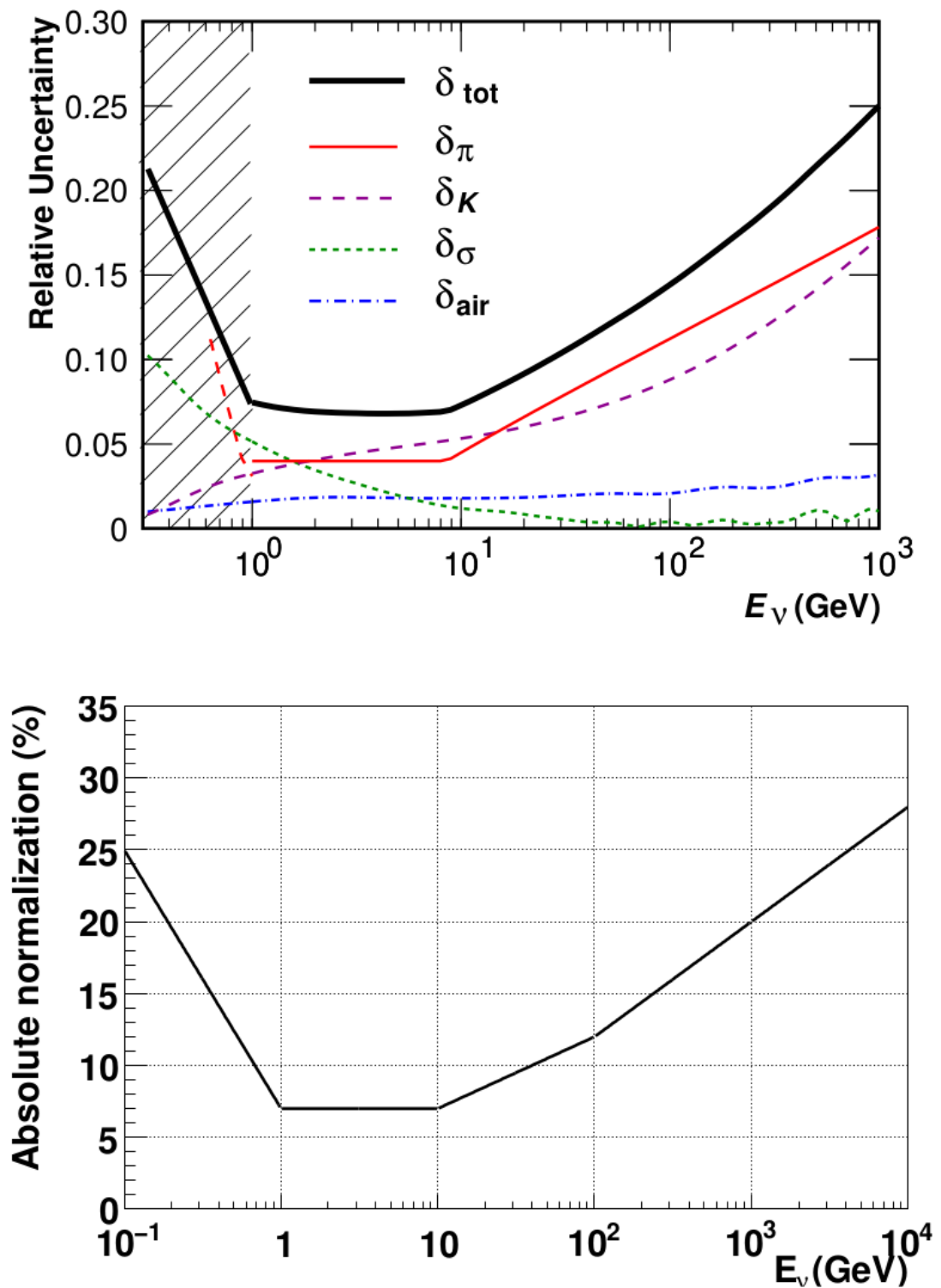


FIGURE 9.15: The top plot shows the relative uncertainty in each aspect of the flux model, where δ_π , δ_K , δ_σ , and δ_{air} are the uncertainties on pion production, kaon production, hadronic interaction cross sections and atmospheric density profile respectively. The bottom plot is the calculated uncertainty on the absolute normalization of the neutrino flux.

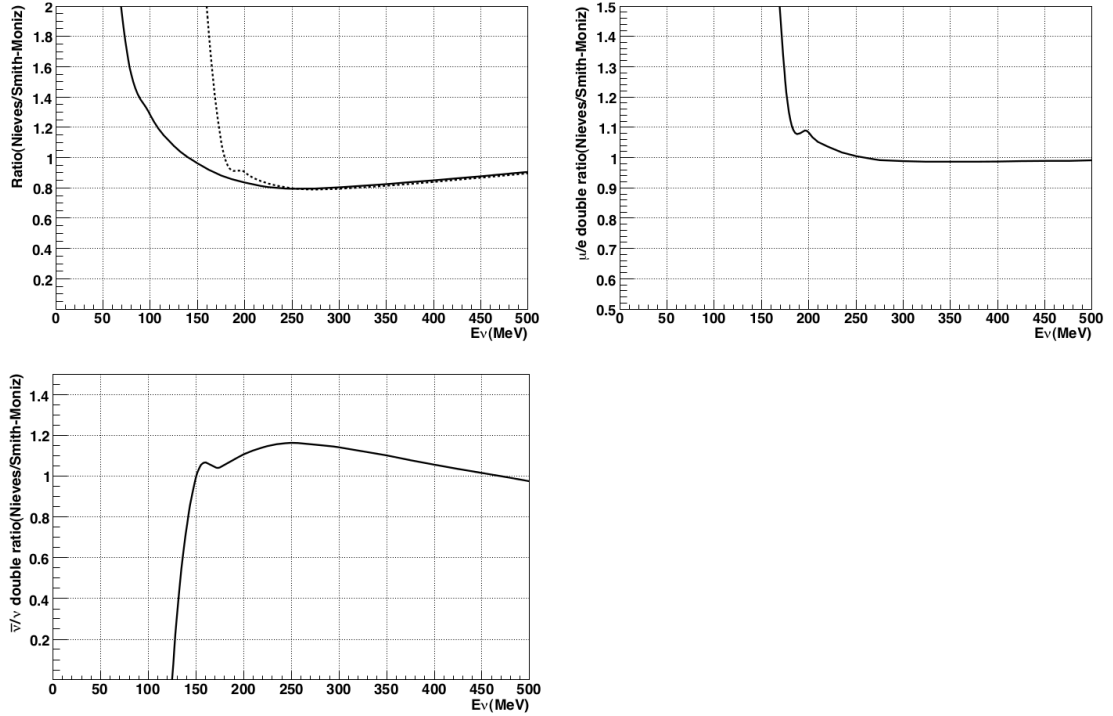


FIGURE 9.16: These plots show the ratio of the CCQE cross section calculated by the Nieves model to that calculated by the fermi gas model used in SK. The top left plot displays $\nu_e + \bar{\nu}_e$ and $\nu_\mu + \bar{\nu}_\mu$ in the solid and dashed lines respectively. The top right plot shows the ratio $(\nu_\mu + \bar{\nu}_\mu)/(\nu_e + \bar{\nu}_e)$, and the bottom plot is $\bar{\nu}/\nu$.

9.3.2.4 Coherent Pion Production

For coherent pion cross section in NC and $CC\nu_e$ interactions, the uncertainty is estimated to be 50% following comparison between measurements by SciBooNE [158], and the Rein and Sehgal model. SciBooNE reported non-existing coherent scattering events, so the uncertainty is taken to be 100%.

9.3.2.5 Deep Inelastic Scattering

The deep inelastic scattering cross section expectation agrees with experiments to within 5%. This uncertainty increases at lower energies, so an additional error is estimated by comparison to the CKMT model [159]. The uncertainty on the deep inelastic scattering cross section's Q^2 dependence is also considered, for both $W < 1.3 \text{ GeV}/c^2$ and $W > 1.3 \text{ GeV}/c^2$, by comparison to the GRV98 model.

9.3.2.6 Other Cross Section Uncertainties

The error on the ν_τ CC cross-section is taken to be 25%, by making a comparison with the Hagiwara model [160]. The uncertainty of the NC/CC ratio is estimated to be 20%.

9.3.3 Systematic Errors related to Reduction and Reconstruction Processes

The reduction process refers to the set of cuts applied to reduce the data into background free neutrino samples. The errors are separate for each of the FC, PC and UPMU event categories. For more information on the selection of these samples, please refer to chapter 7. Reconstruction refers to the calculation of expected energy, vertex, particle-type, and so forth. This is described in detail in chapter 6.

9.3.3.1 FC Reduction

The uncertainty of the FC reduction efficiency is calculated by comparing data and MC distributions, for each of the cuts applied in this reduction. This is estimated to be 0.6%, 0.5%, 0.9%, and 0.4% for SK-I to IV, respectively. An error is also calculated for the background rate in the final sample. The background is estimated by eye-scanning the final data-set and contributes a 0.1 – 0.5% uncertainty (differs depending on reconstructed energy and particle ID. See chapter 7 for details).

FC and PC events are separated by counting the number of PMT hits in the OD hit cluster with highest charge. By comparing the data and MC expectation for this variable, the uncertainties in FC/PC separation are estimated as 0.6%, 0.5%, 0.9% and 0.4% for SK-I to IV.

9.3.3.2 PC Reduction

The PC reduction efficiency uncertainty is estimated by comparing the data and MC for different cut variables at each stage of the reduction process. This error is taken to be 2.5%, 4.8%, 0.5% and 1.0% for SK-I to IV, respectively. There is also an uncertainty on the background rate in the final sample, which is estimated by eye-scanning the selected PC events. This is set to 0.2%, 0.7%, 1.1% and 0.5% for SK-I to IV.

Another PC related uncertainty is the separation between PC stopping events, and PC through-going events (referring to whether the lepton track stops in the OD or continues out of the detector). This separation is decided by assessing the photo-electrons deposited in the OD compared to the expectation, $(p\text{-}e_{obs}/p\text{-}e_{exp})$. The uncertainty is estimated using the difference in this distribution between data and MC, and is assigned separately for each region of the OD.

9.3.3.3 UPMU Reduction

Similar to the previous two reductions, the UPMU reduction efficiency uncertainty is assessed by comparing cut variable distributions between data and MC. For stopping muons, these uncertainties are assigned to 0.7%, 0.7%, 0.7% and 0.5%, for SK-I to IV. For through-going muons, these become 0.5%, 0.5%, 0.5% and 0.3% for SK-I to IV.

The separation between stopping and through-going muons is calculated using the number of OD PMT hits within 8m of the expected tank exit point. The data and MC results for this distribution are compared, and used to calculate the uncertainty, which is estimated as 0.4%, 0.6%, 0.4% and 0.6% for SK-I to IV.

Uncertainty is also assigned to the separation of UPMU showering and non-showering events. The average expected charge for non-showering events is calculated, and the difference between data and MC distributions is taken as the error. This is set as 3.4%, 4.4%, 2.4% and 3.0% for SK-I to IV.

9.3.3.4 Reconstruction errors

The ring separation is based on a likelihood distribution used to determine how many Cherenkov rings an event is fit best with. The uncertainty in this is calculated by comparing these likelihood distributions between data and MC.

The particle identification likelihood is similarly used to distinguish between e-like and μ -like events. The uncertainty in this is also calculated by comparing data to MC.

The error decay electron tagging efficiency is calculated by using cosmic muon data to be 1.5% for SK-I to III. This improves to 0.8% in SK-IV.

9.3.4 Event Selection errors

Event selection errors are related to the division of the dataset into various sub-samples, as described earlier in this chapter. The errors relating to the new samples in this analysis will be described below.

9.3.4.1 Multi-GeV Neutrino and Anti-Neutrino sample errors

Multi-GeV samples are split by neutrino/anti-neutrino, single-ring/multi-ring, and e-like/ μ -like, into a total of 8 samples (plus Multi-Ring Other, which is not discussed here). Each of these samples is assigned an error on the efficiency, of either CC ν or CC

$\bar{\nu}$. For example, in the 1-ring e-like sample the errors allow movement of true CC ν_e and CC $\bar{\nu}_e$ events between the ν_e -like and $\bar{\nu}_e$ -like samples. No additional error is applied to NC or the opposite neutrino type (CC ν_μ in this example).

The total error for each sample is calculated as the sum in quadrature of multiple error sources. The errors utilized are:

- Americium-Beryllium 10% error on neutron tagging efficiency: this is a large source of uncertainty in the efficiency of the CCQE-enriched single-ring samples, however it represents a small uncertainty in the multi-ring samples, which are largely deep inelastic scattering events. In these latter interactions neutron number is a less powerful discriminant, and thus contributes less to the total error.
- Decay-electron tagging efficiency $\sim 1\%$: this error is only significant in SK-I to III, as in SK-IV the neutron tagging error becomes dominant.
- Pion final state interaction cross sections: 24 sets of weights are created, each using an altered set of pion interaction cross-sections to represent an overall 1σ change, as estimated by fits to pion-nucleus scattering data. The parameter set causing the largest deviation in sample efficiency was chosen as the error in each case ($\sim 2 - 10\%$, depending on sample).
- Pion multiplicity error: from comparison between NEUT simulation and CHORUS ν_μ beam experimental data. This error results in a $\sim 5\%$ uncertainty on the efficiency of the μ -like samples.

A neutron production systematic error was also considered by comparing neutron multiplicity following a variety of hadronic particle guns, between the FLUKA event generator with the Geant3 model used in SK. This was however found to be negligible compared to the Americium-Beryllium neutron tagging efficiency error, so was not included in the final estimation.

9.4 Mass Hierarchy Sensitivity

Before fitting to data, it is interesting to evaluate our expected sensitivity to the mass hierarchy with these new samples. This sensitivity can be expressed as $\Delta\chi^2 = \chi^2(NH) - \chi^2(IH)$. A lower value χ^2 represents a better fit, so a negative value of $\Delta\chi^2$ would show a preference to the normal hierarchy.

In the sensitivity study, we perform two fits, firstly using a MC generated assuming normal hierarchy in the place of data, and fitting a MC oscillated according to the

inverted hierarchy, and then vice versa. The χ^2 value at the best fit point represents the expected difference between normal and inverted hierarchy.

The “true” parameters for the sensitivity study are chosen as shown in table 9.7.

Oscillation Parameter	Selected True Value
Δm_{23}^2	$2.5 \times 10^{-3} eV^2$
$\sin^2 \theta_{23}$	0.53
Δm_{12}^2	$7.5 \times 10^{-5} eV^2$
$\sin^2 \theta_{12}$	0.31
$\sin^2 \theta_{13}$	0.025
δ_{CP}	260°

TABLE 9.7: Chosen “true” oscillation parameters for the mass hierarchy sensitivity study.

An identical study was performed with the binning scheme described in [148], to judge the effect of the new sample splitting on the mass hierarchy sensitivity.. This binning does not use neutron tagging, and the Multi-GeV μ -like samples are not split into ν and $\bar{\nu}$ -like. The results are shown below in table 9.8. Plots showing the projected sensitivity contours can be seen in figure 9.17.

	Previous Sample Selection $ \Delta\chi^2 $	New Sample Selection $ \Delta\chi^2 $
True Normal Hierarchy	1.81	1.87
True Inverted Hierarchy	0.83	0.89

TABLE 9.8: Improvement in sensitivity to neutrino mass hierarchy due to the new ν - $\bar{\nu}$ samples.

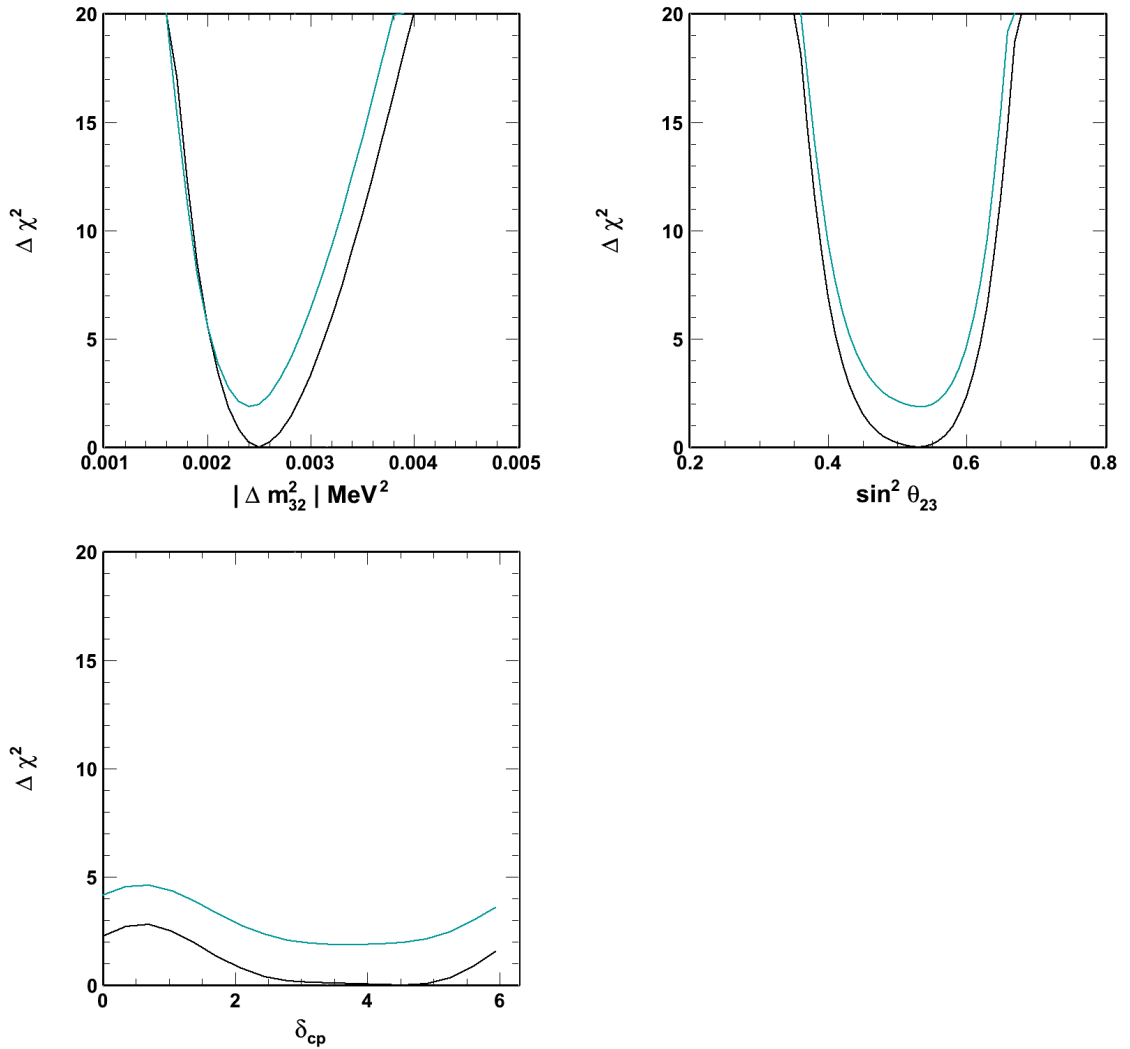


FIGURE 9.17: Projected χ^2 plots for the mass hierarchy sensitivity. The true hierarchy is taken to be normal, and the black and green lines represent fits assuming the normal and inverted hierarchy respectively. The minimum $\Delta\chi^2$ value of the inverted hierarchy at $\Delta\chi^2 = 1.87$ represents our sensitivity to the mass hierarchy in this case.

9.5 Data Fit Results

Our MC simulation is now fit to the dataset from SK-I to IV, for 37,638 different sets of oscillation parameters defined at the start of this chapter. At every point in the parameter space a fit was performed over the systematic errors ϵ_j to find the minimum χ^2 value for that parameter set. Following this, the minimum χ^2 over the whole oscillation parameter space is selected as best fit point. This procedure was performed twice, assuming a normal or an inverted hierarchy. The following parameters are taken as constant: $\sin^2\theta_{13} = 0.025$, $\Delta m_{12}^2 = 7.5 \times 10^{-5} \text{ eV}^2$, and $\sin^2\theta_{12} = 0.31$. The best fit points for each hierarchy are summarized in table 9.9.

	Assumed Normal Hierarchy	Assumed Inverted Hierarchy
Δm_{23}^2	$2.4 \times 10^{-3} eV^2$	$2.3 \times 10^{-3} eV^2$
$\sin^2 \theta_{23}$	0.46	0.56
δ_{CP}	260°	220°
χ^2	636.2/577 DoF	637.1/577 DoF

TABLE 9.9: Oscillation analysis best fit point for normal and inverted hierarchy assumptions.

Thus the normal hierarchy is favoured by $\Delta\chi^2(NH - IH) = -0.9$. The error parameters for the best fit point can be found in the appendix. Contour plots for the normal and inverted hierarchy results are shown in figures 9.18 and 9.19. The 90% confidence levels for $\sin^2 \theta_{23}$, Δm_{23}^2 and δ_{CP} are defined at $\chi^2 = \chi_{min}^2 + 2.7$, and shown in table 9.10.

	Assumed Normal Hierarchy	Assumed Inverted Hierarchy
Δm_{23}^2	$(2.14 < \Delta m_{23}^2 < 2.91) \times 10^{-3} eV^2$	$(2.07 < \Delta m_{23}^2 < 2.83) \times 10^{-3} eV^2$
$\sin^2 \theta_{23}$	$0.397 < \sin^2 \theta_{23} < 0.623$	$0.406 < \sin^2 \theta_{23} < 0.617$
δ_{CP}	$103.0 < \delta_{CP} < 352.8^\circ$	$110.5 < \delta_{CP} < 333.9^\circ$

TABLE 9.10: Oscillation analysis 90% confidence levels for normal and inverted hierarchy assumptions.

An overview of the data and MC agreement after fitting can be seen in figure 9.20. Bin-by-bin plots of the new ν -like, $\bar{\nu}$ -like, and Multi-Ring Other samples can be found in figure 9.21.

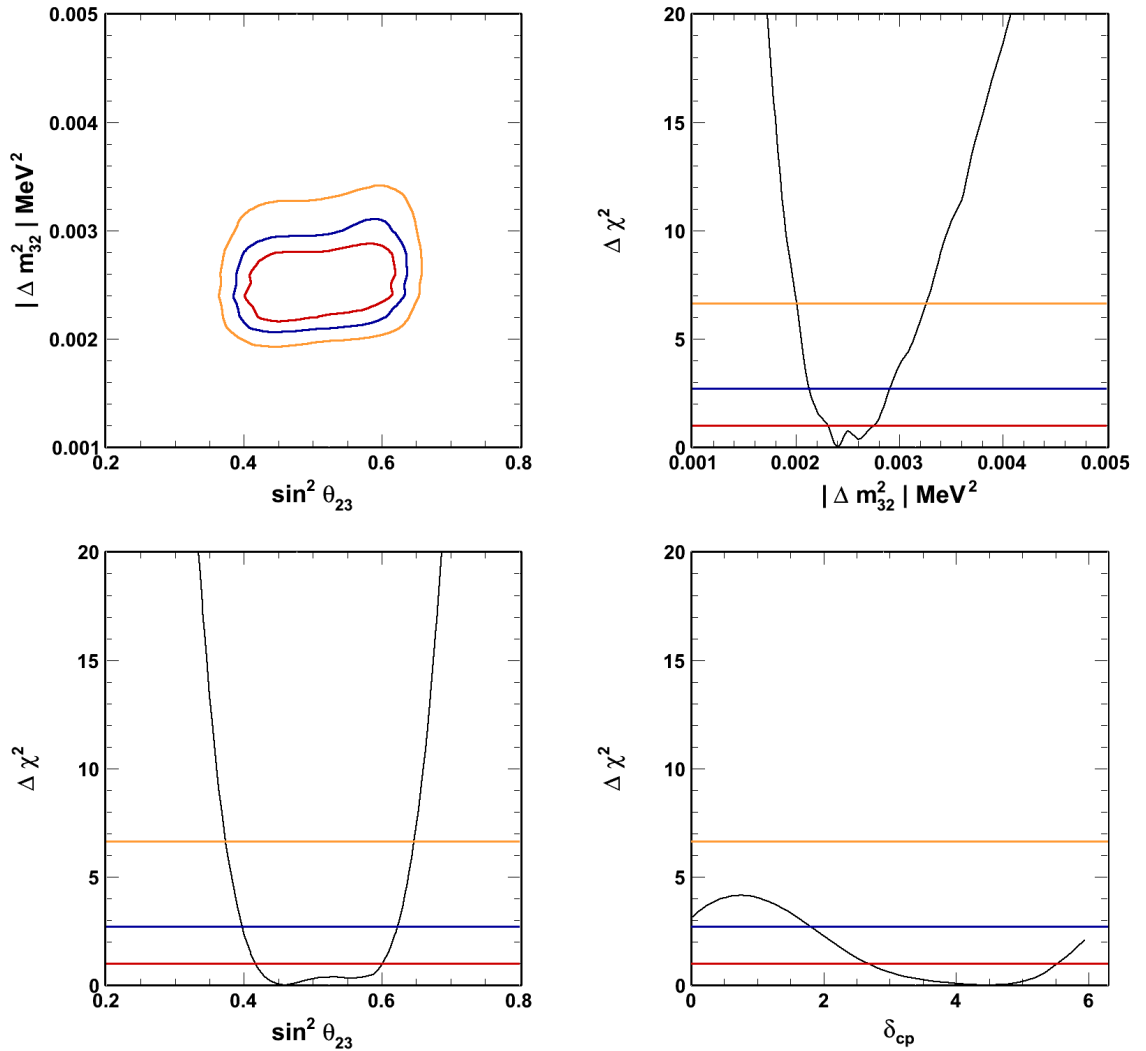


FIGURE 9.18: Assuming the normal hierarchy, these plots show fitted χ^2 values for points across the oscillation parameter space. The minimum value of χ^2 is subtracted from every point. From top right going clockwise the plots show: $\sin^2 \theta_{23} - \Delta m_{23}^2$ contour plot, minimum Δm_{23}^2 , minimum δ_{CP} , and minimum $\sin^2 \theta_{23}$. The coloured lines on the plots represent the confidence level contours, 99% (orange), 90% (blue) and 68% (red). In the 1d plots, these correspond to $\Delta \chi^2 = 6.6, 2.7$ and 1.0 respectively. In the 2d case, these contours correspond to $\Delta \chi^2 = 9.2, 4.6$ and 2.3 . The black line in the 1d plots represents the projected minimum χ^2 values. The dataset is all of SK-I to IV.

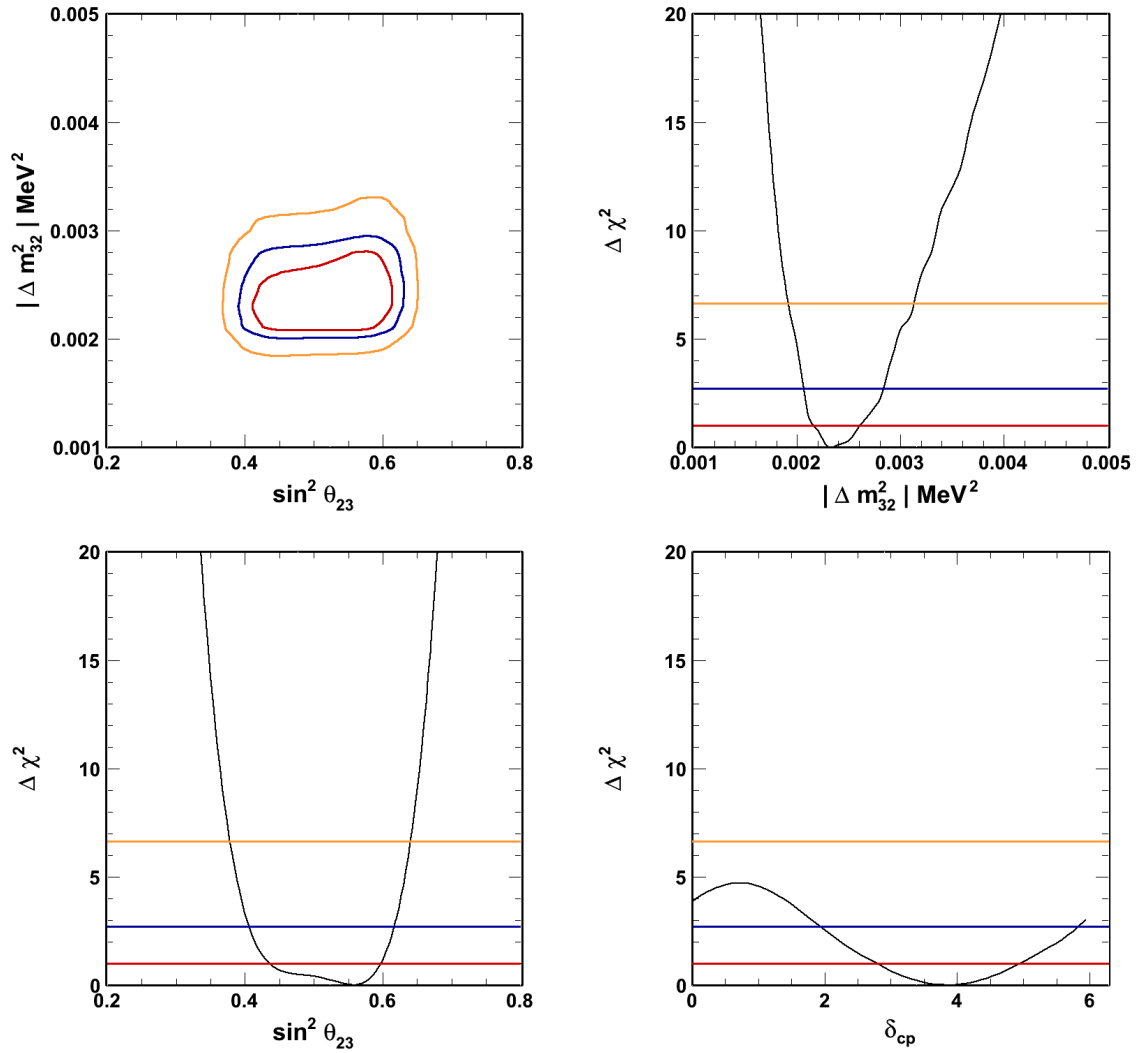


FIGURE 9.19: Assuming the inverted hierarchy, these plots show fitted χ^2 values for points across the oscillation parameter space. The minimum value of χ^2 is subtracted from every point. From top right going clockwise, the plots show: $\sin^2 \theta_{23} - \Delta m_{23}^2$ contour plot, minimum Δm_{23}^2 , minimum δ_{CP} , and minimum $\sin^2 \theta_{23}$. The coloured lines on the plots represent the confidence level contours, 99% (orange), 90% (blue) and 68% (red). The black line in the 1d plots represents the projected minimum χ^2 values. The data-set is all of SK-I to IV.

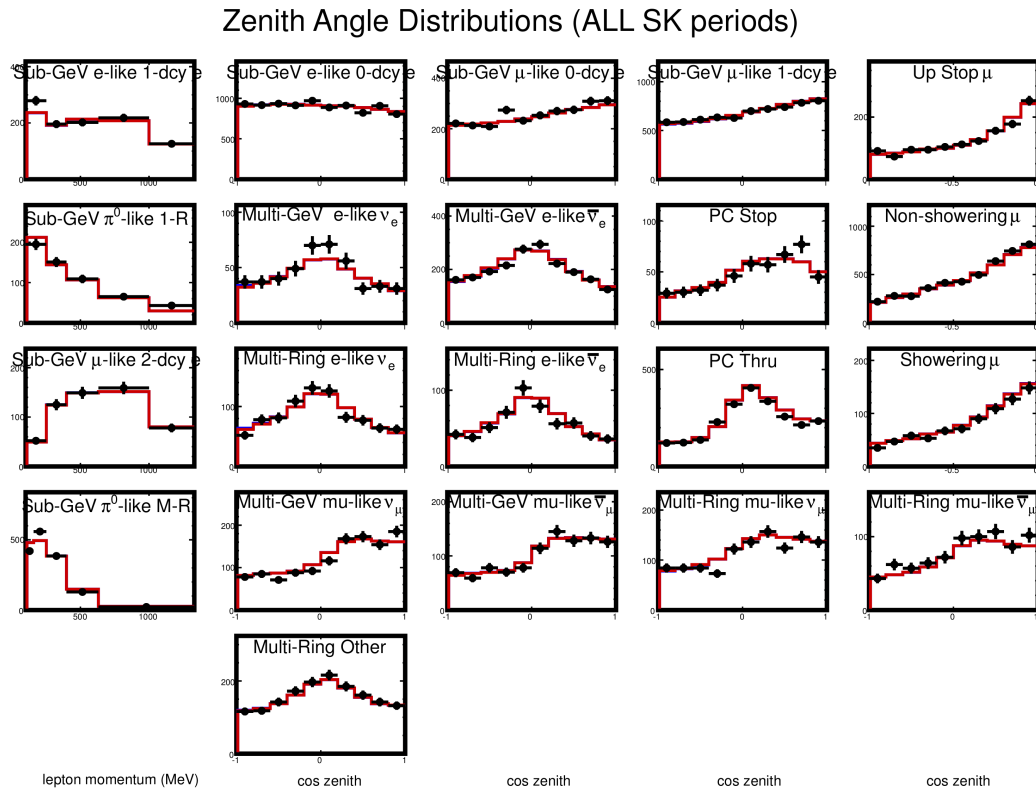


FIGURE 9.20: The data-MC agreement for each sub-sample, after fitting, with combined data from SK-I to IV. The oscillation parameters used can be seen in table 9.9. Multi-GeV refers to the Multi-GeV 1-ring sample, and Multi-Ring refers to the Multi-GeV Multi-Ring sample. The inverted hierarchy best fit is in red, and normal hierarchy in green (these are mostly overlaid and cannot be distinguished). The 4 samples on the left are not divided into zenith bins during analysis, so they are shown in momentum bins. The remaining 4 columns of samples, are divided into momentum and zenith bins in analysis, but here only the projection onto zenith bins is shown.

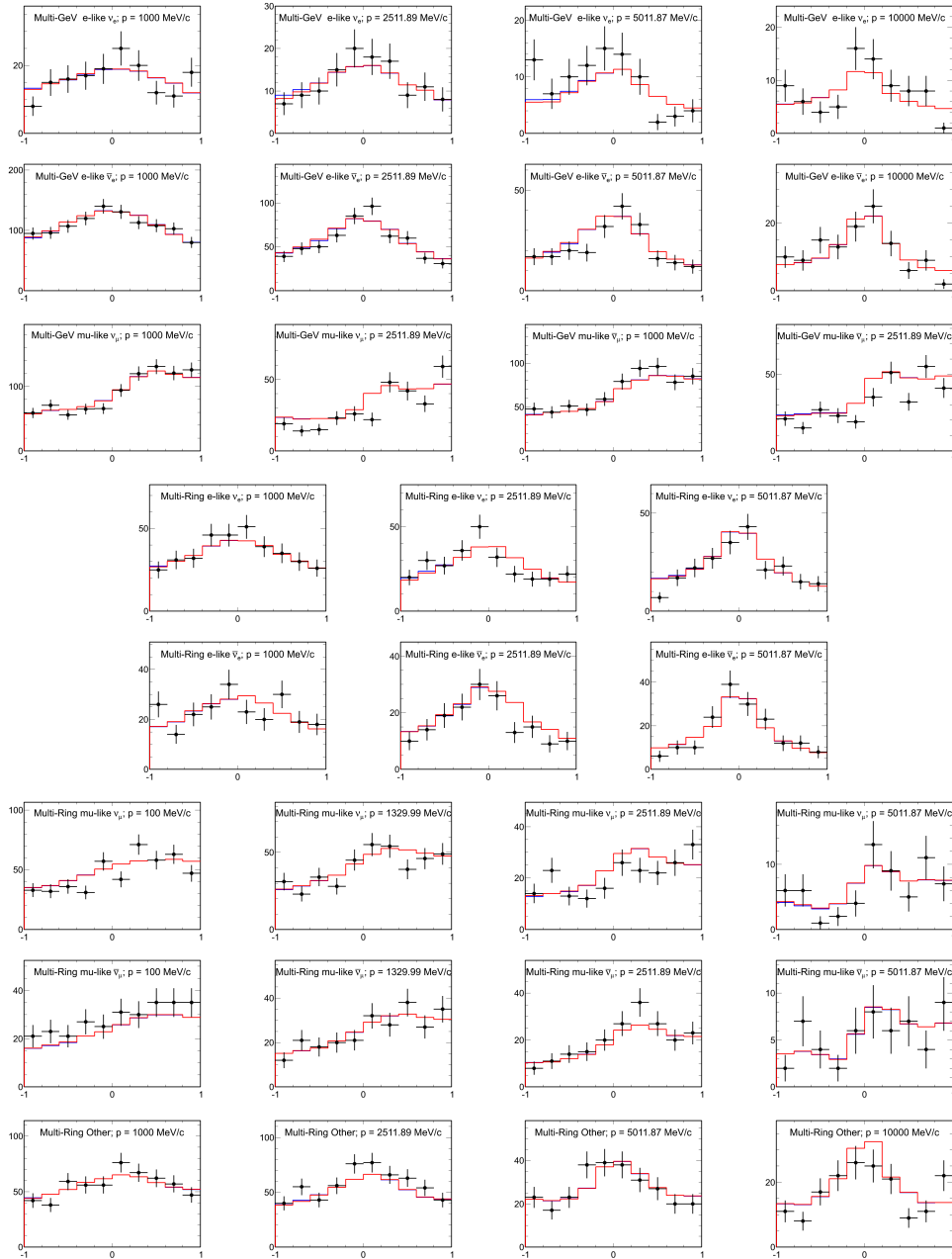


FIGURE 9.21: Data vs MC for the new ν -like, $\bar{\nu}$ -like, and Multi-Ring Other samples. The dataset shown includes all of SK-I to IV. The MC is oscillated using the best fit parameters shown in table 9.9. Multi-GeV refers to the Multi-GeV 1-ring samples, and Multi-Ring to the Multi-GeV Multi-Ring samples. The x-axis shows the zenith angle $\cos\theta$, where $\cos\theta = -1$ represents upward-going events. The blue line represents the normal hierarchy expectation, and the red line the inverted hierarchy. The momentum shown at the top of each plot is the lower end of the momentum bin.

9.6 Discussion and Comparison to other Experiments

Utilizing the new ν - $\bar{\nu}$ separation the sensitivity to neutrino mass hierarchy has improved from $\Delta\chi^2 = 1.81$ to $\Delta\chi^2 = 1.87$ (assuming true normal hierarchy). After fitting to data the difference at the best fit points for each hierarchy is $\Delta\chi^2(\text{NH-IH}) = -0.9$ in both the current official analysis and this analysis. This represents a slight preference for the normal hierarchy, but is unfortunately not sufficient to reach a conclusion. Most of the preference for normal hierarchy comes from the Multi-GeV 1-R e-like ν and $\bar{\nu}$ -like samples, which have a small excess and deficit respectively in the upward going ($\cos\theta < 0$) bins (figure 9.21). The contributions to the value of $\Delta\chi^2$ on a sample-by-sample basis can be seen in figure 9.23. A comparison of the 90% confidence levels of the previous, and updated SK analyses can be seen in figure 9.22. These contours are largely unchanged.

The 90% confidence levels of δCP in the normal hierarchy case are found to be $103.0 < \delta CP < 352.8^\circ$. The exclusion of $\delta CP = 60^\circ$ is primarily driven by an excess in SubGeV e-like events. CP-conservation requires $\sin(\delta CP) = 0$, which is allowed within the 90% confidence level in both the normal hierarchy and inverted hierarchy case.

The MINOS result from 2013 reports a best fit point of $\Delta m_{23}^2 = 2.41 \times 10^{-3} \text{eV}^2$, and $\sin^2 \theta_{23} = 0.39$ [31]. The T2K result from muon disappearance studies gives a best fit of $\Delta m_{23}^2 = 2.51 \times 10^{-3} \text{eV}^2$ and $\sin^2 \theta_{23} = 0.514$ [32]. The agreement of these experiments with the presented analysis at the 90% confidence level is shown in figure 9.24.

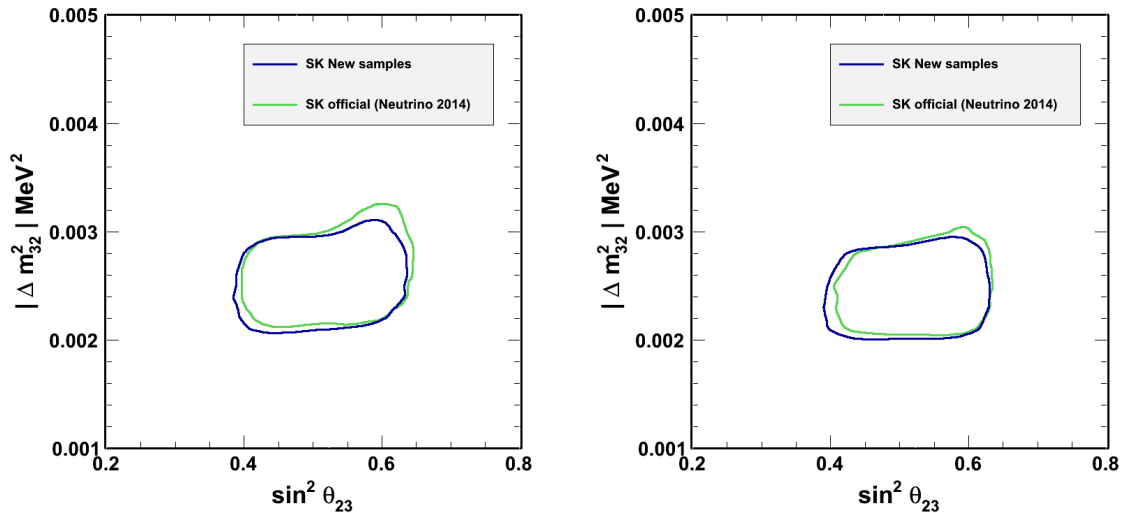


FIGURE 9.22: Comparison of the 90% confidence level contour between the current SK official analysis (green) and analysis with the updated samples presented in this thesis (blue).

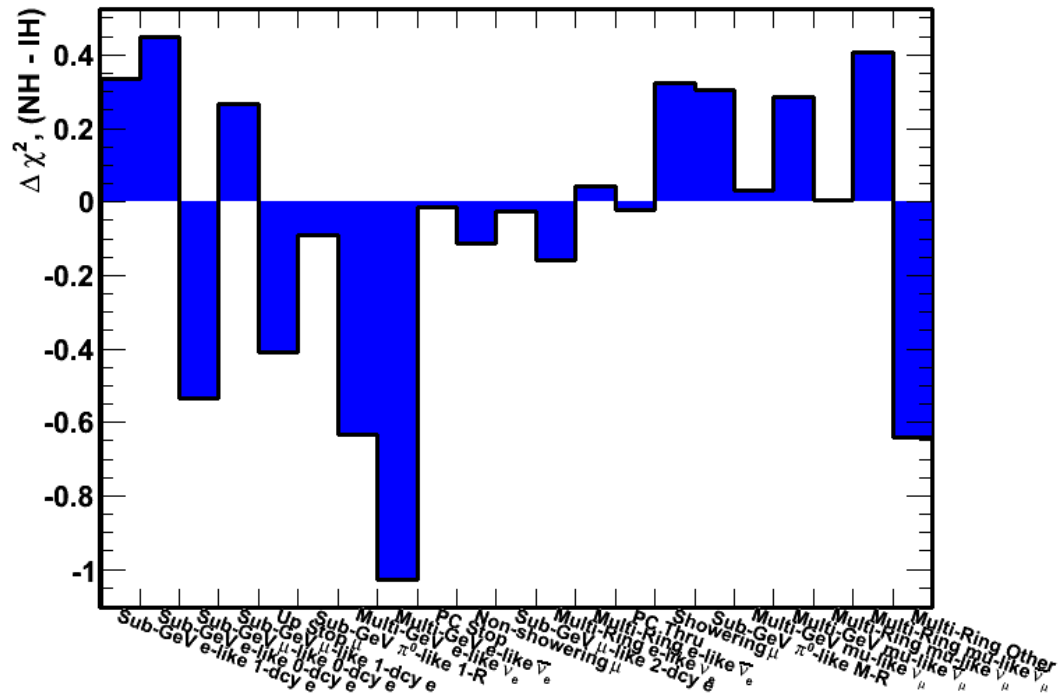


FIGURE 9.23: The contribution to $\Delta\chi^2(\text{NH-IH})$ for each sample in the analysis. The samples favouring normal hierarchy are primarily the Multi-GeV 1-ring e-like samples, and the Multi-GeV Multi-Ring Other sample.

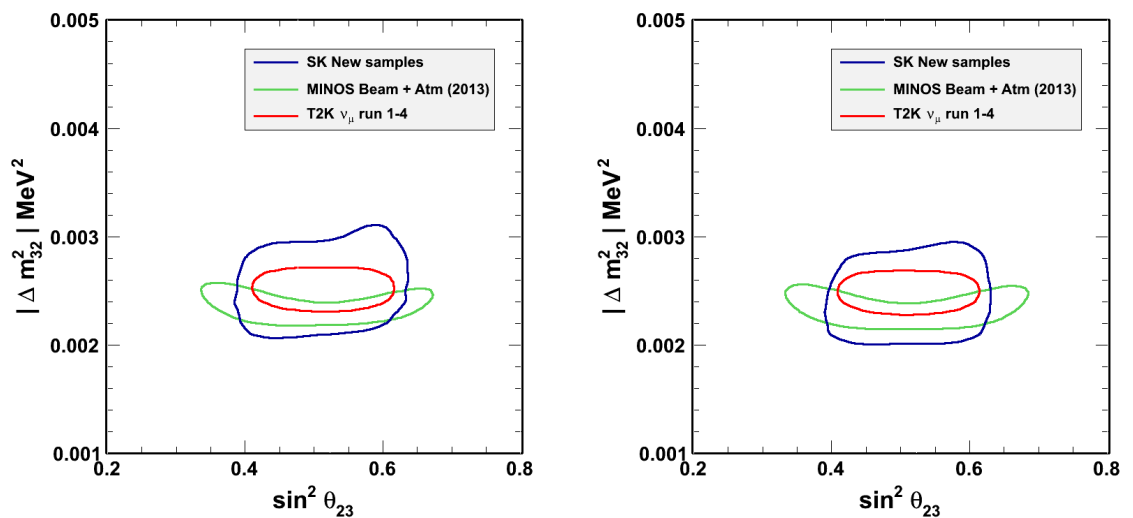


FIGURE 9.24: Comparison of the 90% confidence level contours between the analysis presented in this thesis (blue) and published results from the MINOS (green) [31] and T2K (red) [32] experiments.

9.7 The Future

So the questions remains - if we are not able to deduce the neutrino mass hierarchy using the current generation detector and analysis techniques, how do we proceed from here?

Super-Kamiokande clearly has some sensitivity to the neutrino mass hierarchy, but remains limited by its systematic and statistical errors. If at some point in the future we are able to understand our detector perfectly and reduce systematic error to 0, the mass hierarchy sensitivity (assuming true NH) improves from $\Delta\chi^2 = 1.87 \rightarrow 2.68$. This is a good improvement, however the detector is already mature and well understood, so it is difficult to significantly reduce systematic errors past the current level. Statistical error may be reduced simply by running the detector for a longer time period. An additional 10 years of runtime for Super-K would result in a mass hierarchy sensitivity improvement of $\Delta\chi^2 = 1.87 \rightarrow 3.23$ (see figure 9.25). Unfortunately even after this time a 2σ level of sensitivity cannot be achieved, so without major upgrades to the detector it is unlikely Super-K will make this discovery in the near future.

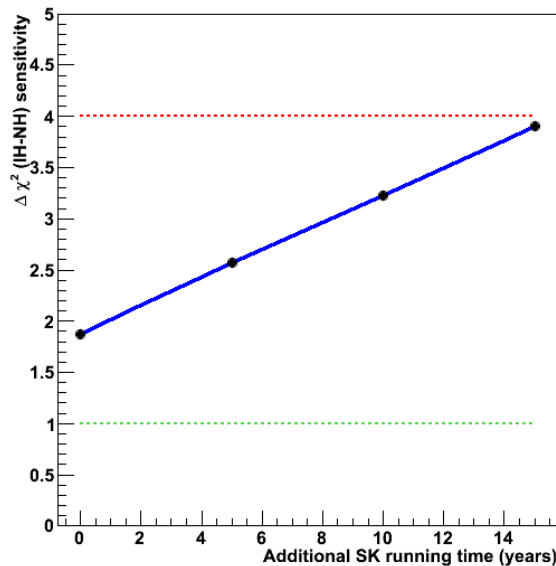


FIGURE 9.25: Expected future significance of neutrino mass hierarchy in Super-Kamiokande. The green and red dotted lines indicate 1σ and 2σ significance respectively. The oscillation parameters are as described at 9.7.

However there are other upcoming experiments that are potentially more sensitive to the neutrino mass hierarchy than Super-K. The NO ν A experiment, which started operation earlier this year (2014), produces a ν_μ beam with a long baseline of 810 km running from Fermilab to Minnesota [33]. This corresponds to a value of L/E well matching the matter effect resonant enhancement, and thus a good sensitivity to the neutrino mass hierarchy is expected. After 3(+3) years of running in neutrino (anti-neutrino) mode,

$\sim 3\sigma$ significance of hierarchy resolution may be achieved depending on the true value of δ_{CP} (figure 9.26).

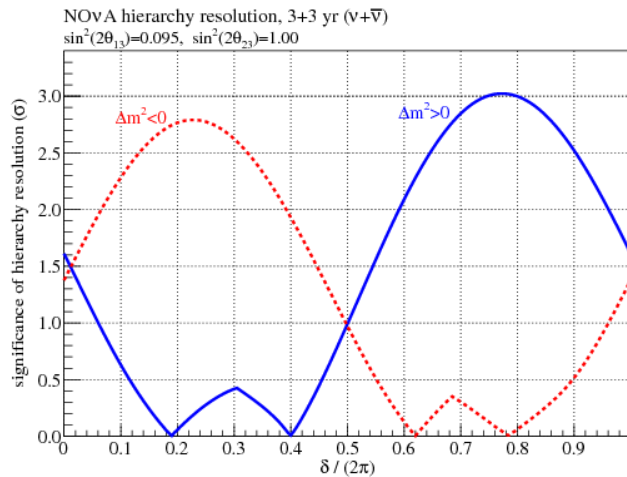


FIGURE 9.26: Expected significance of neutrino mass hierarchy in the NO ν A experiment, after 3 years each of ν_μ and $\bar{\nu}_\mu$ beam. The blue (dashed red) curves show the significance assuming the normal (inverted) hierarchies. Plot taken from [33].

The Indian Neutrino Observatory (INO) is a proposed experiment to further the study of atmospheric neutrinos [161]. It will use a 50 kton magnetized iron calorimeter, which allows for the separation of neutrino from anti-neutrino events based on the lepton track curvature. NO ν A is sensitive to uncertainty in the true value δ_{CP} , however measurements of the atmospheric neutrino matter effect enhancement in INO are virtually independent of this [34]. Depending on the true value of the neutrino oscillation parameters, a $\sim 3\sigma$ significance in the mass hierarchy determination after 10-20 years of running time (figure 9.27).

The direct successor to Super-Kamiokande is the proposed Hyper-Kamiokande experiment. Hyper-K is a 0.99 Mton water Cherenkov detector, with a fiducial volume ~ 25 times larger than Super-K [35]. Compared to Super-K, Hyper-K will have a lower photo-coverage of just 20%, which will make the neutron-tagging study of this thesis more difficult to perform, but mass hierarchy sensitivity can still be achieved from the relative cross sections and fluxes of neutrino and anti-neutrino. Thus a $\sim 3\sigma$ sensitivity is expected within 5 years of operation, depending on the true oscillation parameter values (figure 9.28).

The final experiment that should be discussed, is the PINGU upgrade to the IceCube experiment [162]. PINGU will add a compact set of 40 strings (each used to hold PMTs) to the centre of the experiment, reducing the detector's energy threshold down a few GeV. No direct distinction between neutrino and anti-neutrino is possible; differences in fluxes and cross sections are relied upon for measurements of neutrino mass hierarchy.

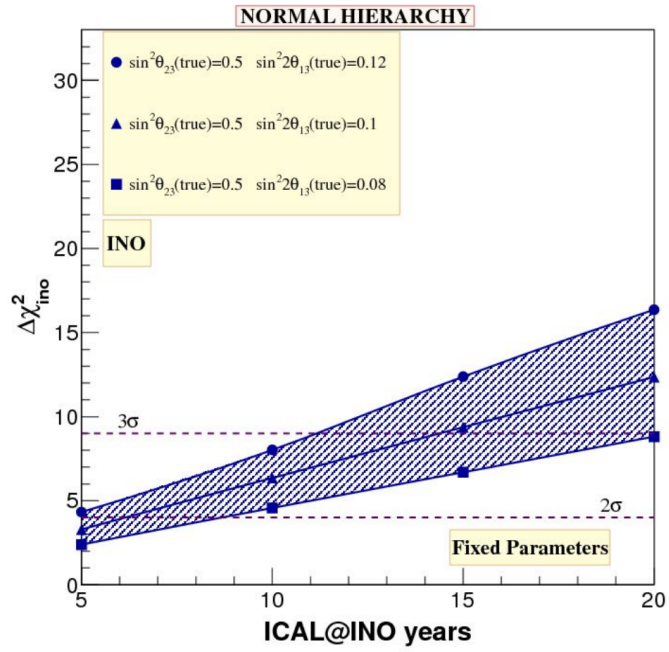


FIGURE 9.27: Expected sensitivity to the neutrino mass hierarchy of the proposed INO experiment. The blue shaded region represents different values for true $\sin^2\theta_{13}$. Plot taken from [34].

Due to a large predicted atmospheric neutrino flux and relative ease of construction, PINGU may be the first experiment to exceed 3σ mass hierarchy sensitivity (figure 9.29).

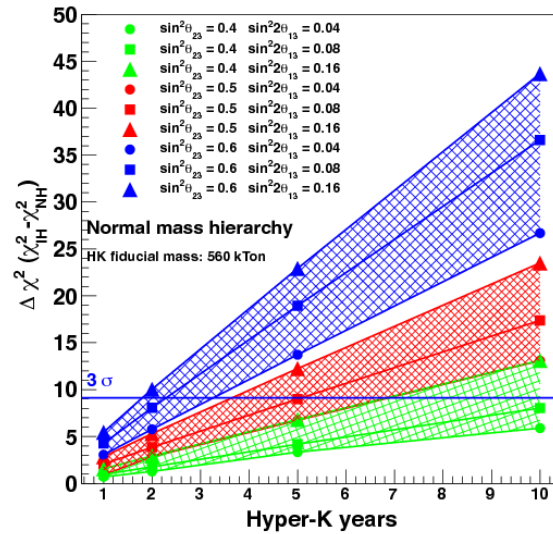


FIGURE 9.28: Expected sensitivity to the neutrino mass hierarchy of the Hyper-Kamiokande experiment. The different colours and shaded regions represent the expected hierarchy sensitivity given different true values of other neutrino oscillation parameters. Plot taken from [35].

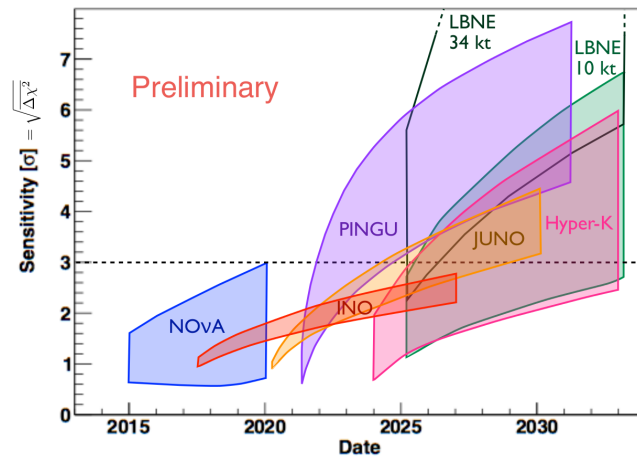


FIGURE 9.29: Expected mass hierarchy sensitivity of various future experiments. The widths represent uncertainty due to oscillation parameters. Plot taken from [36].

Chapter 10

Conclusion

Following atmospheric neutrino events in SK-IV, neutrons have been successfully identified via the characteristic 2.2 MeV γ ray produced after their capture on hydrogen. Using a neural network analysis the achieved neutron detection efficiency is 20.5%, and the expected mis-tagging rate is 1.8% per neutrino event. Neutron capture gamma-rays were effectively simulated and integrated into an atmospheric neutrino Monte-Carlo simulation, and the predicted number of neutrons was found to agree well with SK-IV data. Using this information and other improvements, the splitting of the Multi-GeV e-like samples into ν -like and $\bar{\nu}$ -like was updated. Similar separation was also implemented in Multi-GeV μ -like samples.

With this updated event binning, the neutrino mass hierarchy sensitivity was found to improve by $\Delta\chi^2 = 0.06$ ($\sim 5\%$), in both the true NH and true IH cases. This result represents the current world best neutrino mass hierarchy sensitivity. A three-flavour oscillation analysis was performed using all data from SK-I (1489.2 days FC data), SK-II (798.6 days FC data), SK-III (518.1 days FC data) and SK-IV (1775.6 days FC data). The fit values of Δm_{23}^2 and $\sin^2 \theta_{23}$ are consistent with results from T2K [32] and MINOS [31]. The results favour the normal hierarchy by $\Delta\chi^2(NH - IH) = -0.9$, which is insufficient to definitely determine the mass hierarchy. The fit results disfavour $\delta CP = 60^\circ$, however CP conservation is allowed within the 90% confidence level for both hierarchies.

Despite almost 20 years of operation, statistics still remain the major limiting factor in the measurement of the PMNS oscillation parameters at Super-Kamiokande. Study is ongoing into the possibility of adding a gadolinium compound to SK [163], which would produce an 8 MeV γ cascade following neutron capture. With an absorption efficiency of 90%, and potentially very high detection efficiency, this could further improve the neutrino anti-neutrino separation, and thus the detector's sensitivity to neutrino mass

hierarchy. A new reconstruction algorithm, fitQun [164], is also in development for use in SK, which could grant additional improvements to event sample purities. However, it may be that we must wait for the next generation of experiments, until the neutrino mass hierarchy can be conclusively determined.

Appendix A

Appendix: Systematic Error Tables

The estimated σ values, and ϵ corresponding to the best fit point for every (185) systematic error are shown here. Of the errors, 37 are common to all SK generations, and 37 (x4) are defined separately for SK-I to IV.

Flux Errors		Estimated σ (%)	Best Fit ϵ (%)
Absolute Normalization	$E_\nu < 1$ GeV	25.0	32.0
	$E_\nu > 1$ GeV	15.0	13.5
ν_μ/ν_e	$E_\nu < 1$ GeV	2.0	-1.9
	$1 < E_\nu < 10$ GeV	3.0	2.8
	$E_\nu > 10$ GeV	5.0	6.9
$\bar{\nu}_e/\nu_e$	$E_\nu < 1$ GeV	5.0	6.0
	$1 < E_\nu < 10$ GeV	5.0	4.4
	$E_\nu > 10$ GeV	8.0	-1.8
$\bar{\nu}_\mu/\nu_\mu$	$E_\nu < 1$ GeV	2.0	-0.3
	$1 < E_\nu < 10$ GeV	6.0	-0.8
	$E_\nu > 10$ GeV	15.0	2.6
Up/Down ratio		1.0	-1.8
Horizontal/vertical ratio		1.0	0.5
K/ π ratio		10.0	-7.5
Neutrino path length		10.0	5.9
Relative Normalization	FC MultiGeV	5.0	-6.9
	PC, UPMU Stop	5.0	-3.7
Matter Effect		6.8	- 1.5
Solar Activity	SK-I	20.0	-0.5
	SK-II	50.0	12.5
	SK-III	20.0	1.6
	SK-IV	10.0	0.7

Neutrino Interaction Errors	Estimated σ (%)	Best Fit ϵ (%)
Axial Mass	10.0	-17.7
CC ν_τ Cross Section	25.0	-33.8
CCQE $\bar{\nu}/\nu$ ratio	10.0	15.3
CCQE ν_μ/ν_e ratio	10.0	5.74
CCQE cross section model	10.0	3.65
Coherent π production	100.0	19.5
DIS cross section model ($E_\nu < 10$ GeV)	10.0	-0.2
DIS cross section	5.0	-2.1
DIS Q^2 spectrum ($W < 1.3$ GeV/ c^2)	10.0	4.2
DIS Q^2 spectrum ($W > 1.3$ GeV/ c^2)	10.0	0.0
Hadronic Simulation	10.0	0.8
NC/CC ratio	20.0	3.7
Single π production $\bar{\nu}/\nu$ ratio	10.0	-6.6
Single π production π^0/π^\pm ratio	40.0	-20.2
Single meson production cross section	20.0	11.5
Decay Electron tagging (π interaction)	10.0	-9.1

Oscillation Parameter Errors	Estimated σ (%)	Best Fit ϵ (%)
θ_{13}	1.0	-0.1
θ_{12}	2.1	-0.1

Sample Migration Errors	SK-I		SK-II		SK-III		SK-IV	
	σ	ϵ	σ	ϵ	σ	ϵ	σ	ϵ
Multi-GeV 1-Ring e-like ν -like	10.0	6.0	7.9	0.8	9.3	4.7	12.5	4.9
Multi-GeV 1-Ring e-like $\bar{\nu}$ -like	0.2	-0.1	0.5	0.1	0.2	-0.1	0.3	-0.1
Multi-GeV 1-Ring μ -like ν -like	1.7	0.4	1.5	0.1	1.6	0.2	3.1	-4.1
Multi-GeV 1-Ring μ -like $\bar{\nu}$ -like	1.8	-0.2	1.8	-0.1	1.8	-0.1	2.6	1.7
Multi-GeV Multi-Ring e-like ν -like	1.1	0.1	0.8	0.1	1.0	-0.1	1.0	0.1
Multi-GeV Multi-Ring e-like $\bar{\nu}$ -like	1.0	0.0	1.2	-0.1	1.1	0.0	1.3	-0.1
Multi-GeV Multi-Ring μ -like ν -like	1.9	-1.7	1.7	-0.9	2.6	0.1	3.6	-5.2
Multi-GeV Multi-Ring μ -like $\bar{\nu}$ -like	2.8	0.8	3.1	0.7	2.5	0.0	4.0	1.6
Multi-GeV Multi-Ring Other	10.0	-10.4	10.0	-4.9	10.0	-12.3	10.0	-1.5

Reconstruction Errors	SK-I		SK-II		SK-III		SK-IV	
	σ	ϵ	σ	ϵ	σ	ϵ	σ	ϵ
Single-Ring PID	1.0	-0.1	1.0	0.2	1.0	-0.1	1.0	0.0
Multi-Ring PID	10.0	6.5	10.0	8.5	10.0	-1.2	10.0	3.5
Ring Separation	10.0	4.8	10.0	-8.0	10.0	2.1	10.0	-2.2
Single-Ring π^0 selection	10.0	2.8	10.0	2.1	10.0	2.9	10.0	4.6
Two-Ring π^0 selection	5.6	-0.5	4.4	-2.7	5.9	-1.6	5.6	1.4
Decay-e tagging efficiency 10.0	-5.5	10.0	-2.9	10.0	1.5	10.0	0.1	
Energy Calibration	1.1	-0.1	1.7	-0.5	2.7	0.6	2.3	-0.2
Energy Calibration Up/down ratio	0.6	0.3	0.6	0.0	1.3	0.3	0.3	-0.2

Reduction Errors	SK-I		SK-II		SK-III		SK-IV	
	σ	ϵ	σ	ϵ	σ	ϵ	σ	ϵ
FC Reduction	0.2	0.0	0.2	0.0	0.8	0.1	0.3	0.0
Fiducial Volume	2.0	-0.6	2.0	-0.4	2.0	-0.6	2.0	-0.6
Non- ν BG (μ -like)	1.0	0.3	1.0	0.2	1.0	-0.1	1.0	0.0
Non- ν BG (SubGeV e-like)	1.0	0.1	1.0	0.0	1.0	0.0	1.0	0.0
Non- ν BG (MultiGeV 1R e-like)	13.2	0.9	38.1	-9.9	26.7	2.4	17.6	0.9
Non- ν BG (MultiGeV Multi-Ring e-like)	12.1	11.6	11.1	6.4	11.4	5.5	11.6	4.8
FC/PC Separation	0.6	0.0	0.5	0.1	0.9	0.0	0.0	0.0
PC Reduction	2.4	-1.6	4.8	-4.3	0.5	-0.1	1.0	-0.6
PC Stop-Thru Separation (Barrel)	7.0	1.1	9.4	-6.7	28.7	-12.5	8.5	-2.4
PC Stop-Thru Separation (Bottom)	22.7	-27.0	12.9	-0.9	12.1	-0.9	6.8	-2.3
PC Stop-Thru Separation (Top)	46.1	3.2	19.4	-4.3	86.6	19.2	40.3	-17.5
UPMU Stop-thru separation	0.4	0.0	0.6	0.0	0.4	0.0	0.6	-0.1
UPMU Reduction	1.0	-0.1	1.0	-0.2	1.0	0.2	1.0	0.2
UPMU Stop BG	16.0	16.3	21.0	-1.5	20.0	3.3	17.0	-0.5
UPMU Stop Energy cut	0.9	0.1	1.3	0.2	2.0	0.8	1.7	-0.2
UPMU Thru Path cut	1.5	0.2	2.3	0.8	2.8	-1.2	1.5	-1.8
Non-Showering BG	18.0	-5.9	14.0	-0.2	24.0	0.3	17.0	2.1
Shower Non-shower separation	3.4	5.6	4.4	-1.3	2.4	2.9	3.0	4.1
Showering BG	18.0	-7.3	14.0	-13.0	24.0	2.8	24.0	-1.5

Bibliography

- [1] B. Aharmim et al. (SNO collaboration). *Phys Rev C*, 72:055502, 2005.
- [2] Y. Fukuda et al. (Super Kamiokande Collaboration). *Phys Lett B*, 539:179, 2002.
- [3] P. Adamson et al. (MINOS Collaboration). *Phys. Rev. Lett.*, 106:181801, 2011.
- [4] K. Abe et al. (T2K Collaboration). *arXiv*, 1308:0465.
- [5] F.P. An et al. (DayaBay Collaboration). *Phys. Rev. Lett.*, 108:131801, 2012.
- [6] S. Yamada et. al. Commissioning of the new electronics and online system for the super-kamiokande experiment. *Nuclear Science, IEEE Transactions*, 57:428–432, 2010.
- [7] M. Honda et. al. *Phys. Rev. D*, 83:123001, 2011.
- [8] S.J.Barish et al. *Phys. Rev. D*, 16(3103), 1977.
- [9] S.Bonetti et al. *Nuovo Cimento*, 38(260), 1977.
- [10] S.V.Belikov et. al. *Z. Phys. A*, 320:625, 1985.
- [11] N.Armenise et al. *Nucl. Phys. B*, 152(365), 1979.
- [12] Y. Hayato. *Nucl. Phys. Proc. Suppl.*, 112:171, 2002.
- [13] G.M.Radecky et al. *Phys. Rev. D*, 25(1161), 1982.
- [14] Proc. of the 1979 international symp. on lepton and photon. 1979.
- [15] T.Eichten et al. *Phys. Lett. 64B*, (273), 1973.
- [16] S.Ciampolillo et al. *Phys. Lett. 84B*, (281), 1979.
- [17] J.G.Morfin et al. *Phys. Lett. 104B*, (235), 1981.
- [18] D.S.Baranov et al. *Phys. Lett. 81B*, (255), 1979.
- [19] D.C.Colley et al. *Z.Phys. C2*, (187), 1979.

-
- [20] A.S.Vovenko et al. *Yad. Fiz.* 30, (1014), 1979.
- [21] S.J.Barish et al. *Phys.Rev.D19*, (2521), 1979.
- [22] C.Bltay et al. *Phys.Rev.Lett.*, (916), 1980.
- [23] N.I.Bker et al. *Phys. Rev. D*, 25(617), 1982.
- [24] V.N.Anikeev et al. *Z.Phys. C*, 70(39), 1996.
- [25] O.Erriquez et al. *Phys. Lett. 80B*, (309), 1979.
- [26] J. Formaggio and G. P. Zeller. From ν_e to $\bar{\nu}_e$: Neutrino cross sections across energy scales. *Rev. Mod. Phys.*, 84:1307, 2012.
- [27] D. Ashery et al. *Phys. Rev. C*, (2173), 1981.
- [28] M.Meier et al. *Nucl. Sci. Eng.*, 104(4):339.
- [29] L.A.Charlton T.A.Gabriel. Charged and neutral particle transport methods and applications: The calor code system. 1997.
- [30] J.Galin et al. Neutron multiplmulti measurements in 2 gev p and ^3he induced reactions on thin targets of heavy materials. *Proc. 8th Journees de SATURNE*, 1995.
- [31] P. Adamson et al. (MINOS Collaboration). Measurement of neutrino and antineutrino oscillations using beam and atmospheric data in minos. *Phys. Rev. Lett.*, 110:251801, 2013.
- [32] K. Abe et. al. (T2K Collaboration). Precise measurement of the neutrino mixing parameter θ_{23} from muon neutrino disappearance in an off-axis beam. *Phys. Rev. Lett.*, 112:181801, 2014.
- [33] R.B. Patterson (The NOvA Collaboration). The nova experiment: status and outlook. *Nucl. Phys. B (proc. suppl.)*, 2012.
- [34] A. Ghosh et al. Determining the neutrino mass hierarchy with ino, t2k, nova and reactor experiments. *JHEP*, 04(009), 2013.
- [35] K. Abe et. al. (The Hyper-Kamiokande Collaboration). Letter of intent: The hyper-kamiokande experiment — detector design and physics potential —. *arXiv*, 1109:3262, 2011.
- [36] PINGU collaboration IceCube. Pingu sensitivity to the neutrino mass hierarchy. *arXiv:1306.5846*, 2013.

- [37] J. Chadwick. The intensity distribution in the magnetic spectrum of β particles from radium (b + c). *Verh. Phys. Gesell*, 16:383–391, 1914.
- [38] J. Chadwick. Possible existence of a neutron. *Nature*, 129:312, 1932.
- [39] E. Fermi. An attempt of a theory of beta radiation. *Z. Phys*, 88:161–177, 1934.
- [40] R. Davis and D. Harmer. Attempt to observe the $^{37}\text{Cl}(\nu, e^-)^{37}\text{Ar}$ reaction induced by reactor antineutrinos. *Bull. Am. Phys. Soc.*, 4:217, 1959.
- [41] R. Davis and D. Harmer. Observation of high energy neutrino reactions and the existence of two kinds of neutrinos. *Phys. Rev. Lett.*, 9:36–44, 1962.
- [42] W.; Dakin J. et al. Perl M. L.; Abrams G.; Boyarski, A.; Breidenbach M.; Briggs D.; Bulos F.; Chinowsky. Evidence for anomalous lepton production in e^+e^- annihilation. *Phys. Rev. Lett.*, 35:1489, 1975.
- [43] K. Kodama et al. Observation of tau-neutrino interactions. *Phys. Lett.*, B504: 218–224, 2001.
- [44] J.N. Bahcall. Solar neutrinos. i: Theoretical. *Phys. Rev. Lett.*, 12:300–302, 1964.
- [45] J.N. Bahcall. Solar models: current epoch and time dependences, neutrinos, and helioseismological properties. *Astrophys. J*, 555:990, 2001.
- [46] Raymond Davis Jr.; Don S. Harmer and Kenneth C. Hoffman. Search for neutrinos from the sun. *Phys. Rev. Lett.*, 20:1205–1209, 1968.
- [47] Bruce T. et al. Measurement of the solar electron neutrino flux with the homestake chlorine detector. *Astrophys. J*, 496:505–526, 1998.
- [48] Gian Luigi Fogli; E. Lisi and D. Montanino. A comprehensive analysis of solar, atmospheric, accelerator and reactor neutrino experiments in a hierarchical three generation scheme. *Phys. Rev. D*, 49:3626–2642, 1994.
- [49] Dzh.N. Abdurashitov et. Al. Results from sage. *Phys. Lett. B*, 328:234–248, 1994.
- [50] V. N. Gribov and B. Pontecorvo. Neutrino astronomy and lepton charge. *Phys. Lett.*, B28:493, 1969.
- [51] J. Schechter and J. W. F. Valle. Neutrino decay and spontaneous violation of lepton number. *Phys. Rev. D*, 25:774, 1982.
- [52] K. Hirata et al. Observation of a neutrino burst from the supernova sn 1987a. *Phys. Rev. Lett.*, 58:1490–1493, 1987.

- [53] K. Hirata et al. Observation of a small atmospheric ν_μ/ν_e ratio in kamiokande. *Phys. Lett. B*, 280:146–152, 1992.
- [54] Y. Fukuda et. al. Atmospheric ν_μ/ν_e ratio in the multi-gev energy range. *Phys. Lett. B*, 335:237–245, 1994.
- [55] D. Casper et. al. Measurement of atmospheric neutrino composition with the imb-3 detector. *Phys. Rev. Lett.*, 66:2561, 1991.
- [56] Y. Ashie et. al. Evidence for an oscillatory signature in atmospheric neutrino oscillations. *Phys. Rev. Lett.*, 93:101801, 2004.
- [57] Q. R. Ahmad et al. Measurement of the charged current interactions produced by b-8 solar neutrinos at the sudbury neutrino observatory. *Phys. Rev. Lett.*, 87:071301, 2001.
- [58] Q. R. Ahmad et al. Direct evidence for neutrino flavor transformation from neutral current interactions in the sudbury neutrino observatory. *Phys. Rev. Lett.*, 89:011301, 2002.
- [59] Y-M Yao et al. Review of particle physics. *J. Phys. G: Nucl. Part. Phys.*, 33:1, 2006.
- [60] Masami Nakagawa Ziro Maki and Shoichi Sakata. Remarks on the unified model of elementary particles. *Prog. Theor. Phys.*, 28:870–880, 1962.
- [61] D.E. Groom et al. *Eur. Phys. Jour. C*, 15:1, 2000.
- [62] Lincoln Wolfenstein. Neutrino oscillations in matter. *Phys. Rev. D*, 17:2369–2374, 1978.
- [63] S. P. Mikheev and A. Yu. Smirnov. Resonance enhancement of oscillations in matter and solar neutrino spectroscopy. *Sov. J. Nucl. Phys.*, 42:913–917, 1985.
- [64] V. Barger et al. Matter effects on three-neutrino oscillations. *Phys. Rev. D*, 22:2718, 1980.
- [65] K. Nakamura et al. Neutrino mass, mixing, and oscillations. *Particle Data Group*, pages 1–62, 2013.
- [66] J. H. Christenson J. W. Cronin V. L. Fitch and R. Turlay. Evidence for the 2-pi decay of the $k(2)0$ meson. *Phys. Rev. Lett.*, 13:138–140, 1964.
- [67] K. Nakamura et al. Review of particle physics. *J. Phys. G*, 37:075021, 2010.
- [68] J. Charles et al. Cp violation and the ckm matrix: assessing the impact of the asymmetric b factories. *Eur. Phys. Journal C*, 41:1–131, 2005.

- [69] G. Bellini et al. (Borexino Collaboration). *Phys Rev Lett*, 107:141302, 2011.
- [70] B. Aharmim et al. (SNO collaboration). *Phys Rev C*, 88:025501, 2013.
- [71] K. Abe et al. (Super Kamiokande Collaboration). *Phys Rev D*, 83:052010, 2011.
- [72] K. Eguchi et al. (KamLAND Collaboration). *Phys Rev Lett*, 90:021802, 2003.
- [73] A. Gando et al. (KamLAND Collaboration). *Phys Rev D*, 88:033001, 2013.
- [74] Y. Itow et al. *Nucl. Phys. B (proc. Suppl.)*, 79:235–236, 2013.
- [75] K. Abe et al. (Super Kamiokande Collaboration). *Phys. Rev. Lett.*, 110:181802, 2013.
- [76] M.H. Ahn et al. (K2K Collaboration). *Phys. Rev. D*, 74:072003, 2006.
- [77] P. Adamson et al. (MINOS Collaboration). *Phys. Rev. Lett.*, 107:021801, 2011.
- [78] J. Evans (MINOS collaboration). The minos experiments: results and prospects. *arXiv:1307.0721*, 2013.
- [79] K. Abe et al. (T2K Collaboration). *Phys. Rev. D*, 85:031103, 2012.
- [80] A. Pastore. Talk at eps hep 2013 conference, stockholm. 2013.
- [81] F.P. An et al. (DayaBay Collaboration). *Chinese Phys. C*, 37:011001, 2013.
- [82] S.H. Seo. Talk at xv international workshop on neutrino telescopes, venice. 2013.
- [83] Y. Abe et al. (Double Chooz Collaboration). *Phys. Rev. D*, 86:052008, 2012.
- [84] M. Wilking. Talk at eps hep 2013 conference, stockholm. 2013.
- [85] P. Adamson et al (MINOS Collaboration). Talk at eps hep 2013 conference, stockholm. *Phys. Rev. Lett.*, 110:171801, 2013.
- [86] B. Aharmim et al. (SNO collaboration). *Phys Rev C*, 81:055504, 2010.
- [87] G. L. Fogli et. al. Global analysis of neutrino masses, mixings, and phases: Entering the era of leptonic cp violation searches. *Phys Rev D*, 86:013012, 2012.
- [88] The Super Kamiokande Collaboration. *Nucl. Inst. Meth.*, 501A:418, 2003.
- [89] H. Kume et al. *Nucl. Inst. Meth.*, 205:443, 1983.
- [90] Y. Takeuchi et al. Measurement of radon concentrations at super-kamiokande. *Phys. Lett. B*, 452:418–424, 1999.

-
- [91] H. G. Berns. Radon hut user manual, super kamiokande. *Internal SK Documentation*, 2005.
- [92] H. Ikeda et. al. *Nucl. Inst. and Meth. A*, 320:310, 1992.
- [93] K Abe et. al. (Super Kamiokande Collaboration). Calibration of the superkamiokande detector. *Nucl. Inst. and Meth. A*, 737C, 2014.
- [94] Y. Fukuda et. al. (Super Kamiokande Collaboration). *Nucl. Inst. and Meth. A*, 501:418, 2003.
- [95] E. Pope R. Fry. *Appl. Opt.*, 33:8710, 1997.
- [96] G. Battistoni et al. *Astropart. Phys.*, 19:269, 2003.
- [97] G. Barr et al. *Phys. Rev. D*, 70:0423006, 2004.
- [98] J. Alcaraz et. al. Cosmic protons. *Phys. Lett. B*, 490:27–35, 2000.
- [99] T. Sanuki et al. Precise measurement of cosmic-ray proton and helium spectra with the bess spectrometer. *Astrophys. J*, 545:1135–1142, 2000.
- [100] M. Honda et al. A new calculation of the atmospheric neutrino flux in a 3-dimensional scheme. *Phys. Rev. D*, 70:043008, 2004.
- [101] S. Roesler et al. A new calculation of the atmospheric neutrino flux in a 3-dimensional scheme. *Phys. Rev. D*, 57:2889, 1998.
- [102] K. Niita et al. *Radiation Measurements*, 41:1080, 2006.
- [103] HARP Collaboration. Forward π^\pm production in $p - o_2$ and $p - n_2$ interactions at 12 gev/c. *Astroparticle Physics*, 30:124–132, 2008.
- [104] S. Haino et al. (BESS). *Phys. Lett. B*, 594:35, 2004.
- [105] T. Sanuki et al. *Phys. Lett. B*, 541:234, 2002.
- [106] K. Abe et al. (BESS). *Phys. Lett. B*, 564:8, 2003.
- [107] C.H. Llewellyn Smith. Neutrino reactions at accelerator energies. *Phys. Rept.*, 3: 261–379, 1972.
- [108] R. A. Smith and E. J. Moniz. Neutrino reactions on nuclear targets. *Nucl. Phys. B*, 43:605, 1972.
- [109] L.A. Ahrens et al. Precise determination of $\sin^2 \theta_w$ from measurements of the differential cross-sections for muon-neutrino $p \rightarrow n$ muon-neutrino p and anti-muon-neutrino $p \rightarrow n$ anti-muon-neutrino p . *Phys. Rev. Lett.*, 56:1107, 1986.

-
- [110] C. H. Albright et al. Neutrino - proton elastic scattering: Implications for weak interaction models. *Phys. Rev. D*, 14:1780, 1976.
- [111] R. Gran et. al. *Phys. Rev. D*, 74:052002, 2006.
- [112] A. A. Aguilar-Arevalo et al. et. al. *Phys. Rev. Lett.*, 100:032301, 2008.
- [113] D. Rein and L. M. Sehgal. Neutrino excitation of baryon resonances and single pion production. *Annals Phys.*, 133:79–153, 1981.
- [114] D. Rein. *Z. Phys. C*, 35:43–64, 1987.
- [115] D. Rein and L.M. Sehgal. *Nucl. Phys. B*, 223:29, 1983.
- [116] M. Guck et al. *Eur. Phys. J C*, 5:461, 1998.
- [117] A. Bodek and U.K. Yang. *hep-ex/0308007*.
- [118] S.J.Barish et al. *Phys Rev D*, 17:1, 1978.
- [119] T. Sjostrand et al. *CERN-TH-7112-93*, 1994.
- [120] L. L. Salcedo E. Oset M. J. Vicente-Vacas and C. Garcia-Recio. Computer simulation of inclusive pion nuclear reactions. *Nucl. Phys. A*, 484:557, 1988.
- [121] P. de Perio et. al. *T2K Technical Note 33 v2.0*.
- [122] D. Ashery et al. *Phys. Rev. C*, 23:2173, 1981.
- [123] B.R. Martin and M.K. Pidcock. *Nucl. Phys. B*, 126:266, 1977.
- [124] B.R. Martin and M.K. Pidcock. *Nucl. Phys. B*, 126:285, 1977.
- [125] J.S. Hyslop et al. *Phys. Rev. D*, 46:961, 1992.
- [126] D.A. Sparrow. *Proc. of the Conf. on the intersection between particle and nuclear physics*, 1019, 1984.
- [127] R. Brun and F. Carminati. *CERN Programming Long Writeup W5013*, 1993.
- [128] C. Zeitnitz and T.A. Gabriel. *Nucl. Instr. Meth. A*, 349, 1994.
- [129] A. Fasso et al. Fluka 92. *Proceedings of the Workshop on Simulating Accelerator Radiation Environments*, 1993.
- [130] Hetc: Monte carlo high-energy nucleon-meson transport code. *Oak Ridge National Laboratory RSIC Computer Code Collection CCC-178*.
- [131] J.O.Johnson and T.A.Gabriel. A user's guide to micap: A monte carlo ionization chamber analysis package. *ORNL/TM-10340*, 1988.

- [132] H. W. Bertini. *Phys. Rev.*, 188:1711, 1969.
- [133] E. R. Davies. Machine vision: Theory; algorithms; practicalities. *Morgan Kaufmann Publishers Inc.*, 2004.
- [134] R. A. Wendell. Three flavor oscillation analysis of atmospheric neutrinos in super-kamiokande. *Doctoral Thesis*, 2008.
- [135] T. Barszczak. The efficient discrimination of electron and pi-zero events in a water cherenkov detector and the application to neutrino oscillation experiments. *Doctoral Thesis*, 2005.
- [136] M. Smy (Super Kamiokande Collaboration). The efficient discrimination of electron and pi-zero events in a water cherenkov detector and the application to neutrino oscillation experiments. *Proc. of the 30th ICRC*, 5:1279, 2007.
- [137] S. Desai. High energy neutrino astrophysics with super-kamiokande. *Doctoral Thesis*, 2004.
- [138] S.I. Klimushin; E.V. Bugaev and I. A. Sokalski. Precise parameterizations of muon energy losses in water. *arXiv:hep-ph/0106010v1*, 2001.
- [139] D. Cokinos and E. Melkonian. Measurement of the 2200m/sec neutron-proton capture cross section. *Phys. Rev. C*, 15:1636, 1977.
- [140] H. Zhang et. al (Super Kamiokande Collaboration) H. Watanabe. First study of neutron tagging with a water cherenkov detector. *Astropart. Phys.*, 31:320–328, 2009.
- [141] The Super-Kamiokande Collaboration. The super kamiokande detector. *Nucl. Instr. Meth.*, pages 418–462.
- [142] D. Shanno. Conditioning of quasi-newton methods for function minimization. *Math. Comp.*, 24:647–656, 1970.
- [143] T. Kavzoglu. Determining optimum structure for artificial neural networks. *Annual Technical Conference and Exhibition of the Remote Sensing Society*, 2:675–682, 1999.
- [144] N. Wanas. On the optimal number of hidden nodes in a neural network. *IEEE Canadian Conference*, 2:918–921, 1998.
- [145] H. Zhang. Study of low energy electron anti-neutrinos at super-kamiokande iv. *PhD Thesis*, 2012.

- [146] Gando et. al (The KamLAND Collaboration). Constraints on θ_{13} from a three-flavour oscillation analysis of reactor antineutrinos at kamland. *Phys. Rev. D*, 83:052002, 2011.
- [147] G.L.Fogli et. al. *Phys. Rev. D*, 66:053010, 2002.
- [148] Lee Ka Pik. *Study of the neutrino mass hierarchy with the atmospheric neutrino data observed in Super-Kamiokande*. PhD thesis, University of Tokyo, 2012.
- [149] CERN ROOT. Tmva - multi variate analysis. <http://tmva.sourceforge.net/>.
- [150] G. Ambrosini et al. *Phys. Lett. B*, 420:225, 1998.
- [151] A. E. Hedin. *J. Geophys, Res.* 96:1159, 1991.
- [152] Dziewonski and Anderson. *Phys. Earth. Planet. Int.*, 25:297–356, 1981.
- [153] M. Honda et al. *Phys. Rev. D*, 75:043005, 2007.
- [154] J. Nieves et al. *Phys. Rev. C*, 70:055503, 2004.
- [155] R. Gran et. al. *Phys Rev. D*, 74:052002, 2006.
- [156] M.J. Vicente Vacas J. Nieves, I. Ruiz Simo. The nucleon axial mass and the miniboone quasielastic neutrino-nucleus scattering problem. *arXiv*, 1106.5374v2, 2011.
- [157] E. Hernandez et al. *Phys. Rev. D*, 76:033005, 2007.
- [158] Y. Nakajima et al. (SciBooNE). Measurement of inclusive charged current interactions on carbon in a few-gev neutrino beam. *Phys. Rev. D*, 83:012005, 2011.
- [159] A. Capella et al. *Phys. Lett. B*, 337:358, 1994.
- [160] K. Hagiwara et al. *Nucl. Phys. B*, 668:364, 2003.
- [161] K. Naba Mondal. Status of india-base neutrino observatory (ino). *Proc. Indian National Science Academy*, 70A:71–77, 2004.
- [162] M.G.Aartsen et al. (The IceCube Collaboration). Letter of intent: The precision icecube next generation upgrade (pingu). *arXiv:1401.2046v1*, 2014.
- [163] L. Marti (Super-Kamiokande Collaboration). 32nd international cosmic ray conference, beijing. 2012.
- [164] P.de Perio. Updates to the fitqun event reconstruction and interface to wcsim. In *Hyper-Kamiokande Workshop 3*, 2013.